Ultrafast Carotenoid-Mediated Dynamics in the Light-Harvesting Complex of Green Plants

by

Minjung Son

B.S., Yonsei University (2013)
M.S., Yonsei University (2015)

Submitted to the Department of Chemistry
in partial fulfillment of the requirements for the degree of

Doctor of Philosophy in Chemistry

at the

MASSACHUSETTS INSTITUTE OF TECHNOLOGY

September 2020

Author .....
Department of Chemistry
August 14, 2020

Certified by .....
Gabriela S. Schlau-Cohen
Cabot Career Development Associate Professor
Thesis Supervisor

Accepted by .....
Adam P. Willard
Associate Professor
Graduate Officer

This doctoral thesis has been examined by a Committee of the Department of Chemistry as follows:

Keith A. Nelson .....
Chairman, Thesis Committee
Haslam and Dewey Professor of Chemistry

Gabriela S. Schlau-Cohen .....
Thesis Supervisor
Cabot Career Development Associate Professor of Chemistry

William A. Tisdale .....
Member, Thesis Committee
ARCO Career Development Professor of Chemical Engineering

Ultrafast Carotenoid-Mediated Dynamics in the Light-Harvesting Complex of Green Plants

by

Minjung Son

Submitted to the Department of Chemistry
on August 14, 2020, in partial fulfillment of the
requirements for the degree of
Doctor of Philosophy in Chemistry

Abstract

Photosynthetic organisms, including green plants, have mastered the ability to efficiently capture sunlight and rapidly transport the absorbed energy to drive life-sustaining chemical reactions. At the same time, they have evolved mechanisms to dynamically regulate photosynthetic efficiency to protect against photodamage in excess sunlight, by dissipating excess energy as heat. Both light harvesting and photoprotective dissipation take place within pigment-binding membrane proteins called light-harvesting complexes, and originate from the interactions of the electronic transitions of the bound pigments that span the visible solar spectrum. In particular, carotenoids, the accessory light-harvesting pigments in plants, are thought to play a central role in mediating both light-harvesting and dissipative pathways by leveraging their unique electronic structure with one or more dark states and extreme sensitivity to local environment. However, carotenoid-mediated photophysics in plants have remained poorly understood due to limited spectral bandwidths of previous ultrafast measurements as well as use of unphysiological experimental environments. In this thesis, I describe how I overcome both limitations by combining an ultrabroadband ultrafast spectroscopic technique with improved spectral bandwidth and a near-physiological model membrane to house the light-harvesting complexes with conformations close to their native ones. In Chapter 2, I describe the development of a high-sensitivity ultrabroadband two-dimensional electronic spectrometer that enables interrogation of the energetics and dynamics of the broad range of electronic transitions of photosynthetic light-harvesting complexes across the visible solar spectrum. Then, I discuss the application of this technique on studies of the light-harvesting and dissipative photophysical pathways in light-harvesting complex II (LHCII), the principal light-harvesting complex in green plants. A series of previously uncharacterized carotenoid-mediated light-harvesting and dissipative pathways are uncovered. In Chapter 3, I find that one of the four carotenoids bound within LHCII plays an integral role in mediating the rapid and efficient energy transfer in plants, partially via a previously debated but unobserved dark state. In Chapters 4−6, I discuss the direct observation of a predicted but uncharacterized dissipative energy transfer pathway

involving a short-lived carotenoid dark state. The sensitivity of dissipation to local environment, carotenoid composition, and protein-protein interaction is explored within the near-physiological model membrane platform.

Thesis Supervisor: Gabriela S. Schlau-Cohen
Title: Cabot Career Development Associate Professor

Acknowledgments

I first thank my advisor Prof. Gabriela Schlau-Cohen, who gave me the opportunity to work on and answer some of the coolest questions to be answered in the field of photosynthesis. Gabriela was available whenever I needed her for scientific discussions or just wanted to rant about something that was not going well in lab, and talking to her immediately made me have a little more faith in myself. She also taught me how to be a better writer and speaker, and I am truly grateful to her for the improvements in scientific communication skills I have made over the years I worked with her. I am grateful to my thesis committee members Profs. Keith Nelson and Will Tisdale, for their highly contagious enthusiasm for science and for the great questions and comments they have asked and given me about my research progress throughout the years.

I am indebted to all the members of the Schlau-Cohen group, past and present. I want to start by thanking the very first members of the group that I had the pleasure of interacting with as a first year graduate student. I am grateful to John Ogren and Sandra Mosquera Vázquez for their tremendous help with building the 2D apparatus and the eternal faith they had in me. All of the custom-built adapter plates, optics mounts, and most importantly, the argon chamber that made every experiment in this thesis possible, were carefully designed and machined by them. They were always willing to answer even the stupidest questions I had, and spent many days and nights with me fiddling with the laser (a.k.a Mary Anne) and the 2D setup. Thanks to you two, I can say without hesitation that my first two years in the group were the highlight of my grad school experience and that will never change. Toru Kondo, I admire your mastery of literally everything, and I greatly enjoyed your underappreciated humor, your most roundabout ways of saying things including the famous "Maybe OK"s, and the spontaneous conversations we had in the middle of the night in our office. I thank Ashley Tong and Sam Gordon for being the best biochemistry teachers in my entire life. As a person who was scared of being in wet lab (and I still am!), the biochemistry part of my work would have never been made

possible without the guidance of Ashley and Sam. Ashley, I also really enjoyed our spontaneous trips to the Muddy, working on the quantum mechanics problem sets half-drunk, and my first-ever American Thanksgiving you hosted at your house. I will forever admire your badassery. Wei Jia (Crystal) Chen, thanks for being a terrific lab spouse and for all the fun conversations we had on random topics.

I can't thank enough the members of Team Ensemble; each and every one of them is an incredibly talented scientist and terrific labmate. Steph Hart, thanks for being my one and only − and really awesome − 2D partner for the entirety of my time in the group when I couldn't get anyone else interested enough in 2D. Although we never actually got to work on the same projects, I had a blast training you, working with you, having numerous scientific (and non-scientific) discussions with you, and drinking with you. I very much appreciate your general willingness to help with literally anything. This thesis would look so much worse without your helpful comments and careful read-through. I also thank you for the ride you gave me at the beginning of the coronavirus lockdown. I thank Muath Nairat for being a terrific mentor and colleague in every possible way. He and I overlapped in the darkest moments of my time in grad school, when I was suffering from the final year blues and additional depression from the coronavirus lockdown, but he was one of the very few people that kept me sane during this trying period. Muath, thank you so much for always having so much faith in me, for all your help with laser problems and data collection, for listening to all my complaints, and for driving me home. Olivia Fiebig, thanks for being one of the kindest coworkers I have ever met, and for putting up with my terrible mentoring skills. Dvir Harris, thanks for always being open to talk about anything, whether that is science or not science-related, and for distracting me from thinking too much about work by sharing all those newspaper articles and crazy tweets. Paul Cesana, Courtney Olson and Angela Lee are the three people I had the joy of training/working with in the very final months of grad school. I thank them for being patient with me, especially in these difficult times, and being such great people to work with.

I also express my gratitude towards the other (present and past) members of the

group, whom I unfortunately have not had many chances to directly work with, but definitely enjoyed spending time with. Steve Quinn, we didn't really get to overlap much at work, but you are one of the most thorough and careful scientists I have ever met, and so I learned a lot about how to do science from you. Your extremely detailed and well-organized lab notebooks still amaze me, and I learned about Irn Bru from you, which I can't wait to try when we are allowed to travel again. Julianne Troiano and Raju Regmi were my two go-to postdocs whenever I was having a bad day or wanted to vent about things that were frustrating me. I deeply thank them for putting up with me who never gets tired of complaining and always being willing to listen to me and buying me many many cups of coffee and glasses of beer. Ray Moya, thank you for being that one person in the group who is as negative as (if not more than) me, which really meant a lot to me, and for all the interesting scientific and technical discussions we had in lab. Thanks for always saying to me that I give the best talks in group meeting and that I do cool science, even if I never believed that once. I will definitely miss your moral support. Audrey Norris, thanks for being the cool kid in the group and organizing all the fun group activities and sharing tasty baked goods with the group. Shwetha Srinivasan, Jesse Gordon, thanks for always patiently answering my biology questions, and for caring about my safety in lab. Jesse, I appreciate that you let me know about the existence of the Banana Room, which quickly became my go-to place for quick breaks from the lab. I also appreciate all your help with communicating with the Department of Facilities and making sure the laser labs are maintained well. I will definitely miss all your peanuts and your humor. Mikaila Hoffman, Maddie Hoffmann, Shirley Chen, Jiajia Guo and Prem Manna, thank you all for being terrific labmates.

Outside the Schlau-Cohen group, I was extremely lucky to be able to get help from several members of the Bawendi and Nelson groups. I owe much to (now Prof.) Justin Caram, who sat down with me many many times and went through the detailed theory and principles behind 2D electronic spectroscopy, and shared the valuable experiences he had when he built his own 2D setup during my first year of grad school. Megan Klein kindly helped with the cryogenic absorption measurements of

LHCII, by not only setting up the measurement, but also troubleshooting unexpected sample issues and making sure that I was getting high-quality data. Ben Ofori-Okai, Sam Teitelbaum and Colby Steiner were the senior graduate students who were kind enough to come rescue a miserable first-year student whenever I got stuck working alone in lab late at night. They were always incredibly patient with me, taught me a lot about lasers, optics and FROG, and lent me numerous pieces of equipment that our group didn't have when we were a new group. Andreas Steinbacher was always willing to answer my questions about our ill-behaved oscillator. I would also like to thank Prof. Greg Engel at the University of Chicago for kindly sharing the plans for the ARID assembly with us described in Chapter 2.

I am indebted to my wonderful collaborators Profs. Roberto Bassi and Alberta Pinnola at the University of Verona and the University of Pavia in Italy, who were kind enough to contribute a large amount of high-purity LHCII protein for the vast majority of the work described in this thesis. I also thank them for always carefully reading through our joint manuscripts and providing valuable feedback on the biochemical aspects of the work, and for their hospitality during my visit to Rome. I thank Dr. Peter Adams and Ash Hancock at the University of Leeds, UK, for coming up with the ideas for the Texas Red-LHCII biohybrid work and for their collaborative efforts in the data collection process. I owe much to Andrea Volpato and Prof. Elisabetta Collini at the University of Padova, Italy, who generously shared the 2D global analysis code with us used in the work presented in Chapter 3. I also thank Elisabetta and her students for their generous hospitality during my visit to Padova and their lab. Although the work with them didn't make it into this thesis, I was extremely fortunate to be able to interact with a group of incredible scientists through the BioLEC collaborations, and I thank all of my former and current collaborators for their photochemistry expertise and also being awesome people to hang out with.

I also appreciate the kind help from the administrative assistants and staff in the Department of Chemistry including Peter Giunta, Eliza Hamilton, Paula Robinson, Jennifer Weisman, Rebecca Teixeira, Rich Wilk, and Brian Pretti. I am particularly grateful to Rich and Brian, who were extremely helpful with providing support on the

lab infrastructure and maintenance, and were always willing to listen to my (never-ending) complaints.

There are numerous other people outside the lab that made my time at MIT an enjoyable experience. The pchem cohort (Pyae Phyo, Marty Gelenter, Dmitro Martynowych, Kaitlyn Dwelle, Timothy Sinclair, Nicole Moody, Crystal Chen, Cole Perkinson, Jason Yoo, Shiva Mandala) was a fun group of people to hang out with, which was always a nice break from work and work-related stress. Shiva Mandala, I am especially indebted to you for being a terrific former roommate and an incredible listener to all my complaints. Our regular Skype sessions and coffee breaks are definitely one of the things that keeps me sane during these crazy days. Ben Ofori-Okai, I can't thank you enough for being a wonderful senior scientist to get advice from, and for being one of the greatest friends I made during my time at MIT. Thanks for putting up with me so many times when I was clearly just throwing emotional nonsense to you and having so much more faith in me than I do. I thank Hendrik Utzat for all the advice he has given me about mental health and other things, and admire him for his creativity and enthusiasm. Matthias Ginterseder was kind enough to cook me authentic Wienerschnitzel, which I hope to pay back at some point when we are allowed to gather again. Hyowon Seo, I am grateful for all our fun conversations over coffee and for all the advice you have given me on many things including thesis writing. Jiyoun Chang and Seong Soon Jo, thanks for taking me out to the many tasty restaurants that I would have never found out about otherwise, which made my life in Boston a little more enjoyable. Björn Kriete, I really enjoyed our time spent together in three different continents, first in Seoul (with all the pouring rain), then in Hamburg, then in Boulder. I am glad to have met you as a truly talented fellow scientist and friend, and am curious to see in what random city we would cross paths next time.

Finally, I thank my family for their unwavering support. Thank you for having so much faith in me, and for always being by my side through the good and bad times. This thesis is dedicated to you.

Contents

Chapter 1

Introduction

1.1 Photosynthetic Light Harvesting

Sunlight is the most abundant and renewable source of energy available to mankind. While a dilute energy source, sunlight reaches the surface of the earth at a rate that greatly exceeds that of worldwide energy consumption [1, 2]. In principle, the amount of sunlight that strikes the earth's surface per day is large enough to support human activities for years [3]. The major route for conversion of the solar energy that reaches the earth is photosynthesis. Photosynthetic organisms, such as cyanobacteria, algae, and plants, convert CO_2 into energy-rich chemical bonds, and in turn, biomass, using the light energy from the sun [4]. Responsible for over 150 billion tonnes of biomass production annually, photosynthesis is one of the most important life-sustaining biochemical processes known in nature and has long been considered an attractive renewable source of energy to replace fossil fuels [1, 2, 5, 6].

Despite its potential as a sustainable solution to the growing global energy demand over the next century, natural photosynthesis is an inherently inefficient process with a maximum theoretical efficiency of 11% and experimentally reported efficiencies of only up to ∼3% [7]. To be able to achieve increased yields of energy and biomass production with natural photosynthesis, it is crucial to understand, and potentially optimize, the underlying molecular-level mechanisms by which photosynthetic organisms capture solar energy and transfer the harvested light energy, which is the primary

focus of this thesis.

The initial absorption and subsequent transport of solar energy by photosynthetic organisms are referred to as photosynthetic light harvesting. Photosynthetic light harvesting constitutes the initial ∼250 picoseconds of photosynthesis [4]. The light-harvesting apparatus of photosynthetic organisms consists of a densely packed network of pigment-binding proteins called light-harvesting complexes (LHCs). Each LHC holds a number of light-harvesting pigments within its protein scaffold, and the pigments absorb sunlight by promoting themselves into an electronic excited state. The absorbed excitation energy then migrates through the network of LHCs towards the reaction center (RC), where charge separation takes place as the initial step of the energy conversion reactions. Remarkably, these energy transfer steps proceed rapidly on femto-to-picosecond timescales with near-unity quantum efficiency [4]. The photophysical mechanisms behind such rapid and efficient excitation energy transfer have been a subject of extensive experimental and theoretical investigations in a variety of photosynthetic organisms [8–12]. In this thesis, I focus on the discussions of photosynthetic light harvesting and associated energy transfer processes in green plants, an efficient harvester of visible solar light.

1.2 Photosynthetic Machinery of Green Plants

1.2.1 Overall Architecture

Figure 1-1 illustrates the architecture of the photosynthetic machinery of green plants. The organelle that performs photosynthesis within a plant cell is a chloroplast (Figure 1-1A). Plant chloroplasts have a multi-membrane structure with several layers of lipid bilayer membranes [13–15]. The outer and inner chloroplast membranes constitute the envelope membranes of the chloroplast. The inner space (stroma) consists of stacks of interconnected membranous sacks called thylakoids. The lipid bilayer membranes of the thylakoids contain a number of integral and peripheral membrane proteins, including photosystems I and II, where the light reactions of photosynthesis take

place.

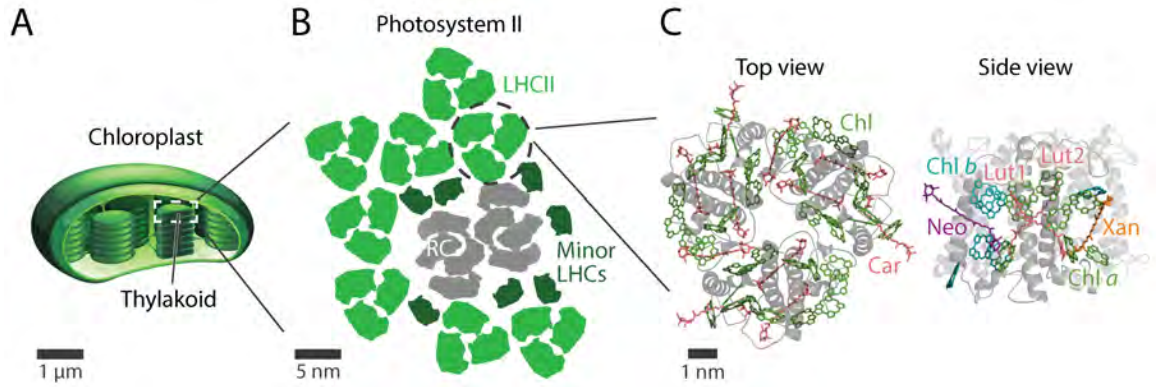

Figure 1-1: **Photosynthetic machinery of green plants.** (A) Cartoon illustration of the plant chloroplast (side view) with a thylakoid labeled with white dashed box. (B) Cartoon illustration of the PSII supercomplex (top view, PDB 5MDX) [16]. LHCIIs, minor LHCs, and core complexes in the RC are shown in light green, dark green, and gray, respectively. (C) Structure of LHCII (PDB 1RWT) [17]. The protein scaffold is shown in gray, and the light-harvesting pigments, Chls and Cars, are shown in green and pink (in the top view), respectively. The different Chls and Cars are labeled in the side view (Lut: lutein, Neo: neoxanthin, Xan: xanthophyll cycle Car). In the side view, the pigments for only one monomeric subunit are shown for clarity.

1.2.2 Photosystem II

Among the membrane proteins embedded in the thylakoid membrane, photosystem II (PSII, Figure 1-1B) is the protein supercomplex that is responsible for the initial light absorption and transfer of excitation energy mentioned above. PSII is a dimeric supercomplex, each monomer of which consists of the core complex and peripheral LHCs, also commonly referred to as antenna complexes [18, 19]. The peripheral LHCs capture the solar energy and rapidly and efficiently funnel the absorbed energy towards the core complex, where the RC is located, thereby serving as the principal mediator of photosynthetic light harvesting in green plants. They are members of the Lhcb multigenic family; the six Lhcb genes ($Lhcb1-6$) each encode six different LHCs [20]. Of the six, the products of $Lhcb1-3$ genes form a heterotrimeric complex called light-harvesting complex II (LHCII, Figure 1-1C) [21, 22]. LHCII is the most abundant membrane protein and LHC in plants, occupying ∼30% of the protein content and ∼40% of the pigment content of the plant thylakoids, and therefore considered

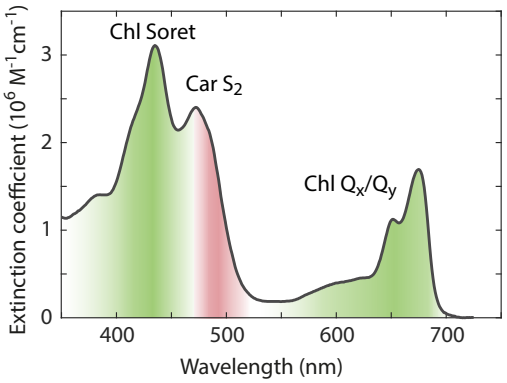

Figure 1-2: **Absorption spectrum of LHCII.** Green and pink shaded areas and text labels indicate the electronic transitions and corresponding absorption range of the Chls and Cars, respectively. The pigment electronic structures are discussed in detail in Section 1.3 below.

the major LHC in plants [23]. Genes $Lhcb4-6$ respectively encode monomeric minor LHCs that are homologous to LHCII, CP29 (*Lhcb4*), CP26 (*Lhcb5*), and CP24 (*Lhcb6*) [24]. Because of its abundance, LHCII is the most extensively characterized member of the PSII supercomplex, in terms of both structural and photophysical properties [17, 25–29], and will be the focus of this thesis.

1.2.3 Light-Harvesting Complex II

The structure of LHCII based on its crystal structure [17] is illustrated in Figure 1-1C. The protein matrix of LHCII, shown in gray ribbons, consists of three transmembrane and two amphiphilic helices per monomeric subunit, which has a molecular weight of 25−27 kDa [30]. The protein matrix possesses pigment-binding pockets with distinct structures, within which chlorophylls (Chls) and carotenoids (Cars) are held as the primary and accessory light-harvesting pigments of LHCII. Each monomeric subunit non-covalently binds fourteen Chls and four Cars. The large number of light-harvesting pigments bound per complex, each with a maximum extinction coefficient of 100,000−150,000 $M^{-1}cm^{-1}$ results in an increased total absorption cross-section, enabling LHCII to efficiently harvest and concentrate the dilute light energy from the sun (Figure 1-2) [2, 5]. The physical, chemical, and electronic structures of the Chl

and Car pigments are discussed in detail in Section 1.3 below.

1.3 Light-Harvesting Pigments of Light-Harvesting Complex II

1.3.1 Chemical and Electronic Structures of Chlorophylls

Chls, the primary light-harvesting pigments in LHCII, consist of a tetrapyrrole ring (chlorin) coordinating a magnesium ion and a long, lipid-soluble hydrocarbon tail commonly referred to as a phytol tail (Figure 1-3A) [4]. Five different types of Chls with different substituents on the chlorin ring have been identified thus far: Chls *a*, *b*, *c*, *d*, and *f*. Among these, LHCII contains Chl *a* and Chl *b*; each monomer binds eight Chl *a* and six Chl *b* pigments. The chemical structures of Chls *a* and *b* only differ by one ring substituent. The replacement of a methyl substituent ($-CH_3$) in Chl *a* with a formyl group ($-CHO$) in Chl *b* results in a shift in the absorption range.

$\pi \rightarrow \pi^*$ transitions of the π-conjugated chlorin ring in Chls give rise to two sets of absorption bands in the visible range, one in the blue region and the other in the red region known as the B bands and the Q bands, respectively (Figure 1-3B, C). The high-energy B bands are also commonly known as the Soret bands. The electronic structure of Chl can be explained by Gouterman's four orbital model, a model that describes the electronic structure of porphyrins [31]. The four π orbitals that participate in the $\pi \rightarrow \pi^*$ transitions are the two highest occupied molecular orbitals (HOMO, HOMO-1) and the two lowest unoccupied molecular orbitals (LUMO, LUMO$+1$). The reduced symmetry of chlorin relative to porphyrin due to the reduction of one of the four pyrroles breaks the degeneracy between the orbital energies of both the HOMO and LUMO pairs. This results in a splitting of the B and Q bands into B_x/B_y and Q_x/Q_y bands. This splitting is not observed in metalloporphyrins, which are highly symmetric molecules and thus exhibit largely preserved orbital degeneracies [32]. The subscripts x and y denote the direction of polarization of the transition in the chlorin ring, as illustrated with gray arrows in Figure 1-3A.

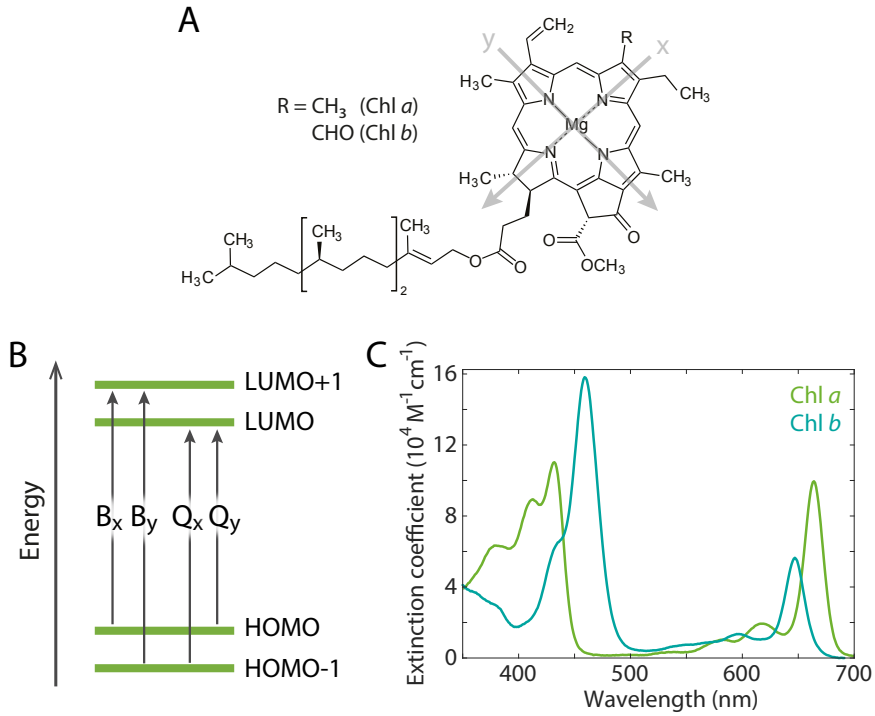

Figure 1-3: **Chemical and electronic structures of Chls.** (A) Chemical structures of Chls *a* and *b*. Gray arrows indicate the two transition dipole moments discussed in the text. (B) Simplified energy level diagram of Chl based on the four orbital model [31]. (C) Steady-state absorption spectra of Chls *a* and *b* measured in methanol.

The intense red-most band that appears at 675 nm (Chl *a*) and 650 nm (Chl *b*) is the Q_y transition of Chl *a* and Chl *b*, respectively, polarized along the y axis of the chlorin ring. The Q_x bands that appear in the $550 - 650$ nm range, however, are not as well-resolved and significantly weaker in intensity, because the transition dipole moment is not perfectly aligned with the x axis [33, 34]. The Q_x transition overlaps in part with the vibronic progression of the Q_y transition, which appears at a similar wavelength range with similarly weak intensities. The exact energy level of the Q_x state and its degree of mixing with the vibronic bands of the Q_y state are still a matter of debate [34–36]. The weak absorption in this green region of the visible solar spectrum gives Chl its characteristic green color. The Soret bands that appear at 400−450 nm and 430−480 nm for Chl *a* and Chl *b*, respectively, originate from a much more complicated electronic structure involving overlapping x- and y-polarized transitions as well as mixing with additional transition dipole moments [37].

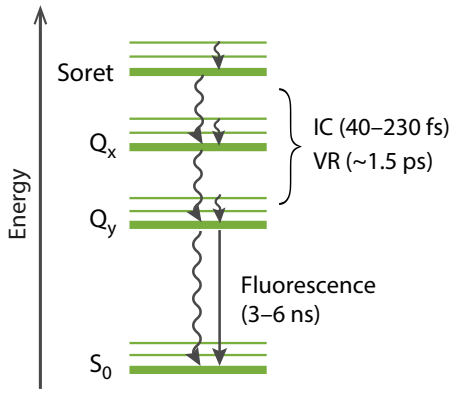

Figure 1-4: **Ultrafast energy relaxation pathways of Chl singlet excited states.** Simplified energy level diagram illustrating the major energy relaxation pathways in a Chl molecule with associated time constants from the literature. Straight and squiggly arrows denote radiative and non-radiative relaxation pathways, respectively. IC: internal conversion, VR: vibrational relaxation.

1.3.2 Ultrafast Photophysical Pathways in Chlorophylls

The primary routes of energy relaxation in Chl singlet excited states after photoexcitation are summarized in Figure 1-4. The most well-characterized relaxation pathway is the radiative transition from Q_y to the ground state with a fluorescence lifetime of several nanoseconds. Measurements of isolated Chl *a* and Chl *b* molecules in solution revealed fluorescence lifetimes of ∼6 ns [38] and ∼3 ns [39], respectively. A shorter lifetime of 3−4 ns is observed for Chl *a* in a protein environment, such as those bound to LHCII [40]. In addition to fluorescence and non-radiative internal conversion to the ground state, the Q_y state also undergoes intersystem crossing to the triplet state on a nanosecond timescale, and subsequently relaxes by phosphorescence (not shown in the figure) [41]. Higher-energy relaxation pathways in Chls are dominated by ultrafast internal conversion from the Soret to the Q states as well as from Q_x to Q_y. A number of theoretical and experimental investigations consistently reported the timescale of internal conversion to be 40−230 fs [36, 42–44]. The rapid internal conversion steps are accompanied by a slower intramolecular vibrational relaxation process reported to occur on a 1.5 ps timescale [45, 46].

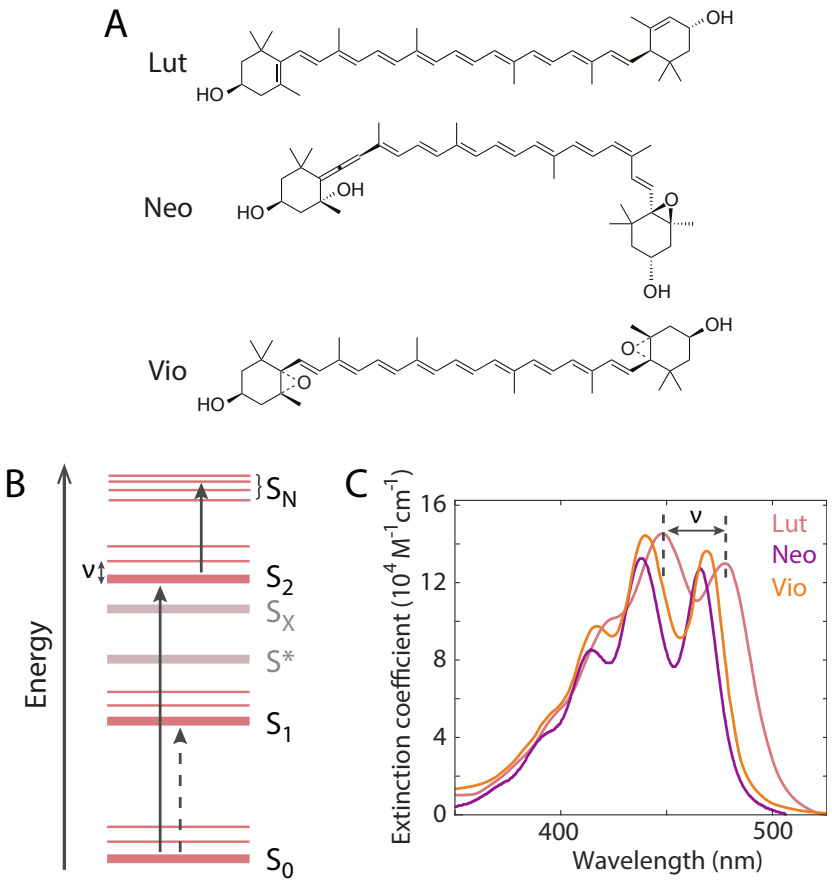

Figure 1-5: **Chemical and electronic structures of Cars.** (A) Chemical structures of the Cars present in LHCII. (B) Simplified energy level diagram of Car. Optically allowed and forbidden transitions are shown in black solid and dashed arrows, respectively. The Greek symbol ν denotes the vibronic spacing shown in (C). The two debated dark states S_X and S* discussed in the text are shown in light pink. (C) Steady-state absorption spectra of the Cars shown in (A) measured in acetone.

1.3.3 Chemical and Electronic Structures of Carotenoids

The inefficient absorption of green light by the Chls is complemented by the Cars, which are linear molecules with a conjugated polyene backbone that mainly absorb at 450−550 nm (Figure 1-5A). Four different Car molecules are bound to each monomer of LHCII: two luteins (Luts; Lut1 and Lut2), one neoxanthin (Neo), and one xanthophyll cycle Car. The xanthophyll cycle Car is either violaxanthin (Vio) or its de-epoxidized form zeaxanthin (Zea), which reversibly interconvert depending on the intensity level of sunlight (see Section 1.5.2 below).

The electronic structure of Cars is largely governed by their conjugated polyene

backbone [47, 48]. The C_{2h} symmetry point group that polyenes belong to gives rise to electronic states with either A_g or B_u symmetry. In Cars, both the ground state (S_0, $1^1A_g^-$) and the lowest-energy singlet excited state (S_1, $2^1A_g^-$) are of A_g symmetry, which makes the transition between these two states symmetry-forbidden (dark). The energy level of the Car S_1 state remains undetermined because of its optically-forbidden nature. A variety of spectroscopic techniques including two-photon excitation, resonance Raman, and near-infrared transient absorption spectroscopies were employed to estimate the S_1 energy levels of a series of Cars [49]. While these experiments were successful in estimating the range within which the S_1 energy falls, the precise energy level could not be unambiguously determined. A commonly used spectroscopic marker for tracking the photophysical properties and evolution of the dark S_1 state is an excited-state absorption (ESA) from S_1 to higher-lying excited states collectively termed S_N, which is a strongly allowed transition and appears in the visible range (500−600 nm) [49].

In contrast to the S_1 state, the second lowest-energy excited state (S_2, $1^1B_u^+$) possesses a different symmetry from that of the ground state. Therefore, the lowest-energy optically allowed electronic transition of Cars is the $S_0 \rightarrow S_2$ transition, which is what gives rise to the intense absorption band shown in Figure 1-5C. The energy level of this transition varies depending on the conjugation length of the Car, defined as the number of conjugated C=C double bonds. Neo and Vio have nine conjugated double bonds, whereas Lut has ten. This increase in conjugation length red-shifts the absorption peak of Lut from those of Neo and Vio by a few nm (Figure 1-5C). The energy level is also sensitive to the physical structure, or conformation, of the Car. For example, a partially non-planar conjugated chain results in a decrease in the effective conjugation length, and blue-shifts the absorption maximum [50]. The S_2 absorption band also exhibits a characteristic vibronic progression consisting of at least three vibronic bands (0−0, 0−1, 0−2, ...) with an energy spacing of $\nu = \sim$1,350 cm^{-1}, representing the combination of C−C (1,150 cm^{-1}) and C=C stretching (1,600 cm^{-1}) motions of the backbone [51].

In addition to the well-established S_1 state, it has been proposed that there exist

additional Car dark states likely between the S_2 and S_1 states. Two such proposed dark states are named S_X and S* [52]. The existence, energy levels, and associated photophysics of these additional dark states remain widely debated despite extensive investigations using transient absorption as well as a number of advanced spectroscopic techniques such as femtosecond stimulated Raman, transient grating, photon echo, and degenerate four-wave mixing spectroscopies [53–59]. The S_X state was initially proposed as an intermediate state between the energies of S_2 and S_1 in an attempt to explain the anomalous trends observed in the $S_2 \rightarrow S_1$ internal conversion rates of Cars that do not follow the energy gap law [60]. However, experiments have not been able to unambiguously detect spectroscopic signatures that could be assigned to the existence of this state. The S* state is associated with a characteristic spectroscopic signature that appears as a high-energy shoulder of the broad $S_1 \rightarrow S_N$ ESA, and so its existence is definitively established. However, open questions remain about the origin of this state; the two leading proposals treat it as either a hot ground state [55, 61] or an electronic excited state associated with a twisted Car conformation [56, 62]. The presence of one or more dark excited states and the resultant ambiguities in the photophysical properties discussed above highlight the complexity of the electronic structure of Cars, which is one of the factors that make Car photophysics notoriously challenging to elucidate.

1.3.4 Sensitivity of Carotenoid Electronic Structure to Environment

Another factor that further complicates the photophysical properties of Cars is the sensitivity of their electronic structure to the surrounding environment. A well-known environment-dependent photophysical behavior is the strong solvatochromism of the energy level and excited-state dynamics observed for the S_2 state [63]. The absorption/fluorescence peak positions as well as the lifetime of the S_2 state exhibit strong dependence on solvent polarizability. A recent solvent-dependent transient absorption study demonstrated that different solvents can activate or deactivate the debated

dark intermediate state S_X by tuning the energy level of the S_2 state, which may be the origin of the conflicting experimental evidence surrounding the presence of this intermediate state, as briefly mentioned earlier [64].

The sensitivity of Car electronic structure to the environment is in part brought about by the sensitivity of their physical structure (conformation) to local environment, which is one of the parameters that controls the photophysical properties of Cars along with their chemical structure. The relatively floppy structure of the long carbon chain backbone of Cars makes them easily undergo torsional structural motions into twisted or bent conformations, which are thought to potentially activate new excited states and photophysical pathways, analogous to the solvent-dependent activation of the dark S_X state mentioned above. For example, the appearance of the dark S* state mentioned earlier has been associated with a twisted Car conformation from comparative spectroscopic investigations of open-chain Cars with systematically varied conjugation lengths [56, 65].

In the case of Cars found in photosynthetic LHCs, the distinct structure of each pigment-binding pocket in the protein scaffold determines the conformation of the bound Car. Even chemically identical Cars can thus possess different conformations, which leads to distinct photophysical behaviors and, in turn, functional roles. For example, the two Luts in LHCII, although chemically identical, have distinct conformations, which results in a 700 cm^{-1} difference in their S_2 energy levels as well as contrasting roles in photosynthesis, one as a primary energy donor to the Chls and the other as a quencher of harmful energy (see Chapter 3 for more detailed discussions about the conformations and different photophysical properties of these two pigments) [66, 67]. Furthermore, a recent computational work predicted a 50% reduction in the fluorescence lifetime of LHCII by a slight tilt ($5-10^{\circ}$) in the backbone of one of the Luts, highlighting the critical role of Car conformation in determining the photophysics [68].

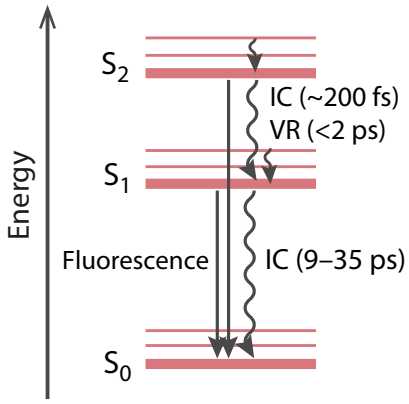

Figure 1-6: **Ultrafast energy relaxation pathways of Car singlet excited states.** Simplified energy level diagram illustrating the major energy relaxation pathways in a Car molecule with associated time constants from the literature. Straight and squiggly arrows denote radiative and non-radiative relaxation pathways, respectively. IC: internal conversion, VR: vibrational relaxation.

1.3.5 Ultrafast Photophysical Pathways in Carotenoids

Figure 1-6 illustrates the major pathways of energy relaxation in the singlet excited states of Cars. Energy relaxation from the bright S_2 state is dominated by rapid, sub-ps $S_2 \rightarrow S_1$ internal conversion. While the time constants vary slightly with different Cars and in different environments, measured timescales of this pathway are in the range of 150−200 fs [49, 69]. Following internal conversion, excitation energy on the dark S_1 state non-radiatively decays within a few to tens of picoseconds. The S_1 lifetimes of the Cars found in LHCII (measured with isolated molecules in solution) are 9−35 ps (Neo: 35 ps, Lut: 14 ps, Vio: 24 ps, Zea: 9 ps) [49]. Radiative decay, *i.e.*, fluorescence emission, from both the S_2 and S_1 states of Cars has been observed, albeit with very weak intensity due to its extremely low quantum yield ($10^{-5} - 10^{-4}$). Whether the S_2 or the S_1 fluorescence dominates the observed fluorescence spectrum is dependent on the conjugation length [70]. In Cars with eight or fewer conjugated double bonds, the S_1 fluorescence dominates. In Cars with nine or more conjugated double bonds, the $S_1 \rightarrow S_0$ non-radiative decay rate increases according to the energy gap law, making the S_1 fluorescence vanishingly weak in intensity and, therefore, S_2 fluorescence the dominant contribution. Vibrational relaxation dynamics of Cars are known to occur on picosecond timescales, as have been extensively characterized

with time-resolved Raman spectroscopic techniques [71, 72]. Intersystem crossing of Cars, reported to occur on a nanosecond timescale (not shown in the figure), has a low quantum yield due to the rapid timescale of internal conversion, the competing pathway [73]. A more dominant pathway of Car triplet formation is via triplet-triplet energy transfer from a triplet energy donor, such as the triplet excited state of Chls [69].

1.3.6 Diverse Roles of Carotenoids in Photosynthesis

The unique and intricate electronic structure of Cars discussed above enables them to play multiple distinct roles that are critical to the fitness and function of photosynthetic organisms. In their light-harvesting role as accessory pigments, Cars mediate the rapid and efficient energy transfer steps in photosynthetic light harvesting by connecting energetically distant transitions of the primary light-harvesting pigments. In LHCII, the bright S_2 state of the Cars, located between the Soret and Q states of the Chls, bridges the large gap between them by accepting excitation energy from the higher-lying Chl Soret states and donating it to the lower-lying Q states [74–76].

On the other hand, the dark S_1 state is thought to be primarily involved in protective mechanisms against photodamage from excess sunlight, along with triplet-mediated photoprotective pathways, *i.e.* quenching of Chl triplet and singlet oxygen by Car triplet state [77–79]. Although the detailed photophysical mechanism remains undetermined due to the ambiguity of the S_1 energy, the short, picosecond-order lifetime of this state enables rapid quenching of deleterious energy through non-radiative relaxation back to the ground state [49, 52]. Detailed discussions about photoprotection and associated photophysics are provided in Section 1.5.

From a structural perspective, Cars are required for the assembly, stabilization and macro-organization of many bacterial and plant LHCs [80–82]. In the case of LHCII, it was shown that the presence of Luts in their binding sites is critical for proper folding of the protein, highlighting the indispensable structural role that Luts play in the organization of plant LHCs [83, 84].

1.4 Ultrafast Energy Transfer Dynamics in Light-Harvesting Complex II

The pathways and timescales of energy transfer in LHCII have been extensively characterized with ultrafast spectroscopic techniques such as femtosecond transient absorption [75, 76, 85–87], three-pulse photon echo peak shift [88, 89], transient grating [88], and more recently multidimensional electronic spectroscopies [90–95]. The timescales of energy transfer from Car S_2 to the Chl Q states were measured to be 50−170 fs with transient absorption, assigned by the decay of Car S_2 population and growth of Chl Q population observed upon photoexcitation into the Car S_2 states [75, 76, 86]. Narrowband pump pulses were utilized to selectively excite the S_2 states of the different Cars present in LHCII, which revealed that Luts and Neo primarily transfer energy to Chls *a* and Chls *b*, respectively. Additionally, a slower, 1 ps decay of the Car $S_1 \rightarrow S_N$ ESA was identified in the transient absorption spectra and assigned to energy transfer from Car S_1 to the Chl Q states with a lower amplitude than that of the transfer directly from the S_2 state [75]. The overall efficiency of the Car-to-Chl energy transfer was estimated to be 80−90%, consistent with the estimate from steady-state fluorescence excitation spectroscopy [96].

Energy transfer within the Chl Q manifold is much more extensively characterized than Car-to-Chl transfer, with both spectroscopic experiments and theoretical modeling. Energy transfer occurs both from Chl *b* to Chl *a* (inter-band) and among the same types of Chl pigments (intra-band). The Chl *b*-to-Chl *a* energy transfer appears as a growth in Chl *a* Q_y population upon photoexcitation into the Chl *b* Q_y state, and exhibits multi-component kinetics with time constants of 150−300 fs and 600 fs, and a minor picosecond component [97]. Two-dimensional (2D) and three-dimensional (3D) spectroscopy experiments with improved spectral resolution compared to one-dimensional transient absorption spectroscopy identified that the Chl *a* pigments can be grouped into high-energy and low-energy pigment pools, and reported energy transfer between the two Chl *a* pools on a few ps timescale [90, 93]. Dynamics of intra-band energy transfer among Chl *b* or Chl *a* pigments, *i.e.*, energy

equilibration, were investigated with transient absorption [98, 99], three-pulse photon echo peak shift [88, 89], fluorescence upconversion [100], and more recently 2D electronic spectroscopy [101]. For Chl *b* intra-band transfer, a rapid timescale of 300 fs was measured. In the case of Chl *a*, a slower component with a time constant of 5−7 ps was revealed in addition to the sub-ps component.

All of the energy transfer timescales summarized above represent energy flow within an individual LHCII measured with isolated LHCs in solution. In the native photosynthetic machinery of plants, the dynamics of energy transfer between LHCs contribute to the overall efficiency and rate of charge separation in the RC, along with the transfer within LHCs. The timescale of energy transfer between LHCs was estimated with singlet-singlet annihilation experiments, which revealed time constants of a few tens to hundreds of ps that depend on the size of the LHC array [102].

1.5 Regulation of Photosynthetic Light Harvesting in Plants

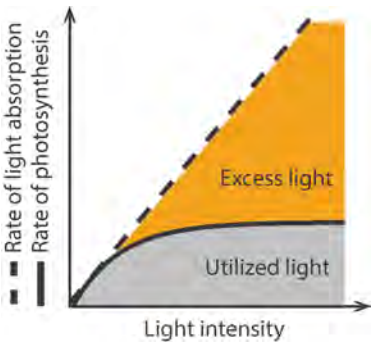

Figure 1-7: **Intensity of sunlight and the rate of photosynthesis.** In low light, photosynthetic efficiency is limited by the light intensity. In high light, the rate of light absorption exceeds the capacity of the RC, resulting in excess light that leads to photooxidative damage of the cells in photosynthetic organisms.

1.5.1 Non-photochemical Quenching

The rapid and efficient capture and transfer of energy by photosynthetic LHCs ensure that a sufficient amount of sunlight is absorbed to fuel the growth of the photosyn-

thetic organism. However, the intensity of sunlight fluctuates by the diurnal and seasonal cycles, or even transiently, for example by passing of clouds, and so the organisms are exposed to fluctuating levels of sunlight [103]. Figure 1-7 illustrates the rates of light absorption and photosynthesis as a function of light intensity. Under light-limited conditions, *e.g.*, on a cloudy day, photosynthetic efficiency increases with the intensity of sunlight in order to power growth. In contrast, under high-light (sunny) conditions, the rate of light absorption exceeds the capacity of the RC, *i.e.*, the rate of photosynthesis, resulting in excess light that causes photooxidative damage to the cells via generation of harmful photoproducts such as reactive oxygen species [104, 105]. To prevent photodamage, the LHCs of oxygenic photosynthetic organisms, including green plants, have evolved a mechanism to dynamically regulate their light-harvesting capacity by quenching the excess energy, broadly known as photoprotection. In response to the fluctuating levels of sunlight, the LHCs undergo a rapid and reversible interconversion between a light-harvesting (unquenched) and a photoprotective (quenched) state. In the quenched state, the deleterious excess energy is dissipated as heat in a process called non-photochemical quenching (NPQ) [69, 106, 107]. NPQ consists of three components that primarily differ in their relaxation kinetics. The major and fastest component of NPQ in green plants is called energy-dependent quenching (qE), which is a rapid and reversible component that leads to dissipation within a few minutes [108]. The other two components exhibit much slower kinetics and are known to play minor roles in energy dissipation in plants [106]. Therefore, the discussions of NPQ in the remainder of this thesis will be focused exclusively on the qE component.

1.5.2 pH- and Zeaxanthin Dependence of Non-photochemical Quenching

In vivo, NPQ is triggered by a buildup of a proton gradient (ΔpH) across the thylakoid membrane (Figure 1-8). The proton gradient is the consequence of increased proton pumping into the thylakoid lumen in high light, resulting in reduction of the luminal

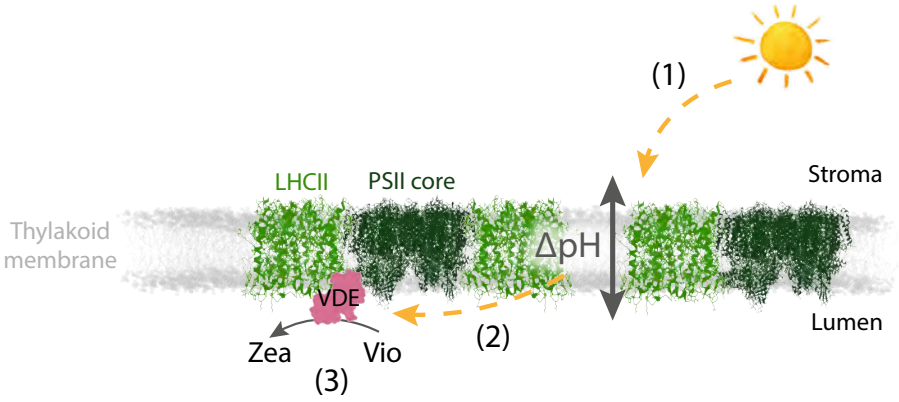

Figure 1-8: **Activation of NPQ.** Illustration of the series of events triggered in the presence of excess light. (1) A proton gradient across the thylakoid membrane, or ΔpH, is formed by a drop in the luminal pH. (2) The drop in luminal pH activates the enzyme VDE, which (3) catalyzes the xanthophyll cycle, where Vio is converted into Zea.

pH. The acidification of the thylakoid lumen activates the xanthophyll cycle (Figure 1-9A), in which Vio, the Car bound to the V1 site in LHCII, undergoes reversible chemical transformations into its de-epoxidized form Zea via an intermediate Car antheraxanthin (Anth) [109]. The de-epoxidation reaction extends the conjugation length of the xanthophyll cycle Car by creating two additional conjugated double bonds, resulting in a red-shifted S_2 energy level of Zea compared to that of Vio (Figure 1-9B). The activity of the enzyme that catalyzes the de-epoxidation reaction, violaxanthin de-epoxidase (VDE), is pH-dependent and maximal at pH ∼5 [110, 111]. Thus, de-epoxidation of Vio into Zea is activated in high light, where the reduction in the luminal pH enhances the catalytic activity of VDE, which is located in the lumen. Conversely, Zea and Anth can be re-epoxidized into Vio in low light by another enzyme called zeaxanthin epoxidase (ZE), located on the stromal side of the thylakoid membrane with optimal activity at alkaline pH (pH 8). In summary, excess light triggers a chain of events in the plant thylakoids that leads to the appearance of ΔpH and Zea, and this is the reason why these two parameters have long been considered to be responsible for the activation of NPQ. Indeed, the pH- and Zea dependence of NPQ has been confirmed by *in vivo* characterizations that showed a correlation between ΔpH and/or the Zea content and the extent of NPQ [112–114].

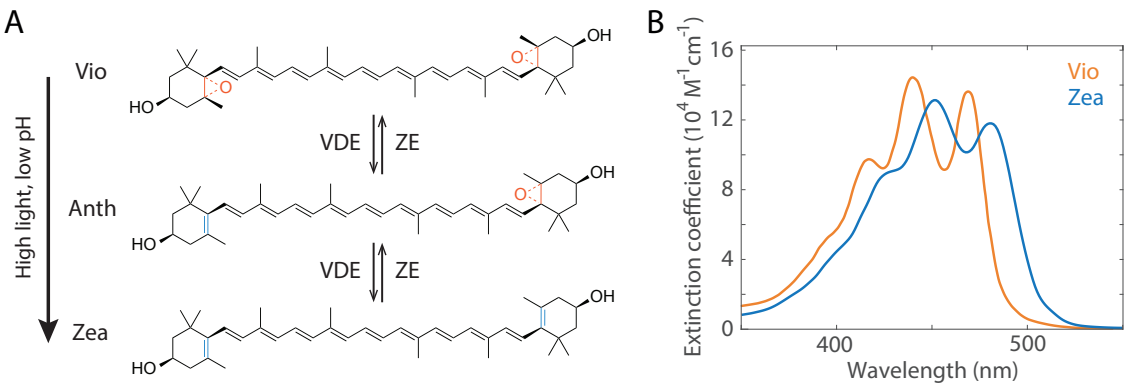

Figure 1-9: **The xanthophyll cycle.** (A) Chemical structures of Vio, Anth, Zea and the interconversion among them in the xanthophyll cycle. (B) Steady-state absorption spectra of Vio and Zea in acetone.

1.5.3 Site and Mechanisms of Non-photochemical Quenching

The exact site and mechanisms of NPQ have been a matter of intense debate in the field for the past few decades. Being the most abundant and thus major LHC in green plants, LHCII was naturally hypothesized to be the site of NPQ and has been most extensively investigated to date. In an attempt to disentangle the molecular parameters that activate quenching, *in vitro* aggregates of LHCII were prepared as a mimic of the native arrays of LHCII found *in vivo* [115]. Pronounced quenching of LHCII fluorescence was observed upon aggregation, similarly to the fluorescence quenching observed *in vivo* under high-light conditions [116–119]. Furthermore, the extent of quenching was enhanced at low pH and in the presence of Zea. These observations led to the proposal that LHCII is the site of NPQ activated by conformational changes brought about by aggregation. In an alternative model, the minor LHCs were proposed to be the site of quenching rather than LHCII, based on the observations that the minor LHCs CP29 and CP26 have high proton- and Zea affinity [120, 121]. It was also suggested that the two models mentioned above are not mutually exclusive. A recent mutagenesis study with a knockout mutant that lacks all minor LHCs and only retains LHCII revealed that both LHCIIs and minor LHCs contribute to the activation of NPQ, but with distinct timescales and molecular mechanisms [121].

It is generally accepted that conformational changes of the LHCs, whether LHCII

or the minor complexes, are responsible for opening up quenching sites and activating dissipative pathways. Due to the highly sensitive physical and electronic structure of the Cars to the surrounding environment as discussed earlier, the conformational changes responsible for induction of NPQ are thought to involve structural changes in one or more Cars, *e.g.*, bending or twisting of part of their conjugated backbones. The conformational changes are thought to originate from the interaction of the LHCs with the surrounding lipid bilayer membrane or with neighboring proteins, *i.e.*, protein-protein interaction. Molecular dynamics simulations of LHCII embedded in a membrane revealed that the overall structure of LHCII and Car conformations significantly differ from those in other environments, highlighting the importance of understanding the interaction between LHCs with the lipid membrane environment [28]. In terms of interactions with neighboring proteins, two of the proposed protein-protein interactions suggested to activate NPQ are the interactions among multiple LHCIIs and those between LHCII and a non-pigment-binding protein, photosystem II subunit S (PsbS). The former interactions were mimicked by *in vitro* aggregates of LHCII as mentioned above, and quenching levels dependent on the extent of aggregation were observed [122–124]. It was proposed based on resonance Raman and transient absorption results that conformational changes of the peripheral domains of LHCII containing Neo and Lut1 are responsible for the induction of the observed quenching [122]. The nature and role of the latter interactions, between LHCII and PsbS, are unclear. PsbS serves as a pH sensor by being protonated under high-light conditions, and was shown to be required for full induction of NPQ [125–130]. Because PsbS does not bind any pigments, it is established that PsbS cannot act as a direct quencher. Rather, it is thought to allosterically activate NPQ via inducing conformational changes to the LHCII complex. However, it remains an open question what structural changes it causes to the neighboring LHCII after protonation, and whether those changes are capable of activating NPQ.

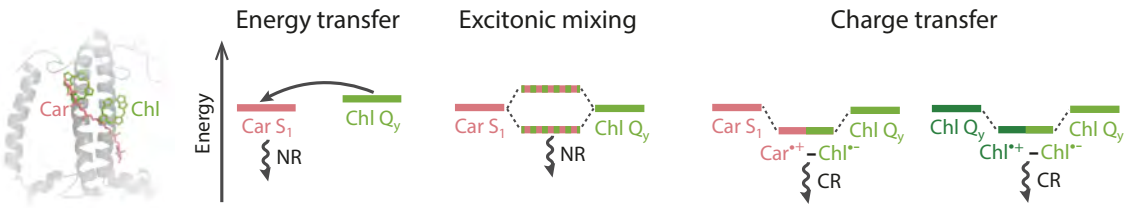

Figure 1-10: **Models for the photophysical mechanism of NPQ.** The four current proposed models for the photophysical mechanisms of NPQ are shown: Chl-to-Car energy transfer, excitonic mixing of Car-Chl excited states, Car-to-Chl charge transfer, and Chl-Chl charge transfer. NR: non-radiative decay, CR: charge recombination.

1.5.4 Models for the Photophysical Mechanisms of Dissipation

Along with the debate surrounding the site and mechanisms of NPQ from a structural perspective described in Section 1.5.3, the photophysical mechanisms of NPQ, *i.e.*, the nature and origin of dissipative photophysical pathways, are another widely debated topic in the field. Dissipative photophysics originate from electronic interactions between the Chl and Car pigments. However, the nature of the interactions and the associated dynamics have not been definitively elucidated to date. Currently, there are four proposals as to the nature and dynamics of dissipative photophysics (Figure 1-10).

In most of these proposals, the dark Car S_1 state is implicated to mediate dissipation leveraging its rapid timescale of non-radiative relaxation. The most straightforward proposal is energy transfer from the Chl Q_y to the Car S_1 state [122, 131]. Spectroscopically, this pathway would appear as a correlated population decay of Chl Q_y and growth of Car S_1 on the timescale of energy transfer. However, previous ultrafast measurements were unable to observe such features [132, 133]. Instead, the observed dynamics were better supported by an excitonic mixing between these two states, leading to the birth of the excitonic mixing model [134, 135]. In this proposal, in contrast to the energy transfer proposal, the absence of correlated decay and rise of the Chl and Car populations is explained by assuming delocalization between the Car S_1 and Chl Q_y states. The delocalized excitonic state is thought to relax rapidly via non-radiative decay, rapidly dissipating energy. The validity of these two proposals

has not yet been definitely determined, largely due to the ambiguity of the Car S_1 energy originating from its low oscillator strength.

The other two models propose that a charge transfer state, formed either between Car and Chl or between Chls, opens up dissipative channels. The Car-to-Chl charge transfer proposal is supported by a clear spectroscopic signature of the Car radical cation formed upon photoexcitation into the Chl Q_y state in the near-infrared region [136–139]. The formation of the charge transfer state and subsequent charge recombination were measured to occur within 150 ps, which enables rapid dissipation of energy. However, the small amplitude of the observed Car radical cation signature has prevented clear assignment and analysis. The Chl-Chl charge transfer proposal also relies on a characteristic signature in the 77 K fluorescence spectrum of the LHCs; a red-shifted emission band appears at 700 nm on top of the main fluorescence peak at ∼680 nm and has been associated with charge transfer between Chls based on the distinct kinetics of this feature compared to that of the main peak [119, 140, 141]. However, a recent study concluded that the red-emitting feature is distinct from that arising from quenched species [142].

1.6 Model Membranes as a Platform for Accommodating Photosynthetic Light-Harvesting Proteins

The conflicting observations and debated models about the site and mechanisms of NPQ described in Sections 1.5.3 and 1.5.4 partly stem from the multiplicity of the environments that have been used to accommodate the LHCs, which results in vastly different, including far-from-native, conformations and, in turn, different photophysical properties. A commonly used environment for isolating and solubilizing membrane proteins including photosynthetic LHCs is detergent micelles. However, detergents are known to induce non-native conformations to the protein, and therefore obscure the physiologically relevant conformational changes responsible for activation of dissipation as well as potentially distort the photophysics [143]. On the other

extreme is the native *in vivo* environment, such as whole leaves, which often leads to convoluted spectroscopic signatures from the large number of homologous LHCs that cannot be disentangled, and is prone to laser-induced artifacts such as singlet-singlet annihilation [102, 144, 145].

In order to overcome the limitations of the two most commonly adopted environments mentioned above, model membranes, meaning the assembly of near-physiological membranes, are being increasingly utilized to accommodate the LHCs [40, 146–149]. A widely utilized model membrane platform for photosynthetic LHCs has been liposomes, which are micron-sized spherical vesicles of lipid bilayer membranes. While liposomes provide a near-native and controllable environment for the embedded LHCs, their size and protein content tend to be heterogeneous. Furthermore, their large size leads to high levels of scattered light, making spectroscopic measurements of liposomes challenging [150, 151].

1.6.1 Nanodiscs

One class of model membranes, known as nanodiscs, are a discoidal structure with control over both membrane size and composition [152, 153]. As shown in Figure 1-11, a lipid bilayer with the embedded membrane protein of interest is encircled by an amphiphilic membrane scaffold protein, which solubilizes the nanodisc.

Nanodiscs self-assemble *in vitro* upon mixing the membrane protein of interest, lipids, and the membrane scaffold protein in a pre-designed stoichiometry. The ratio of lipids to the membrane protein controls the membrane protein content of the nanodisc. The length of the membrane scaffold protein and ratio of this protein to lipids control the size of the nanodisc. A desired size and protein content can be further selected by purification with size-exclusion and ion exchange chromatography.

Nanodiscs offer several advantages over liposomes. First, their smaller size (a few to tens of nm), and the resultant reduction in scattered light, make them much more amenable for spectroscopic studies. Second, the flat membrane architecture of nanodiscs, in contrast to the highly curved topology of the membranes in liposomes, better mimics the lateral membrane pressure that the embedded protein experiences

Figure 1-11: **Components of a membrane nanodisc.** Cartoon illustration of a membrane nanodisc with a single LHCII protein (green) embedded. The lipid bilayer and membrane scaffold protein are shown in light gray and dark gray, respectively.

in native biological membranes. Third, the tunability of the membrane area (size) imposed by the length and stoichiometry of the membrane scaffold protein enables a more systematic control of the size and protein content, thereby yielding a more homogeneous distribution of size and protein density compared to liposomes.

Nanodiscs, therefore, are a promising platform for ultrafast spectroscopic studies of photosynthetic LHCs that provides both a physiologically relevant membrane environment and systematic control over local membrane composition. Chapters 4−6 of this thesis describe how the nanodisc platform can be applied to spectroscopic studies of LHCII, and how it can be extended towards mimicking the native photosynthetic machinery of plants.

Chapter 2

Ultrabroadband Two-Dimensional Electronic Spectroscopy

Adapted from: Son, M., Mosquera-Vázquez, S. & Schlau-Cohen, G. S. "Ultrabroadband 2D Electronic Spectroscopy with High-Speed, Shot-to-Shot Detection", *Opt. Express* **16**, 18950−18962 (2017).

2.1 Chapter Summary

Two-dimensional electronic spectroscopy (2DES) is an incisive tool for disentangling excited-state energies and dynamics in the condensed phase, which directly maps out the correlation between excitation and emission frequencies as a function of time. The spectral range of detection in the vast majority of conventional 2DES apparatuses is limited to sub-100 nm, thereby encompassing only a narrow subset of the excited states of the system, whereas the electronic structure of many condensed-phase systems is typically spread over the entire visible range. In this chapter, I describe the construction of an ultrabroadband 2DES apparatus with a detection range that spans the entire visible region (450−800 nm), which enables a simultaneous interrogation of electronic transitions over a ∼200 nm bandwidth. The ultrabroadband laser spectrum is generated by gas filamentation in argon, and combined with an all-reflective 2DES setup, the optical, optomechanical and electronic components of which are discussed

in detail. To address the deterioration of detection sensitivity due to the inherent instability of ultrabroadband sources, a shot-to-shot, dual chopping data acquisition scheme is implemented. Comparison of the 2D spectra of a laser dye acquired by shot-to-shot detection and conventional, averaged detection shows a 15-fold improvement in the signal-to-noise ratio (SNR). This significant improvement in sensitivity enables the application of the ultrabroadband 2DES instrument for biological samples, which typically lead to a high level of scatter and cannot be measured with high excitation powers, as discussed in later chapters.

2.2 Introduction

Coherent two-dimensional (2D) optical spectroscopy is a powerful spectroscopic tool for studying the energy landscapes and dynamics of condensed-phase systems [154]. In particular, 2DES, which uses ultrafast visible pulses to excite electronic transitions of the system, has been extensively utilized to unravel couplings between electronic and vibronic states [155–160], energy relaxation pathways and quantum coherence in a variety of systems including photosynthetic light-harvesting complexes [161–164] as well as organic and inorganic nanostructures [165–174]. 2DES has proven to be particularly incisive for interrogating complex systems with highly congested energy states; the time evolution of the emitted third-order signal along one frequency axis (emission frequency, ω_t) is spread out on a second frequency axis (excitation frequency, ω_τ), resulting in a correlation map between ω_τ and ω_t of the system. This grants 2DES a significant advantage over the one-dimensional pump-probe technique, an enhanced spectral (frequency) resolution while maintaining its ultrafast temporal resolution.

Since the first demonstration of 2DES technique as an optical analog of 2D nuclear magnetic resonance (NMR) two decades ago [175, 176], various experimental implementations are being developed and examined towards enhanced phase stability, a broader spectral window, and faster data acquisition with improved sensitivity [177]. Early instrumental developments in 2DES were focused on achieving interferometric temporal precision and phase stability, which are critical for accurate retrieval of the

excitation frequency axis [178–181]. More recent efforts have been centered towards generation of broader excitation sources and improvements in data acquisition and processing methods for a broader detection window as well as higher-throughput data collection [182–186].

The spectral window of the measured 2D frequency correlation map is directly limited by the bandwidth of the laser spectrum used. Until recently, a non-collinear optical parametric amplifier (NOPA) was the most widely used and accessible source of excitation for 2DES [187]. Although the wavelength range of a NOPA is readily tunable by varying the phase matching angle [188], in most cases its bandwidth is limited to sub-100 nm in the visible region, which limits the detection window to a few tens of nm in wavelength. This limitation makes NOPA-based apparatuses unable to simultaneously probe the broad range of electronic and vibronic transitions across the entire visible range typically seen in condensed-phase systems. To be able to capture the complete picture of the energy landscape and relaxation pathways, a broadband light source is required, as has been recently implemented in transient absorption spectroscopy experiments [189–192]. Several works demonstrating the applicability of broadband, few-cycle supercontinuum pulses to 2DES were published in recent years [182, 193–196]. While there are several different approaches to generate supercontinua [172, 185, 197, 198], a popular method of supercontinuum generation reported for 2DES is gas filamentation, where a high-power output of a femtosecond regenerative amplifier is focused into a chamber filled with pressurized gas, such as argon, neon, nitrogen, or air [199–201]. Gas filamentation is a simple and robust solution to the drawbacks of white light generation in bulk media, because it provides $2-3$ orders of magnitude higher pulse energies than those with bulk crystals, and offers a higher damage threshold and lower dispersion as no bulk material is present in the medium [198].

However, a major drawback of using ultrabroadband pulses generated by filamentation is that they are inherently less stable than a NOPA [182]. Thus, a high-sensitivity detection method that is resistant to the fluctuations of the ultrabroadband source is required. Highly sensitive 2DES enables resolution of weak cross peaks or

measurements of photochemically unstable samples or with low pulse energy. Following method developments for transient absorption spectroscopy [202–204], balanced detection with a reference pulse [183] and shot-to-shot acquisition [184] have been implemented in 2DES, and up to a 10-fold improvement in sensitivity was reported. While these examples directly characterized the impact of balanced and shot-to-shot detection methods on detection sensitivity, the pulses were generated using a NOPA and a solid-state crystal, respectively, which are fundamentally different mechanisms with different noise profiles from gas filamentation. Although gas filamentation is being increasingly adopted in ultrafast spectroscopy as an alternative to NOPAs or bulk continuum generation, quantitative analysis of the noise profiles and stability of filamentation-based supercontinuum has not yet been reported. Furthermore, implementation of high-sensitivity detection methods to overcome the instability of filamentation-based supercontinuum sources has not yet been demonstrated.

In this chapter, I report the construction of an all-reflective 2D electronic spectrometer that combines an 8 fs ultrabroadband pulse spanning the entire visible region generated by gas filamentation and high-speed, 5 kHz shot-to-shot data acquisition. The high-speed detection method is enabled by a shot-to-shot dual chopping scheme using two optical choppers that operate at different frequencies, which leads to an improved sensitivity by removing scattered light from the 2D signal every laser shot. This is a simple and robust 2DES setup with only conventional optics that provides a broad spectral window (200 nm) as well as overcomes the limited stability of filamentation-based supercontinuum with high-sensitivity detection. The enhancement in sensitivity with shot-to-shot detection is quantitatively analyzed, and a 15-fold improvement was obtained relative to the conventional, averaged detection. The functionality of the constructed apparatus is examined by 2DES measurements on a laser dye, Nile Blue A perchlorate.

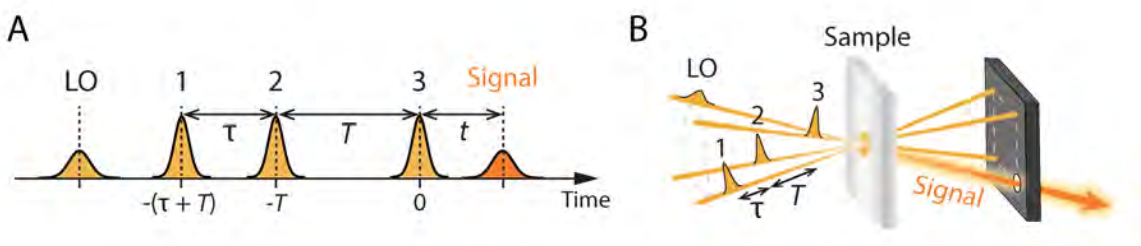

Figure 2-1: **Pulse sequence of 2DES.** (A) Pulse sequence of a 2DES experiment. Time zero is arbitrarily set to the point where pulses 1−3 are coincident on the sample. The LO is temporally delayed for heterodyne detection. The LO precedes the other three pulses to prevent pump-probe background from interfering with the 2D signal. (B) Illustration of the pulse sequence shown in (A) for a BOXCARS phase-matching geometry. The emitted third-order signal propagates in the same direction as the LO, and the interference between the two is detected. After exciting the sample, beams $1-3$ are blocked with a spatial mask, and only the signal/LO propagates towards the detector.

2.3 Principles of Two-Dimensional Electronic Spectroscopy

2DES is a third-order, transient four-wave mixing spectroscopic technique, in which the light-matter interactions between the system and three pulses lead to emission of a nonlinear signal that encodes the third-order susceptibility of the system in a certain phased-matched direction [205, 206]. Readers interested in details of the quantum mechanical theory of 2D spectroscopy are referred to the discussions in [205, 207].

A typical pulse sequence of 2DES and the time intervals between pulses are displayed in Figure 2-1A. The laser pulses utilized in 2DES are typically several tens of fs in duration and tens of nm in spectral bandwidth. The first pulse (pulse 1) excites the system and generates a coherent superposition between the ground state and the first excited state of the system. The generated coherence evolves in time for the time period of τ, typically known as the coherence time. The second pulse (pulse 2) creates a population or an excited-state coherence, which evolves for a second time interval, known as the waiting time (T). The light-matter interaction with the third pulse (pulse 3) creates another coherence (emission coherence), which reads out the current state of the system and leads to the emission of the third-order signal. The fourth

pulse, commonly referred to as local oscillator (LO), does not directly participate in the third-order nonlinear process. Instead, it serves as a reference pulse in the heterodyne detection scheme of 2DES, where the emitted third-order signal is mixed with the LO, and the interference between the signal and the LO is detected. Heterodyne detection enables acquisition of both the amplitude and phase of the signal, allowing for the separation of the real and imaginary parts of the signal. Furthermore, mixing of the weak, third-order signal with a more intense reference pulse results in an amplification of the detected signal intensity. A widely used phase-matching geometry in a 2DES experiment is a fully non-collinear, square-like geometry called the BOXCARS geometry, as illustrated in Figure 2-1B. In this geometry, the third-order signal is emitted in the same direction as that of LO propagation, creating an interference between them. The benefit of using the BOXCARS phase-matching geometry, as opposed to a collinear, pump-probe geometry, which is another widely implemented phase-matching geometry for 2DES, is that it allows for a background-free detection of the signal with improved sensitivity.

2.4 Generation and Characterization of Ultrabroadband Laser Pulses

2.4.1 Supercontinuum Generation by Gas Filamentation

The ultrabroadband excitation source is produced by supercontinuum generation via self-guided argon gas filamentation, as has been reported previously [182, 193, 200]. A 5 kHz Ti:sapphire regenerative amplifier (Libra, Coherent) provides the initial input pulse centered at 800 nm (32 nm full-width at half maximum (FWHM)) with a pulse duration of less than 40 fs. To generate the supercontinuum, an attenuated output of the regenerative amplifier, the power of which is varied with a half-wave plate (HWP in Figure 2-2), is focused with an achromatic lens ($f = 1,000$ mm) into a 1 m long steel chamber filled with pressurized argon gas at 20 psi. The argon chamber is sealed at both ends with two 1 mm thick fused silica Brewster windows. Typically, a

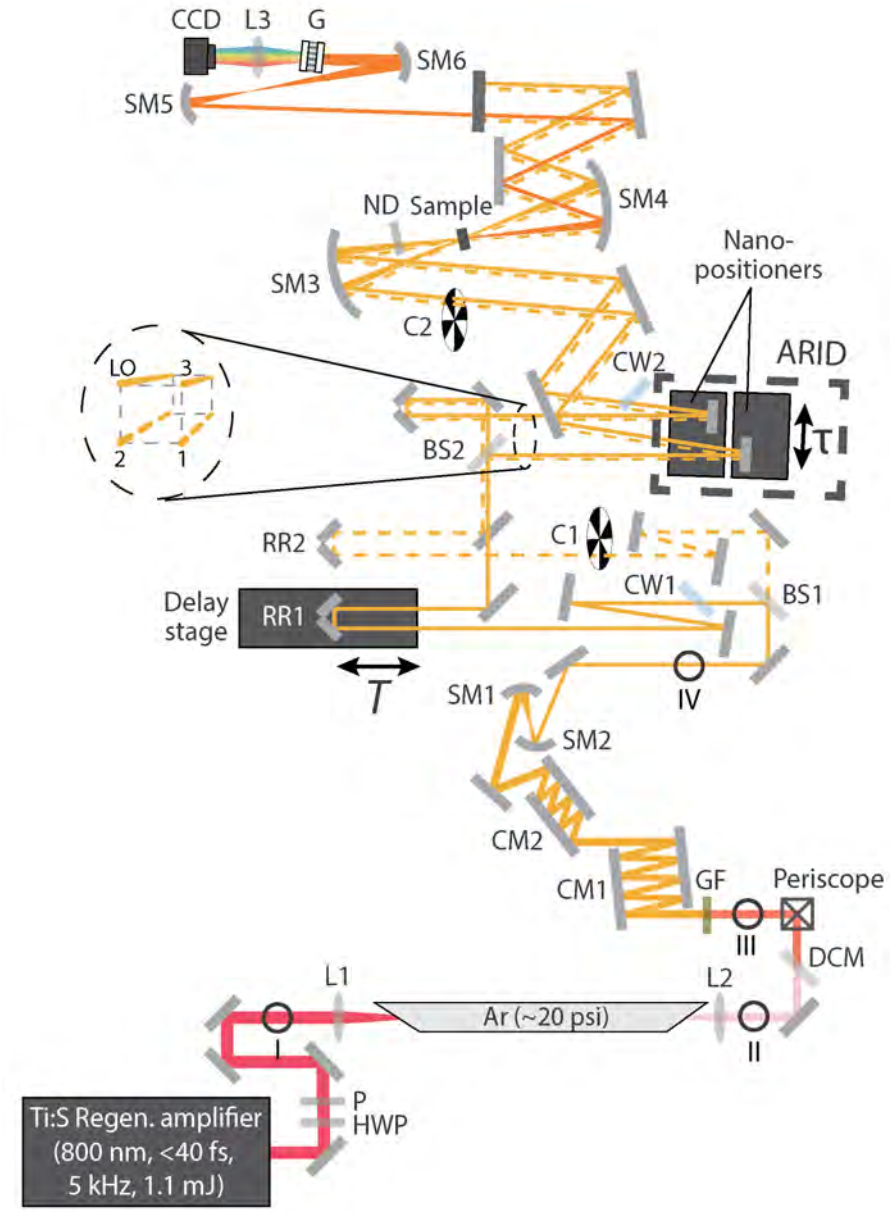

Figure 2-2: **Optical layout of the ultrabroadband 2DES apparatus.** HWP: Half-wave plate; P: Thin film polarizer; L1, L2: Focusing and collimating lenses for supercontinuum generation (f = 1,000 mm and 750 mm, respectively); DCM: Shortpass dichroic mirror (805 nm cutoff); GF: Glass bandpass filter(s); CM1, CM2: Chirped mirror pairs; SM1, SM2: Spherical (concave) mirrors for beam size reduction (f = 150 mm and 100 mm, respectively); BS1, BS2: 50/50 Beam splitters; CW1, CW2: Fused silica compensating windows (1 mm thick); C1, C2: Optical choppers; RR1, RR2: Retroreflectors; SM3, SM4: Spherical (concave) mirrors (f = 250 mm); ND: Neutral density filter; SM5, SM6: Spherical (concave) mirrors for beam expansion for the spectrometer (f = 150 mm and 500 mm, respectively); G: Grating; L3: Focusing lens (f = 150 mm). The ARID assembly is labeled with a dashed box. The dashed oval illustrates the side view of the four beams propagating towards the ARID.

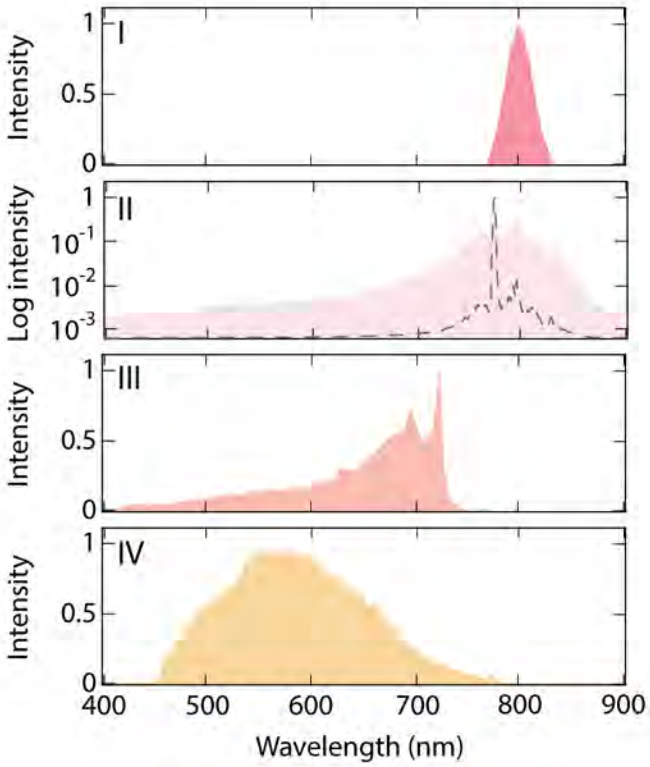

Figure 2-3: **Generation and spectral tailoring of the ultrabroadband pulse.** Spectra measured at different stages of ultrabroadband pulse generation. The positions where each spectrum is measured are labeled in Figure 2-2 with roman numerals I−IV. I: Before supercontinuum generation, II: Untailored output of the supercontinuum generation, III: Attenuation of > 800 nm light with a DCM, IV: Final spectrum employed for 2DES measurements. Due to the weak intensity at $400 - 700$ nm, spectrum II is plotted on a logarithmic scale with the linear-scale spectrum overlaid in dashed gray line.

minimum input pulse energy of 540 μJ is required for supercontinuum generation to take place. The resultant spectrum exhibits spectral broadening around the center wavelength of the fundamental (Figure 2-3, I and II), although the intensity at < 700 nm is $2-3$ orders of magnitude lower than that around 800 nm. Only a minor power loss was observed; an output energy of 500 μJ was measured, which corresponds to 92.6% of the input energy. To attenuate the intense residual from the fundamental, the collimated supercontinuum is passed through a shortpass dichroic mirror with a cutoff wavelength of 805 nm (DMSP805, Thorlabs; DCM in Figure 2-2), resulting in spectrum III shown in Figure 2-3. After attenuation, a pulse energy of 260 μJ was measured, which is 52% of the 500 μJ energy before attenuation and 48.2% of the initial input energy, 540 μJ. The conversion efficiency of 48.2% is comparable to what was reported in the literature with similar methods [200]. To achieve a smooth spectral profile with evenly distributed light intensity across the entire spectral range, the spectrum is further tailored with one or more glass bandpass filters (GF). The number and cutoff wavelength of the filters are routinely varied depending on the absorption spectrum of the sample being measured (see Chapters 3−6 for more detailed discussions). Spectrum IV shown in Figure 2-3 was produced with two identical glass bandpass filters with transmittance at $330 - 665$ nm (FGS600, Thorlabs). The spectrum spans the entire visible range ($450 - 800$ nm) with a center wavelength of 580 nm and a FHWM bandwidth of 180 nm. The lack of intensity at < 450 nm is due to a zero reflectance of the chirped mirror pairs (CM1 and CM2) in this range. The energy of the pulse after all spectral filtering was 12 μJ, which corresponds to 2.2% of the minimum input energy 540 μJ.

2.4.2 Characterization of Stability

The stability of the generated ultrabroadband pulse was characterized by measuring the fluctuation of its intensity over time. The shot-to-shot intensity fluctuation was measured by recording 1,024 spectra at 5 kHz, and revealed a relative standard deviation (RSD) of 1.5% in the integrated intensity and 1.3% at a single wavelength (580 nm), respectively. The long-term stability was also examined by collecting the

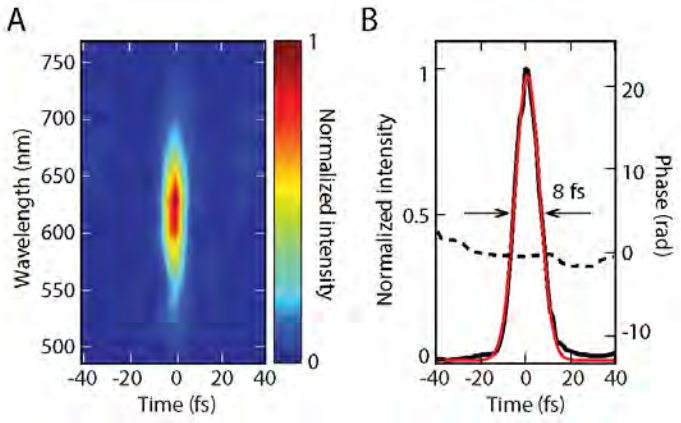

Figure 2-4: **Compression of the ultrabroadband pulse.** (A) TG-FROG trace of the ultrabroadband pulse (spectrum IV in Figure 2-3) measured at the sample position. (B) Temporal intensity (black solid line) fitted with a Gaussian function (red) and phase (black dashed line) profiles retrieved from the FROG trace.

spectrum every 30 seconds over 4 hours. An intensity fluctuation of 2.0% and a spectral fluctuation of 1.7% at 580 nm were observed. These are comparable to the fluctuation of the input fundamental beam, with an RSD of 1.7% for the integrated intensity fluctuation and 1.3% measured at 800 nm. These results indicate that the intensity fluctuation of the generated ultrabroadband pulse predominantly arises from the fluctuation of the laser, and that there is no long-term drift in the intensity.

2.4.3 Characterization of Pulse Duration

The ultrabroadband pulse is compressed with two pairs of group velocity delay (GVD)-oscillation-compensated chirped mirrors (PC70, Ultrafast Innovations; CM1, CM2) with an average GVD of -40 fs^2/mm per double bounce [208]. A variable amount of fused silica (typically $1-2$ mm) is used for fine tuning of the dispersion. The temporal profile of the pulse was measured with transient grating frequency-resolved optical gating (TG-FROG) [209] on a 5 mm thick N-BK7 glass window at the sample position with a 200 nJ pulse energy (Figure 2-4). The TG-FROG trace shows that the entire spectral range of the ultrabroadband pulse is compressed to a FWHM of 8 fs. The beam diameter of the compressed pulse is reduced from 6 mm to 4 mm using two concave mirrors (SM1 and SM2) before being sent into the 2DES setup described

in detail below.

2.5 Ultrabroadband Two-Dimensional Electronic Spectrometer

The optical layout of the ultrabroadband 2DES apparatus is illustrated in Figure 2-2. To minimize any wavelength-dependent dispersion, which is a critical experimental consideration for broadband ultrafast spectroscopic techniques, I designed an all-reflective setup similar to the one reported in [180]. No transmissive optic was used throughout the system with the exception of two 1 mm thick ultrafast beam splitters (BS1 and BS2; 106896, Layertec) and two fused silica compensating windows (CW1 and CW2).

2.5.1 Generation of the Four Beams in a BOXCARS Phase-Matching Geometry

The two beam splitters create four beams in a fully non-collinear, BOXCARS phase-matching geometry. The first beam splitter (BS1) creates the first pulse pair with a vertical separation of 0.5", the two arms of which are illustrated with solid (upper arm; beam 3 and the LO) and dashed (lower arm; beams 1 and 2) lines in Figure 2-2. The second beam splitter (BS2) then introduces a 0.5" horizontal separation to the vertically separated pulse pair, thus giving rise to four beams in a 0.5"×0.5" BOXCARS geometry (see dashed oval in Figure 2-2). T is introduced by moving beam 3 and the LO away from beams 1 and 2 by a retroreflector (RR1) mounted on a motorized translational stage (PRO115SL-200, Aerotech). Two 1 mm thick fused silica windows (CW1, CW2) are added in the arm reflected off each beam splitter to compensate for the dispersion introduced to the other arm that goes through the beam splitter.

2.5.2 Control of Coherence Time Delays

τ, the time delay between pulses 1 and 2, is varied with two identical motorized nanopositioner stages (ANT95-25-L, Aerotech), each of which records the rephasing and nonrephasing halves of the 2D data. Because 2DES is a Fourier-transform spectroscopic technique, it is critical to ensure an interferometric precision in the timing between pulses. Timing jitters as small as 0.5 fs can lead to peaks appearing at incorrect ω_τ frequencies or cause artifactual peaks to appear [154, 177, 205]. To control τ with interferometric precision but without introducing dispersion, the all-reflective interferometric delay (ARID) system reported in [193] is utilized (Figure 2-5A). The ARID assembly consists of four square mirrors arranged in a four-quadrant fashion [210]. Of the four, the bottom two mirrors (M1 and M2), which reflect beams 1 and 2, are mounted respectively on the two nanopositioners at a small angle ($\theta = 0.3°$) to the plane normal to the beam propagation. In this angled geometry, the effective increment (Δx) in nanopositioner position is greatly reduced from the actual increment (Δd) when θ is small because of the relationship $\Delta x = \Delta d \sin\theta$ (Figure 2-5B). Therefore, the ARID system enables a much more precise control over the τ steps without approaching the mechanical limit of the precision of the nanopositioner, which, in this case, is 100 nm. At the chosen angle of $\theta = 0.3°$, $\Delta d/\Delta x = \sin\theta = 191$. For example, moving the nanopositioners in 500 nm steps ($\Delta d = 500$ nm), which corresponds to a τ step size of 1.67 fs, translates to $\Delta x = 2.62$ nm, and in turn, an effective τ step size of 0.0087 fs. While the former results in a sampling rate below the Nyquist frequency for visible light and will cause aliasing of ω_τ, the latter corresponds to a sampling rate well above the Nyquist frequency due to the 191-fold reduction in the effective step size [205, 211]. This example highlights the utility of the ARID in precise control of τ delays, particularly when the mechanical precision of the stage is the major limitation.

In my system, the two nanopositioners are mounted on a baseplate with screw holes at variable positions so that θ can be readily varied without having to unmount the individual optical components. Of the two top mirrors, one mirror (M_{LO}) is

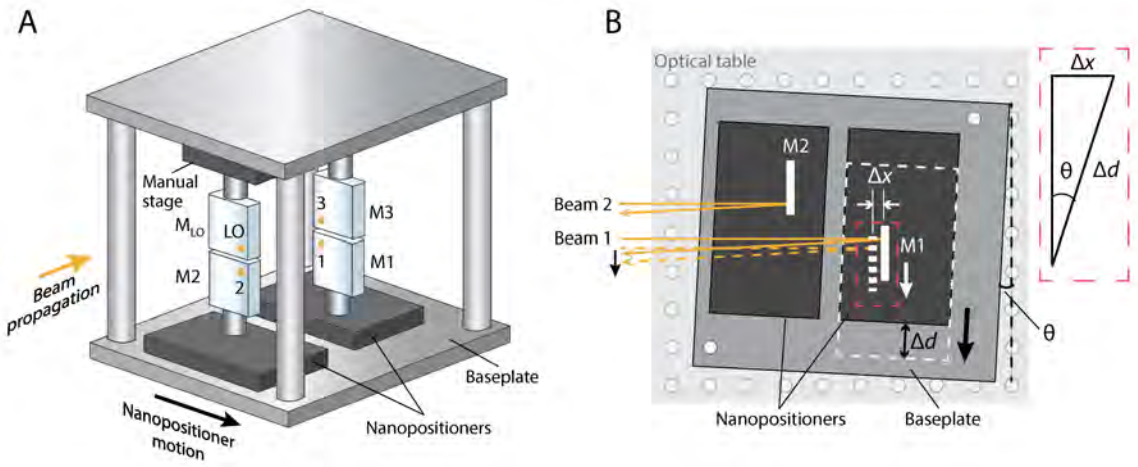

Figure 2-5: **ARID assembly.** (A) Illustration of the overall layout and components. (B) Detailed view of the bottom part illustrating the principle of coherence time control with the ARID.

mounted on a manual linear translational stage, which introduces a temporal delay to the LO from the other three beams. In the BOXCARS geometry, the rephasing ($k_{\mathrm{R}} = -k_1 + k_2 + k_3$) and nonrephasing ($k_{\mathrm{NR}} = k_1 - k_2 + k_3$) contributions of the signal are collected separately by reversing the timing between pulses 1 and 2 (Figure 2-1). Specifically, at any given waiting time T, beam 1 is scanned from $-(\tau + T)$ to $-T$ for the rephasing half, and beam 2 is swept from $-T$ to $-(\tau + T)$ to obtain the nonrephasing half by alternating the two nanopositioners.

The wavelength-dependent calibration factor, which is the conversion factor between the nanopositioner step size (Δd) and the coherence time step ($\Delta\tau$), is determined before each 2DES measurement by recording the spectral interferogram between beams 1 and 2 at $T = 0$ at the sample position (Figure 2-6A). The calibration factor was obtained by calculating the proportionality constant between Δd and the known wavelength of light, and then dividing the constant by the speed of light at each wavelength. In the case of $\theta = 0.3°$, a calibration factor of $40 - 45$ fs/mm was typically obtained, which is $148 - 167$ times smaller than what would be achieved by scanning the nanopositioners in the direction of beam propagation ($\theta = 90°$), as mentioned earlier. A typical RSD of the calibration factor across the spectral range of the ultrabroadband spectrum is 0.15% (Figure 2-6B), which translates to

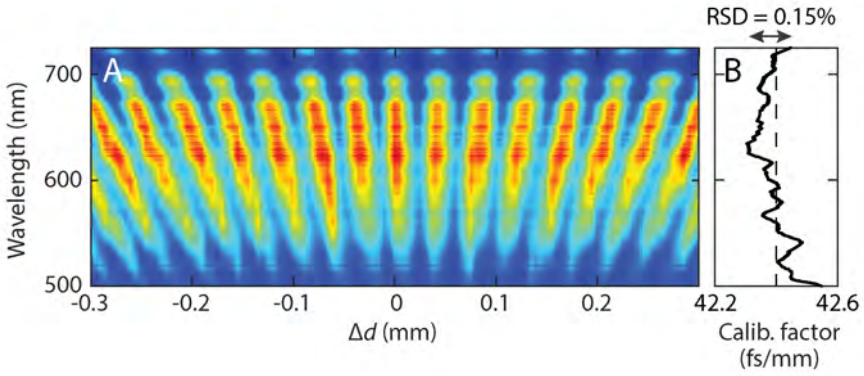

Figure 2-6: **Calibration of τ step size.** (A) Spectral interferogram of beams $1-2$ obtained by scanning the nanopositioners. (B) Calibration factor as a function of wavelength.

only a 0.0017 fs uncertainty in the case of $\Delta\tau = 1$ fs, a commonly employed τ step size in 2DES measurements [212, 213]. This highlights that the all-reflective design of my ultrabroadband 2DES setup indeed leads to minimal wavelength-dependent dispersion across the entire spectral range, which is not achievable with glass wedge pairs, a more widely adopted method for controlling τ steps [177]. Depending on the application, the angle θ can be easily adjusted to a larger value, which allows one to access a longer τ range at the cost of the precision of $\Delta\tau$.

2.5.3 Phase Stability

In addition to ensuring an interferometric precision in $\Delta\tau$, maintaining phase stability is another critical experimental consideration in 2DES. A commonly used method to achieve phase stability for a fully non-collinear, BOXCARS-geometry 2DES setup is to design a (near-)common-path instrument by using common optics for all four beams. This method takes advantage of the fact that the phase fluctuations between pulse pairs $1-2$ and $3-\mathrm{LO}$ are anti-correlated [178, 214]. In the case of the rephasing pathway ($k_\mathrm{R} = -k_1 + k_2 + k_3$), the heterodyne-detected third-order signal (S_R) can be written as

$$S_\mathrm{R}(\omega) = \hat{\chi}^{(3)}(\omega_R; \omega_1, \omega_2, \omega_3)|E(\omega)|^4 e^{-i\omega(-t_1+t_2+t_3-t_{LO})} e^{i\omega(-\varphi_1+\varphi_2+\varphi_3-\varphi_{LO})}, \qquad (2.1)$$

where $\hat{\chi}^{(3)}$ is the third-order nonlinear susceptibility, ω_{R} is the frequency of the rephasing 2D signal, $E(\omega)$ is the electric field, t_i and φ_i are the delay and phase of the ith pulse ($i = 1, 2, 3$; subscript LO is used instead for the fourth pulse) [215]. Thus, the total phase of the rephasing signal (φ_{R}) is

$$\varphi_{\mathrm{R}} = -i\omega(-t_1 + t_2 + t_3 - t_{\mathrm{LO}}) + i\omega(-\varphi_1 + \varphi_2 + \varphi_3 - \varphi_{\mathrm{LO}}). \tag{2.2}$$

Because the first term is measured during the 2DES experiment and can be removed, the phase offset from the incident pulses to the signal ($\Delta\varphi_R$) can be written as

$$\Delta\varphi_R = -\varphi_1 + \varphi_2 + \varphi_3 - \varphi_{\mathrm{LO}} = (\varphi_2 - \varphi_1) + (\varphi_3 - \varphi_{\mathrm{LO}}). \tag{2.3}$$

The overall phase fluctuation that the signal experiences ($\delta(\Delta\varphi_R)$) can then be written as [214]

$$\delta(\Delta\varphi_R) = (\delta\varphi_2 - \delta\varphi_1) + (\delta\varphi_3 - \delta\varphi_{\mathrm{LO}}). \tag{2.4}$$

Therefore, phase stability is achieved in a 2DES apparatus using common paths to generate the four beams, because $(\delta\varphi_2 - \delta\varphi_1)$ and $(\delta\varphi_3 - \delta\varphi_{\mathrm{LO}})$ cancel out even if the individual terms are non-zero [178, 214]. The 2DES setup described here also relies on this passive phase stabilization method. However, because the ARID system has four separate mirrors for the four beams, the phase fluctuations between the two pulse pairs are not completely anti-correlated. Each phase fluctuation term ($\delta\varphi_i$) in Eq. (2.4) can be explicitly written out as the sum of the fluctuation originating from each optic in the beam path. Eventually, all other terms cancel out between the pulse pairs $1-2$ and $3-\mathrm{LO}$, and the overall phase fluctuation of the rephasing signal consists of only four terms that correspond to the phase fluctuation of the four mirrors in the ARID system:

$$\delta(\Delta\varphi_R) = (\delta\varphi_{\mathrm{M2}} - \delta\varphi_{\mathrm{M1}}) + (\delta\varphi_{\mathrm{M3}} - \delta\varphi_{\mathrm{M_{LO}}}). \tag{2.5}$$

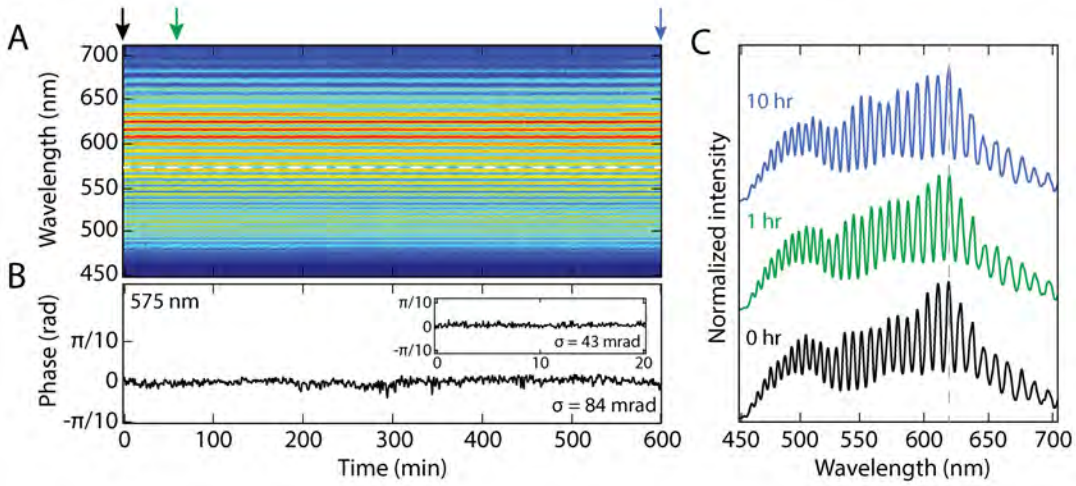

Figure 2-7: **Phase stability.** (A) Spectral interferogram of beams 1 and 2 measured every minute over 10 hours. (B) Long-term phase stability of the spectral interferogram at 575 nm (white dashed line in (A).) Short-term phase stability at this wavelength, measured every 20 seconds over 20 minutes, is also shown in the inset. (C) Time slices of the spectral interferogram at the start of the measurement (black), after 1 hour (green), and after 10 hours (blue), as labeled with arrows in (A). The traces are vertically offset for clarity. A gray vertical dashed line at 620 nm is shown as a guide to the eye.

To minimize the above-mentioned phase fluctuation from the mirrors, the entire ARID system was constructed with steel, and steel mounts were used for all optical components. The phase stability of the setup was evaluated from the interferogram between beams 1 and 2 at fixed stage and nanopositioner positions recorded repeatedly over a period of time (Figure 2-7A). The standard deviation (σ) of the phase retrieved from the interferogram near the center wavelength of the ultrabroadband pulse (575 nm) was 43 mrad over 20 minutes and 84 mrad over 10 hours, which corresponds to a short-term and long-term phase stability of $\lambda/146$ (20 minutes) and $\lambda/75$ (10 hours), respectively (Figure 2-7B). Figure 2-7C shows that the spectral interferograms measured after one hour and after 10 hours are in phase with the one measured at the beginning of the scan, which confirms that the setup maintains good phase stability over a period of at least 10 hours.

After the four beams are reflected off the mirrors in the ARID assembly, they are focused to a 100 μm diameter spot on the sample with a concave mirror (f = 250 mm). The LO is attenuated by three orders of magnitude before entering the

sample and temporally delayed by ∼500 fs by translating M_{LO} on a manual linear translational stage (see Figure 2-5A), such that it enters the sample before beams $1-3$. After recollimation, a spatial mask blocks beams $1-3$ to prevent scattered light from going into the detection system. Finally, the heterodyned signal is sent into a home-built spectrometer, in which a transmissive volume-phase holographic grating (450 grooves/mm, Wasatch Photonics) spectrally disperses the signal and an achromatic focusing lens ($f = 150$ mm) focuses it into a 1×2048 pixel line-scan charge-coupled device (CCD; Aviiva EM4-BA8, e2v). The spectral resolution of the spectrometer is 0.145 nm/pixel, and a typical detection range of the emission wavelength is $470-770$ nm.

2.5.4 5 kHz Shot-to-Shot Data Acquisition and Scatter Removal

In order to enhance the sensitivity of the measurement while reducing the data acquisition time, a high-speed, shot-to-shot (5 kHz) data acquisition method was implemented. Two optical choppers (C1 and C2) that operate at subharmonics of the laser frequency were synchronized with the 5 kHz detection rate to subtract scatter contributions from the raw data, which is known to be a major source of artifact in 2DES [216].

Figure 2-8A illustrates the connectivity diagram of the electronic components in the detection system. Here, the two optical choppers, which operate at 2.5 kHz (C1) and 1.25 kHz (C2), respectively, are synchronized to the 5 kHz transistor-transistor-logic (TTL) output from the synchronization and delay generator (SDG) of the laser. C1 modulates beams 1 and 2, and C2 modulates beam 3 as described in Figure 2-8B. This dual chopping leads to a unique sequence of four different combinations of blocked and unblocked pulses, which are labeled A−D in the figure. The 2D signal is emitted only when all three of beams $1-3$ are unblocked, *i.e.*, in A, and B−D contain scatter originating from the beams unblocked in each pulse combination. The scatter-subtracted 2D signal can be obtained by calculating $A-B-C+D$ every four

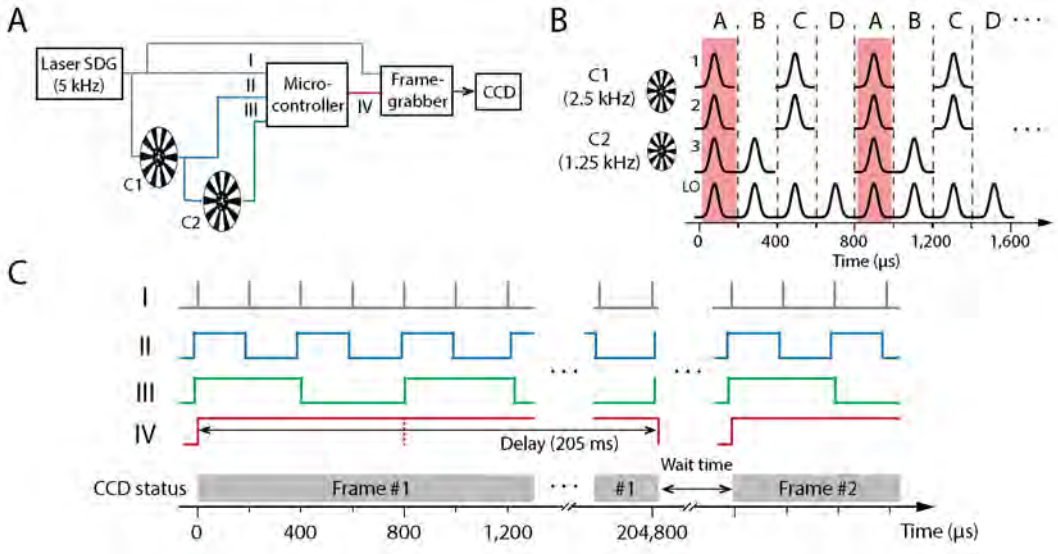

Figure 2-8: **Dual chopping scatter subtraction and synchronization schemes for data acquisition.** (A) Schematic drawing of the hardware connections in the detection part. The TTL output signals of the laser (I) and two choppers (II, III) serve as a trigger input of the microcontroller. The microcontroller output (IV), along with the 5 kHz trigger from the laser, trigger the frame grabber, and in turn, data acquisition in the CCD. (B) Dual chopping scheme for scatter subtraction. The 2D signal is emitted only in the shaded parts of the sequence, where all three of beams 1−3 are unblocked. (C) Timing diagram showing the electronic input/output signals of each hardware component labeled in (A) and their synchronization. Wait time denotes the time interval between adjacent frames during which no data acquisition occurs. This ensures that the acquisition of every frame is synchronized to the pulse sequence A−D in the correct order.

shots, where the terms $A-D$ denote the signal intensity for each pulse combination A−D. This cancels out most of the scatter terms originating from different pulse combinations in the sequence [179, 217]:

$$\begin{aligned} A-B-C+D = & \\ & |s_1+s_2+s_3+E_{\mathrm{sig}}+E_{\mathrm{LO}}|^2-|s_3+E_{\mathrm{LO}}|^2-|s_1+s_2+E_{\mathrm{LO}}|^2+|E_{\mathrm{LO}}|^2 \\ & =|E_{\mathrm{sig}}|^2+2Re\{s_1E_{\mathrm{sig}}^*\}+2Re\{s_2E_{\mathrm{sig}}^*\}+2Re\{s_3E_{\mathrm{sig}}^*\} \\ & \quad +2Re\{s_1s_3^*\}+2Re\{s_2s_3^*\}+2Re\{E_{\mathrm{sig}}E_{\mathrm{LO}}^*\}, \end{aligned} \quad (2.6)$$

where s_i $(i=1,2,3)$ denotes the scatter originating from beam i, and E_{sig} and E_{LO} denote the electric field of the third-order 2D signal and of the LO, respectively. Thus, the data acquisition program computes $A-B-C+D$ and saves the scatter-subtracted 2D signal at each τ at a given T. To circumvent the issue of many conventional electronics being too slow for a 5 kHz detection, I employ a microcontroller (Arduino Mega) and a line-scan CCD that can operate at a frequency as high as 70 kHz. The microcontroller mediates the synchronization among the laser, choppers and the frame grabber; its TTL output IV becomes high only if all inputs I−III are high, which are the TTL output signals from the laser (I) and the two choppers (II and III). The microcontroller output IV serves as an AND gate for the frame grabber along with the 5 kHz trigger from the laser, *i.e.*, the frame grabber begins acquiring 2D spectra when the laser trigger comes in and IV is high at the same time. Typically, the frame grabber acquires 1,024 consecutive lines of data before transferring them to the computer. Therefore, in practice, the minimal unit of data acquisition is a 2D array ("frame") of 1,024 lines × 2,048 pixels. With the 5 kHz shot-to-shot detection, it takes (1,024 lines)/(5,000 lines/s) = 204.8 ms to collect each frame, which contains 256 pulse combinations A−D recorded every laser shot. For synchronization of frame-by-frame acquisition, a delay time that is slightly greater than 204.8 ms (205 ms) is programmed into the microcontroller so that the AND gate signal IV stays high for 1,024 consecutive shots and a full frame of 1,024 lines is collected. After the collection of first frame, IV returns to low and waits for the next A (all beams unblocked) to

initiate the collection of the next frame (Figure 2-8C).

2.6 Preliminary Data on Nile Blue A Perchlorate

To demonstrate the functionality of the setup, 2D spectra of a laser dye Nile Blue A perchlorate were measured. Nile Blue A perchlorate was purchased from Sigma Aldrich and used without further purification. The dye was dissolved in spectroscopic grade ethanol, and the optical density (OD) of the sample was 0.2 (per 0.1 mm) at the absorption maximum (628 nm). The measurement was carried out with a pulse energy of 7 nJ in a 0.1 mm thick quartz cuvette. τ was incremented in 0.4 fs steps over a range of $-100 - 100$ fs, and T was sampled every 5 fs for $0 - 600$ fs. The LO was attenuated by three orders of magnitude, and temporally delayed from pulses $1 - 3$ by 500 fs.

Figure 2-9A shows a representative 2D spectrum of Nile Blue A perchlorate at $T = 200$ fs. The absolute-value spectrum contains a positive diagonal peak at the absorption maximum, which originates from the ground-state bleach (GSB) of the dye. To separate out the real and imaginary parts of the complex-valued data as well as retrieve the correct signs of the peaks, the absolute-value spectrum was phased according to the projection slice theorem [154]. Auxiliary pump-probe spectra of the dye were measured by blocking beams 1 and 3, and using beam 2 as the pump and LO as the probe. The pump-probe spectra were also acquired shot-to-shot by modulating beam 2 using the 2.5 kHz chopper (C1). The complex-valued 2D spectrum was iteratively multiplied by a series of phase factors until the projection of the real part onto the ω_t axis matched the normalized pump-probe spectrum at each T (see Section 2.9.2 for detailed descriptions of the phasing procedure) [179].

The phased absorptive 2D spectrum is shown in Figure 2-9A (right panel), which shows very little difference from the absolute-value spectrum except for a slight frequency shift along the ω_t axis. This indicates that the 2D signal of Nile Blue A perchlorate is dominated by the GSB contribution, in agreement with previously reported results [179, 196]. The 2D signal intensity plotted along T reveals strong os-

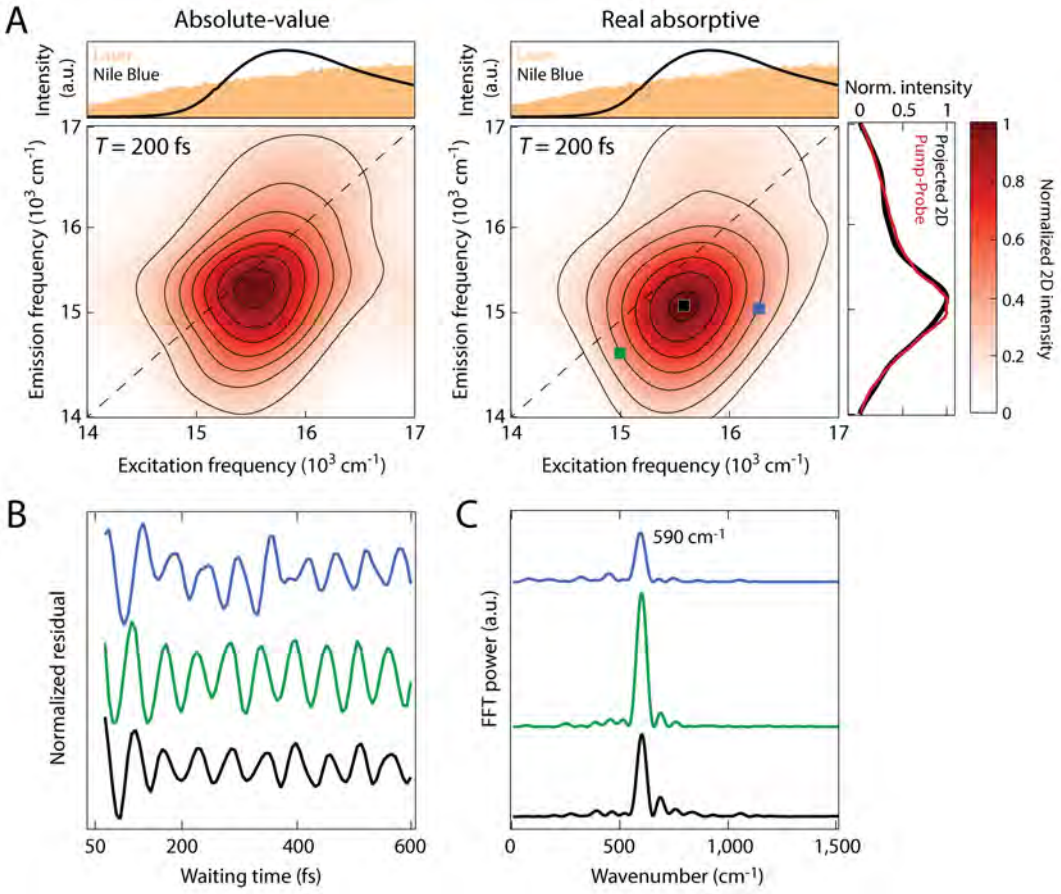

Figure 2-9: **Phasing of the 2D spectrum and vibrational wavepacket dynamics of Nile Blue A perchlorate.** (A) Absolute-value (left) and real absorptive (right) 2D spectrum of Nile Blue A perchlorate at $T = 200$ fs. An overlay of the laser spectrum (orange area) with the dye linear absorption (black line) is shown above each spectrum. To show the quality of phasing, an overlay of the pump-probe spectrum (red) and the projected 2D spectrum after phasing is shown on the right side of the absorptive spectrum. (B) Oscillatory feature showing vibrational wavepacket motions of Nile Blue A perchlorate, obtained by subtracting the exponential decay component from the raw waiting time traces. The three points at which the traces are generated are labeled with colored squares in the absorptive spectrum in (A): (ω_τ, ω_t) = (16,300, 15,000) (blue); (15,000, 14,500) (green); (15,600, 15,100) (black, in cm^{-1}). (C) Fast Fourier transform (FFT) power spectra of the oscillations in (B). The traces in (B) and (C) are plotted with vertical offsets for clarity.

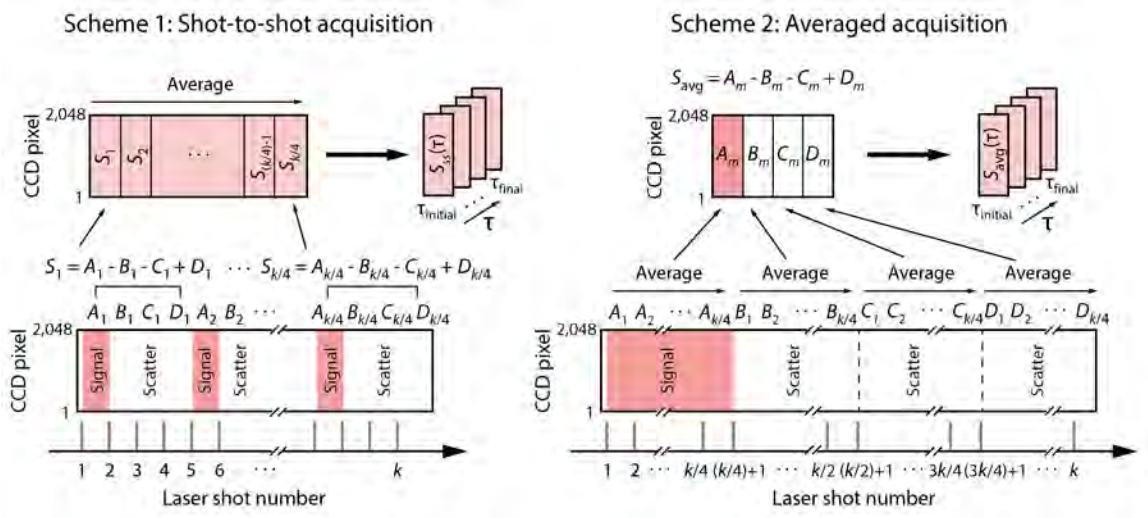

Figure 2-10: **Data acquisition schemes.** Schematic illustration of the shot-to-shot acquisition scheme developed in this work (Scheme 1) and the traditional, averaged data acquisition scheme (Scheme 2) for k consecutive laser shots.

cillations superimposed on the population dynamics, which originate from vibrational wavepacket motions of the dye [196, 218]. To separate out the oscillatory part of the signal from population dynamics, the exponential decay component was subtracted from the raw waiting time traces (Figure 2-9B). Fourier transform of the residuals reveals an intense peak at a frequency of 590 cm^{-1} (Figure 2-9C), which is known to originate from the ring distortion mode of Nile Blue A perchlorate [218].

2.7 Characterization of Detection Sensitivity with Shot-to-Shot Data Acquisition

In this section, I quantitatively characterize the improvement in detection sensitivity with the 5 kHz shot-to-shot acquisition scheme developed in this work by comparing the sensitivity of the shot-to-shot acquisition with that of the traditional, averaged data acquisition.

Figure 2-10 illustrates the two different data acquisition mechanisms for data collection with k consecutive laser shots. Scheme 1 is the shot-to-shot acquisition scheme implemented in this work and described in detail earlier. The four pulse

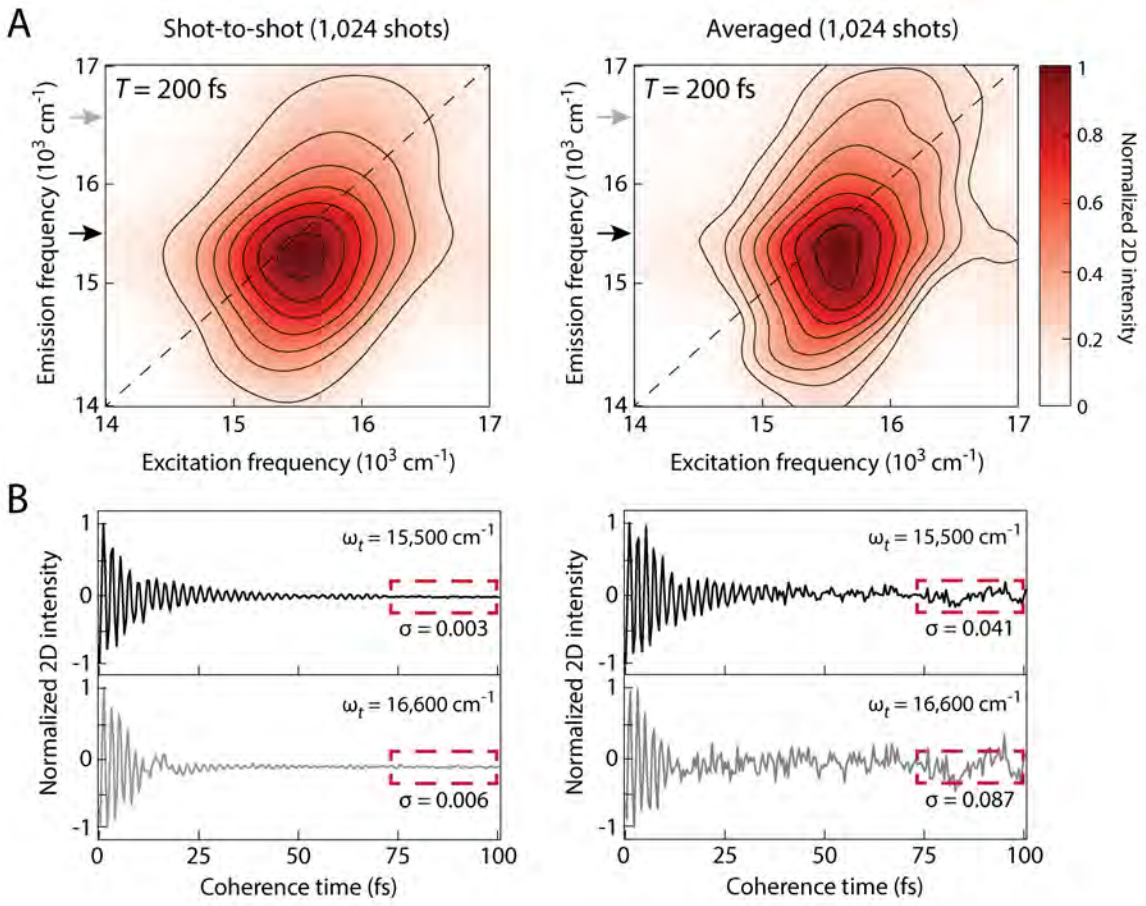

Figure 2-11: **Quantitative comparison of the SNR.** (A) Comparison of the absolute-value 2D data of Nile Blue A perchlorate at $T = 200$ fs acquired with Scheme 1 (left) and Scheme 2 (right), using 1,024 laser shots. (B) Normalized raw time-domain traces at $\omega_t = 15,500$ cm^{-1} (black) and $16,600$ cm^{-1} (gray). The two emission frequencies probed are labeled with arrows in (A). σ was evaluated for the $\tau = 75 - 100$ fs range (red dashed boxes).

combinations A−D as described in Figure 2-8B are collected sequentially, shot by shot. A $(k/4) \times 2048$ scatter-subtracted data array $[S_1, S_2, ...S_{(k/4)-1}, S_{k/4}]$ is constructed by computing $S_i = A_i - B_i - C_i + D_i$ $(i = 1, 2, 3, ..., k/4)$, and averaged to yield the final data vector $S_{\mathrm{ss}}(\tau)$ for each τ. In the averaged acquisition scheme (Scheme 2), which is commonly used in traditional shutter-based 2DES setups [179], each element of the four pulse combinations A−D, A_i, B_i, C_i, and D_i, is recorded in blocks for $(k/4)$ consecutive shots and averaged first to give a 4×2048 array $[A_m, B_m, C_m, D_m]$, instead of alternating the four cases every shot, where $X_m = (\sum_{i=1}^{k/4} X_i)/(k/4)$ $(X = A, B, C, D)$. Thus, the final, scatter-subtracted data vector, $S_{\mathrm{avg}}(\tau)$, is obtained after collecting all k shots $(S_{\mathrm{avg}}(\tau) = A_m - B_m - C_m + D_m)$.

To characterize the improvement in sensitivity with the implementation of the shot-to-shot data acquisition scheme, the 2D spectra of Nile Blue A perchlorate were measured with both schemes and compared (Figure 2-11). Clear differences in data quality are observed in both the processed 2D spectra and the raw interferograms in the τ domain. Although the position of the main diagonal peak is not changed, the 2D spectrum acquired with Scheme 2 exhibits spurious structures in the peak (Figure 2-11A). These structures are not observed in the 2D spectrum acquired with Scheme 1, which suggests that they are artifacts caused by noise.

The SNR was calculated from the noise level of the raw interferograms in the τ domain. As shown in Figure 2-11B, normalized τ-domain traces for $\tau = 0 - 100$ fs were analyzed at $\omega_t = 15,500$ and $16,600$ cm^{-1}, close to the center frequency and high-frequency edge of the diagonal peak, respectively. Following a previously established analysis method [184, 219], the SNR was defined as the reciprocal of the standard deviation (σ) of the noise (SNR$= 1/\sigma$). σ was calculated in the range of $\tau = 75 - 100$ fs, where the oscillatory signal has completely dephased, and thus only noise contributes to the data. Although the absolute noise level is greater at $16,600$ cm^{-1} due to the weaker intensity of the 2D signal, Scheme 1 consistently reveals a ∼15-fold improvement in the SNR over Scheme 2 at both emission frequencies (13.7-fold at $\omega_t = 15,500$ cm^{-1}, 14.5-fold at $\omega_t = 16,600$ cm^{-1}). Notably, Scheme 2 fails to resolve the oscillatory feature of the signal at $\tau = 40 - 75$ fs, which is clearly resolved in the

shot-to-shot interferogram. These results demonstrate that the shot-to-shot acquisition method developed and implemented here provides a significant improvement in detection sensitivity, which helps address the instability issue of filamentation-based ultrabroadband light sources as well as reduces the duration of data collection. A simple calculation suggests that one would need $(0.041/0.003)^2 = 187$ times more signal averaging with Scheme 2 to acquire 2D data of comparable SNR with that of Scheme 1.

2.8 Conclusion

I described the construction of an improved 2D electronic spectrometer by combining ultrabroadband pulses generated by gas filamentation with a high-speed, shot-to-shot data acquisition scheme. A dispersion-free method was adopted for interferometric control of the coherence time delays, which features high precision as well as a long-term phase stability of $\lambda/75$. The shot-to-shot data acquisition method resulted in a 15-fold improvement in the detection sensitivity, thereby enabling a significant reduction in data acquisition time. The improved sensitivity enables filamentation-based supercontinuum sources to be employed for broadband 2DES measurements of a wide range of systems, including those with inherently weak signals or that are easily photodegradable. Furthermore, the much-expanded spectral coverage compared to conventional 2DES setups will allow the detection of previously inaccessible spectroscopic signatures in many visible-light-absorbing systems, in particular pathways of energy transfer between energetically distant transitions.

2.9 Supplementary Information

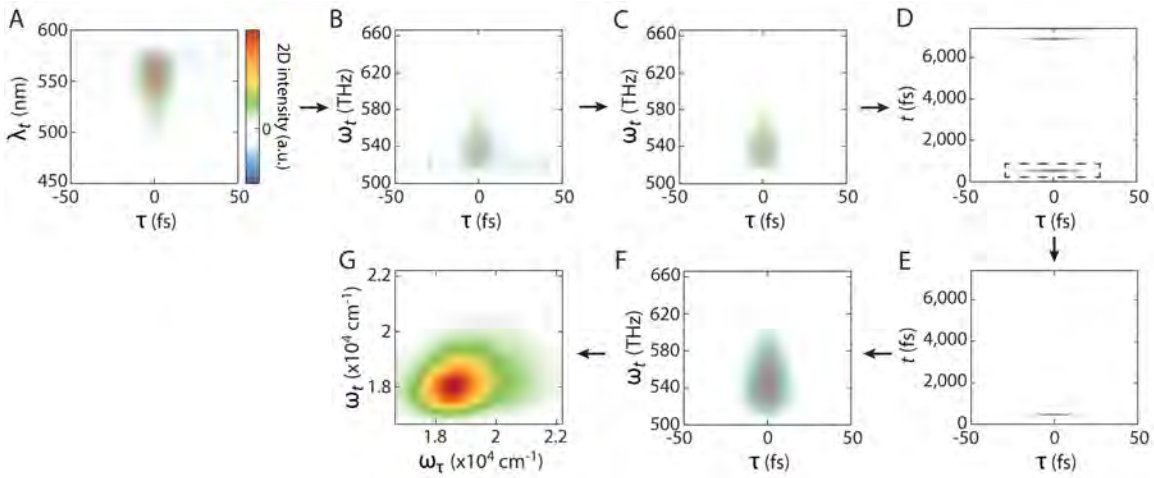

Figure 2-12: **Illustration of the data processing procedure.** Each panel illustrates the plot of the 2D array at each step of the data processing procedure, as described in detail in the text. In (D), the black dashed box indicates the region of the 2D array that was windowed in the t windowing step. The example data presented here are a 2D spectrum of $[Fe(bpy)_3](PF_6)_2$ in acetonitrile, at $T = 1,000$ fs.

2.9.1 Data Processing Procedure

Figure 2-12 outlines the step-by-step procedure of constructing the 2D frequency correlation map (2D spectrum) from the raw data at each T. Data processing is performed with a home-written MATLAB code that follows standard 2D data processing procedures as previously reported in [179] and [220]. The raw, time-domain data are a 2D interferogram in τ and emission wavelength, λ_t ($\lambda_t = c/\omega_t$, A). First, the λ_t axis is converted into a linear frequency axis, ω_t (B), and an apodization function, typically a Hann window, is applied along τ (C). The τ-window 2D array is then inverse Fourier transformed along the ω_t axis, resulting in a $\tau - t$ array as shown in (D). The portion of the $\tau - t$ array that contains the signal is selected by applying an apodization function along t (E). Here, similarly to τ windowing, a Hann window is typically applied. The windowed time-domain array is Fourier transformed back along t, resulting in a $\tau - \omega_t$ array, and then normalized by dividing by the LO intensity (F). Finally, the 2D array in (F) is Fourier transformed along τ to generate the ω_τ axis, which gives rise to a complex-valued 2D frequency correlation map between

ω_τ and ω_t (G). The procedure is repeated for each T to yield a 2D spectrum at each T.

2.9.2 Phasing

Following the generation of the 2D frequency correlation maps as described in Section 2.9.1, the maps are phased according to the projection slice theorem [154], using a home-written MATLAB fitting routine. The complex-valued 2D spectrum at each T, $S_{2D}(\omega_\tau, T, \omega_t)$, is iteratively multiplied by a series of phase factors until the projection of the real part onto the ω_t axis converges to the normalized pump-probe spectrum, $PP(T, \omega_t)$ [179]:

$$PP(T,\omega_t) = Re\Big\{ \int_{-\infty}^{\infty} S_{2D}(\omega_\tau, T, \omega_t) exp\Big(i(\phi + (\omega_t - \omega_0)t_c + (\omega_t - \omega_0)^2 t_q^2 + (\omega_\tau - \omega_0)\tau_c)\Big) d\omega_\tau \Big\}, \tag{2.7}$$

where ω_0 is the laser center frequency. Four different phase factors are used to phase the 2D spectrum. ϕ is an overall constant phase correction, t_c and t_q correct for linear and quadratic errors in the time delay between beam 3 and the LO, and τ_c is the correction term for the drift in $\tau = 0$ [170, 220]. In most cases τ_c is not needed, which confirms the phase stability of the setup as shown earlier.

Chapter 3

Carotenoid-Mediated Light-Harvesting Pathways in Light-Harvesting Complex II

Adapted from: Son, M., Pinnola, A., Bassi, R. & Schlau-Cohen, G. S. "The Electronic Structure of Lutein 2 Is Optimized for Light Harvesting in Plants", *Chem* **5**, 575−584 (2019).

3.1 Chapter Summary

This chapter discusses the application of the ultrabroadband two-dimensional electronic spectroscopy (2DES) apparatus described in Chapter 2 to reveal energy relaxation pathways in light-harvesting complex II (LHCII), the major light-harvesting complex in green plants and algae, across the visible solar spectrum. Due to their narrow spectral bandwidth, previous 2DES measurements of LHCII had been limited to the two lowest-energy transitions of the antenna complex, which correspond to only 20% of its total absorption range by area. Using ultrabroadband 2DES, I map out the pathways of energy flow involving higher-lying electronic states that had not been explored previously, *i.e.*, how the high-energy states funnel energy rapidly and efficiently downhill towards the low-lying states. In particular, I elucidate the

electronic structure and photophysical pathways of carotenoids (Cars), the accessory light-harvesting pigments, which dominate the high-energy absorption range of LHCII as well as bridge the large energy gap between the high-energy (Soret) and low-energy (Q_x/Q_y) states of the chlorophylls (Chls). Cars possess a convoluted electronic structure with one or more dark states. LHCII contains four Cars, each within its own protein pocket with distinct structure and energetics, which, along with the complexity of Car electronic structure, makes the identification of Car-mediated photophysics challenging. The high spectral resolution of 2DES and improved spectral bandwidth of my ultrabroadband 2D apparatus enable mapping of the energy transfer dynamics and electronic structure of the Cars bound within LHCII. I find that one Car, lutein 2 (Lut2), provides a nexus for light harvesting, collecting energy from higher-lying states and funneling it downhill, partially via a debated dark state unambiguously identified by wavepacket analysis. The data indicate that this dark state is present exclusively in Lut2, but not in the other three Cars. The results presented here demonstrate that the protein pocket can tune Car electronic structure via tuning the geometry, a mechanism by which plants control the photophysics of solar energy capture.

3.2 Introduction

LHCII, the major light-harvesting complex in green plants, absorbs across the visible solar spectrum. Its broad absorption spectrum is a combination of the absorption of the constituent light-harvesting pigments, Chls and Cars, which are the primary and accessory pigments in LHCII. Cars have an absorption maximum in the blue-green region (450−550 nm) of the solar spectrum, where Chls poorly absorb [4]. The bright S_2 state of Cars rapidly transfers energy to the lower-lying Chl Q states through multiple parallel pathways, both directly and indirectly via their dark, *i.e.*, optically forbidden, S_1 state and/or higher-lying vibronic states of Chls [75, 76]. At the same time, Cars prevent the formation of deleterious photoproducts by quenching excess absorbed energy, potentially via the S_1 state [122, 134, 136]. However, how Cars

balance these two seemingly-contradictory functions has been debated [66, 83, 121, 122, 134, 136] due to their complicated electronic structure, which depends strongly on local environment [49, 64, 221, 222]. Furthermore, the presence of several intermediate dark states between S_2 and S_1 has been proposed, most notably S_X [52, 59, 223].

Found as a trimer in nature, each monomeric subunit of LHCII binds fourteen Chls, eight Chl *a* and six Chl *b*, and four Cars, including two luteins (Lut1, Lut2) located at the center of the complex (Figure 3-1A) [17]. Although identical in chemical structure, the two Luts are known to possess distinct physical structures induced by their protein binding pockets [66, 68]; the red-shift of Lut2 energy from that of Lut1 is only present in trimeric LHCIIs due to the steric hindrance imposed on its binding site upon trimerization [224, 225], suggesting photophysical differences between the two Cars. In fact, it has been reported that Lut1 plays a unique protective role by dissipating triplet excited states of Chls [83, 225]. In their role as accessory light harvesters, the S_2 state of the Cars has been reported to transfer energy to Chl Q states with time constants of $50 - 130$ fs [75, 76]. However, due to the large energy gaps and ultrafast timescales of these processes over a congested energy landscape, the pathways and dynamics of many of the primary events in the Car-to-Chl energy transfer cascade remain uncharacterized, including the photophysical role of S_X, if present.

In this work, I elucidate the dynamics of Car-to-Chl energy transfer in LHCII using ultrabroadband 2DES. It is observed that the S_2 state of Lut1 and the high-energy Soret band of the Chls rapidly funnel energy to the lower-lying S_2 state of Lut2, which serves as a direct donor state for energy transfer to Chls. Energy transfer from the Chl Soret state to a Car S_2 state as well as between two Car S_2 states, as seen here, had been proposed but unobserved in previous experimental work, and therefore represents an unprecedented mechanism for redistribution of energy. Through wavepacket analysis, I uncover a dark state at the proposed energy of S_X selective to Lut2 populated in < 20 fs by a non-adiabatic transition from its S_2 state. The newly-revealed dark state also serves as a direct donor for energy transfer to the Chls, opening up an additional channel for Car-to-Chl energy transfer with a reduced en-

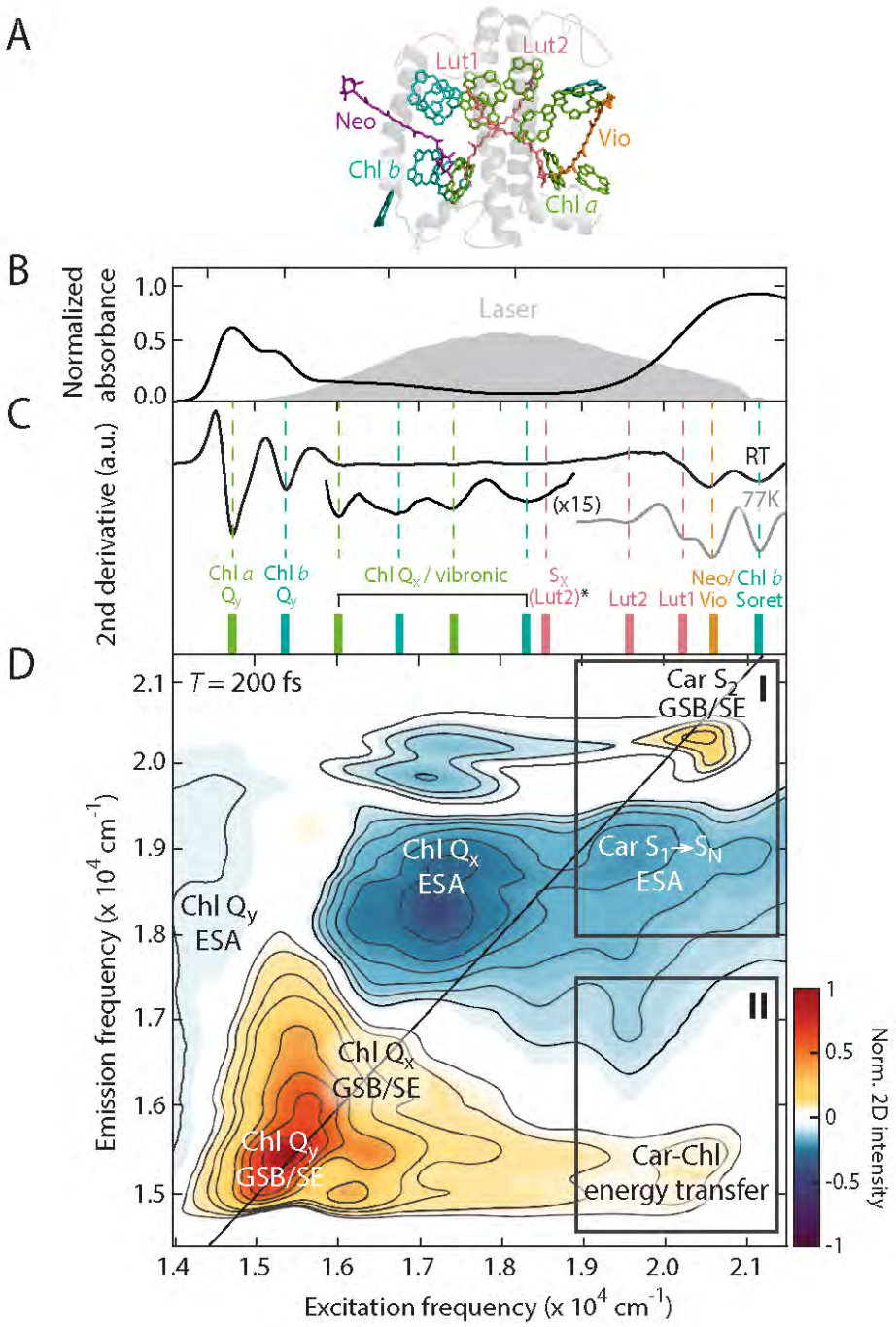

Figure 3-1: **Structure and pigment energy levels of LHCII.** (A) Structure of a monomeric subunit of LHCII with the pigments labeled and color-coded. The phytol tails and side groups of the Chls are omitted for clarity. Neo: neoxanthin, Vio: violaxanthin. (B) Linear absorption and (C) second-derivative absorption spectra (black: room temperature (RT), gray: 77 K). Stick plots display the pigment transitions identified via second-derivative analysis. The S_X energy, marked with an asterisk, is not resolved in second-derivative analysis, but assigned from analysis of 2D spectra. (D) Absorptive ultrabroadband 2D spectrum at $T = 200$ fs. Laser spectrum is shown in (B) in gray. The main features further discussed in the text are labeled with black boxes (**I**, **II**).

ergy gap. Strikingly, S_X is absent in the other three Cars in LHCII, showing that this dark state is not universal to all Cars. These results demonstrate that the binding pocket tunes the physical, and in turn, electronic structure of Lut2 to provide a nexus of light harvesting in plants, connecting states that span the visible solar spectrum. These observations highlight that the dynamics, electronic structure, and, therefore, function of Cars are exquisitely sensitive to conformation, which enables control over the balance of light harvesting and photoprotection in plants.

3.3 Ultrabroadband Two-Dimensional Electronic Spectrum of Light-Harvesting Complex II

2DES maps out excitation energy flow through the pigment energy levels by producing correlation plots of the excitation (ω_τ) and emission frequencies (ω_t) that evolve as a function of the waiting time (T), the delay time between excitation and emission [162]. The ultrabroadband 2DES apparatus described in Chapter 2 expands the detection range to cover the broad range of excited states in LHCII over a 7,500 cm^{-1} energy gap with high spectral and sub-10 fs time resolution, as illustrated in Figure 3-1D [226]. The pigment energy levels, determined by second-derivative analysis of the linear absorption spectrum, are shown in Figure 3-1B, C.

3.4 Ultrafast Energy Redistribution of High-Lying Excited States onto Lutein 2

For detailed analyses of the energy transfer pathways, I discuss the ultrabroadband 2D spectrum in sections below (see boxes **I** and **II** in Figure 3-1D). On the upper right corner of the ultrabroadband 2D spectrum (**I**; $\omega_\tau = 19,000 - 21,500$ cm^{-1}, $\omega_t = 18,000 - 21,500$ cm^{-1}, Figure 3-2A), the positive signal spread along the diagonal originates from the ground-state bleach (GSB) and stimulated emission (SE) of Car S_2 and Chl b Soret states, and the negative feature down-shifted in ω_t ($17,000 - 18,800$

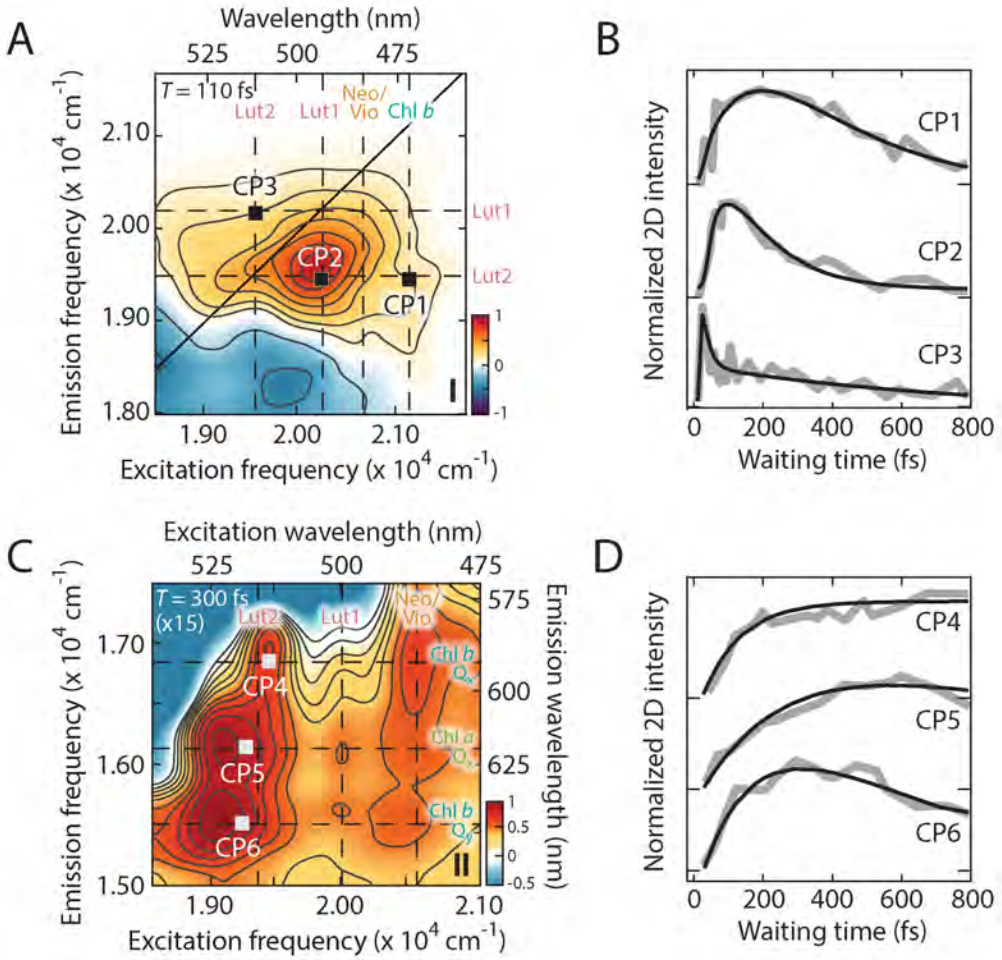

Figure 3-2: **Energy redistribution between the Luts and Car S_2-to-Chl Q energy transfer.** (A) Absorptive 2D spectrum at $T = 110$ fs, zoomed in on section **I** of the ultrabroadband 2D spectrum shown in Figure 3-1. (B) Waiting time traces (gray) and exponential fits (black) of cross peaks CP1−3. $(\omega_\tau, \omega_t) = (21{,}160, 19{,}430)$ (CP1), (20,200, 19,500) (CP2), (19,450, 20,200) (CP3, in cm^{-1}). (C) Absorptive 2D spectrum at $T = 300$ fs, zoomed in on section **II** of the ultrabroadband 2D spectrum (scaled by a factor of 15 due to the weak signal intensity in this range). (D) Waiting time traces (gray) and exponential fits (black) of cross peaks CP4−6. $(\omega_\tau, \omega_t) = (19{,}500, 16{,}870)$ (CP4), (19,250, 16,110) (CP5), (19,250, 15,540) (CP6, in cm^{-1}). In (A) and (C), the energy levels of the relevant pigment transitions as determined by second-derivative analysis are indicated with dashed lines and labeled. The traces in (B) and (D) are plotted with vertical offsets.

cm^{-1}) corresponds to the ESA of Car S_1 to higher excited states (S_N). The S_1 state cannot be directly accessed by photoexcitation from the ground (S_0) state due to the identical symmetry between the two states, and so the $S_1 \rightarrow S_N$ ESA serves as a reporter of the Car S_1 population. Population dynamics in this region are dominated by the well-known sub-200 fs $S_2 \rightarrow S_1$ internal conversion of Cars, visualized by concomitant decay of the S_2 GSB/SE and rise of the S_1 ESA [49]. The observed internal conversion timescale of $135 - 200$ fs agrees with previously reported Car internal conversion rates [69, 227].

A global analysis of this region (see Section 3.7 and Figure 3-7 for a detailed discussion of the global analysis results) shows strong off-diagonal features in the 60 fs component, which correspond to coupling and rapid energy transfer. These features emerge from the cross peaks in the early waiting time ($T < 200$ fs) 2D spectra (labeled CP1−3 in Figure 3-2A), revealing additional rapid deactivation channels from Car S_2 that compete with the internal conversion process. CP1 is assigned to an energy transfer pathway from Chl *b* Soret to Car S_2 states, based on the position where the peak emerges. This cross peak grows in with a time constant of 92 ± 6 fs and decays on a 360 ± 27 fs timescale, the former of which is assigned to the timescale of this energy transfer (Figure 3-2B, top trace). This energy transfer pathway has been predicted theoretically, potentially as a shortcut for energy flow from Chl Soret to Q states [74], and observed experimentally for the first time in this work. Another cross peak, CP2, appears at the excitation frequency of Lut1 and emission frequency of Lut2, which rises within the first 64 ± 15 fs and decays on a 140 ± 25 fs timescale (Figure 3-2B, middle trace). This cross peak is assigned to an energy transfer from the S_2 of Lut1 to that of Lut2. While there are other possible origins that can give rise to a cross peak at this position, such as a dynamic Stokes shift of Lut1 and vibrational coherence of Lut2, I assign this cross peak to inter-Lut energy transfer as mentioned above, because I do not observe changes in the lineshape [228] or a vibrational cross peak pattern on the 2D spectra (see Section 3.12 for detailed discussions and supplementary data on the origin of this cross peak) [229]. Although the possibility of energy transfer between Cars has been completely neglected so far,

a computational study reported the presence of non-negligible Coulombic coupling between multiple Cars within LHCII [230]. The coupling strength between Lut1 and Lut2 was found to be the strongest of all possible Car pairs, because they are in close proximity to each other (center-to-center distance 12.6 Å). The presence of a corresponding above-diagonal cross peak, CP3, also suggests that coupling between the two Lut S_2 states exist, further corroborating the strong interaction between them [231]. Therefore, the observed 64 ± 15 fs and 140 ± 25 fs time constants are assigned to energy transfer from Lut1 S_2 into Lut2 S_2, and energy flow out of Lut2 S_2 to lower-lying state, respectively. These cross peaks are the first observation of energy transfer between Car S_2 states, uncovering a previously unknown mechanism of energy redistribution within the manifold of higher-lying states in LHCII.

3.5 Direct Ultrafast Energy Transfer from Carotenoid S_2 States to the Chlorophyll Q_x/Q_y Manifold

Direct energy transfer from Car S_2 to the Chl Q_x/Q_y states is visualized as cross peaks on the lower right corner of the ultrabroadband 2D spectrum (**II**, $\omega_\tau = 19,000 - 21,000$ cm^{-1}, $\omega_t = 15,000 - 17,500$ cm^{-1}, Figure 3-2C). Three clusters of cross peaks are observed at $\omega_\tau = 19,000 - 19,500$ cm^{-1} (Lut2), 20,000 cm^{-1} (Lut1), and $20,500 - 20,600$ cm^{-1} (Neo/Vio), which correspond to the energy of the three Car S_2 transitions identified in the second-derivative analysis (Figures 3-1C and 3-10). The cross peaks originating from Neo and Vio are unable to be separated out due to the significant overlap of their S_2 transitions. However, based on previous observations that Vio does not participate in light harvesting [232], the data were interpreted with the assumption that the cross peaks at $\omega_\tau = 20,500 - 20,600$ cm^{-1} originate exclusively from Neo. Due to a low signal-to-noise ratio in this region, only the time traces of CP4−6, at the excitation frequency of Lut2, were able to be analyzed in a reliable manner (Figure 3-2D). All three cross peaks exhibit an initial growth in intensity with rise time constants of 90−150 fs. These time constants, assigned to

the rates of Lut2 $S_2 \rightarrow$ Chl Q_x/Q_y energy transfer, are in agreement with the energy transfer rates reported in previous pump-probe studies [75, 76]. Interestingly, the intensities of the cross peaks at the excitation frequency of Lut1 are 1.6−4 times weaker than those of the surrounding cross peaks at the excitation frequencies of Neo/Vio and Lut2. In conjunction with the Lut1 $\rightarrow$ Lut2 energy transfer pathway identified in the high-frequency corner of the 2D spectrum (**I**), I propose that the majority of excitation on Lut1 is depopulated by funneling energy to Lut2, not to Chls, *i.e.*, via a stepwise energy migration Lut1 $S_2 \rightarrow$ Lut2 $S_2 \rightarrow$ Chl Q. In contrast to Lut1, Lut2, the lower-energy Lut and also the lowest-energy one of all four Cars bound to LHCII, is the primary donor of energy to Chls, as seen by the strongest cross peak intensities at the excitation frequency of Lut2.

3.6 Identification of Lutein 2 Dark State S_X

Strong modulations of the 2D intensity were observed in the high-frequency range of the ultrabroadband 2D spectrum due to impulsive excitation of Car vibrational modes by the sub-10 fs pulse employed [218, 233, 234]. The period of the oscillation is ∼29 fs (Figure 3-3), consistent with the frequency of symmetric C−C stretching motions of Cars (1,160 cm^{-1}) [50]. The ω_τ dependence of the oscillations shows that the wavepacket motions are produced by photoexcitation into the S_2 state of Lut2, as the maximum amplitude of oscillation is found near the energy of Lut2 S_2 (Figure 3-4).

The nature of the observed wavepacket motions was further investigated by monitoring the amplitude (A, see Figure 3-5B) and phase of the beating signal as a function of ω_t (Figure 3-5C). This analysis, called wavepacket analysis hereafter, is a widely used analysis method in transient absorption spectroscopy to reveal the energy landscape of molecular and biological systems [235–238]. Briefly, a potential energy well is identified at an energy at which the oscillations undergo a phase flip by π and converge to an amplitude minimum. Through this analysis, I find evidence for the existence of a Lut2 dark state, S_X, which I discuss below.

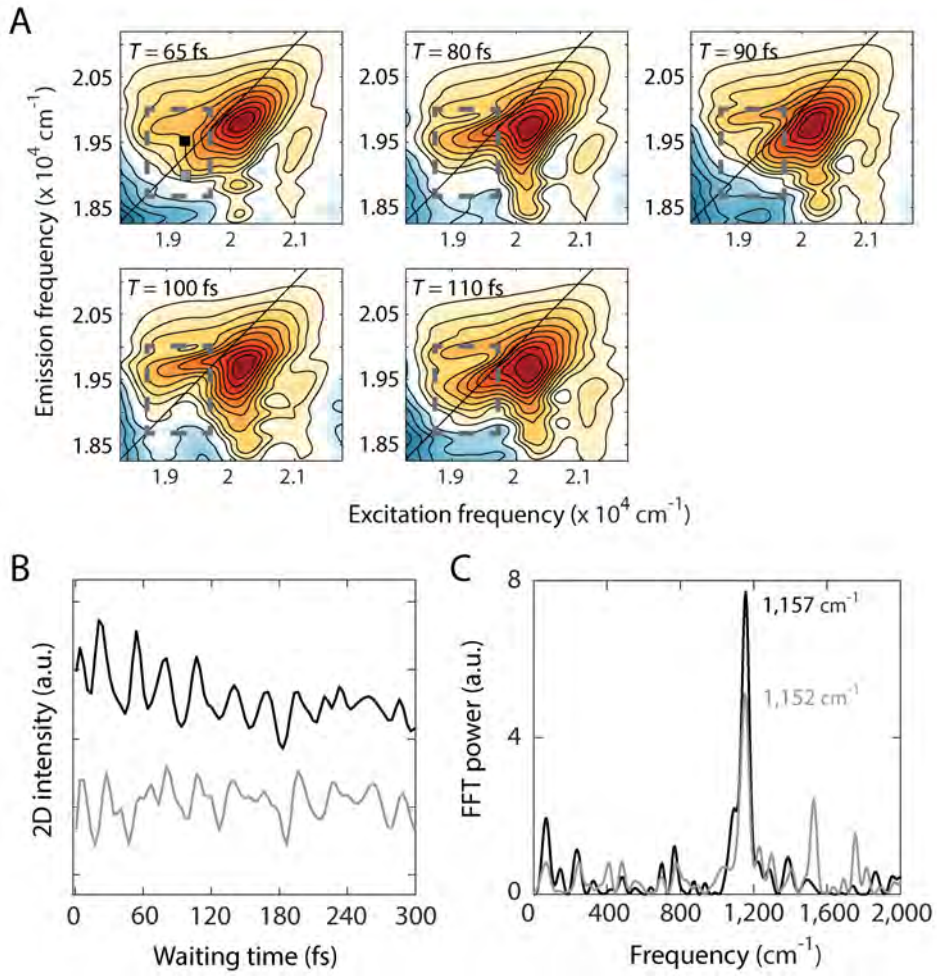

Figure 3-3: **Early-time 2D spectra of Car S_2 peaks showing vibrational wavepacket motions.** (A) Zoom-in of the Car S_2 GSB/SE region at early waiting times (normalized to an arbitrary scale of -1 to 1). The frequency range where the oscillations are most pronounced is indicated with dashed boxes. (B) Representative waiting time traces showing oscillatory features. The peak positions where the time traces were generated are labeled with black ($\omega_\tau = 19,250$ cm^{-1}, $\omega_t = 19,600$ cm^{-1}) and gray ($\omega_\tau = 19,250$ cm^{-1}, $\omega_t = 18,900$ cm^{-1}) filled squares in (A). The traces are plotted with a vertical offset for clarity. (C) Fast Fourier transform (FFT) power spectrum of the oscillatory traces presented in (B).

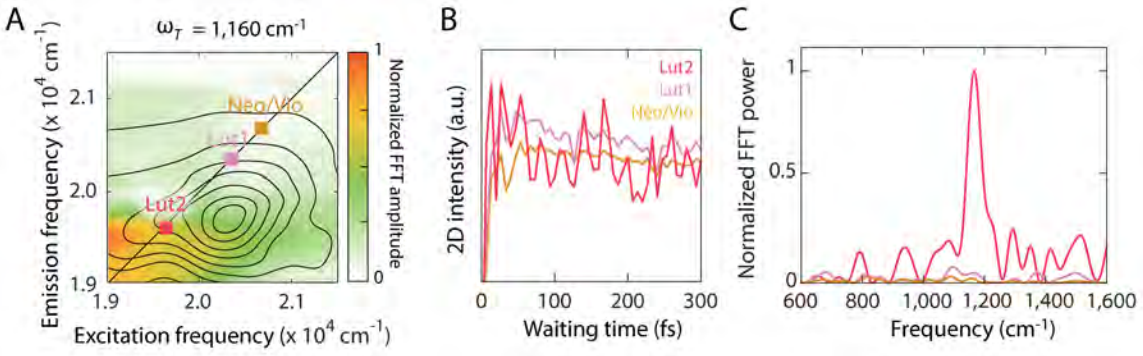

Figure 3-4: **Excitation frequency dependence of Car oscillations** (A) Fourier amplitude map at ω_T = 1,160 cm^{-1}, zoomed in on the Car S_2 frequency range. The three Car diagonal peaks are labeled with filled squares. Contour lines show the absorptive 2D spectrum in this range at T = 110 fs. (B) Raw waiting time traces of the three Car diagonal peaks as labeled in (A). (C) FFT power spectra of the oscillatory part of the time traces shown in (B).

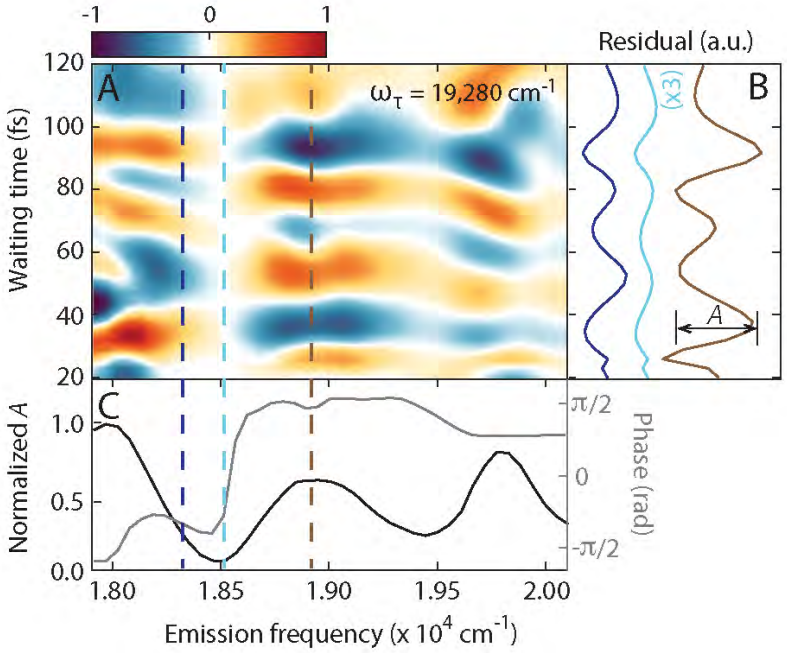

Figure 3-5: **Identification of the S_X state of Lut2 by wavepacket analysis.** (A) 2D map of Car oscillations plotted as a function of T and ω_t, obtained by subtracting the exponential population dynamics from the raw time traces. ω_τ is fixed at 19,280 cm^{-1}. (B) Slices of the 2D map in (A) at selected ω_t frequencies, labeled with colored dashed lines: 18,330 (dark blue), 18,500 (light blue), and 18,920 cm^{-1} (brown). (C) Plot of the normalized amplitude (A, black) and phase (gray) of the oscillations as a function of ω_t.

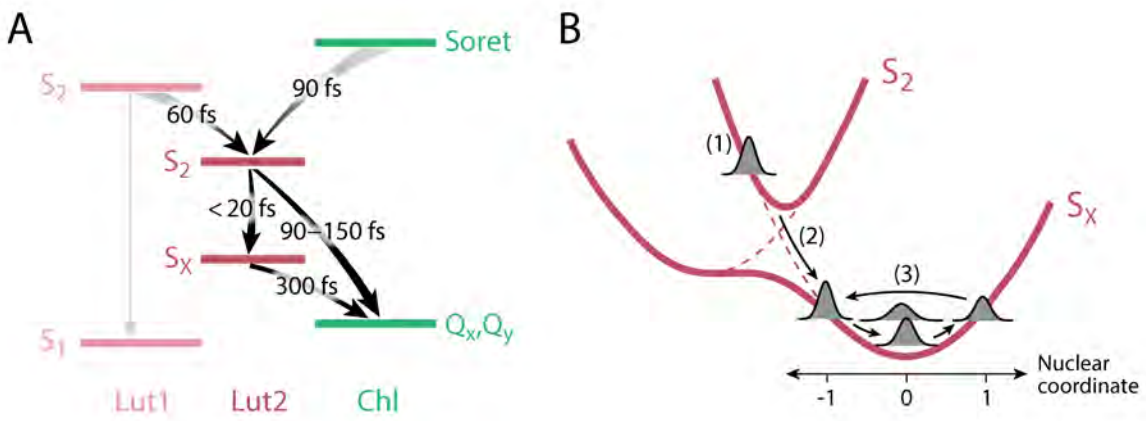

Figure 3-6: **Summary of Lut2-mediated light harvesting in LHCII.** (A) Summary of the newly observed energy transfer pathways mediated by Lut2 and their timescales (energy levels not to scale). (B) Schematic illustration of the potential energy surfaces of S_2 and S_X states of Lut2 and the non-adiabatic dynamics between them: (1) Vertical excitation into the S_2 Franck-Condon state, (2) non-adiabatic transfer onto the S_X surface, (3) propagation of the wavepacket on the S_X surface.

At ω_t = 18,500 cm^{-1}, a clear near-π phase flip in the oscillation is observed as well as the minimum amplitude of oscillation (Figure 3-5C). These characteristics point to the presence of a potential energy well at this energy, as mentioned above and schematized in Figure 3-6B. This analysis is a clear and direct observation of the controversial Car S_X state. I infer that S_X is populated via a non-adiabatic transition from the S_2 state of Lut2, because the coherence is initially prepared on the S_2 state of Lut2 but transferred in < 20 fs to the S_X energy surface. Notably, this state shows strong and likely exclusive coupling to S_2 state of Lut2, as seen by the maximal amplitude of oscillation at the excitation frequency of Lut2. In contrast, no such dark states were observed for the other three Cars, reflected by the significantly reduced A at $\omega_\tau > 20{,}000$ cm^{-1}, where the other three Cars are predominantly photoexcited. Based on these observations, the S_X stated identified is assigned to be a dark state specific to the lowest-lying Car Lut2.

While broad negative ESA of Chl Q_x and vibronic Q_y states dominates the 2D spectrum above the diagonal around the position of S_X ($\omega_\tau = 16,500 - 19,000$ cm^{-1}, $\omega_t = 17,000 - 21,000$ cm^{-1}), a rapid buildup of a peak near $\omega_\tau = \omega_t$ = 18,500 cm^{-1} is observed on a 60 fs timescale, consistent with the position of an S_X diagonal peak

and potentially growing in due to an increase in oscillator strength upon vibrational relaxation (labeled S_X in Figure 3-18). Due to the broad linewidths of the peaks at RT and spectral congestion from overlapping positive and negative contributions, I also performed global analysis for this region [239]. The 60 fs component (2D-DAS2 in Figure 3-7) of the global analysis revealed a positive diagonal feature with distinct dynamics relative to those of the surrounding Chl and Car ESA (see Section for detailed discussions of the global analysis results). The negative sign of this peak in the 2D spectra, while being on the diagonal, is likely due to contamination from the very intense neighboring ESA of Chls. A similar diagonal feature, although positive in sign, was observed in the 2D spectra of a light-harvesting complex of purple bacteria, LH2, and assigned to a dark state X of the Cars therein [58]. The diagonal peak relaxes an order of magnitude faster ($<$ 500 fs) than the neighboring ESA (ESA1, 2 in Figure 3-18), also consistent with an assignment to S_X [52]. An initial growth of population was observed on a 300 fs timescale at the excitation frequency of S_X and emission frequency of Chl Q states (Figure 3-19). This demonstrates that the S_X state is capable of transferring energy directly to Chls on this timescale. The proposed model for the branching of Lut2 excited-state population, partially into S_X, is illustrated in Figure 3-6A and described in detail in Section 3.8.

3.7 Global Analysis

To obtain a more comprehensive understanding of the concerted dynamics of energy flow in LHCII, I have also performed global analysis of the 2D data [239]. The data were analyzed with a parallel kinetic scheme, which reports a series of 2D decay-associated spectra (2D-DAS), because it does not require any preliminary information or additional assumptions to be applied in the kinetic model, as opposed to sequential schemes used for evolution-associated spectra or species-associated spectra [240]. Four time components were needed to obtain a reasonable fit, independent of the initial parameters. Using more than four components yielded unphysical results. To ensure the robustness of the fit, the fitting routine was executed multiple times by changing

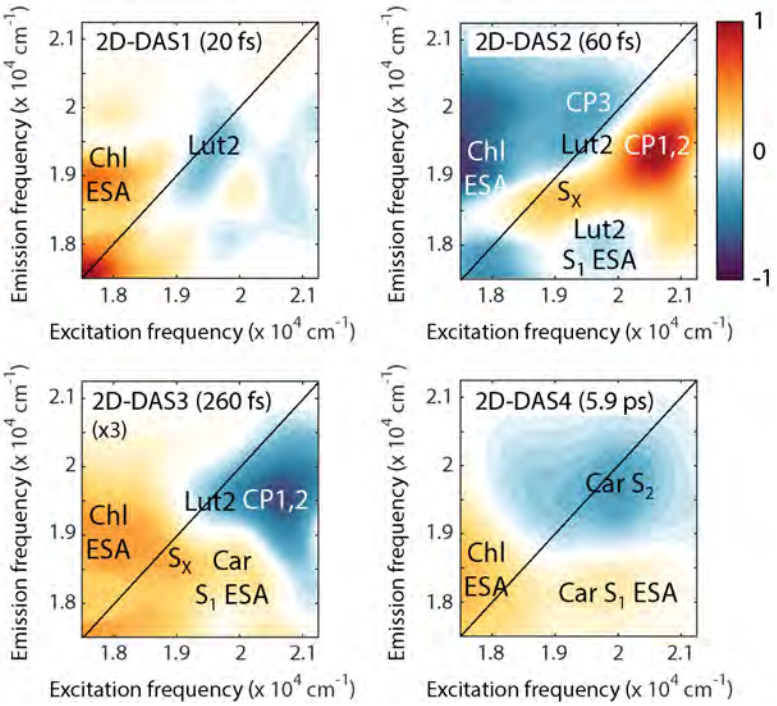

Figure 3-7: **Global analysis.** 2D-DAS extracted from global analysis of the 2DES data. The four time constants associated with each DAS are labeled in each panel. All DAS are normalized to the amplitude scale used for 2D-DAS2. 2D-DAS3 is multiplied by a factor of 3. Negative amplitude denotes exponential decay, and positive amplitude denotes exponential growth.

the initial parameters. The four 2D-DAS obtained from the best fit are shown in Figure 3-7.

2D-DAS1 shows a very rapid decay of Car S_2 excited-state population on a 20 fs timescale (labeled Lut2 in Figure 3-7). Since this timescale is very close to the pulse duration, this DAS exhibits some structure that could be residual artifacts from pulse overlap. The decay amplitude is localized on the lower-frequency side of the diagonal ($19,000 - 20,000$ cm^{-1}), consistent with the fastest S_2 decay of Lut2 observed when comparing individual traces of the 2D spectra. There is a small positive-amplitude feature directly below the Lut2 diagonal peak, consistent with the beginning of population in the S_X state. However, this region is likely contaminated from the strong negative Lut2 peak, precluding a definitive assignment.

In 2D-DAS2, a growth of CP1 and CP2 is observed below the diagonal as energy transfers into Lut2 from higher-lying states, as discussed earlier. Above the diagonal,

a negative-amplitude feature is seen around the position of CP3, consistent with the decay of this cross peak on a 30 ± 15 fs timescale (Table 3.1). This DAS also shows the grow-in of a below-diagonal cross peak centered at the emission energy of S_X ($18,500$ cm^{-1}). The positive sign clearly demonstrates that this feature is of a different origin from the neighboring negative Chl ESA or Lut2 S_1 ESA. The 60 fs timescale is consistent with the dynamics shown in Figure 3-18, and related to the population of the S_X state based on the spectral features of DAS. Nevertheless, global analysis cannot definitively determine the precise timescale of population because of the finite number of fit components employed to model the temporal evolution of an extremely congested energy manifold with the vast majority of the dynamics of interest taking place on similar timescales, *i.e.*, not well-separated in time.

2D-DAS3 reveals the decay of CP1 and CP2 as well as the diagonal Car S_2 feature due to energy flow out of Lut2 to the Chls. While the 260 fs time constant is slower than the Car-to-Chl energy transfer timescales obtained by directly fitting the waiting time traces of CP4−6 ($90 - 150$ fs, Figure 3-2C, D and Table 3.1), shortening this time constant to as short as 150 fs did not make any qualitative difference to the DAS, and adding a fifth component of $100 - 150$ fs yielded unphysical results. This DAS also shows non-negligible amplitudes on the frequency coordinate for S_X, which is roughly consistent with the S_X relaxation time of 450 ± 50 fs and/or the 300 ± 30 fs time constant for energy transfer to the Chls (Figure 3-19 and Table 3.1). Finally, 2DDAS-4 reports the slower-timescale decay of both Car and Chl populations on a ∼6 ps timescale.

3.8 Kinetic Model for the Branching of Lutein 2 S_2 Population

To estimate the branching ratio of the excited-state population from S_2 (Lut2) onto S_1, S_X and Chl Q states by the proposed kinetic scheme in Figure 3-6, a simple kinetic model was constructed by considering the pathways of energy flow out of S_2 (Lut2)

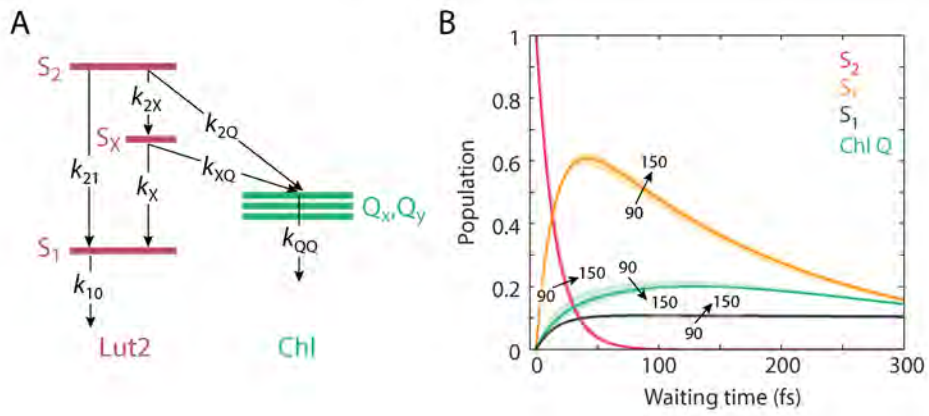

Figure 3-8: **Kinetic model describing the branching of Lut2 excited-state population.** (A) Kinetic model with the relevant rate constants labeled. The experimentally determined rate constants are k_{21} = (150 fs)$^{-1}$, k_{2X} = (20 fs)$^{-1}$, and k_{XQ} = (300 fs)$^{-1}$. k_{2Q} was varied from (90 fs)$^{-1}$ to (150 fs)$^{-1}$ according to the initial rise times of CP4−6, and k_{QQ} was set to the internal conversion rate of Chl Q states, (150 fs)$^{-1}$ [43]. The relaxation rate of S_X, k_X, was set to (450 fs)$^{-1}$ as reported in the literature [52]. The rate of relaxation out of Lut2 S_1 to the ground state, k_{10}, was neglected in the model due to its slow timescale (tens of ps) [49]. (B) Population of Lut2 S_2, S_X, S_1, and Chl Q states estimated from the kinetic model. The traces are normalized such that the initial population of Lut2 S_2 is 1. Solid lines are the populations obtained with a fixed k_{2Q} value of (120 fs)$^{-1}$, and the surrounding shaded regions illustrate how the population changes when k_{2Q} is varied from (90 fs)$^{-1}$ to (150 fs)$^{-1}$ as described in (A).

observed in the 2D spectra.

The time-dependent relative population on each state was then estimated by solving the following set of rate equations (see Figure 4-8A for the pathway each rate constant denotes):

$$\begin{aligned}
\frac{dS_2}{dT} &= -(k_{21} + k_{2X} + k_{2Q})S_2 \\
\frac{dS_X}{dT} &= k_{2X}S_2 - (k_{XQ} + k_X)S_X \\
\frac{dQ}{dT} &= k_{2Q}S_2 + k_{XQ}S_X - k_{QQ}Q \\
\frac{dS_1}{dT} &= k_{21}S_2 - k_{10}S_1 \simeq k_{21}S_2
\end{aligned}$$

Most rate constants were obtained by fitting the waiting time trace for the corresponding pathway from 2DES measurements. Literature values were used for those

that were not determined from the experiment. Figure 4-8B is the plot of the solution of the rate equations above, which shows the relative population on each state as a function of waiting time. The population maxima are related to the intensities of the cross peaks observed in the 2D spectra. The maximum population of the Chl Q states is ∼20% of the initial population of Lut2 S_2, and is nearly insensitive to the exact rate constant of Car-to-Chl energy transfer (19.8−21.5%, variation is only 1.7% as k_{2Q} is varied from $(90\text{ fs})^{-1}$ to $(150\text{ fs})^{-1}$). Experimentally observed cross peak intensities for CP4−6 are 9−10% of the initial intensity of the Lut2 S_2 diagonal peak, ∼10% lower than the estimate from the kinetic model. This discrepancy likely originates from the intensity profile of the ultrabroadband spectrum; the laser spectrum employed in this work has a significantly lower intensity for the Chl Q absorption range than for the Car S_2 range, which could lead to weaker cross peaks than theoretically predicted.

3.9 Discussion

Energy transfer rates from Car S_2 to Chl Q states are a crucial parameter to optimize energy flow in plants; they need to be sufficiently fast to be able to compete with the sub-200 fs timescale of Car internal conversion, or all energy will be rapidly trapped to the S_1 state of the Cars. Remarkably, the observed timescales of Car-to-Chl energy transfer, spanning an extremely broad energy range of $2,800 - 5,100$ cm^{-1}, are as fast as 90 fs, significantly faster than predicted theoretically [75]. In the bacterial light-harvesting complex LH2, a Car dark state X was identified and proposed to facilitate energy transfer to bacteriochlorophylls [58]. My results both unambiguously identify S_X and reveal that it serves the same role in plants, reducing the donor-acceptor energy gap by over 2,000 cm^{-1}. Notably, unlike in LH2, the S_X state is resolved exclusively for Lut2, which is only one of the four Cars bound to LHCII. This observation suggests that the presence of this dark state is highly sensitive to the conformation of the Car molecule imposed by the structure of each protein binding pocket [222]. This may be the origin of conflicting models in the literature about the existence of additional Car dark states [52]. Partially mediated

by S_X, Lut2 accepts excitation energy from the higher-lying Chl Soret and Lut1 S_2 states, and donates energy to the lower-lying Chl Q states. These results uncover the central role of Lut2 in mediating energy transfer in LHCII with an electronic structure optimized for light harvesting (Figure 3-6). In contrast, Lut1 exhibits little direct energy transfer to Chls, as seen in the weak Car-Chl cross peak intensities at the excitation frequency of Lut1 (Figure 3-2C). As suggested in the literature, Lut1 may have a primarily photoprotective role including quenching Chl triplet states [83]. Structural studies showed that the conjugated polyene plane of Lut1 possesses a less twisted conformation compared to that of Lut2, which may underlie the distinct energetics and photophysics observed for the two chemically identical Lut molecules [66].

3.10 Conclusion

The electronic structure of Cars is governed by their conformation, which, in photosynthesis, is controlled by the surrounding protein scaffold. In this work, one of the Luts in green plants, Lut2, was found to play a critical role in enabling light harvesting across the visible solar spectrum. While further experimental and theoretical studies are required to determine the molecular parameters behind Car function, the results shown here demonstrate that ultrabroadband 2DES provides the spectral bandwidth and temporal resolution to reveal how Cars specialize in photosynthetic light harvesting.

3.11 Materials and Methods

3.11.1 Sample Preparation

Details on extraction and purification of the LHCII complexes from spinach leaves as well as pigment composition analysis can be found in Appendix A, Section A.1. Immediately before each 2DES measurement, the sample stored at $-80°$C was thawed and diluted in a 0.01 M HEPES, 0.02 M NaCl buffer solution (pH 7.5) containing

0.03% *n*-dodecyl α-D-maltopyranoside (α-DM) detergent (Anatrace) to adjust the optical density (OD). The final OD of the sample used for 2DES was 0.45 (per 0.2 mm) at the Chl *a* Q_y peak (675 nm).

3.11.2 Linear Absorption

Linear absorption spectra were measured with Cary 5000 spectrophotometer (Agilent) in a 1 cm pathlength quartz cuvette. For measurements at 77 K, the LHCII detergent solution was mixed with 70% (v/v) glycerol and held in a cold finger cryostat (Janis ST-100) filled with liquid nitrogen.

3.11.3 Raman Spectroscopy

The resonant Raman spectrum was measured with an Invia Reflex Micro Raman spectrometer (Renishaw) at RT, in a 1 mm pathlength quartz cuvette. The sample was excited at 473 nm.

3.11.4 Ultrabroadband Two-Dimensional Electronic Spectroscopy

A detailed description of the ultrabraodband 2DES setup is provided in Chapter 2 and in [226]. The supercontinuum generated by argon filamentation was further filtered by a glass bandpass filter (FGB39, Thorlabs) for optimal excitation of the Car S_2 absorption range. The final laser spectrum was centered at 550 nm ($18,182$ cm^{-1}) with a FWHM of 117 nm ($3,934$ cm^{-1}, Figure 3-1B). The pulse was compressed to 6.2 fs as characterized with transient grating frequency resolved optical gating (TG-FROG, Figure 3-9). A pulse energy of 10 nJ was employed with a beam waist of 150 μm at the sample position, which corresponds to an excitation density of 3.9×10^{13} photons per pulse per cm^2. This excitation energy was previously reported to be in the linear, *i.e.*, annihilation-free, regime [94]. τ was sampled in 0.4 fs steps in the range of $-200 - 200$ fs, resulting in a 43.8 cm^{-1} resolution of the ω_τ axis. T was incremented in steps of 33 fs for $T = -99 - 0$ fs, 10 fs for $T = 0 - 100$ fs, 33 fs for $T = 100 - 467$ fs, 67 fs for $T = 467$ fs $- 1$ ps, and 1 ps for $T = 1 - 8$ ps. The

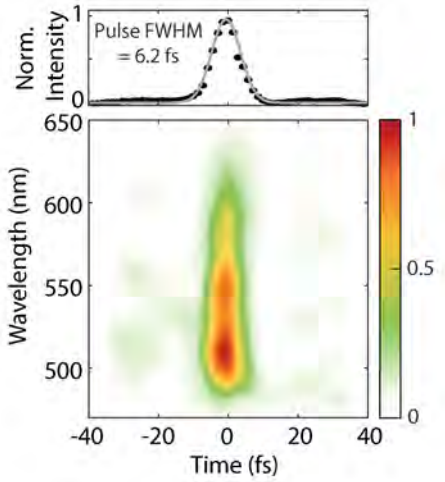

Figure 3-9: **TG-FROG of the ultrabroadband laser pulse employed in 2DES.** TG-FROG trace with the retrieved temporal profile (filled circles) fitted with a Gaussian function (solid line).

frequency resolution of the ω_t axis was 4.2 cm^{-1}. At each T, for each τ, 1,280 lines of each chopper sequence of the dual chopping data acquisition scheme were collected and averaged. A separate dataset was measured using linear T steps of 6.6 fs for $T = 0 - 660$ fs in order to better resolve the Car beating signal. The sample was circulated in a 0.2 mm pathlength quartz flow cell with a peristaltic pump to prevent photodegradation and repetitive excitation of the same spot. The sample reservoir was kept at 4°C throughout the measurement with a home-built water jacket cooling system. The data were collected three times with the coarse T steps and one time with the fine T steps on different days to ensure reproducibility. Following each set of measurement, the integrity of the sample was confirmed by comparing the linear absorption spectra before and after the experiment.

3.11.5 Analysis of Two-Dimensional Spectra

Each waiting time trace reported here was generated by integrating the 2D signal intensity over finite frequency intervals in both frequencies (100 cm^{-1} in $\omega_\tau\times$ 50 cm^{-1} in ω_t) around the center frequencies reported in parentheses (ω_τ, ω_t). Time constants were extracted by fitting each waiting time trace to an exponential function

convolved with a Gaussian pulse with the time resolution (6.2 fs) of the experiment. Global analysis was performed using a MATLAB fitting routine developed by Volpato *et al.* [239].

3.12 Supplementary Information

3.12.1 Identification of Pigment Excited-State Energies by Second-Derivative Analysis

Second-derivative analysis of the linear absorption spectrum of LHCII was used to identify the excited-state energy levels of the pigments in LHCII (Figure 3-10). Due to the congestion of the absorption spectrum at room temperature (RT), the 77 K spectrum was also analyzed, which gave enhanced separation of weak or overlapping transitions with narrower spectral linewidths [241].

On the high-energy side ($19,500 - 21,500$ cm^{-1}), where the absorption predominantly originates from Car S_2 transitions, three new states are identified at $20,580 - 20,600$, $20,280 - 20,300$, and 19,560 cm^{-1}, in addition to the well-resolved Chl *b* Soret band at 21,160 cm^{-1}. Based on earlier work [232], these states are assigned to the $0-0$ vibronic level of the S_2 transition of Neo/Vio, higher-energy lutein (Lut1) and lower-energy (red-shifted) lutein (Lut2) pigments, respectively. Due to the very small difference in the energy level of the S_2 transitions of Neo and Vio (< 100 cm^{-1}), these two states are resolved neither in second-derivative analysis nor in the 2D spectra.

The lower-energy side of the spectrum ($14,000 - 19,000$ cm^{-1}) comprises the Q_x and Q_y states of Chls as well as their vibronic states. In the Q_y region ($14,000 - 15,500$ cm^{-1}), the two well-established Q_y bands of Chl *b* and Chl *a* are observed at $15,400$ and $14,750$ cm^{-1}. At 77 K, two additional peaks appear between these two states, at $15,130$ and $14,950$ cm^{-1}, previously assigned to high-energy subpopulations of Chl *a* [242]. The $15,500 - 19,000$ cm^{-1} frequency range has been collectively referred to as Chl Q_x and vibronic Q_y states [227]. Second-derivative analysis reveals

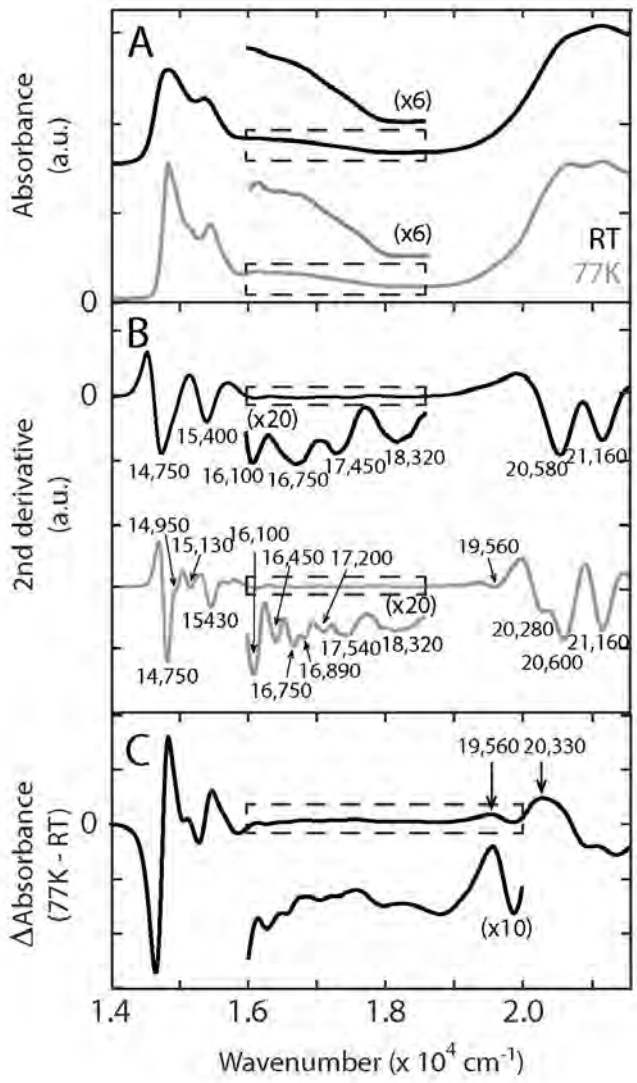

Figure 3-10: **Temperature-dependent linear absorption and second-derivative linear absorption spectra.** (A) Linear absorption and (B) second-derivative absorption spectra of LHCII measured at room temperature (RT, black) and 77 K (gray, vertically offset for clarity). Enlarged spectra of the intermediate region ($16,000 - 18,500$ cm^{-1}, dashed boxes) are also shown. In (B), data at $19,000 - 21,500$ cm^{-1} are multiplied by a factor of 3 for both temperatures. (C) Difference absorbance spectrum obtained by subtracting the normalized RT spectrum from the normalized 77 K spectrum in (A). Data at $16,000 - 20,000$ cm^{-1} are multiplied by a factor of 10 and shown below the original data.

four distinct energy levels in this range. A constant energy spacing of $1,350$ cm^{-1} was found between the Chl Q_y peaks and these intermediate peaks, leading to an assignment of a vibronic progression for a Chl vibrational mode. Similar energy spacings ($1,100 - 1,300$ cm^{-1}) have been observed in isolated Chl *a* [35, 243, 244] and Chl *b* chromophores [245]. While it is generally accepted that the Q_x state is strongly mixed with higher vibronic states of Q_y, it is still unclear whether the mixing is with the $Q_y(0,1)$ or the $Q_y(0,2)$ state [34, 244]. This work follows the former regime, *i.e*, the two lower-energy transitions of the vibronic progression are assigned to the Q_x state of Chl *a* ($16,100$ cm^{-1}) and Chl *b* ($16,750$ cm^{-1}), respectively.

3.12.2 Raman and Fourier Map Analyses of Cross Peaks

To eliminate the possibility of a vibrational origin for cross peaks CP2 and CP3 (Figure 3-2A), a Fourier map analysis of the $700 - 1,000$ cm^{-1} frequency range was performed. A resonant Raman spectrum was first measured for identification of the major vibrational frequencies of LHCII. The Raman spectrum in Figure 3-11 shows that the $700 - 1,000$ cm^{-1} frequency range is almost Raman-silent with the exception of two modes at 745 cm^{-1} and 1,004 cm^{-1}. Of these two modes, the former is a very well-known Chl vibrational mode [34, 43, 246, 247]. Thus, the only vibrational mode that could give rise to a Car vibrational cross peak is the 1,004 cm^{-1} mode, which has been attributed to in-plane rocking motions of the methyl groups in Cars [224].

It is well known that ground-state and excited-state vibrational coherences of a system give rise to a set of vibrational cross peaks in 2D spectra, which are displaced by the vibrational energy spacing from the main diagonal peak (also known as the "chair pattern"), as described in detail in [229]. If CP2 and CP3 were to arise from a chair pattern due to the 1,004 cm^{-1} vibrational mode, both of these peaks should show beating in the 2D signal intensity at this frequency [229, 238]. However, as seen in Figure 3-12A, the decay-subtracted residual of neither CP2 nor CP3 shows no oscillations in contrast to peaks with strong vibrational contributions, such as the Lut2 diagonal peak. Consistently, the FFT power spectra of these peaks are orders of magnitude weaker than those for the Lut2 diagonal peak (Figure 3-12B).

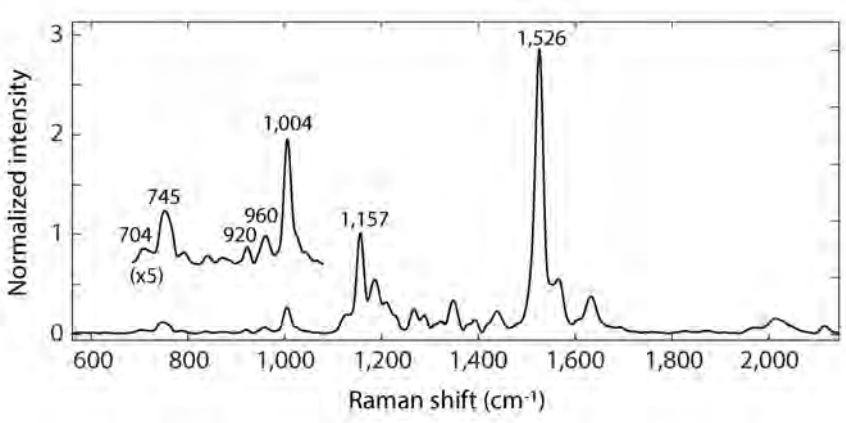

Figure 3-11: **Resonant Raman spectrum of LHCII.** The spectrum is normalized such that the intensity of the $1,157\ \text{cm}^{-1}$ peak is 1. A five-fold multipled plot of the $680 - 1,100\ \text{cm}^{-1}$ range is shown above the original spectrum for clarity.

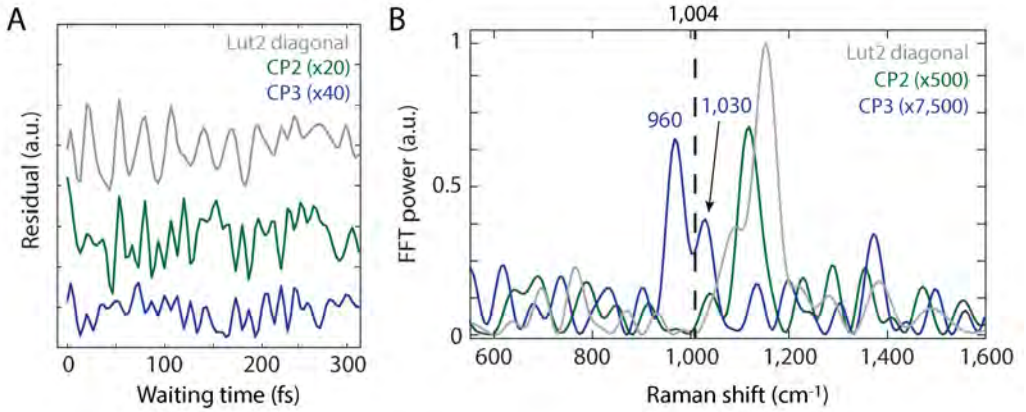

Figure 3-12: **Absence of Car vibrational coherence in CP2 and CP3.** (A) Oscillatory residuals of Lut2 diagonal peak and the cross peaks CP2, 3 obtained by subtracting exponential population dynamics from the raw waiting time traces. (B) FFT power spectra of the residuals shown in (A).

Furthermore, no peak is detected at 1,004 cm^{-1} on the FFT power spectrum.

The Fourier amplitude map for $\omega_T = 1,005\ \text{cm}^{-1}$ is shown for a more straightforward comparison(Figure 3-13A). The map clearly shows that the FFT amplitude is localized along the diagonal, and that the small FFT amplitude on both CP2 and CP3 originates from the adjacent diagonal peak. In the case of vibrational cross peaks, the Fourier map should exhibit significant FFT amplitude centered on these cross peak positions. Furthermore, I see a negligible (<2%) FFT amplitude at the predicted peak positions of CP2 and CP3 (orange open squares in Figure 3-13A) at

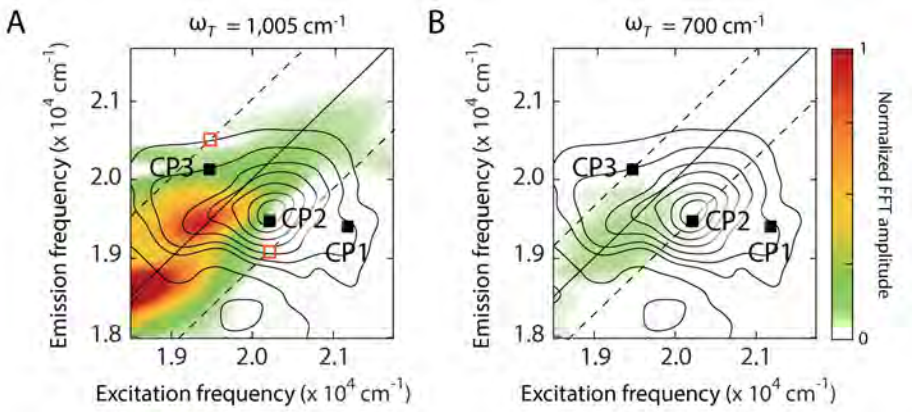

Figure 3-13: **Fourier amplitude maps of the Car S_2 region of the 2D spectra.** Fourier amplitude maps plotted for (A) $\omega_T = 1,005$ cm^{-1} and (B) $\omega_T = 700$ cm^{-1}. Orange open squares in (A) indicate the vibrational cross peak positions as predicted by the displaced harmonic oscillator model ("chair pattern"). Both maps are normalized to the maximum intensity of the $\omega_T = 1,005$ cm^{-1} map. Contour lines show the absorptive 2D spectrum at $T = 110$ fs. Dashed lines are shifted by the corresponding ω_T frequency parallel to the diagonal.

the energy spacing of $1,005$ cm^{-1}, which in theory should show the maximal FFT amplitudes as part of the chair pattern. The Fourier amplitude map for $\omega_T = 700$ cm^{-1} is also examined (Figure 3-13B), which better matches the energy spacing of CP2 and CP3 from the diagonal observed in the 2D spectra. At $\omega_T = 700$ cm^{-1}, the maximum FFT amplitude is only 7% of that for $1,005$ cm^{-1}, *i.e.*, exhibiting negligible oscillatory feature across the entire frequency range monitored. Based on these results, the possibility of CP2 and CP3 being vibrational cross peaks is ruled out.

3.12.3 Fourier Map Analysis of Lutein 2 Wavepacket Motions

Along with the analysis of the wavepacket motions for individual frequency coordinates, a Fourier map analysis was performed to collectively analyze the amplitude and phase of oscillations across the Car S_2 frequency range of the 2D spectra [229, 248]. Figure 3-14 show the Fourier amplitude and phase maps at the beating frequency of 1,160 cm^{-1}. In experimental data, the presence of multiple chromophores and rapid dephasing that occurs at RT can introduce deviations from the expected chair pattern based on a simple two-level displaced harmonic oscillator model, complicating the interpretation [43, 246, 249]. However, consistent with the results in Section 3.6,

the Fourier maps show an amplitude minimum and phase flip uniquely at $\omega_t = 18,500$ cm^{-1}, the energy of S_X.

The vertical slice of the amplitude map (Figure 3-14A) taken along an excitation frequency of 19,560 cm^{-1} (Figure 3-14C) unambiguously shows the decrease of the Fourier amplitude towards the emission frequency of 18,500 cm^{-1}. The excitation frequency of 19,560 cm^{-1} is purely of Lut2 origin, none of the other three Cars shows absorbance at this energy, corroborating that the decrease of the FFT amplitude towards $\omega_t = 18,500$ cm^{-1} is related exclusively to Lut2. The amplitude map also shows a chair-pattern-like structure centered on the diagonal at $\omega_\tau = \omega_t = 18{,}000$ cm^{-1} (labeled with gray squares in Figure 3-14A), where there is no Car absorption but the Chl ESA dominates. This is likely a result of interference from a Chl vibrational mode known to be at $\sim 1,120$ cm^{-1} [246, 249], because the peaks have broad line profiles (> 60 cm^{-1} FWHM) and thus a 1,120 cm^{-1} mode and a 1160 cm^{-1} mode cannot be distinguished. The excitation frequency of 19,560 cm^{-1} is still well separated from the expected $\omega_\tau = \omega_t = 19,120$ cm^{-1} associated with a chair pattern from a Chl vibrational mode.

Figure 3-14B shows the Fourier phase map generated at the 1,160 cm^{-1} beating frequency. This phase map is the output of an automated MATLAB routine that calculates the arctangent of the imaginary and real parts of the complex FFT for each pixel on the 2D spectra. While some parts of the phase map show phase evolution parallel to the diagonal as predicted by the simple displaced harmonic oscillator model (e.g. $19,500 - 21,000$ cm^{-1}) [250, 251], this behavior does not apply to the entire phase map, likely due to energy transfer, congested nature of LHCII as compared to simple models, and interference between multiple oscillations resulting from multiple chromophore vibrational modes. In particular, unlike the amplitude, the phase is extremely sensitive to the noise in the data, as highlighted in Figure 3-14D. This is due to the high frequency of the oscillations of interest (1,160 cm^{-1}, which is 28.7 fs in time) as well as the relatively low sampling frequency (6.7 fs, limited by the specification of the translational stage) relative to the Nyquist frequency of 14.4 fs. Therefore, phase at discontinuities on the phase map shown in Figure 3-14B was

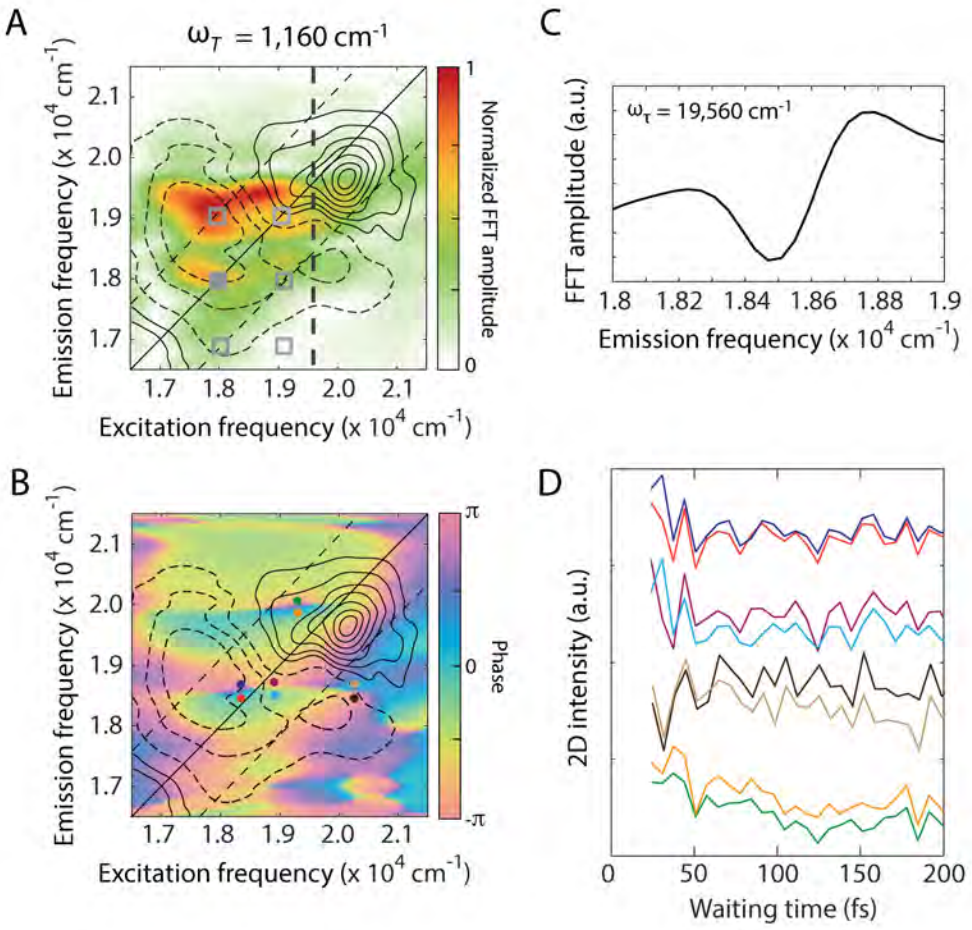

Figure 3-14: **Fourier amplitude and phase maps of the Car wavepacket motions.** (A) Amplitude and (B) phase map at $\omega_T = 1,160$ cm^{-1}. The dashed diagonal lines are drawn shifted from the diagonal by 1,160 cm^{-1}. Solid and dashed contour lines show the positive and negative parts of the absorptive 2D spectrum at $T = 110$ fs. (C) Slice of the Fourier amplitude map taken $\omega_\tau = 19,560$ cm^{-1} (indicated with a vertical dashed line in (A)). (D) Raw waiting time traces probed at the frequency coordinates labeled with colored dots in (B) (plotted with vertical offsets for clarity).

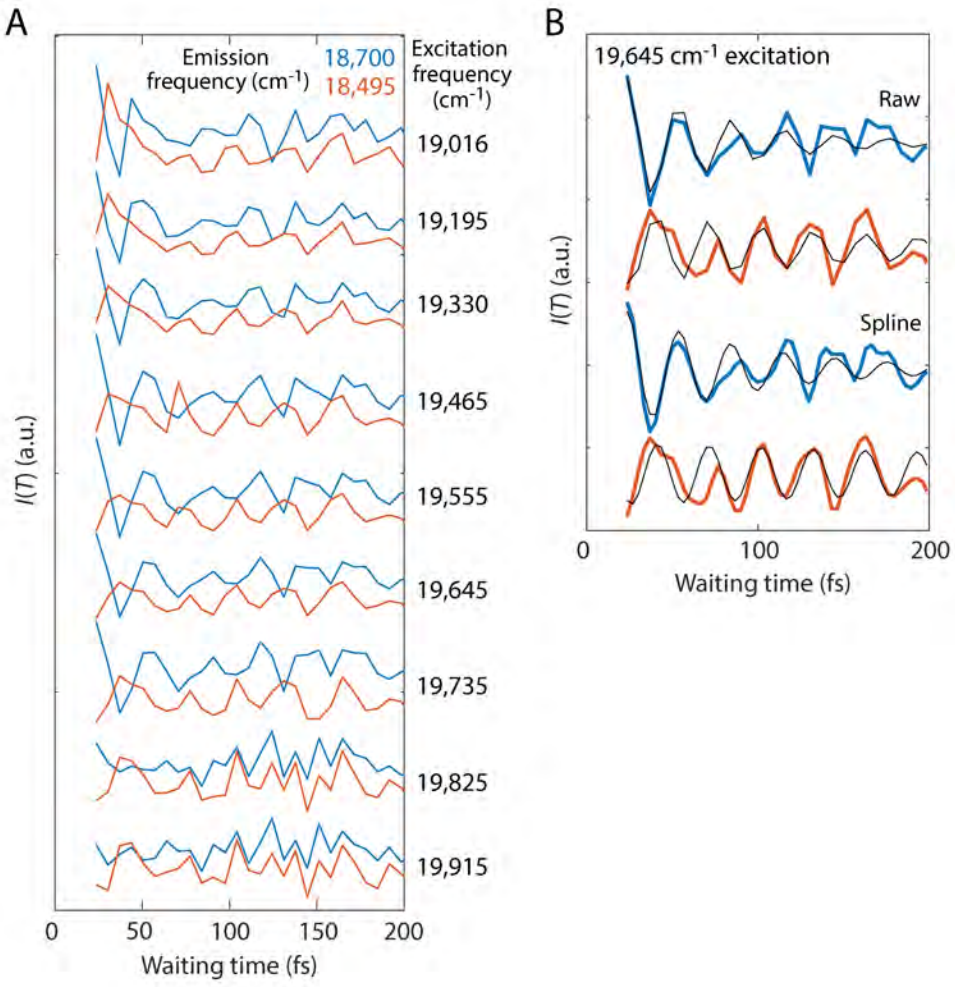

Figure 3-15: **Additional waiting time traces and fit curves for Car wavepacket motions.** (A) Raw waiting time traces plotted at the emission frequencies of 18,700 (blue) and 18,495 cm^{-1} (orange) for the excitation frequencies as listed on the right side of each trace. (B) Representative fits to the damped sinusoidal function for the traces at $\omega_\tau = 19,645\ \text{cm}^{-1}$. Top two traces are the raw traces taken from (A), and the bottom two traces are spline-interpolated, which did not affect the fit parameters or the goodness of the fit (plotted with vertical offsets for clarity).

manually evaluated by manually fitting the purely oscillatory waiting time traces (obtained by subtracting the exponential dynamics from the raw absorptive traces) to a damped sinusoidal function with a single frequency of 1,160±50 cm^{-1}:

$$I(T) = Ae(\frac{-T}{\tau_1})sin(\frac{2\pi(T-T_0)}{\tau_2}) + B \tag{3.1}$$

where $I(T)$ is the purely oscillatory time trace, A is a pre-exponential factor, τ_1 and τ_2 are the damping time constant and period of the oscillation, respectively, T_0 is the offset in time, thus leading to the phase of oscillation $\phi = -2\pi T_0/\tau_2$. Figure 3-14D shows traces at the phase discontinuities that do not correspond to S_X, highlighting that even a slight deviation of a single data point from the sinusoidal pattern, which cannot be systematically corrected for, leads to a dramatic shift, although not a flip, on the phase map. In contrast, Figure 3-15A shows traces at emission frequencies before and after the phase shift associated with S_X (18,495 and 18,700 cm^{-1}), clearly showing the phase jump at $\omega_\tau = 19,465 - 19,735$ cm^{-1} (S_2 state of Lut2). As shown in Figure 3-15B, fitting of these traces finds a phase shift of (1.154±0.22)π.

3.12.4 Supplementary Figures and Table

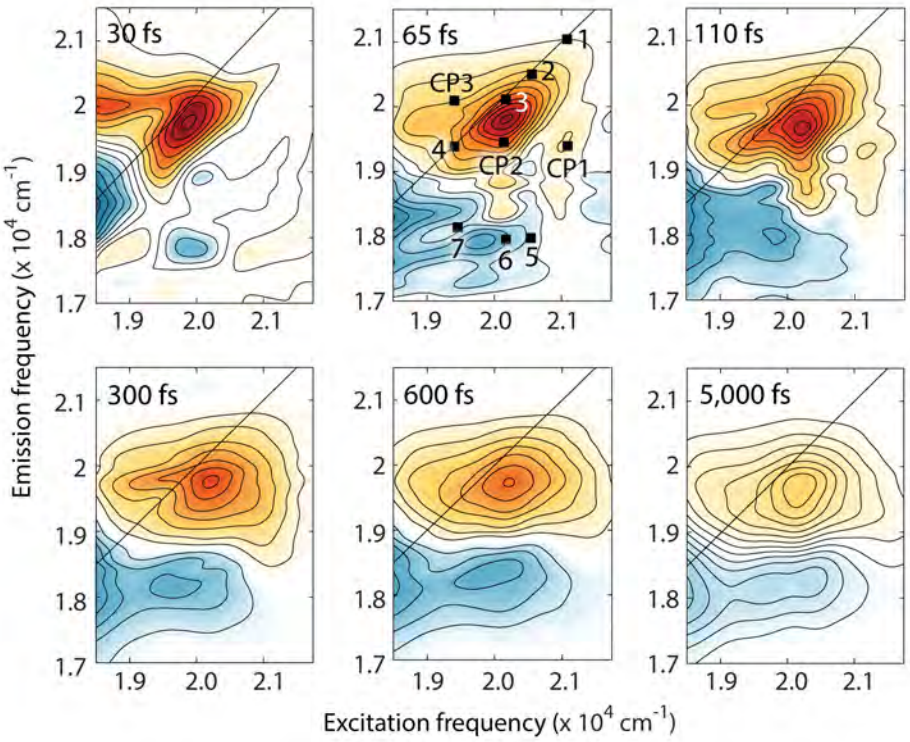

Figure 3-16: **2D spectra in the Car S_2/S_1 region.** Absorptive 2D spectra zoomed in on the Car S_2/S_1 frequency range at selected waiting times. The spectra are normalized to the maximum and minimum amplitudes of the $T = 30$ fs spectrum.

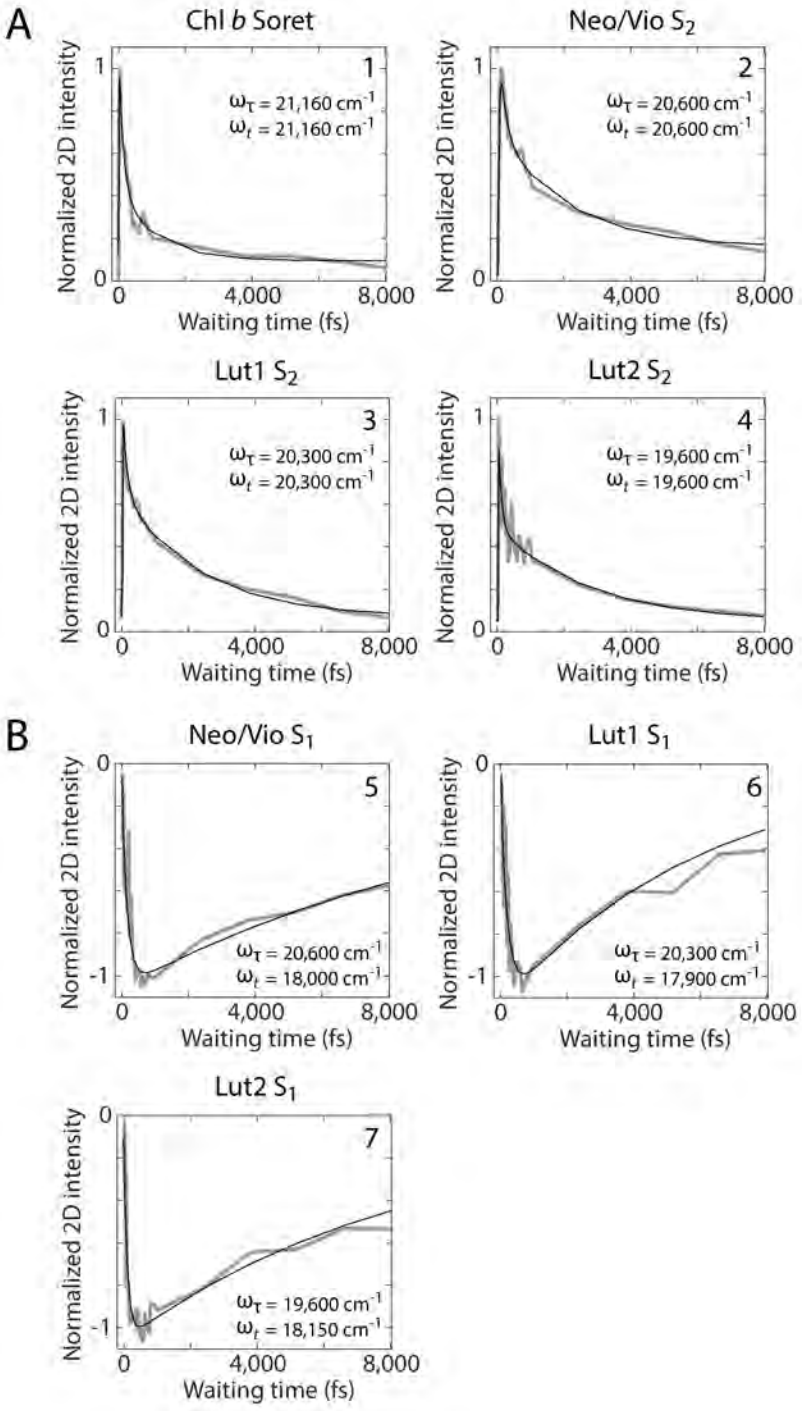

Figure 3-17: **Waiting time traces of Chl *b* Soret and Car S_2/S_1 peaks.** Fitted waiting time traces of GSB/SE peaks of (A) Chl *b* Soret and Car S_2 and (B) Car S_1 ESA labeled in Figure 3-16. The traces are normalized to a scale of 0 to 1 (positive peaks) or -1 to 0 (negative peaks). The center frequencies around which the traces were generated are indicated in each panel.

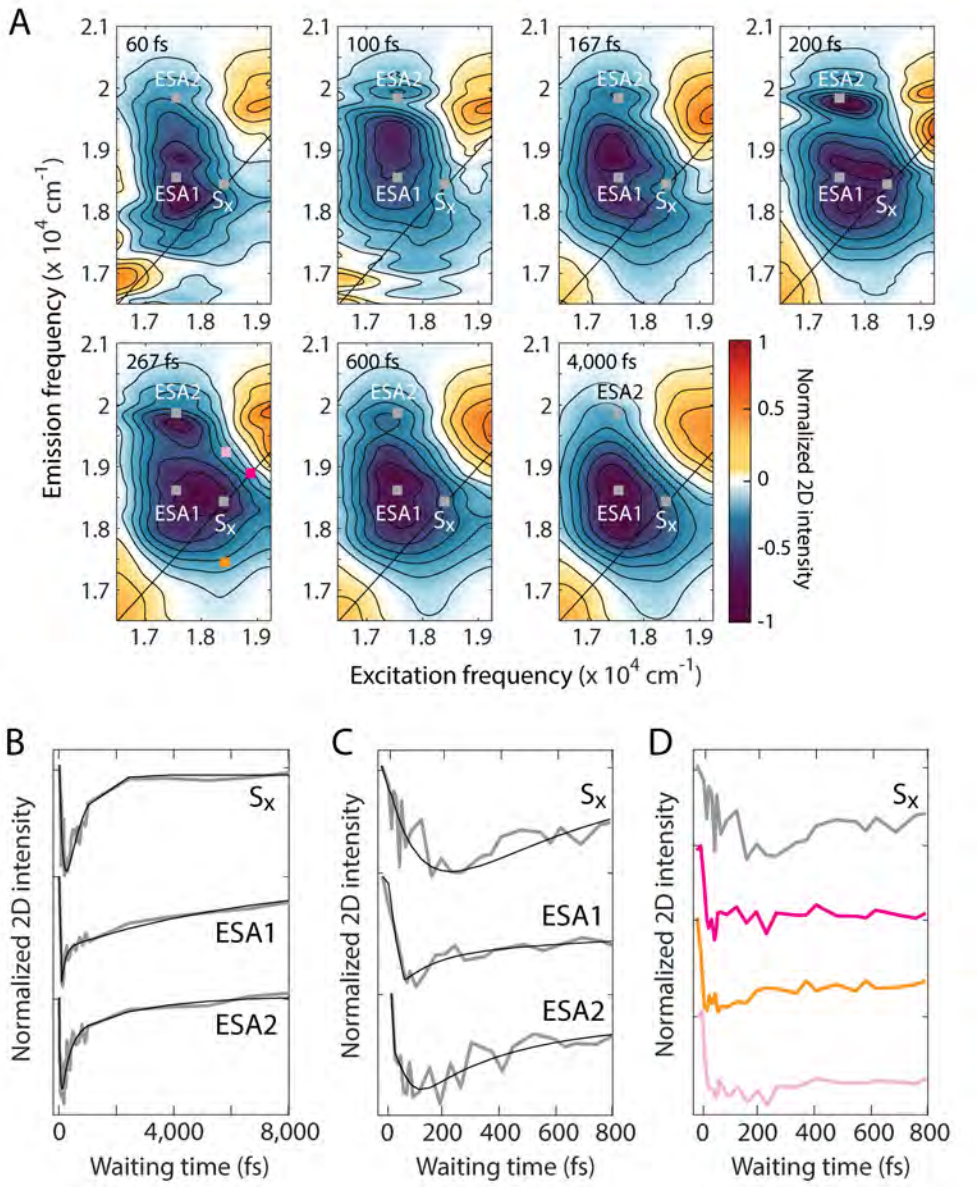

Figure 3-18: **2D spectra in the Car S_X/Chl Q_x region.** (A) Normalized absorptive 2D spectra of the Car S_X/Chl Q_x region at selected waiting times. The three peaks mentioned in the text (ESA1, ESA2, S_X) are labeled with gray filled squares. (B, C) Fitted waiting time traces of the peaks labeled in (A), on a 0−8,000 fs (B) and a 0−800 fs time window (C). (D) Additional time traces at frequency coordinates labeled in the $T = 267$ fs spectrum, showing the reliability of the early-time growth of S_X. In (B)−(D), all traces are normalized to a scale of −1 to 0, and vertically offset for clarity. (ω_τ, ω_t) = (18,400, 18,400) (S_X), (17,750, 18,580) (ESA1), (17,750, 19,900) (ESA2), (18,940, 18,950) (magenta), (18,400, 17,400) (orange), (18,400, 19,240) (light pink, in cm^{-1}).

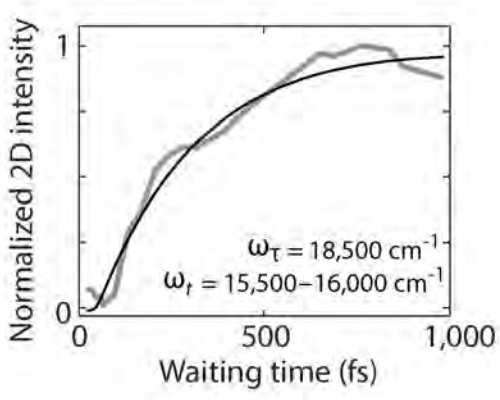

Figure 3-19: **S_X−Chl Q cross peak dynamics.** Fitted waiting time trace at the excitation frequency of S_X (18,500 cm^{-1}) and emission frequency of Chl Q states (15,500−16,000 cm^{-1}), showing a 300 fs rise component.

Table 3.1: **Fit parameters for the waiting time traces presented in Figures 3-2, 3-17, 3-18, 3-19.**[a]

Peak	A_1 (%)	τ_1 (fs)	A_2 (%)	τ_2 (fs)	A_3 (%)	τ_3 (fs)
1	65 ± 10	80 ± 20	35 ± 10	1,000 ± 240		
2	42 ± 5	115 ± 10	58 ± 5	3,040 ± 300		
3	32 ± 7	110 ± 25	68 ± 7	2,500 ± 270		
4	56 ± 3	80 ± 25	44 ± 3	2,630 ± 570		
5	-46 ± 7	200 ± 50	54 ± 7	10,000 ± 2,660		
6	-36 ± 5	160 ± 30	64 ± 5	6,220 ± 1,080		
7	-25 ± 13	135 ± 27	75 ± 13	7,100 ± 1,900		
CP1	-50 ± 3	92 ± 6	50 ± 3	360 ± 27		
CP2	-61 ± 8	64 ± 15	39 ± 8	140 ± 25		
CP3	58 ± 5	30 ± 15	42 ± 5	1,320 ± 255		
CP4	-100	90 ± 25				
CP5	-100	120 ± 45				
CP6	-52 ± 8	150 ± 30	48 ± 8	600 ± 270		
ESA1	30 ± 9	120 ± 20	70 ± 9	7,600 ± 2,850		
ESA2	-42 ± 10	44 ± 7	43 ± 10	140 ± 25	15 ± 10	8,000 ± 3,500
S_X	-50 ± 8	60 ± 8	50 ± 8	450 ± 50		
S_X−Q cross peak	-100	300 ± 30				

[a] Each entry reports the 95% confidence interval from fitting to a mono-, bi- or tri-exponential function convolved with the pulse width of the 2DES measurement. A and τ report the normalized amplitude in percentage (negative amplitude indicates exponential rise) and the fitted time constant for each component.

Chapter 4

Ultrafast Energy Transfer and Dissipative Pathways in Light-Harvesting Complex II Embedded in a Membrane Nanodisc

Adapted from: Son, M., Pinnola, A., Gordon, S. C., Bassi, R. & Schlau-Cohen, G. S. "Observation of Dissipative Chlorophyll-to-Carotenoid Energy Transfer in Light-Harvesting Complex II in Membrane Nanodiscs", *Nat. Commun.* **11**, 1295 (2020).

4.1 Chapter Summary

Green plants protect themselves against photodamage under high light by transitioning into a photoprotective state, where excess energy is dissipated as heat. Conformational changes of the photosynthetic antenna complexes, including light-harvesting complex II (LHCII), the major antenna complex in plants, activate dissipative pathways by leveraging the sensitivity of their photophysics to the protein structure. The photophysical mechanisms of dissipation remain widely debated, primarily due to two challenges. First, previous measurements lacked the temporal resolution or spectral bandwidth to be able to resolve the ultrafast timescales and large energy

gaps involved in dissipative pathways. Second, experiments have been performed in non-physiological or experimentally intractable environments. The most commonly used method is to solubilize the antenna complex in a detergent micelle, which is a far-from-native environment that induces non-native conformations. *In vivo* measurements on whole leaves or intact chloroplast report on the native photophysics, but due to the inherent complexity, contributions from homologous antenna complexes cannot be disentangled. Furthermore, measurements of native systems are prone to laser-induced artifacts, such as singlet-singlet annihilation, due to the high density of antenna complexes, and in turn, high pigment density in native systems. In this chapter, I describe the development of a reduced near-native membrane platform, known as a "nanodisc", to house the LHCII protein. The nanodisc platform overcomes the limitations of both the detergent micelle and *in vivo* environments by providing a near-native lipid bilayer membrane environment as well as incorporating a single, isolated LHCII, thereby enabling the investigation of photophysics in a well-controlled, near-physiological environment. The light-harvesting and dissipative pathways of LHCII embedded in the membrane nanodisc were interrogated with ultrabroadband two-dimensional electronic spectroscopy (2DES), and compared with those of LHCII in detergent micelles. The data reveal that the membrane environment enhances two dissipative pathways, one of which is a previously hypothesized but uncharacterized chlorophyll (Chl)-to-carotenoid (Car) energy transfer. The results presented here highlight the sensitivity of the photophysics to local environment, which may control the subtle balance between light harvesting and dissipation in response to fluctuating levels of sunlight *in vivo*.

4.2 Introduction

In green plants, the light-harvesting machinery is a complex network of multiple antenna complexes that absorb sunlight and funnel the solar energy to the reaction center, where charge separation takes place to initiate the chemical reactions of photosynthesis [4, 5]. In parallel to its primary light-harvesting functionality, the protein

network has evolved to react sensitively to fluctuating light conditions in order to prevent the generation of deleterious photoproducts. In the presence of excess light, the network transitions reversibly and rapidly from a fully light-harvesting to a photoprotective state, where harmful excess energy is dissipated as heat in a process called non-photochemical quenching (NPQ) [69, 126, 252]. The individual antenna complexes exhibit photophysics that include energy transfer, dissipative, and deleterious pathways. The timescales and amplitudes of these pathways are known to vary with conformation for these complexes. This complexity, along with the complexity intrinsic to a multi-protein network, has made it difficult to determine the balance of energy transfer and dissipation, as well as the underlying photophysical mechanisms.

The antenna complexes are membrane proteins that bind a dense network of primary (Chls) and accessory (Cars) light-harvesting pigments. The electronic interactions between the Chls and the Cars give rise to rapid and efficient energy transfer, which provides the power for chemical reactions [67, 75, 76], and, in parallel, dissipative pathways. However, proposals as to the nature and dynamics of the dissipative pathways vary widely. The four primary proposals are (1) energy transfer from the Chl Q_y to the Car S_1 state [122, 131]; (2) excitonic states constructed from a linear combination of the Chl Q_y and the Car S_1 states [134, 135]; (3) charge transfer from the Car S_1 to the Chl Q_y state [136, 137]; and (4) charge transfer among the Chls [119, 140, 141]. In the first two proposals, the short-lived dark Car S_1 state mediates dissipation, which has a lifetime of a few to several tens of picoseconds [49]. While the first proposal had been suggested as the most likely pathway, previous ultrafast experiments were unable to observe energy transfer [132, 133]. The measured dynamics were rather consistent with the characteristics of an excitonic state, leading to the development of the second proposal. However, the ambiguity of the Car S_1 energy due to its low oscillator strength has made it difficult to definitively evaluate these two proposals. The third proposal is supported by spectroscopic signatures of a Car radical cation [138], although their small amplitude has prevented clear analysis. In the fourth proposal, the states with charge transfer character are thought to appear as red-shifted fluorescence peaks, yet recent results indicate that the red-shifted and

the quenched species are distinct [142]. This series of observations and their associated limitations highlights the challenges in understanding the photophysics in green plants.

The primary antenna complex in green plants is LHCII, and therefore its photophysics have been the most extensively characterized. Previous investigations on LHCII suggested that a conformational change of the antenna complex is an important trigger for the transition into the dissipative state [28, 66, 122, 221, 222]. This transition is thought to leverage the sensitivity of the electronic interactions to the relative orientation and distance between the Chls and Cars. Therefore, various conformational changes have been proposed that result in a modulation of the structural and, in turn, photophysical properties of the Cars [66, 122, 221]. Several strategies were used to induce conformational changes, involving dramatically different local environments for LHCII ranging from crystals [26, 221] to protein aggregates [122, 253] to whole leaves [122]. While the results provided some insight into dissipative photophysics, the aforementioned multiplicity of environments led to the multiplicity of proposed conformational and photophysical mechanisms of photoprotection. For example, the fluorescence lifetime of LHCII has been reported to be different in a lipid vesicle from that in a detergent micelle [40, 146]. The *in vitro* environments, which employ detergent or crystallization, may introduce additional, non-native conformational changes that could alter or even denature the functional structure of membrane proteins [143, 254, 255]. In contrast, *in vivo* spectroscopy on whole leaves provides physiological information [145, 256, 257]. However, identifying the photophysical pathways in each of the many homologous antenna complexes is not possible. Furthermore, *in vivo* transient absorption measurements have been shown to inevitably lead to laser-induced artifacts such as singlet-singlet annihilation in the measured photophysics due to the large absorption cross-section of the intact protein network [144, 257]. Due to these challenges and limitations, a simple, yet physiological environment has been lacking, leaving the photophysical pathways of individual antenna complexes undetermined.

In this work, I benchmark the photophysics of an individual LHCII in a membrane

disc, known as a "nanodisc", using ultrabroadband 2DES. In nanodiscs, the membrane protein of interest is embedded in a discoidal lipid bilayer membrane, providing a well-controlled, near-native membrane environment without the complexity of the intact protein network [153, 258]. The 2D spectra show differences of up to 40% in the energy transfer timescales between the two environments, including an enhancement of two dissipative pathways in the membrane. Conformational changes of two Cars at the periphery of the LHCII trimer increase energy transfer to the dissipative Car S_1 state via two parallel pathways, rapid internal conversion from the Car S_2 state and energy transfer from low-energy Chls. While the latter energy transfer pathway had been proposed based on indirect evidence, here I report a direct observation of this dissipative pathway. Furthermore, the measured sub-ps timescale implies energy transfer between strongly coupled states, in contrast to previous theoretical predictions. The results shown here demonstrate the ability of the local environment to control the photophysical pathways in LHCII, which may be used to balance light harvesting and dissipation in the native thylakoid membrane.

4.3 Membrane-Induced Conformational Changes in Light-Harvesting Complex II

Membrane nanodiscs containing a single trimeric LHCII complex were prepared according to a previously reported protocol with minor modifications [146, 147]. Initial characterizations with gel electrophoresis and transmission electron microscopy (TEM) confirmed the formation of discoidal lipoprotein particles with the desired size of ∼13 nm diameter (Figure 4-2A−D). Fluorescence correlation spectroscopy (FCS) was used to verify the absence of LHCII self-aggregation in the nanodiscs, which is known to induce quenching of LHCII fluorescence [122]. The fluorescence correlogram revealed a single-component diffusion kinetics with a diffusion time constant of 1.52 ± 0.20 ms, confirming the absence of LHCII aggregates, which would exhibit a multi-component diffusion profile with a significantly longer diffusion time constant

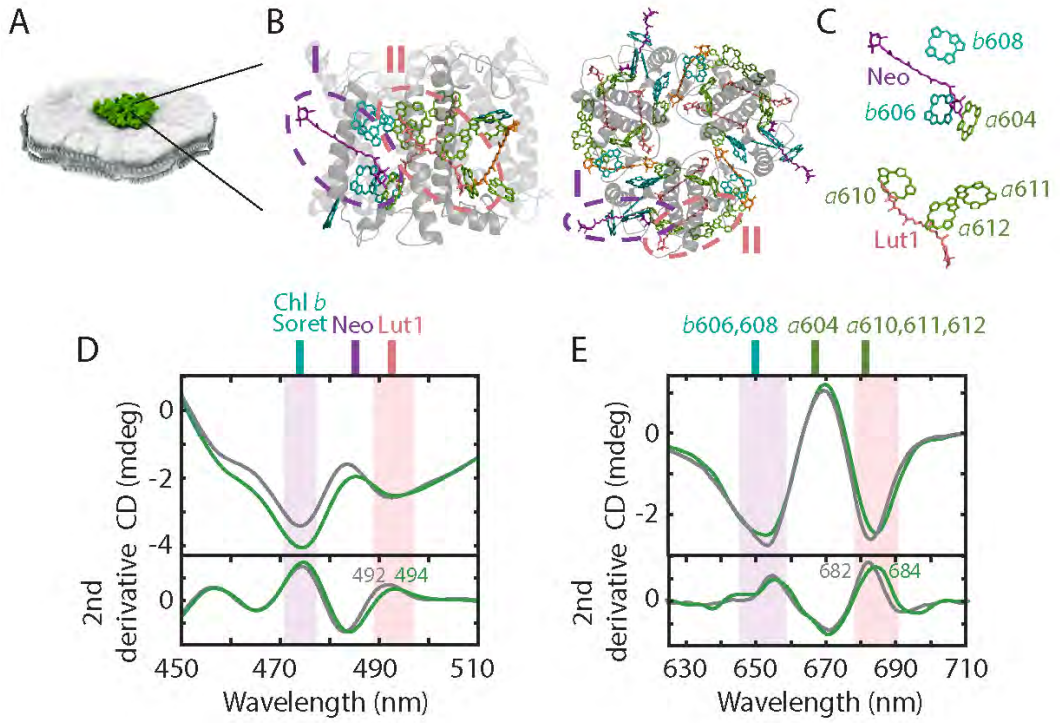

Figure 4-1: **Changes in LHCII pigment orientations upon incorporation into membrane discs.** (A) Schematic illustration of the membrane disc containing a single trimeric LHCII complex (shown in green). (B) Side (left) and top view (right) of the LHCII trimer. Chl *a* are displayed in green, Chl *b* in teal, luteins (Luts) in pink, neoxanthin (Neo) in purple, and violaxanthin (Vio) in orange. Roman numerals indicate the two pigment clusters perturbed upon disc formation. (C) Pigment-only side views of clusters **I** (top) and **II** (bottom). (D, E) CD (top) and second-derivative CD spectra (bottom) of LHCII in detergent (gray) and in membrane discs (green), plotted for the (D) Car S_2 and (E) Chl Q_y absorption range. Stick plots indicate the absorption peak wavelengths of the pigments shown in (C). The peak positions for Chls are taken from [90]. Purple and pink shaded regions highlight membrane-induced changes in CD for the two domains **I** and **II**.

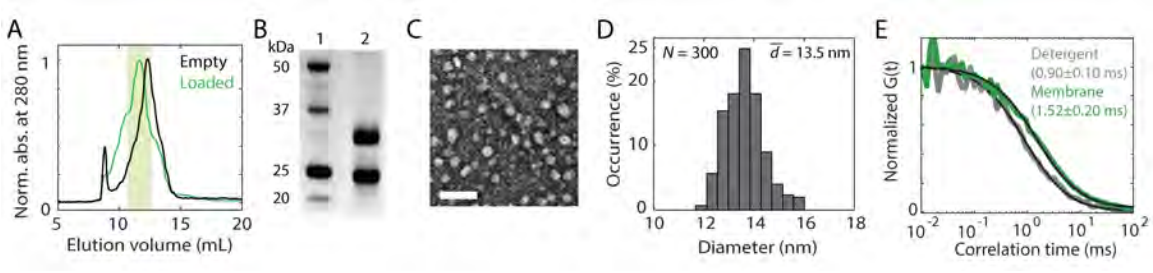

Figure 4-2: **Characterization of LHCII nanodiscs.** (A) Fast protein liquid chromatogram of empty (black) and loaded (green) LHCII nanodisc. Shaded area indicates the fraction of loaded discs that was stored for spectroscopic measurements. (B) Gel electrophoresis of LHCII nanodisc (lane 1: protein standard, lane 2: LHCII nanodisc). Both the membrane scaffold protein (MSP1E3D1, 32.6 kDa) and LHCII (25−27 kDa) bands are identified. (C) Representative TEM image of the produced LHCII nanodiscs. Scale bar is 50 nm. (D) Size distribution analyzed for 300 objects imaged with TEM. Mean diameter ($\bar{d}$) is 13.5 nm. (E) Fluorescence correlogram of LHCII in detergent (gray) and in nanodisc (green). Both curves are normalized to the maximum G value at 10^{-2} ms, and fit curves are shown in black. The fitted diffusion constants with 95% confidence intervals are indicated inside the figure.

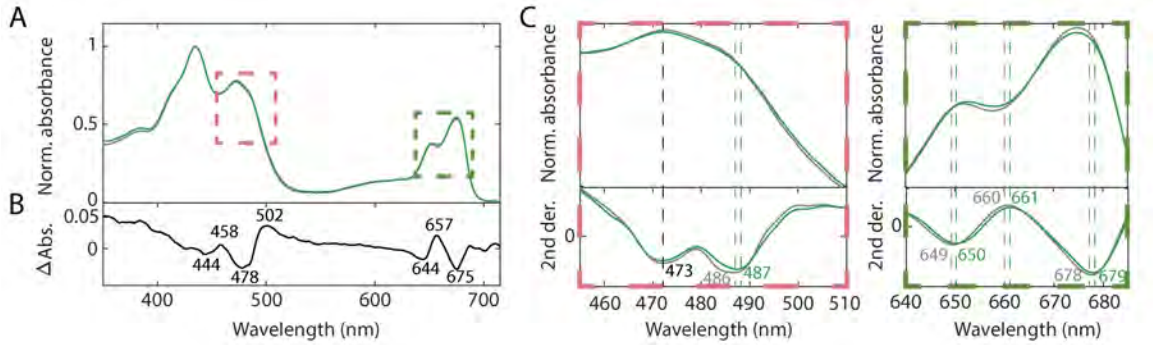

Figure 4-3: **Linear absorption of LHCII in detergent and in membrane nanodiscs.** (A) Linear absorption of LHCII in detergent (gray) and in nanodiscs (green), normalized to the 650 nm peak. (B) Difference absorbance spectrum obtained by subtracting the detergent spectrum from that of nanodiscs. (C) Zoom-ins of the Car S_2 and Chl Q_y regions (labeled with dashed boxes) from (A). Bottom panels show the second derivative of the top panels.

(Figure 4-2E).

The linear absorption spectra of LHCII (Figure 4-3A) in detergent and in membrane nanodiscs demonstrate its successful incorporation into nanodiscs in intact trimeric form, based on similar overall peak location and profiles. A closer inspection of the spectra shows subtle changes in peak position and/or intensity in the Car S_2 states ($470-510$ nm) as well as the two Q_y bands of Chls ($640-690$ nm), suggesting changes in the arrangement of both the Cars and Chls resulting from introduction of the membrane environment.

Circular dichroism (CD) spectra of LHCII in detergent and in nanodiscs provide a sensitive measure of the spatial configuration of the constituent pigments in each environment, because CD peak shape and intensity are directly related to the mutual orientation of the transition dipoles and the strength of their interactions [259, 260]. Comparison of the CD spectra reveals two differences involving two peripheral Cars, Neo and Lut1 (Figure 4-1B, C). First, the relative peak intensities between 474 nm and 492 nm (494 nm) change, which has been reported to originate from the interactions between the Soret band of the Chls *b* and Neo (Figure 4-1D) [143, 259, 261]. A similar change in the peak ratio was previously observed in LHCII nanodiscs [147]. Second, the negative 492 nm peak red-shifts by 2 nm, reported to originate from the interactions between the high-energy Lut (Lut1) and the Soret band of Chl *a*612 [259]. Thus, the observed changes point to alterations in the spatial arrangement of Neo and Lut1 caused by the membrane. In contrast, no difference was observed in the CD signal at $500-510$ nm, where the lower-energy Lut (Lut2) absorbs.

CD in the Chl Q_y region (Figure 4-1E) reveals a slight broadening of the 653 nm peak and a 2 nm red-shift of the 682 nm peak, attributed to excitonic interactions between Chl *a*604−Chl *b*606 and Chl *a*610−Chl *b*608, and between Chls *a*611 and *a*612, respectively [259]. These are the Chls that are strongly coupled with Neo (Chl *a*604, Chl *b*606, Chl *b*608) and Lut1 (Chls *a*610, *a*611, *a*612) [262], illustrated as domains **I** and **II**, respectively, in Figure 4-1B, C. Given that Neo and Lut1 are the two Cars impacted upon incorporation into the membrane, it is speculated that the observed changes in the rotational strengths of the Chls could arise from changes

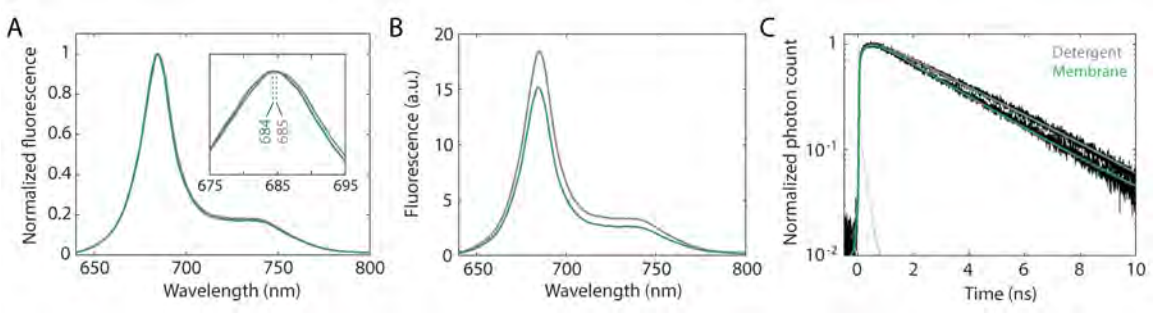

Figure 4-4: **Comparison of LHCII fluorescence in different environments.** (A, B) Fluorescence spectra of LHCII in detergent (gray) and in soy asolectin nanodiscs (green), normalized to the maximum fluorescence peak (A) and to the absorbance at the excitation wavelength (630 nm) for comparison of fluorescence quantum yield (B). Inset of (A) displays zoom-in of the $675-695$ nm range to show the shift in peak wavelength. In (B), the integrated area of fluorescence in nanodiscs was 83% of that in detergent. (C) Fitted fluorescence decay profiles of LHCII in detergent (gray) and in soy asolectin nanodiscs (green). The best fit parameters are shown in Table 4.1.

in their excitonic interactions with the neighboring Cars, rather than independent structural reorganization of the Chls in the membrane.

Perturbation of domain **II**, which contains the three lowest-energy Chl *a* pigments that form the emissive locus of LHCII (Chls *a*610, *a*611, *a*612) [263], is further supported by a reduction of fluorescence in the membrane nanodisc environment. The steady-state fluorescence quantum yield and fluorescence lifetime are reduced in the membrane discs by 17% and 18%, respectively (Figure 4-4). The slight quenching of the fluorescence upon membrane insertion is consistent with previous results on LHCII nanodiscs [146], and is independent of the lipids used to prepare the nanodiscs (Figure 4-14 and Table 4.1). These results strongly indicate that the observed fluorescence quenching is a consequence of structural perturbations in LHCII induced by the membrane environment, not of specific protein-lipid interactions. The observed average fluorescence lifetime (2.8 ns) is still significantly longer than that measured *in vivo* ($<$ 2 ns) [264] or in crystals (1 ns) [221], suggesting additional interactions are present in these systems due to the presence of multiple antenna complexes, and therefore, protein-protein interactions.

Domains **I** and **II** are located at the periphery of the trimeric LHCII complex (Figure 4-1B). Compared to their counterparts located closer to the core that are

shielded by the surrounding pigments and protein matrix, these domains are more exposed to the lipid bilayer. Thus, they are more susceptible to structural changes induced by the membrane, consistent with my results. In particular, a significant part of the conjugated chain of Neo protrudes outward from the protein matrix, which may allow severe twisting of the chain by interactions with the surrounding environment. Such a distortion in the conjugated chain of Neo has, in fact, been predicted theoretically [28].

4.4 Energetics and Ultrafast Dynamics of the Peripheral Carotenoids in the Membrane Environment

Ultrabroadband 2DES was used to determine the impact of the membrane environment on the ultrafast photophysical pathways in LHCII. As discussed in Chapters 2 and 3, by using a laser spectrum with a significantly broader bandwidth than in conventional 2DES [226], it is possible to map out energy transfer and dissipation across the broad range of Car and Chl excited states (see Figure 3-1D in Chapter 3).

Figure 4-5A shows the 2D spectra of LHCII in the detergent and the membrane environment (T = 533 fs) in the frequency range of the Car S_2 states. Two major changes are observed. The first is increased transfer of the Car S_2 population into the dark S_1 state ($S_2 \rightarrow S_1$ internal conversion), which results in decreased energy transfer to the lower-lying Chls, the competing pathway (Figure 4-15). The relative population in S_1 is estimated by the ratio of the magnitude of the S_1 excited-state absorption (ESA) to that of the initial ground-state bleach (GSB) of S_2 immediately after photoexcitation. The ratio increases by 40% in the membrane, showing the increase in transfer to S_1 (Figures 4-5B and 4-16). The increase is pronounced at the excitation frequencies of Neo and Lut1, showing 35−43% more efficient relaxation to the S_1 state. While the excitation frequency of Neo and that of Vio have a significant overlap [67, 232], and so the contribution from these two Cars cannot be distinguished,

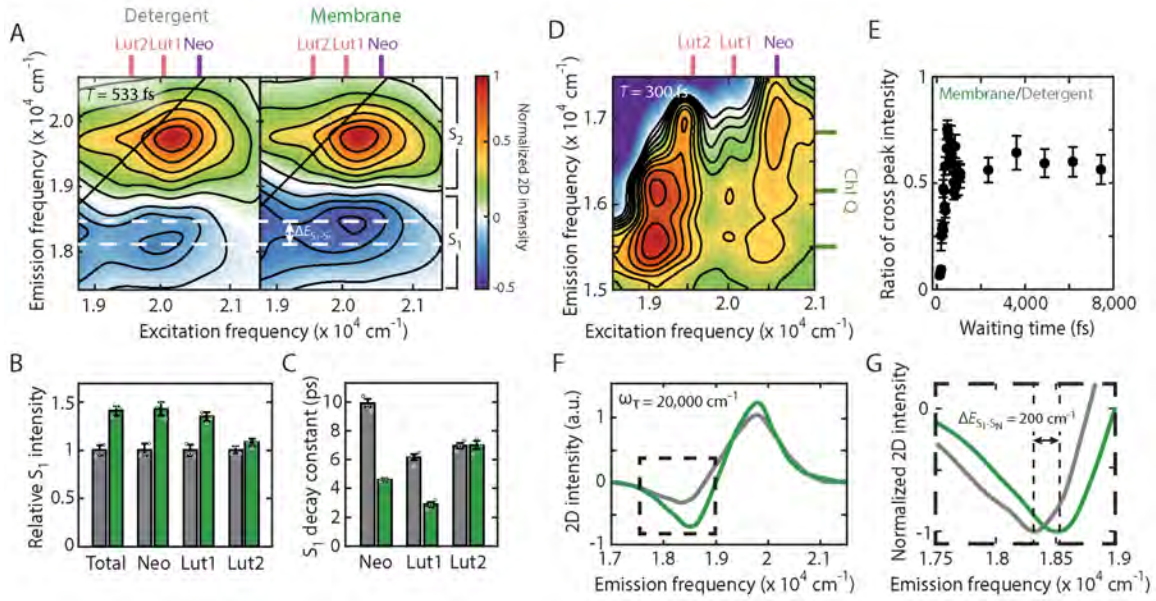

Figure 4-5: **Impact of the membrane environment on the energetics and relaxation dynamics of Cars.** (A) Absorptive 2D spectrum of LHCII in detergent (left) and in nanodiscs (right) in the Car S_2/S_1 region at $T = 533$ fs. White dashed lines indicate the shift in Car $S_1 \rightarrow S_N$ transition energy ($\Delta E_{S_1\text{-}S_N}$). Colored sticks indicate the energy levels of the Car S_2 states. (B) Relative Car S_1 ESA intensity at $T = 533$ fs in detergent (gray) and in nanodiscs (green), obtained by normalizing the S_1 ESA intensity to the initial S_2 GSB intensity immediately after photoexcitation ($T = 30$ fs). (C) Comparison of Car S_1 ESA decay constants in detergent (gray) and in nanodiscs (green). (D) Absorptive 2D spectrum of the Car-Chl cross peak region at $T = 300$ fs (in detergent). Colored sticks indicate the energy levels of the Car S_2 and Chl Q states. (E) Ratio of Car-Chl cross peak intensity obtained by dividing the sum of all cross peak intensities in nanodiscs by that in detergent. Error bars in (B), (C), and (E) are the std. dev. from three independent measurements. (F) Projection of the 2D spectra shown in (A) onto the ω_t axis for a 600 cm $^{-1}$ ω_τ interval centered at $\omega_\tau = 20{,}000$ cm^{-1} (gray: detergent, green: nanodisc). (G) Closer view of the dashed box in (F), where both traces are normalized to the same scale to emphasize the energy shift.

Neo is the likely origin of the increase based on the dramatic changes observed in the CD spectra. Unlike in the case of Neo and Lut1, the relaxation dynamics of Lut2 are independent of environment (Figure 4-5B, C). Lut2 is located at the inner core of the trimeric LHCII (Figure 4-1B), and thus relatively protected from direct exposure to the protein-lipid interface, as mentioned earlier. This may be the origin of its environment-independent dynamics. The Car-Chl cross peaks directly visualize energy transfer from the Car S_2 to the lower-lying Chl Q states, and so further report on Car S_2 dynamics. The cross peak intensities decrease by 35% in the membrane (Figure 4-5D, E), consistent with the increased relative S_1 intensities shown in Figure 4-5B, the competing pathway.

The second major change is a blue-shift of the Car S_1 ESA by $\sim$200 cm^{-1}, indicating that the $S_1 \rightarrow S_N$ energy gap increases in the membrane (Figure 4-5A, F, G and Figure 4-17). This blue-shift can originate from either a red-shift in S_1 energy or a blue-shift in S_N energies. The former is more likely, because S_N is a broad manifold of multiple higher-lying states that are unlikely to all shift in a correlated manner, especially given the environment-independent transition energy of the S_2 state. This energy level shift is an environment-induced static effect present at all waiting times, separate from a dynamic shift due to vibrational cooling of the hot S_1 state [265, 266]. Additional dynamic shifts in the S_2-S_1 zero-crossing frequency are observed in the initial 500 fs, where the contribution from vibrational cooling is significant (Figure 4-18). These dynamic effects are independent of environment. In contrast to the $S_1 \rightarrow S_N$ transition, no energy shift is observed for the S_2 states.

Along with the changes in spectral features, an acceleration of the decay of the S_1 population of Neo/Vio (54%) and Lut1 (53%) is observed in the membrane nanodisc environment (Figure 4-5C). This can originate from two different processes: a decrease in the S_1-S_0 energy gap, which speeds up non-radiative decay, or an increase in energy transfer to the energetically close-lying Chl Q_y states, which accelerates the depletion of the S_1 population [134]. The observed acceleration of the decay is attributed to the former mechanism, faster non-radiative decay, based on two results. First, an increase in energy transfer from Car S_1 to Chl Q_y would result in an increase in magnitude

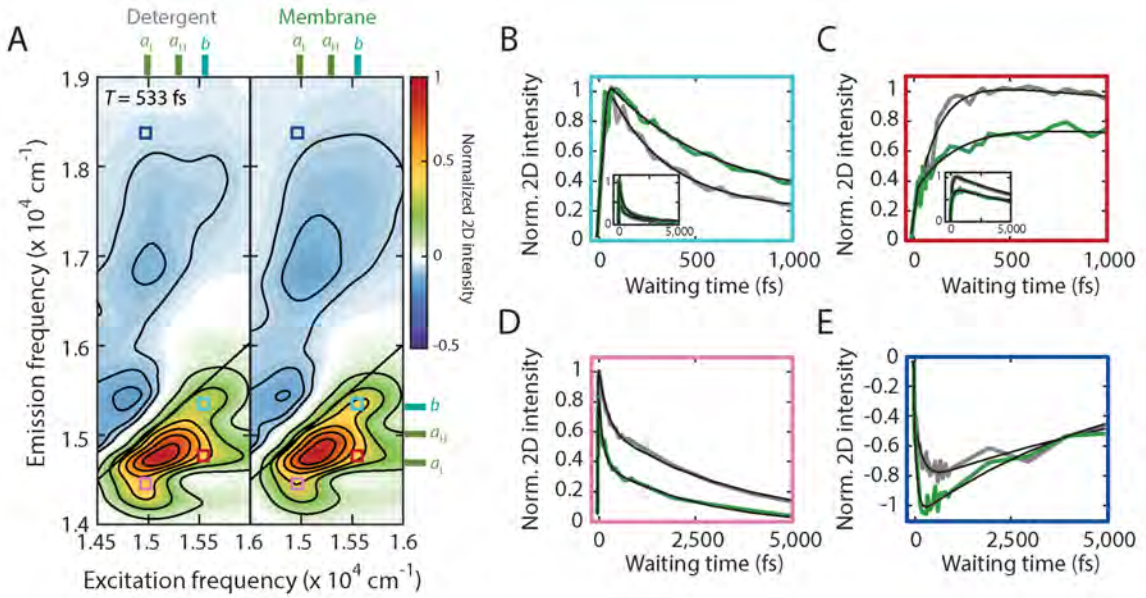

Figure 4-6: **Impact of the membrane environment on Chl relaxation dynamics.** (A) Absorptive 2D spectrum of LHCII in detergent (left) and in nanodiscs (right) in the Chl Q_y region at T = 533 fs. Colored sticks indicate the energy levels of the Chl Q_y states. (B)−(E) Waiting time traces of the peaks labeled with colored boxes in (A): Chl b diagonal peak (B, cyan), Chl $b \rightarrow$ Chl a energy transfer cross peak (C, red), Chl SE (D, pink), and Car S_1 ESA upon excitation of the terminal Chls (E, blue). Insets in (B) and (C) show longer-timescale dynamics. (ω_τ, ω_t) = (15,540, 15,300) (B), (15,540, 14,750) (C), (14,925, 14,470) (D), (14,925, 18,400) (E, in cm^{-1}). Traces in (D) and (E) were generated by integrating the 2D intensity over a 300 cm^{-1} (ω_τ) × 400 cm^{-1} (ω_t) interval.

of the Car-Chl cross peaks on the timescale of the S_1 decay, and no such feature is observed. Second, the S_1 state likely red-shifts in the nanodisc, as discussed above. Consistent with the trend observed in the relative S_1 intensity, the kinetics of Lut2 is independent of environment.

4.5 Suppression of Chlorophyll *b*-to-Chlorophyll *a* Energy Transfer in the Membrane Nanodisc Environment

The low-frequency range of the ultrabroadband 2D spectra reveal the relaxation pathways within the Chl Q manifold (Figure 4-6A). In agreement with previously results

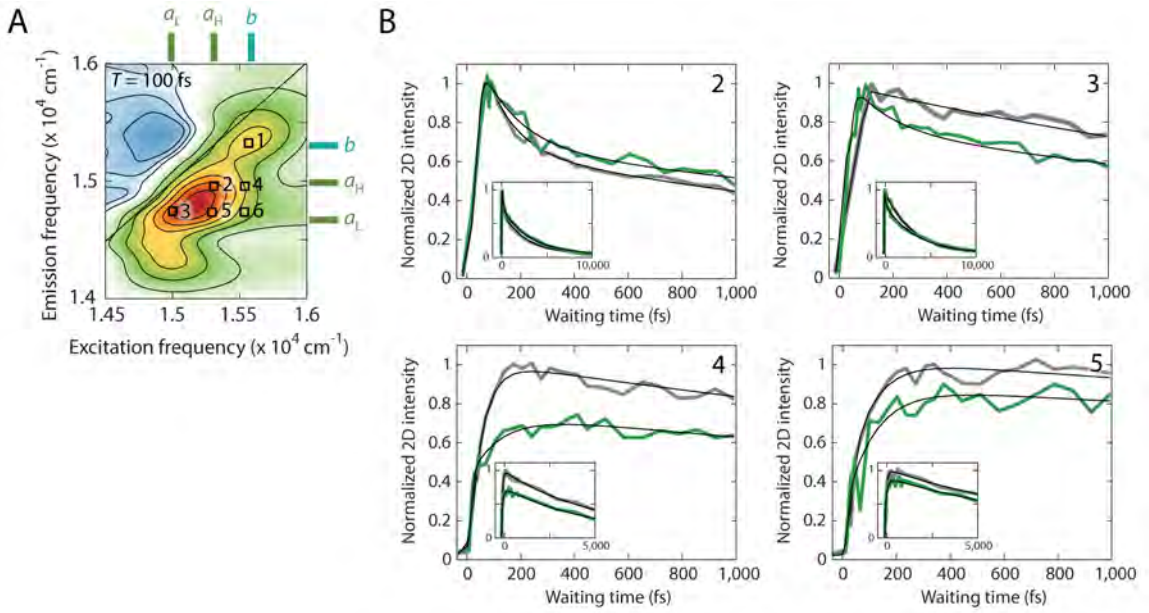

Figure 4-7: **Peak assignment of the Chl Q region and dynamics of Chl relaxation.** (A) Absorptive 2D spectrum of LHCII in detergent at T = 100 fs, zoomed in on the Chl Q region. Colored sticks indicate the energy levels of the Chl Q_y states, and the six peaks discussed in the text are labeled with black open squares. (B) Waiting time traces of peaks 2−5 for the initial 1,000 fs (insets show longer-timescale dynamics). Gray and green traces are traces measured in detergent and in nanodiscs, respectively, and black lines are the fit curves. (ω_τ, ω_t) = (15,300, 14,950) (2), (15,000, 14,750) (3), (15,540, 14,950) (4), (15,300, 14,750) (5, in cm^{-1}). Waiting time traces of peaks 1 and 6 are shown in Figure 4-6B, C.

[90, 94], the 2D spectra in this range show diagonal peaks at the energies of the Q_y bands of Chl *b* and Chl *a* (peaks 1−3, Figure 4-7). The pronounced elongation of the Chl *a* peak implies the presence of the higher-energy (a_H) and lower-energy pools (a_L) of Chl *a*, which are resolved into two separate peaks at cryogenic temperatures but not at room temperature (RT) [90]. At the intersections of the frequencies of 1−3, cross peaks (peaks 4−6) grow in at early waiting times as energy migrates from Chl *b* to the lower-lying Chl *a* pools. The data also contain non-negligible contribution from the stimulated emission (SE) of low-energy Chl *a* at $\omega_t < 14{,}500$ cm^{-1} due to the broad bandwidth of the laser spectrum that covers part of the Chl fluorescence [247].

The relaxation dynamics of the Chls reveal two prominent changes in the membrane environment. First, the downhill energy transfer from Chl *b* to Chl *a* [90, 92, 94]

is slowed down in the membrane (Figure 4-6A−C). The timescales of the energy transfer pathways, obtained by fitting the initial rise time of the cross peaks, become longer in the membrane, from 80 ± 20 to 132 ± 22 fs (Chl $b \rightarrow$ Chl a_{H}) and from 130 ± 20 to 225 ± 20 fs (Chl $b \rightarrow$ Chl a_{L}), indicating a $39-42\%$ reduction in the energy transfer rates and resulting in diminished cross peak intensities in the membrane. The same trend is observed in the kinetics of the Chl b diagonal peak, which decays 40% slower in the membrane due to the decreased rate of energy transfer to Chl a (Figure 4-6B). The energy transfer between the high- and low-energy Chl a pools (Chl a_{H} and Chl a_{L}) is also slowed down, but to a much lesser extent (14%).

The specific pigment structural changes responsible for the observed deceleration of Chl $b \rightarrow$ Chl a energy transfer cannot definitively be identified. Although LHCII is thought to compact overall in the membrane environment as compared to in a detergent micelle, the slower Chl $b \rightarrow$ Chl a energy transfer observed here suggests that the specific pigments involved actually move further apart. As discussed above, several Chl b pigments form a strongly coupled pigment cluster with Neo (domain **I** in Figure 4-1B, C), the Car that is positioned to most easily undergo large structural motions [28], which may induce displacement of these Chl b molecules. Even minor perturbations to inter-pigment distances can significantly change the dynamics due to the nonlinear relationship between distance and energy transfer rate [267].

4.6 Observation of Dissipative Low-energy Chlorophyll *a*-to-Carotenoid S_1 Energy Transfer

The second prominent change appears on the red side of the lower-energy Chl a pool (a_{L}). This pool consists of the three Chl a's in domain **II** that interact strongly with Lut1 and form the terminal locus of energy, collecting energy from higher-lying states and emitting fluorescence in isolated LHCIIs [263, 268]. The waiting time traces of the red half of the Chl SE reveal pronounced rapid decay components with time constants and amplitudes of 350 ± 30 fs (39%) in detergent and 270 ± 20 fs (53%) in

the membrane (Figure 4-6D). This rapid decay is followed by slower, picosecond components, likely reflecting vibrational relaxation of the Chls [45, 269]. The amplitude of the sub-ps decay component shows a strong dependence on emission frequency; the amplitude increases as the emission frequency decreases, and is non-negligible only when the red side of the Chl a_{L} band is probed, which corresponds to the red half of the Chl a fluorescence emission range (Figure 4-19). The biexponential decay kinetics of Chl a_{L} imply two subpopulations with different levels of quenching, likely reflecting a quenched conformation and an unquenched one [270, 271]. Recent transient absorption studies on CP29, a minor antenna complex homologous to LHCII, found a similar biexponential decay of the terminal Chl a excited state, which was attributed to the coexistence of quenched and unquenched conformations [272]. The coexistence of multiple conformations with distinct photophysics is further supported by single-molecule fluorescence measurements, which identified unquenched and quenched conformations of LHCII [273, 274] and other homologous complexes [275, 276].

The presence of a rapid, sub-ps decay component points towards an energy sink that accepts energy from the terminal locus. Notably, I find concurrent rise of the population at the excitation frequency of Chl a_{L} and emission frequency of Car S_1 ESA, which indicates that the Car S_1 states are the energy sink populated by energy transfer from the terminal Chl a's (Figure 4-6E). Although this region of the 2D spectra contains a contribution from the ESA of the Chls [132], the absence of an increase in Chl a population on the corresponding timescale supports the assignment that the rise originates from the ESA of the Car S_1, not that of the Chls (Figure 4-20). Following energy transfer from the Chls, the Car S_1 state dissipates the excitation energy via a picosecond non-radiative relaxation pathway, as mentioned earlier. This is a clear and direct observation of the dissipative energy transfer pathway from the terminal Chl a locus into the dark S_1 state of the Cars, one of the mechanisms of photoprotection proposed but not well understood [122, 132, 133, 222, 277]. Correlated decay of Chl a and rise of Car S_1 populations, similar to those identified here but on a slower timescale (2.1 ps), have been observed in a cyanobacterial ancestor of plant

antenna complexes, high light-inducible protein (Hlip), and assigned to Chl-to-Car energy transfer [277].

The terminal Chl $a \rightarrow$ Car S_1 energy transfer pathway is present for LHCII in both detergent and membrane nanodisc environments. The efficiency of this pathway increases by $12-14\%$ in the membrane, as seen by the increased amplitude of the sub-ps decay and rise components in nanodiscs relative to that in detergent. This is qualitatively in agreement with the observation of fluorescence quenching in the membrane discussed in Section 4.3. The enhancement of this Chl $a \rightarrow$ Car S_1 pathway in the membrane could arise from the red-shift of the Car S_1 energy level as discussed earlier. Although the exact energy gap between the Chl a Q_y and Car S_1 states cannot be determined due to the ambiguity in the energy level of the dark Car S_1 transition, such a red-shift could bring the two states closer to resonance, and thus increase the rate of energy transfer.

4.7 Kinetic Modeling of Membrane-Induced Changes in Photophysics

A set of coarse-grained kinetic models was constructed to simulate the dynamics observed in the experimental data. Detailed descriptions of each model and comparison with experimental data are provided below.

4.7.1 Branching of Carotenoid Population

The kinetic scheme for the Car S_2 state is shown in Figure 4-8A. The excited-state population on the S_2 state of the Cars decays via two channels: internal conversion to the S_1 state (k_{21}) and energy transfer to Chl Q states (k_{2q}). $k_{d'}$ and k_d denote the relaxation rate constants out of the Car S_1 and Chl Q states, respectively. The

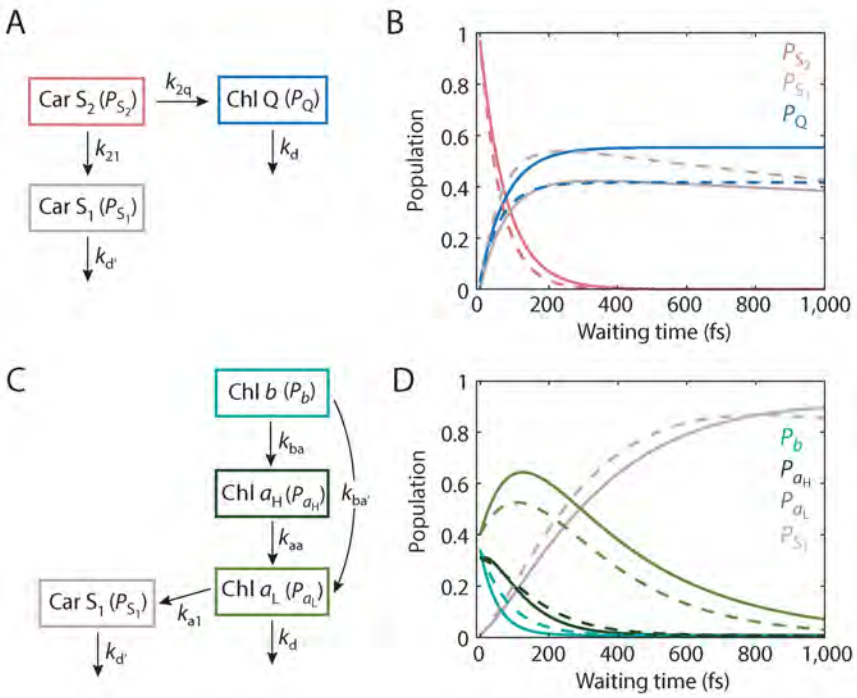

Figure 4-8: **Kinetic models.** (A) and (C) show the kinetic schemes with the relevant pigment states and rate constants that describe branching of Car S_2 and Chl-to-Car energy transfer, respectively. (B) and (D) illustrate the temporal evolution of the population on each state shown in the schemes in (A) and (C), calculated using the experimental rate constants obtained for detergent-solubilized (solid) and membrane-embedded LHCII (dashed curves): $k_{21} = (160\text{ fs})^{-1}/(110\text{ fs})^{-1}$, $k_{2q} = (150\text{ fs})^{-1}/(150\text{ fs})^{-1}$, $k_d = (3.4\text{ ns})^{-1}/(2.8\text{ ns})^{-1}$, $k_{d'} = (7.7\text{ ps})^{-1}/(3.8\text{ ps})^{-1}$, $k_{ba} = (80\text{ fs})^{-1}/(130\text{ fs})^{-1}$, $k_{ba'} = (130\text{ fs})^{-1}/(225\text{ fs})^{-1}$, $k_{aa} = (90\text{ fs})^{-1}/(105\text{ fs})^{-1}$, $k_{a1} = (350\text{ fs})^{-1}/(270\text{ fs})^{-1}$ (detergent/membrane).

differential equations that describe the temporal evolution of populations are

$$\dot{P_{S_2}} = -(k_{21} + k_{2q})P_{S_2}$$

$$\dot{P_{S_1}} = k_{21}P_{S_2} - k_{d'}P_{S_1}$$

$$\dot{P_Q} = k_{2q}P_{S_2} - k_dP_Q$$

The initial populations are estimated based on the extinction coefficient and laser intensity (spectrum 1, Figure 4-11) at the wavelength of each transition, and scaled such that $P_{S_2} + P_{S_1} + P_Q = 1$ at $T = 0$. Pathways involving the terminal Chl a locus were excluded given the negligible probability for direct Chl a excitation with spectrum 1.

Figure 4-8B shows the temporal evolution of populations in both environments, calculated using the rate constants for each pathway obtained from the experimental 2D data. Consistent with the 35 ± 9% decrease in the Car-Chl cross peak intensity in the 2D spectra (Figure 4-5D, E), Chl Q population decreases by 28%. At the same time, Car S_1 population increases by 30%, also consistent with the increase in Car S_1 ESA intensity in the membrane. Varying the rate constants did not result in any significant changes to the population dynamics (< 3% difference), demonstrating the robustness of the model.

4.7.2 Branching of Chlorophyll Population and Chlorophyll-to-Carotenoid Energy Transfer

The kinetic scheme describing the population transfer within and out of the Chl Q states is shown in Figure 4-8C. The differential equations describing the temporal evolution of the populations are

$$\dot{P_b} = -(k_{ba} + k_{ba'})P_b$$
$$\dot{P_{a_H}} = k_{ba}P_b - k_{aa}P_{a_H}$$
$$\dot{P_{a_L}} = k_{aa}P_{a_H} + k_{ba'}P_b - k_dP_{a_L} - k_{a1}P_{a_L}$$
$$\dot{P_{S_1}} = k_{a1}P_{a_L} - k_{d'}P_{S_1}$$

The initial populations are estimated based on the extinction coefficient and laser intensity (spectrum 2, Figure 4-11) at the wavelength of each transition, and scaled such that $P_b + P_{a_H} + P_{a_L} = 1$ at $T = 0$. Pathways involving the Car S_2 state were excluded given the negligible probability for direct Car S_2 excitation with spectrum 2. Figure 4-8D shows the temporal evolution of populations using the rate constants obtained from the 2D experiment. Similarly to the kinetic model describing Car S_2 population branching, the model was robust to modest changes in the rate constants. The relative populations on the terminal Chl *a* locus as well as the Car S_1 state in the membrane predicted by the kinetic model show quantitative agreement with the experimental data with small deviations (Figure 4-9B). The quantitative agreement

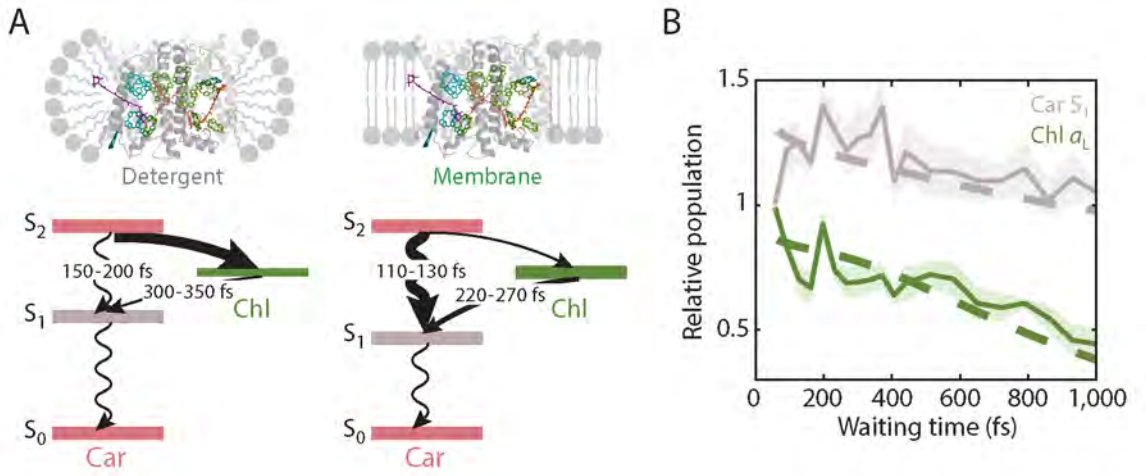

Figure 4-9: **Impact of the membrane on the photophysics and proposed kinetic model.** (A) Schematic illustration of the alteration of LHCII photophysics by the membrane environment. The cartoons and energy level diagrams (not to scale) illustrate the quenched subpopulation of LHCII embedded in the detergent (left) and membrane nanodisc (right) environments, respectively. Curved arrows illustrate energy transfer between Cars and Chls, and squiggly arrows illustrate non-radiative decay pathways of the Cars. The thickness of the arrows qualitatively shows the relative efficiency of the corresponding pathway. (B) Relative population of the low-energy Chl *a* locus (green) and Car S_1 (gray) for the membrane relative to detergent. Dashed lines are obtained from the kinetic model in Section 4.7, and solid lines show the peak ratio of the Chl a_L diagonal and Car S_1 ESA peaks from the 2D data with error bars (shaded regions, std. dev. from three independent measurements).

between the experimental and simulated populations illustrates that the minimal set of photophysical pathways included here is sufficient to describe the observed dynamics.

4.8 Discussion

The mechanism of photoprotective quenching has been extensively debated in the field. One of the likely mechanisms, the dissipative Chl Q $\rightarrow$ Car S_1 energy transfer pathway observed here, appears spectroscopically as a rise in the Car S_1 population after photoexcitation into the Chl Q state. Previous work reported differences in the long-time decay dynamics of the Car S_1 between unquenched and quenched LHCII. However, unlike my results, an instantaneous initial rise of the Car S_1 population was

observed, potentially due to limitations in temporal or spectral resolution of earlier ultrafast experiments [122, 132]. This led to the development of an excitonic mixing model between Chl Q_y and Car S_1 states, where the observed instantaneous Car S_1 rise was attributed to strong excitonic interactions between the Chl and the Car states [133, 135]. Here, as illustrated in Figure 4-9A, the initial rise of Car S_1 ESA is resolved, characteristic of a directional energy transfer rather than a delocalized Car-Chl excited state predicted by the excitonic mixing model. Theoretically predicted timescales for this energy transfer pathway are > 20 ps due to the optically forbidden nature of the Car S_1 state [68, 262, 278], which is two orders of magnitude longer than the sub-ps (<400 fs) timescale observed in this work. This discrepancy suggests that a more complex picture is required, such as directional Chl $\rightarrow$ Car energy transfer mediated by partial mixing of the excited states, along the lines of previous proposals [133–135].

The comparison between detergent and membrane environments presented here demonstrates that the local environment is able to control the photophysical pathways in plants, including altering the balance between light harvesting and photoprotection. Both the experimental data and simulated results from the kinetic models show that the two major energy transfer pathways for efficient light harvesting in LHCII, Car $S_2 \rightarrow$ Chl Q and Chl *b* $Q_y \rightarrow$ Chl *a* Q_y energy transfer, are both suppressed in the membrane nanodisc environment. The Chl *a* Q_y state then transfers energy to neighboring antenna complexes for transport towards the reaction center. Consistently, the experimental and simulated results also demonstrate that two dissipative pathways, Car $S_2 \rightarrow$ Car S_1 and Chl *a* $\rightarrow$ Car S_1 energy transfer, are both enhanced in the membrane nanodisc environment. The short-lived dark S_1 state of the Cars then rapidly quenches the excitation via non-radiative decay. Taken together, the aforementioned changes enhance the dissipative pathways relative to light harvesting ones by increasing the relative population of the Car S_1 state and decreasing that of the Chl Q states, as illustrated in Figure 4-9B.

The data presented here, both in the steady state (CD) and on ultrafast timescales (2DES), suggest that the two peripheral pigment domains (Neo and Lut1 and the Chls

strongly coupled to them) are the molecular origin of the observed energetic and dynamical changes in the membrane. On the other hand, Lut2 is found to be completely immune to the introduction of the lipid bilayer, maintaining its light-harvesting role as the principal energy donor to the Chls [67]. While the nanodisc platform cannot fully replicate the complex architecture of the native thylakoid membrane in the chloroplast, these observations show that Car conformation is readily modulated by interaction with the surrounding local environment, which can impact the excited-state dynamics, and potentially enhance dissipative pathways. Consistent with these experimental results, a recent theoretical work found that even a $5 - 10^{\circ}$ tilt in the Car backbone causes a 50% drop in the fluorescence lifetime of LHCII, highlighting the integral role of Car conformations on the photophysics of LHCII under varying light conditions [68].

It is interesting to note that the two strongly perturbed peripheral domains identified herein correspond to two of the proposed photoprotective quenching sites in LHCII from previous work. Twisting of the conjugated chain of Neo has been postulated as a potential mechanism for quenching in crystals of LHCII based on a correlation between the twist and quenching [221]. Furthermore, Lut1 was speculated to undergo a conformational change that opens up a quenching site with the terminal Chl *a*'s in aggregated LHCIIs [66, 122]. Here, quenching is observed even in the non-aggregated, individual trimeric LHCIIs through the reduced fluorescence lifetime of 2.8 ns and the associated dissipative photophysics. This suggests that the native structure of LHCII trimers enhances quenching upon environmental perturbation, which may be a similar effect to that observed in LHCII aggregates. Considering that the two strongly perturbed pigment domains would be located at the interface of adjacent LHCII trimers *in vivo*, protein-protein interactions in the native system may introduce a similar effect and further amplify the structural and photophysical modulations observed here. These interactions may be either between multiple neighboring LHCIIs or between LHCII and the photosystem II subunit S (PsbS), which is a non-pigment binding protein required for quenching *in vivo*, potentially via induction of a conformational change in LHCII [26, 129]. In order for a dissipative pathway to

be relevant for photoprotection, it must be activable under high light conditions, and these interactions may be the mechanism behind activation.

4.9 Conclusion

In this chapter, I benchmarked the dynamics and pathways of light harvesting and dissipation in LHCII embedded within a near-native membrane environment. Two dissipative pathways were identified and characterized, both of which utilize the dark Car S_1 state as energy sink. One of these dissipative pathways, sub-picosecond energy transfer from the terminal Chl locus to the Car S_1 state, was directly uncovered for the first time. The observation of this hypothesized, but previously uncharacterized dissipative pathway opens the door to studies of its role in photoprotection that takes place *in vivo*. Furthermore, comparison of the photophysics of LHCII in non-native detergent and near-native membrane environments provides evidence that dissipation is enhanced in the membrane, likely through an increase in the population of a quenched conformation via perturbation of two peripheral pigment clusters. These results point to the ability of the local environment to control the conformation and dynamics − and therefore function − of the photosynthetic apparatus in green plants.

4.10 Materials and Methods

4.10.1 Sample Preparation

Trimeric LHCII complexes were extracted from spinach leaves, purified and characterized as detailed in Appendix A, Section A.1. The detergent-solubilized sample was prepared by thawing the purified LHCII aliquots stored at −80°C and adjusting the concentration in a 0.01 M HEPES, 0.02 M NaCl buffer solution (pH 7.5) containing 0.03% *n*-dodecyl α-D-maltopyranoside (α-DM). Membrane nanodiscs containing a single trimeric LHCII were prepared following the protocols reported in [146] and [147] with minor modifications, with MSP1E3D1 as the membrane scaffold protein and soy asolectin lipid. Control samples were also prepared and comparatively charac-

terized in order to verify the absence of undesired interactions between LHCII and the membrane scaffold protein or lipid-dependent photophysical behaviors, as discussed in detail in Section 4.11.1. A detailed protocol for nanodisc production is provided in Appendix A, Section A.2. The 2DES data reported in this chapter were from the measurements of LHCII nanodiscs with MSP1E3D1 membrane scaffold protein and asolectin lipid. The final optical density (OD) of both detergent-solubilized and nanodisc samples used for 2DES was 0.45 (per 0.2 mm) at the Chl *a* Q_y peak (675 nm).

4.10.2 Steady-State Spectroscopy

Linear absorption and steady-state fluorescence spectra were measured with a Cary 5000 spectrophotometer and a Cary Eclipse fluorimeter (Agilent), respectively, in 1 cm pathlength quartz cuvettes. For fluorescence measurements, the OD of the sample at the excitation wavelength was kept at $0.05 - 0.07$ per cm to ensure absence of any reabsorption effect. Excitation wavelengths of 436, 600, and 640 nm were used, and no excitation wavelength dependence was found in the fluorescence spectra. Relative fluorescence quantum yield of LHCII in nanodiscs compared to LHCII in detergent was calculated by comparing the integrated area of the fluorescence spectrum normalized by the OD at the excitation wavelength. CD spectra were measured at 20°C on a Jasco J-1500 spectropolarimeter, in a 1 mm pathlength quartz cuvette. The OD of the sample was 0.08 per mm at 670 nm.

4.10.3 Fluorescence Lifetime Measurement

The fluorescence lifetime of LHCII was measured with time-correlated single photon counting (TCSPC). The excitation source was generated by focusing the output of a Ti:sapphire laser (Vitara-S, Coherent, centered at 800 nm, 80 MHz repetition rate) into a nonlinear photonic crystal fiber (FemtoWhite 800, NKT Photonics). The generated broadband supercontinuum was then filtered with a $630 - 655$ nm bandpass filter (ET645/30x, Chroma) to produce the excitation laser spectrum (Figure 4-10,

II). The excitation beam was focused on a 1 mm pathlength quartz cuvette containing the sample. The emission from the sample was detected at a 90° angle from the excitation path. A 665.2 nm longpass emission filter (BLP01-647R-25, Semrock) was used to remove scattered excitation light (Figure 4-10, **IV**). A single-photon-detecting avalanche photodiode (PDM Series, Micro Photon Devices) was connected to a timing module (PicoHarp 300, PicoQuant), which detects the arrival time of each photon. The instrument response function (IRF) was determined by measuring scattered excitation light using a dilute solution of colloidal silica (Ludox, MilliporeSigma) [279], and had a width of 50 ps. Fluorescence decay curves were individually fitted with a monoexponential or biexponential decay function with the IRF using iterative reconvolution. To prevent reabsorption effect, the OD of all samples at the excitation wavelength range was kept at ∼0.07 per mm. The excitation pulse energy was 10 fJ for all samples.

4.10.4 Fluorescence Correlation Spectroscopy

FCS measurements were performed on a home-built confocal microscope. The excitation source was generated by tuning the wavelength of a fiber laser (FemtoFiber pro, Toptica Photonics; 80 MHz repetition rate), and was centered at 610 nm with a 4 nm FWHM bandwidth (Figure 4-10, **I**). The fluorescence signal was isolated using a dichroic mirror (T635lpxr, Chroma) and a bandpass filter (ET700/75m, Chroma; **III** in Figure 4-10). The sample solution at 5 nM concentration was allowed to freely diffuse within a 25 mm diameter hybridization chamber sealed to a glass cover slip. Sample excitation and collection of the fluorescence were accomplished by the same oil-immersion objective (UPLSAPO100XO, Olympus; NA = 1.4). The excitation laser fluence on the sample plane was 504 nJ per cm^2. Fluorescence signal was detected using an avalanche photodiode (SPCM-AQRH-15, Excelitas). The diffusion time constant (τ_D) was determined by fitting the autocorrelation of the detected photons ($G(t)$, typically $2{\times}10^6$ photons were collected to construct each correlation

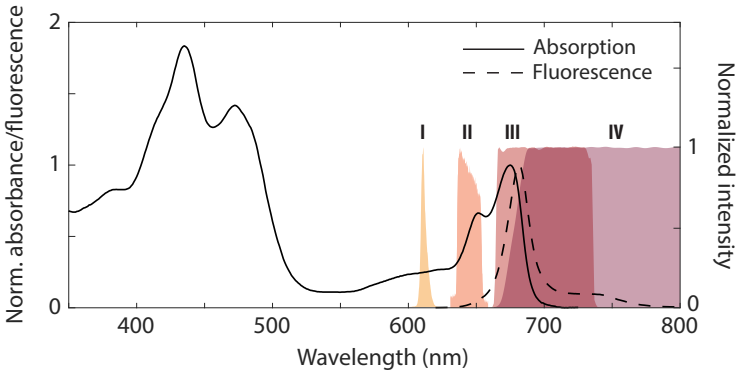

Figure 4-10: **Experimental condition for TCSPC and FCS measurements.** Transmission spectra of the excitation (**I** for FCS, **II** for TCSPC) and emission (**III** for FCS, **IV** for TCSPC) filters overlaid with the absorption (black solid line) and fluorescence (black dashed line) spectra of LHCII.

curve) to Eq. (4.1) [280],

$$G(t) = C + \left(\frac{1}{N}\right)\left(\frac{1}{1+\frac{t}{\tau_{\mathrm{D}}}}\right)\left(\frac{1}{\sqrt{1+\frac{t}{V^2\tau_{\mathrm{D}}}}}\right)\left(1 - f_{\mathrm{T}} + f_{\mathrm{T}}\mathrm{e}^{\frac{-t}{\tau_{\mathrm{T}}}}\right) \tag{4.1}$$

where t is the correlation time, C is a constant, N is the number of molecules in the focal volume, τ_{D} is the diffusion time constant, V is a measure of the detection volume defined as Z_o/w_o, where Z_o and w_o are the effective half axial and radial dimensions of the focal volume, respectively, f_{T} is the fractional population of the triplet state, and τ_{T} is the triplet lifetime. The diffusion constant (D) and the hydrodynamic radius (r) of each sample were determined using Eqs. (4.2) and (4.3) (the Stokes-Einstein relation):

$$\tau_{\mathrm{D}} = \frac{{w_o}^2}{4D} \tag{4.2}$$

$$D = \frac{k_B T}{6\pi\eta r} \tag{4.3}$$

where k_B is the Boltzmann constant, T is the temperature ($T = 20°\mathrm{C}$ was used in this work), and η is the viscosity of the medium.

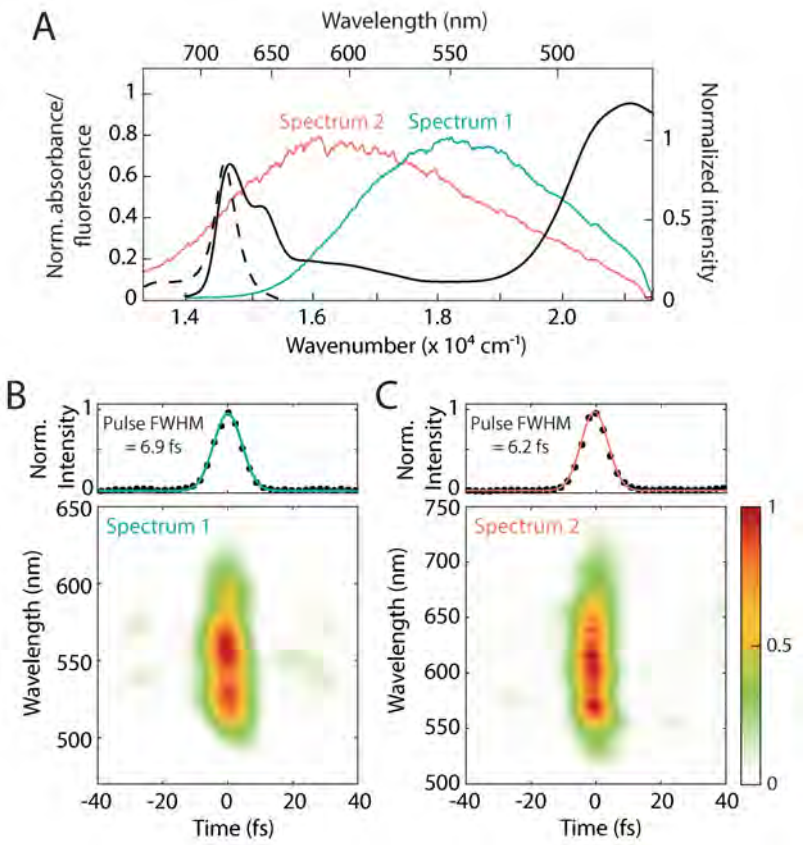

Figure 4-11: **Spectral and temporal profiles of the laser pulses used in 2DES.** (A) Ultrabroadband laser spectra used in 2DES overlaid with the linear absorption (black solid) and fluorescence spectra (black dashed) of LHCII. (B)−(C), TG-FROG trace of (B) spectrum 1 and (C) spectrum 2 with the retrieved temporal profiles (filled circles) fitted with a Gaussian function (solid line).

4.10.5 Ultrabroadband Two-Dimensional Electronic Spectroscopy

A detailed description of the ultrabroadband 2DES setup is provided in Chapter 2 and in [226]. The supercontinuum generated by argon filamentation was further filtered by two different sets of glass bandpass filters for optimal excitation of the blue (Car S_2; FGB39, Thorlabs) and red (Chl Q_x/Q_y; three FGS600 filters, Thorlabs) wavelength range of the LHCII absorption spectrum (Figure 4-11A). Spectrum 1 is centered at 550 nm (18,182 cm^{-1}) with a FWHM of 113 nm (3,819 cm^{-1}), and spectrum 2 is centered at 614 nm (16,287 cm^{-1}) with a FWHM of 168 nm (4,807 cm^{-1}). Transient grating frequency resolved optical gating (TG-FROG) measured a pulse duration of 6.9 fs and 6.2 fs for spectrum 1 and spectrum 2, respectively (Figure 4-11B, C).

A pulse energy of 10 nJ was employed with a beam waist of 150 μm at the sample position, corresponding to an excitation density of $3.9-4.4\times10^{13}$ photons per pulse per cm^2, previously reported to be in the linear regime [94]. τ was sampled in 0.4 fs steps in the range of $-200-200$ fs, resulting in a 43.8 cm^{-1} resolution of the ω_τ axis. T was incremented in steps of 33 fs for $T=-99-0$ fs, 10 fs for $T=0-100$ fs, 33 fs for $T=100-467$ fs, 67 fs for $T=467$ fs $-$ 1 ps, and 1 ps for $T=1-8$ ps (dataset with spectrum 1) or $T=1-10$ ps (dataset with spectrum 2). The frequency resolution of the ω_t axis was 4.2 cm^{-1}. At each T, for each τ, 1,280 lines of each chopper sequence of the dual chopping data acquisition scheme were collected and averaged. The sample was circulated in a 0.2 mm pathlength quartz flow cell with a peristaltic pump to prevent photodegradation and repetitive excitation of the same spot. The sample reservoir was kept at 4°C throughout the measurement with a home-built water jacket cooling system. Each dataset was collected three times, on separate days with freshly prepared samples, to ensure reproducibility of the data. The integrity of the sample was confirmed by comparing the linear absorption spectra and fluorescence decay profiles before and after collection of each dataset.

4.10.6 Analysis of Two-Dimensional Spectra

Each waiting time trace reported here was generated by integrating the 2D signal intensity over finite frequency intervals in both frequencies (100 cm^{-1} in $\omega_\tau\times$ 100 cm^{-1} in ω_t, unless otherwise noted) around the center frequencies reported in parentheses (ω_τ, ω_t). Time constants were extracted by fitting each waiting time trace to an exponential function convolved with a Gaussian pulse with the time resolution (6.2 fs or 6.9 fs) of the experiment.

4.11 Supplementary Information

4.11.1 Supplementary Characterizations of Nanodiscs

Absence of direct interactions between peripheral regions of LHCII and the membrane scaffold protein

It is possible that undesired interactions take place between the peripheral regions of LHCII and the membrane scaffold protein (MSP3E3D1) due to the limited membrane surface area and the close proximity between them. To evaluate whether such interactions are present, the photophysical properties of LHCII nanodiscs of two different sizes were compared.

In addition to the ∼13 nm nanodiscs formed with MSP1E3D1 membrane scaffold protein, larger nanodiscs were produced with ApoE422K membrane scaffold protein that afford a ∼25 nm diameter, and thus have a larger membrane area, reducing the probability of direct interactions between LHCII and the membrane scaffold protein [281]. As shown in Figure 4-12, the absorption and fluorescence properties of LHCII nanodiscs are independent of the size, *i.e.*, membrane area of the nanodiscs, indicating that the interactions between LHCII and the lipid bilayer is the origin of the observed changes in the photophysics of LHCII upon membrane insertion.

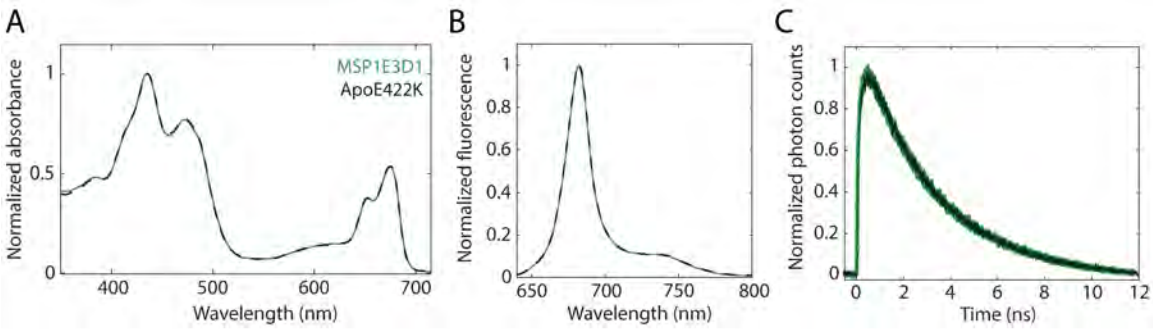

Figure 4-12: **Comparison of the photophysical properties of LHCII nanodiscs with MSP1E3D1 and ApoE422K membrane scaffold proteins.** (A) Normalized linear absorption spectra, (B) fluorescence spectra, and (C) fluorescence decay traces with MSP1E3D1 nanodiscs as green and ApoE422K nanodiscs as dark green.

Lipid dependence of the photophysical properties of LHCII nanodiscs

To examine lipid dependence of the observed photophysical changes in LHCII upon membrane incorporation as well as achieve a closer mimic of the native lipid composition of the plant thylakoid membrane, nanodisc assembly reactions were performed with several different lipid mixtures. The asolectin lipid, which is the main lipid used for nanodisc production in this work due to its low cost, is a mixture of phospholipids. However, phospholipids are not the predominant component of the native thylakoid membrane. In order to more closely mimic the lipid composition of the native thylakoid membrane, nanodisc assembly reactions with glycolipids, which are the predominant type of lipids *in vivo* [282, 283], were performed. Two different mixtures of the four major components, monogalactosyldiacylglycerol (MGDG), digalactosyldiacylglycerol (DGDG), sulfoquinovosyldiacylglycerol (SQDG), and phosphatidylglycerol (PG), were utilized: 62% DGDG, 17% SQDG, 21% PG and 50% MGDG, 27% DGDG, 12% SQDG and 11% PG. The latter mixture contains a non-bilayer lipid MGDG, which is known to display distinct behaviors from the other three, which are bilayer lipids [284, 285].

The CD and fluorescence decay profiles of LHCII nanodiscs with the three lipid mixtures were compared, as shown in Figures 4-13, 4-14 and Table 4.1. Neither the CD spectra nor the fluorescence decay profiles reveals non-negligible lipid dependence, leading to the conclusion that the changes in LHCII photophysics upon membrane insertion are caused by introduction of the membrane environment, not by specific protein-lipid interactions. Furthermore, the absence of lipid dependence demonstrates the validity of asolectin as an economical alternative for LHCII nanodisc assembly to glycolipids.

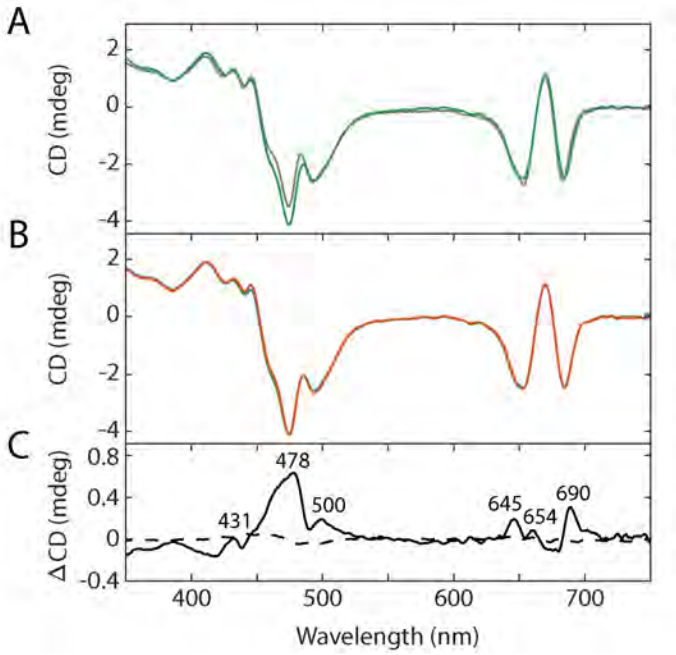

Figure 4-13: **Comparison of CD spectra in different environments.** (A) Comparison between detergent-solubilized (gray) and nanodisc-embedded LHCII (green) with soy asolectin lipid. (B) Comparison between soy asolectin nanodiscs (green) and native thylakoid lipid nanodiscs (orange, 50% MGDG, 27% DGDG, 12% SQDG and 11% PG). The spectra in (A) and (B) are normalized to the sample absorbance at 675 nm. (C) Difference CD between detergent and soy asolectin nanodiscs in (A) (solid line) showing the effect of membrane environment. Dashed line shows the difference CD between soy asolectin and native thylakoid lipid nanodiscs, indicating independence of the CD response on the lipid mixture used.

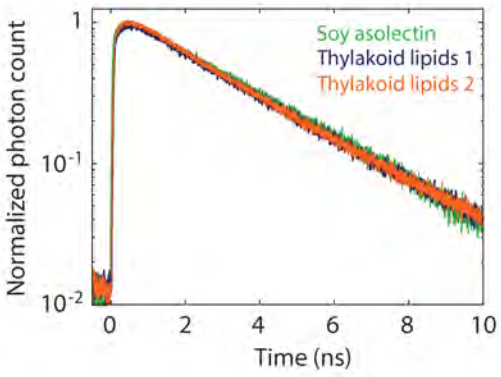

Figure 4-14: **Lipid independence of the fluorescence dynamics of LHCII nanodiscs.** Overlay of the fluorescence profiles of LHCII nanodiscs prepared with different lipids. Green: soy asolectin, dark blue: thylakoid lipid mixture 1 (62% DGDG, 17% SQDG, 21% PG), orange: thylakoid lipid mixture 2 (50% MGDG, 27% DGDG, 12% SQDG and 11% PG).

4.11.2 Supplementary Figures and Tables

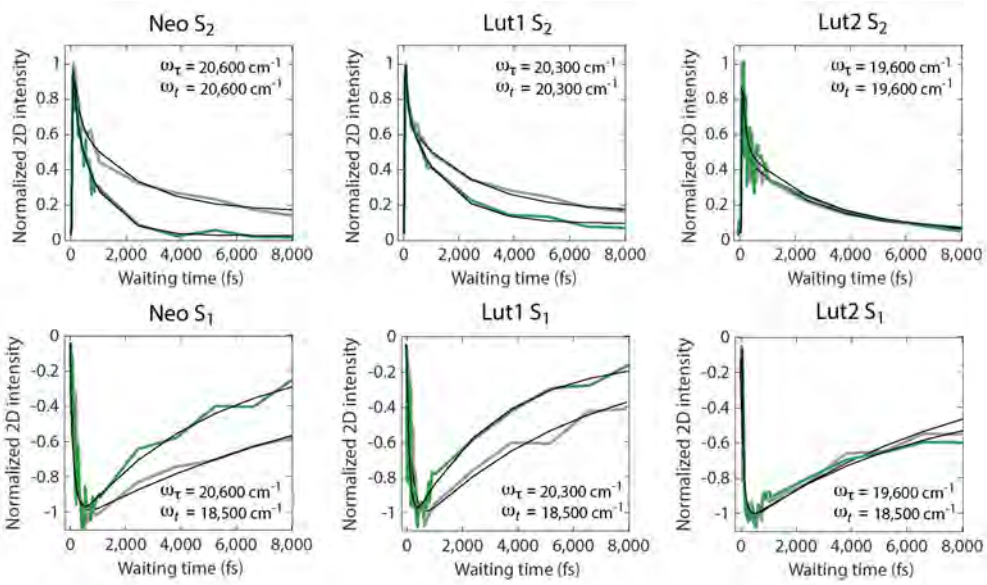

Figure 4-15: **Waiting time traces of Car S_2/S_1 peaks.** Gray and green traces correspond to LHCII in detergent and in membrane discs, respectively. All traces were generated by integrating the 2D intensity over frequency intervals of 100 cm^{-1} (ω_τ) $\times$ 100 cm^{-1} (ω_t) around the center frequencies specified in each figure. Fit parameters are listed in Table 4.2.

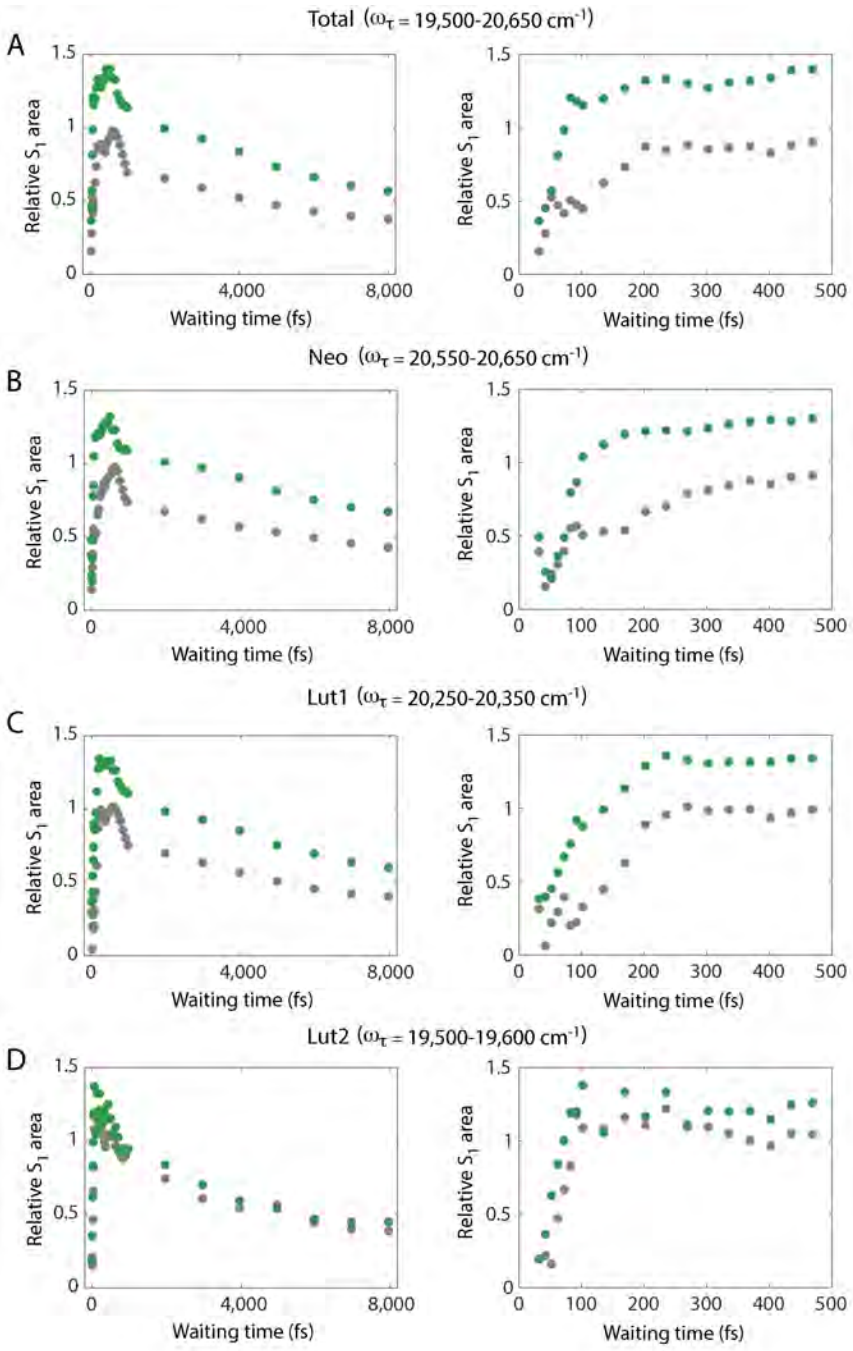

Figure 4-16: **Relative area of Car S_1 ESA normalized to the initial S_2 population.** Traces in detergent and in membrane discs are shown in gray and green, respectively. Relative S_1 areas are calculated by normalizing the S_1 ESA intensity at each T to the initial S_2 GSB intensity at $T = 30$ fs. Right panels show zoom-ins of the initial 500 fs. (A) shows the ratio between the total integrated area using the broad ω_τ range as indicated in the figure. (B)−(D) are calculated with narrower ω_τ ranges to account for the response from the three individual Cars. Fixed ranges of $\omega_t = 19,200 - 21,000$ cm^{-1} (S_2 GSB, for both detergent and membrane) and $17,500 - 18,700$ cm^{-1} (S_1 ESA, detergent)/$17,700 - 18,900$ cm^{-1} (S_1 ESA, membrane) were used.

Table 4.1: **Fitted parameters from fluorescence lifetime measurements.**

Sample	A_1 (%)[a]	τ_1 (ns)[b]	A_2 (%)	τ_2 (ns)	$< \tau_{fl} >$[c]
Detergent	–	–	1.00	3.4	3.4
Nanodisc (asolectin)	0.09	0.3	0.91	3.1	2.8
Nanodisc (thylakoid lipids 1)[d]	0.10	0.3	0.90	3.1	2.8
Nanodisc (thylakoid lipids 2)[d]	0.10	0.3	0.90	3.1	2.8

[a] Normalized amplitude in percentage.
[b] Fitted time constant.
[c] Average fluorescence lifetime calculated by weighted average of the fitted components.
[d] Thylakoid lipids 1: 62% DGDG, 17% SQDG, 21% PG, thylakoid lipids 2: 50% MGDG, 27% DGDG, 12% SQDG and 11% PG.

Table 4.2: **Fitted parameters from Car S_2/S_1 region of 2D spectra.**

		A_1[a]	τ_1 (fs)[b]	A_2	τ_2 (fs)
Detergent	Neo S_2	0.42	115 ± 10	0.58	3,040 ± 300
	Lut1 S_2	0.32	110 ± 25	0.68	2,500 ± 270
	Lut2 S_2	0.56	80 ± 25	0.44	2,630 ± 570
	Neo S_1	-0.46	200 ± 50	0.54	10,000 ± 2,660
	Lut1 S_1	-0.36	160 ± 30	0.64	6,220 ± 1,080
	Lut2 S_1	-0.25	135 ± 27	0.75	7,100 ± 1,900
Nanodisc	Neo S_2	0.49	63 ± 8	0.51	1,255 ± 150
	Lut1 S_2	0.38	100 ± 20	0.62	1,458 ± 138
	Lut2 S_2	0.50	88 ± 17	0.50	2,600 ± 550
	Neo S_1	-0.49	130 ± 33	0.51	4,620 ± 1,000
	Lut1 S_1	-0.42	110 ± 25	0.58	2,900 ± 600
	Lut2 S_1	-0.30	125 ± 25	0.70	7,150 ± 1,860

[a] Normalized amplitude in percentage. Negative amplitude indicates exponential rise.
[b] Fitted time constant with 90% confidence interval.

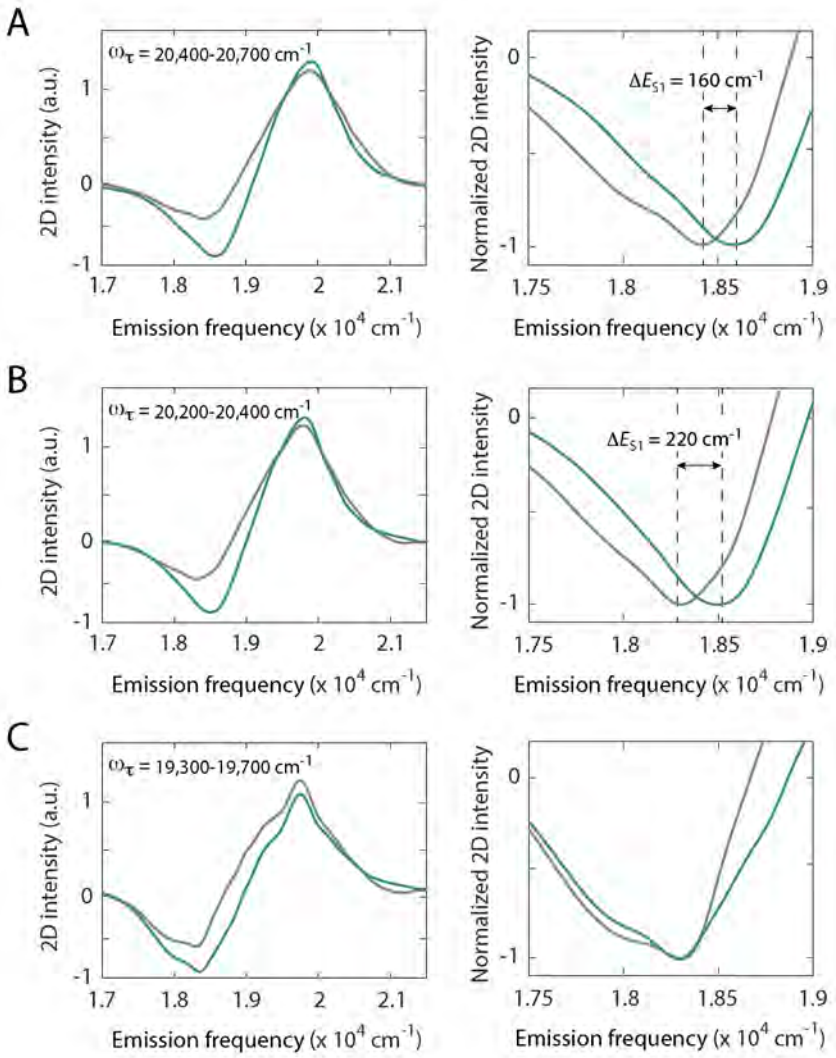

Figure 4-17: **S_1 energy shift of the Cars.** Projection of the 2D spectra at $T = 500$ fs onto the ω_t axis for ω_τ ranges indicated inside each figure on the left column, which are the excitation frequencies for (A) Neo, (B) Lut1, and (C) Lut2, respectively. Right column shows a closer view of the ESA, where both traces are normalized to the same scale. Gray and green traces correspond to LHCII in detergent and in membrane discs, respectively.

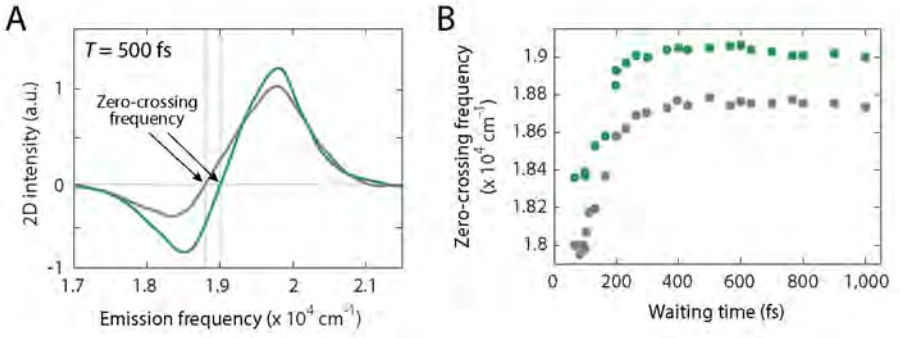

Figure 4-18: **Vibrational cooling dynamics of the Cars.** (A) is a replicate of Figure 4-5F with guidelines (light gray) added to show the definition of the zero-crossing frequency. (B) shows the evolution of the zero-crossing frequency over time for the first 1,000 fs. Gray trace corresponds to detergent-solubilized and green to disc-embedded sample, respectively.

Table 4.3: **Fitted parameters from Chl Q_y region of 2D spectra.**

		A_1[c]	τ_1 (fs)[d]	A_2	τ_2 (fs)
Detergent	1 (Chl *b* Q_y)	0.67	240 ± 20	0.33	2,950 ± 360
	2 (Chl a_H Q_y)	0.33	168 ± 20	0.67	2,670 ± 350
	3 (Chl a_L Q_y)	–	–	1.00	3,085 ± 400
	4 ($b \rightarrow a_H$ transfer)	-0.48	80 ± 20	0.52	4,400 ± 600
	5 ($a_H \rightarrow a_L$ transfer)	-0.38	90 ± 23	0.62	9,550 ± 2,500
	6 ($b \rightarrow a_L$ transfer)	-0.47	130 ± 20	0.53	8,300 ± 1,600
	Chl SE [a]	0.39	350 ± 30	0.61	4,100 ± 450
	Car S_1 ESA[b]	-0.33	300 ± 60	0.67	7,645 ± 500
Nanodisc	1 (Chl *b* Q_y)	0.58	400 ± 35	0.42	2,970 ± 340
	2 (Chl a_H Q_y)	0.33	165 ± 20	0.67	2,930 ± 420
	3 (Chl a_L Q_y)	0.39	195 ± 30	0.61	2,600 ± 375
	4 ($b \rightarrow a_H$ transfer)	-0.37	132 ± 22	0.63	4,900 ± 950
	5 ($a_H \rightarrow a_L$ transfer)	-0.40	105 ± 20	0.60	10,400 ± 2,500
	6 ($b \rightarrow a_L$ transfer)	-0.38	225 ± 20	0.62	8,680 ± 1,300
	Chl SE [a]	0.53	270 ± 20	0.47	3,270 ± 300
	Car S_1 ESA[b]	-0.45	220 ± 50	0.55	3,810 ± 350

[a] Integrated over the area $\omega_\tau = 14,775 - 15,075$ cm^{-1}, $\omega_t = 14,270 - 14,670$ cm^{-1}.
[b] Integrated over the area $\omega_\tau = 14,775 - 15,075$ cm^{-1}, $\omega_t = 18,200 - 18,600$ cm^{-1}.
[c] Normalized amplitude in percentage. Negative amplitude indicates exponential rise.
[d] Fitted time constant with 90% confidence interval.

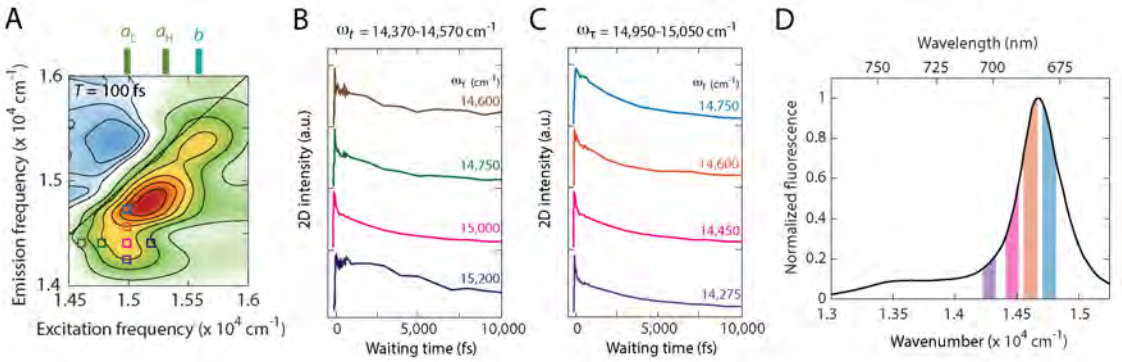

Figure 4-19: **Frequency dependence of the low-energy Chl *a* decay.** Waiting time traces of terminal Chl *a* SE monitored as a function of (B) excitation frequency (ω_t fixed at $14,370 - 14,570$ cm^{-1}) and (C) emission frequency (ω_τ fixed at $14,950 - 15,050$ cm^{-1}). The peak positions at which the time traces are plotted are labeled with color-coded open squares in (A), and indicated in (B) and (C). All traces are normalized to the same scale, and vertically offset for clarity. Only detergent data are shown, but the same trends were observed in nanodiscs. (D) Overlay of the steady-state fluorescence spectrum of LHCII with the probe ranges shown in (C).

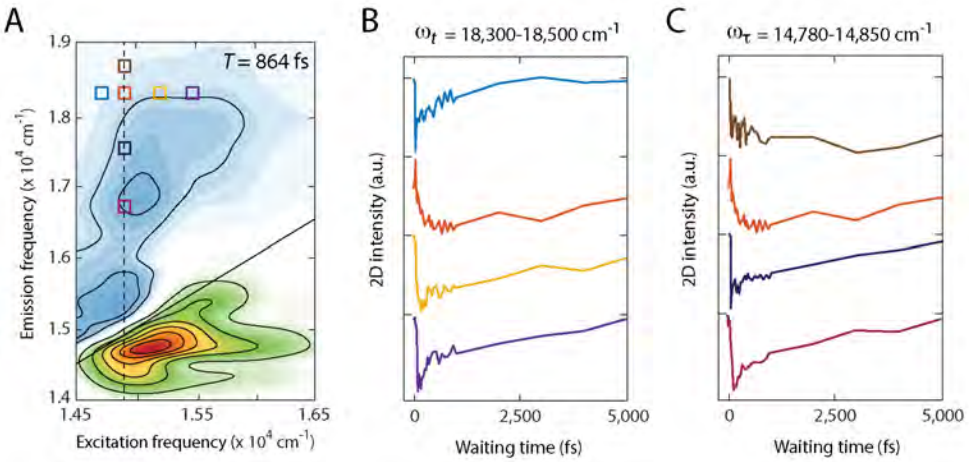

Figure 4-20: **Waiting time traces of Chl *a* ESA.** Waiting time traces of ESA monitored as a function of (B) excitation frequency (ω_t fixed at $18,300 - 18,500$ cm^{-1}) and (C) emission frequency (ω_τ fixed at $14,780 - 14,850$ cm^{-1}). The peak positions at which the time traces are plotted are labeled with color-coded open squares in (A). All traces are normalized to the same scale, and vertically offset for clarity. Only detergent data are shown, but the same trends were observed in nanodiscs.

Chapter 5

Impact of Zeaxanthin on the Dissipative Photophysics of Light-Harvesting Complex II in the Membrane Nanodisc Environment

Adapted from: Son, M., Pinnola, A. & Schlau-Cohen, G. S. "Zeaxanthin Independence of Photophysics in Light-Harvesting Complex II in a Membrane Environment", *Biochim. Biophys. Acta − Bioenerg.* **1861**, 148115 (2020).

5.1 Chapter Summary

This chapter describes the investigation of zeaxanthin (Zea)- and pH dependence of dissipative photophysical pathways in light-harvesting complex II (LHCII), two of the molecular parameters known to be responsible for the induction of photoprotective dissipation. Photoprotective dissipation in green plants is activated by a drop in the luminal pH of the plant thylakoid membrane. This reduction in pH triggers (1) conformational changes of the antenna complexes, which activate quenching channels and (2) de-epoxidation of violaxanthin (Vio) into Zea. Therefore, the amplitude of non-photochemical quenching (NPQ) *in vivo* has been shown to increase in the

presence of Zea and at low pH. *In vitro* studies on LHCII compared different solubilization environments, which give rise to different levels of quenching and so partially mimic NPQ *in vivo*. However, in these studies both completely Zea-independent and Zea-dependent quenching have been reported, potentially due to the multiplicity of solubilization environments. In this chapter, I characterize the Zea dependence of the photophysics in LHCII in the membrane environment by incorporating dark-adapted (Vio-binding) and *in vitro* de-epoxidized (Zea-binding) forms of LHCII into nanodiscs, representative of the low-light and high-light conditions *in vivo*, respectively. Using ultrabroadband two-dimensional electronic spectroscopy (2DES) and building on the ultrafast dissipative pathways identified in Chapter 4, I compare the amplitude and timescales of dissipative photophysics in these two systems, in particular the chlorophyll (Chl)-to-carotenoid (Car) energy transfer pathway. To mimic the acidification of the plant thylakoid membrane under high light conditions, pH dependence of the photophysics was also examined. The data reveal that the amplitude of quenching as well as the dissipative photophysics are unaffected by Zea or pH at the level of individual LHCIIs, suggesting that Zea-dependent quenching is independent of the membrane-activated quenching channels identified in Chapter 4. Furthermore, the results presented here demonstrate that additional factors beyond Zea accumulation in LHCII are required for full development of NPQ.

5.2 Introduction

The light-harvesting apparatus of photosystem II in green plants consists of a dense array of pigment-binding membrane proteins called antenna complexes. The antenna complexes capture solar energy and deliver the absorbed energy to the reaction center, where charge separation occurs [4, 5]. Under high-light (*i.e.*, sunny) conditions, the rate of light absorption exceeds the capacity of the reaction center, which can lead to photooxidative damage via the production of deleterious photoproducts such as singlet oxygen [104, 105]. To prevent damage, the light-harvesting apparatus has evolved a dynamic feedback system in which the antenna complexes rapidly and

reversibly interconvert between a light-harvesting and a quenched state. In the latter, excess energy is dissipated as heat, a process known as NPQ [69, 106, 107]. Extensive *in vivo* measurements have established the existence of NPQ and demonstrated that it is critical for fitness. However, *in vitro* measurements of NPQ have yielded conflicting results, and thus have been unable to identify the photophysical mechanisms.

NPQ is known to be activated by the buildup of a proton gradient (ΔpH) across the thylakoid membrane from acidification of the lumen under high-light conditions [106, 117]. The ΔpH induces (1) conformational changes of the antenna complexes into a quenched form, mediated by a non-pigment-binding pH sensor protein, photosystem II subunit S (PsbS) [125–130] and (2) activation of the xanthophyll cycle, where Vio is reversibly de-epoxidized to Zea by violaxanthin de-epoxidase (VDE) [109, 110, 286]. Therefore, the presence of Zea and low pH are implicated as two of the factors that activate NPQ *in vivo*. While these two factors have been identified, whether they primarily impact function at the level of individual antenna complexes or via mediating changes to protein-protein interactions remains unclear.

The contribution of Zea to NPQ has been confirmed with studies showing a correlation between Zea content and the extent of NPQ *in vivo* [112, 113]. To disentangle its contribution, *in vitro* measurements on isolated antenna complexes with and without Zea have been performed, focusing on LHCII, the major antenna complex in plants. Each monomeric subunit of the trimeric LHCII complex has a binding site for the xanthophyll cycle Car (V1). This binding site is located at the monomer-monomer interface (Figure 5-1A) [17]. In contrast to the *in vivo* results, *in vitro* measurements on LHCII reported a negligible dependence of NPQ on Zea, leaving the amplitude and mechanisms of Zea-dependent quenching, if any, undetermined at the level of individual antenna complexes [134, 232, 287, 288].

One challenge in comparing *in vivo* and *in vitro* results is the multiplicity of the solubilization environments used to accommodate the membrane-bound antenna complexes, which introduce different levels of quenching [143, 149]. Antenna complexes solubilized in detergent are considered to be in the fully unquenched state. However, detergent environments can induce non-native conformational changes [40, 143], and

thus may not represent the true *in vivo* state of the protein. Aggregation of the antenna complexes in low levels of detergent produces a quenched state, which has been commonly used to mimic the quenched conformation of the protein [253]. However, it has not been determined whether the conformation and dissipative pathways that result from aggregation are the physiological ones. Experiments have demonstrated that incorporating LHCII alone into a near-physiological membrane environment produces a partially quenched state [146, 147, 289, 290]. Whether the quenching that emerges in the membrane depends on Zea has not been measured, because previous measurements were limited to detergent-solubilized antenna complexes. This limitation, and the resultant conflicting results on the Zea dependence of NPQ, necessitate a careful characterization of the Zea dependence while maintaining a near-physiological membrane environment.

In this work, I characterize how the presence of Zea impacts the photophysics and amplitude of dissipation in an individual LHCII embedded in a nanodisc. Nanodiscs containing a dark-adapted, Vio-binding LHCII (LHCII-Vio) and an *in vitro* de-epoxidized, Zea-binding LHCII (LHCII-Zea) were assembled. The conformation and photophysics of LHCII-Vio and LHCII-Zea were compared at two different pH levels that mimic the low-light and high-light conditions using steady-state and time-resolved absorption and fluorescence spectroscopies. The data reveal no differences in the conformation or the photophysics between LHCII-Vio and LHCII-Zea, indicating that the dissipative pathways enhanced in the membrane are different from the Zea-dependent ones observed *in vivo*. These observations suggest that accumulation of Zea is not sufficient for pH-activated quenching at the level of individual LHCIIs even in the membrane, and that protein-protein interactions are likely required for activation of NPQ.

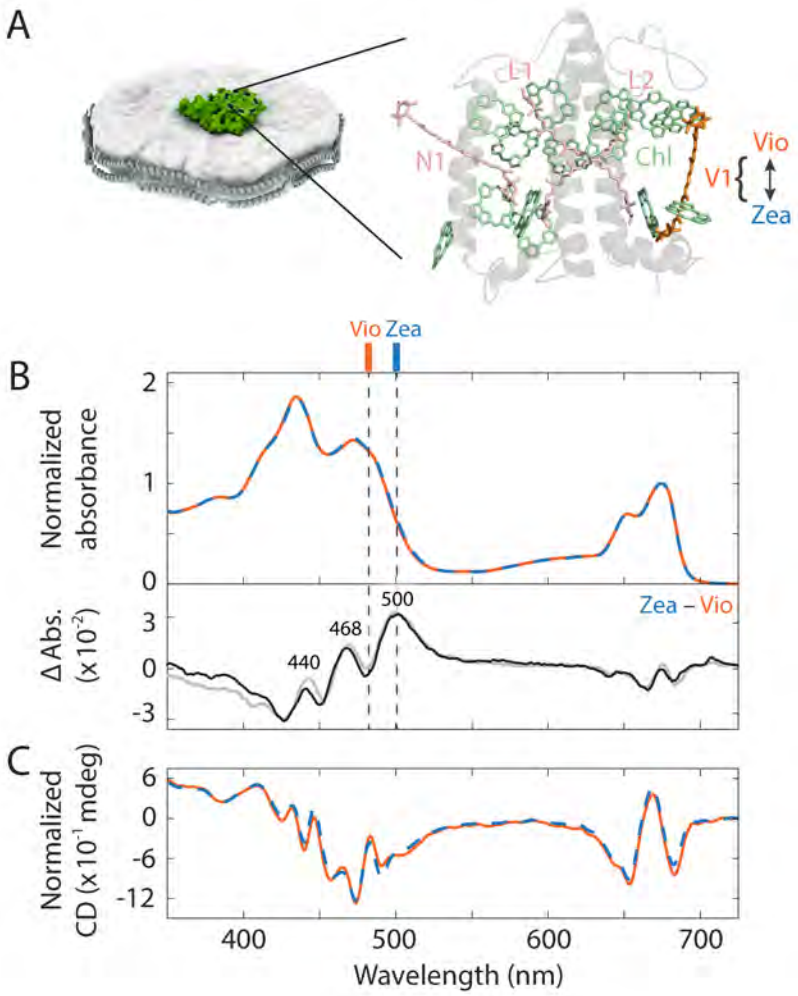

Figure 5-1: **Structure and absorption properties of LHCII-Vio and LHCII-Zea in membrane nanodisc.** (A) Cartoon illustration of the membrane nanodisc with an LHCII trimer inserted. A detailed view of a monomeric subunit (dashed oval) is shown on the right. The Vio/Zea-binding site V1 is highlighted in orange, and the other Car-binding sites are displayed in light pink. N1, L1, L2 are the binding sites for neoxanthin (Neo) and luteins (Lut1 and Lut2), respectively. The protein scaffold and Chls (without phytol tails) are displayed in gray and light green. (B) Linear absorption (normalized at 675 nm, top) and difference absorption spectra (bottom) of LHCII-Vio (orange) and LHCII-Zea (blue, dashed) in the membrane nanodisc, pH 7.5. The difference spectrum is obtained by subtracting the normalized LHCII-Vio absorption spectrum from that of LHCII-Zea. For comparison, the difference absorption spectrum measured in detergent is displayed in gray. Stick plots indicate the absorption wavelength of the S_2 (0−0) state of Vio and Zea. (C) CD spectra of LHCII-Vio (orange) and LHCII-Zea (blue, dashed) in the membrane nanodisc, pH 7.5. Both spectra are normalized to their respective absorbance at 675 nm.

5.3 Zeaxanthin Independence of Steady-State Spectra and Fluorescence Lifetime

Figure 5-1B shows the linear absorption spectra of LHCII-Vio and LHCII-Zea in the membrane nanodisc environment. Comparison of the spectra reveals subtle changes in peak position and intensity, predominantly in the Car S_2 absorption range (400−500 nm). The vibronic pattern at 440, 468, and 500 nm with an energy spacing of ∼1370 cm^{-1} observed in the difference absorption spectrum is consistent with the vibronic structure of Zea [232, 291]. This vibronic progression is also observed in the difference absorption spectrum in detergent, verifying that the weakly-binding Zea is retained during membrane insertion. The Zea S_2 (0−0) absorption red-shifts by 15 nm (600 cm^{-1}) from that of Vio due to an increase in the conjugation length upon de-epoxidation [49]. The Chl Q_y absorption range (630−700 nm) exhibits minor changes that likely originate from Chls *a*613 and *a*614, which are the Chls that most strongly couple to the Car bound to the V1 site [262]. Difference absorption spectra between detergent and the membrane environment were also calculated for LHCII-Vio and LHCII-Zea (Figure 5-2). The overall shape and intensity of the difference spectra, regardless of the xanthophyll cycle Car, are nearly identical, suggesting that the electronic structures of Vio and Zea exhibit comparable sensitivity to the membrane environment.

Circular dichroism (CD) spectra were measured to examine the spatial arrangement and interactions of the pigments in LHCII-Vio and LHCII-Zea in the membrane environment [143]. Comparison of the CD spectra of LHCII-Vio and LHCII-Zea in the membrane reveals negligible differences, suggesting that the conformation of the xanthophyll cycle Car is preserved during (de-)epoxidation (Figure 5-1C). Only minor changes in the CD intensity were observed in the 400−500 nm range, which have been observed in detergent-solubilized LHCII and attributed to simply reflect the change in the Car composition (Figure 5-9) [232, 287]. My results measured in membrane nanodiscs show that this trend persists in the membrane, indicating that Zea is unable to directly induce the conformational change of LHCII that activates NPQ.

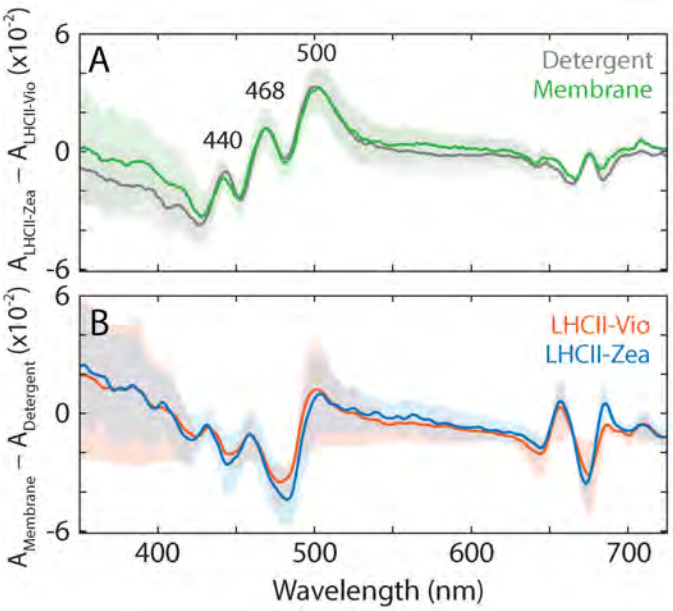

Figure 5-2: **Comparison of the absorption spectra of LHCII-Vio and LHCII-Zea in detergent and membrane nanodisc environments.** (A) Difference between LHCII-Vio and LHCII-Zea in both environments. (B) Difference between the detergent and membrane environments for LHCII-Vio and LHCII-Zea. All spectra are plotted as the mean (solid lines) ± std. dev. (shaded area) from five independent measurements.

Comparative analysis of the CD spectra of LHCII in detergent and in nanodiscs revealed distinct changes in the shape and intensity of Neo and Lut1 CD signals upon membrane insertion, as discussed in detail in Chapter 4 [289]. These membrane-induced changes in CD from Neo and Lut1 are preserved in both LHCII-Vio and LHCII-Zea. However, neither Vio nor Zea causes changes to the CD spectrum upon membrane incorporation, suggesting that the above-mentioned membrane-induced conformational changes are independent of the xanthophyll cycle Car. This stark contrast in the conformational behaviors between Neo/Lut1 and the xanthophyll cycle Car is likely associated with the location and geometry of their binding sites. The binding sites of Neo and Lut1, N1 and L1, are located on the periphery of the LHCII trimer, which allows them to easily undergo large structural motions by increasing their contact with the lipid bilayer [28]. In fact, part of the polyene chains of Neo and Lut1 protrude out of the protein matrix into the membrane [17]. On the other hand, while peripheral, the Vio/Zea-binding site V1 is located at the interface of

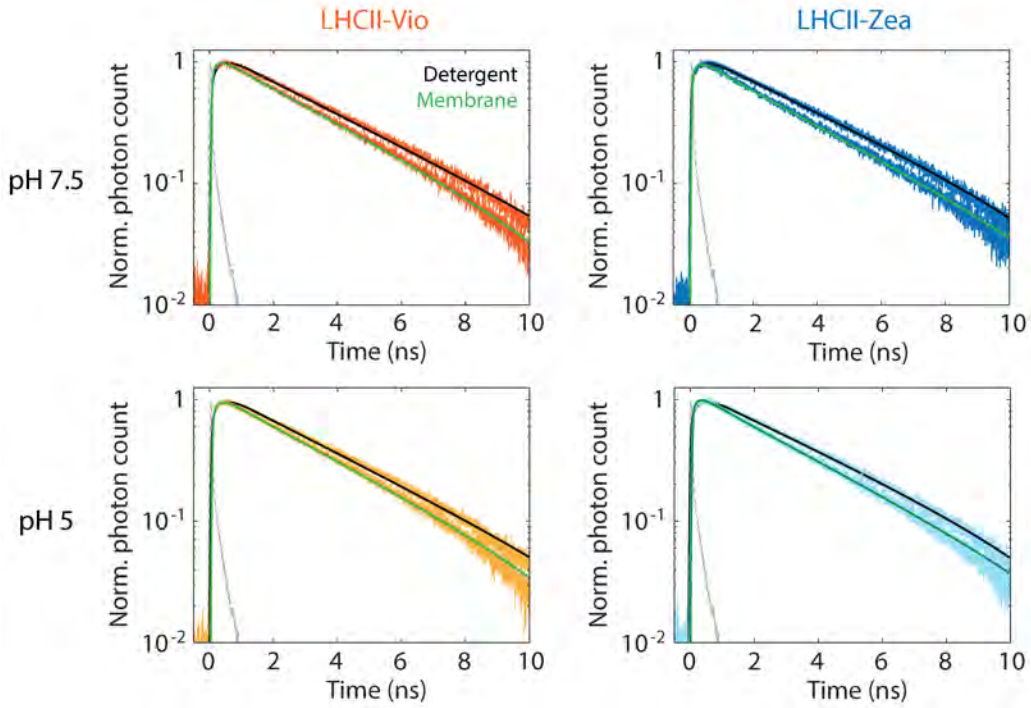

Figure 5-3: **Comparison of the fluorescence decay profiles.** Normalized fluorescence decay profiles of LHCII-Vio (left column) and LHCII-Zea (right column) in both environments at pH 7.5 (top row) and pH 5 (bottom row). The instrument response function (IRF) and the fit curves are shown as gray dashed lines and black (detergent)/green solid lines (nanodisc).

the monomeric subunits of LHCII. Although exposed to the membrane along one side (Figure 5-1A), this binding pocket likely results in reduced structural flexibility for the embedded xanthophyll cycle Car due to the steric restrictions from the surrounding protein matrix in both lateral directions. Furthermore, the V1 binding site possesses a dramatically decreased tilt angle with respect to the membrane normal (34°) compared to that of Neo (58°) and Lut1 (59°) [17]. The reduced tilt angle makes it unlikely for the polyene chain of the Car in this site to protrude towards the membrane, unlike in the case of Neo and Lut1.

The steady-state fluorescence spectra of LHCII-Vio and LHCII-Zea exhibit identical profiles, and the relative fluorescence quantum yield (Φ_{fl}) is the same for both LHCII-Vio and LHCII-Zea in the membrane, where the 13($\pm$4)% reduction in Φ_{fl} relative to that in detergent is due to the introduction of the membrane environment (Figure 5-10) [289]. Furthermore, the fluorescence decay profiles are identical,

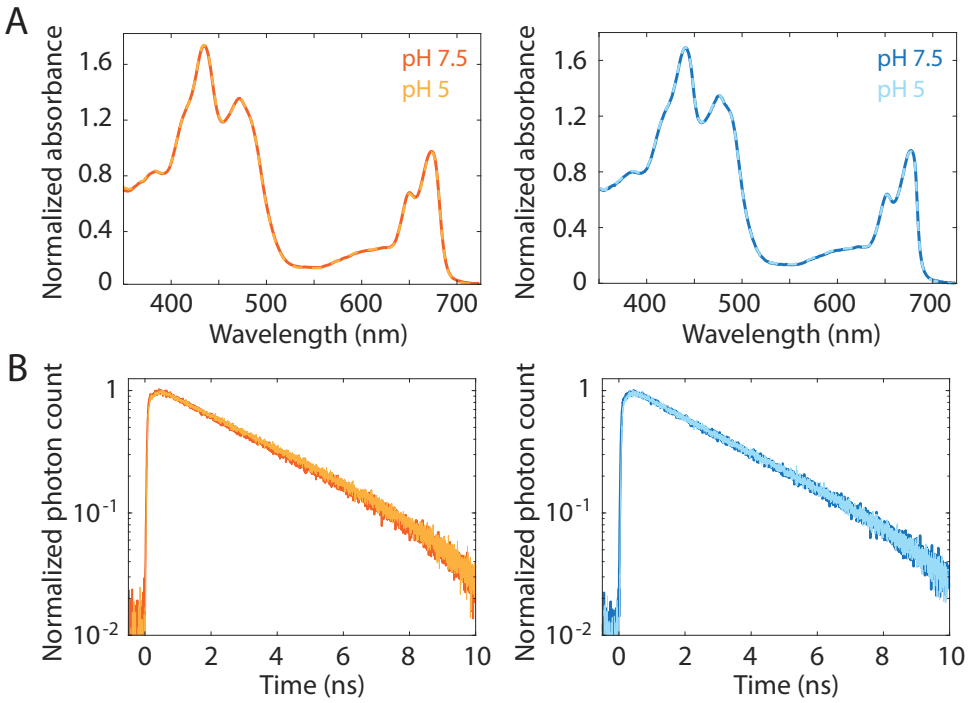

Figure 5-4: **Absorption and fluorescence of LHCII-Vio and LHCII-Zea nanodiscs measured at neutral and acidic pH.** (A) Linear absorption spectra (normalized to the 675 nm peak, pH 5 data shown in dashed lines) and (B) normalized fluorescence decay traces of LHCII-Vio (left) and LHCII-Zea (right) in nanodiscs, measured at pH 7.5 (LHCII-Vio: orange, LHCII-Zea: blue) and pH 5 (LHCII-Vio: yellow, LHCII-Zea: light blue).

both with an average fluorescence lifetime ($< \tau_{fl} >$) of 2.8 ns (Figure 5-3 and Table 5.1). The absence of further fluorescence quenching in LHCII-Zea as compared to in LHCII-Vio indicates that Zea is able to neither open up additional quenching sites nor induce conformational changes in LHCII that enhance quenching even in the membrane environment.

5.4 pH Independence of Steady-State Spectra and Fluorescence Lifetime

To mimic the acidification of the thylakoid lumen *in vivo* under excess light, the steady-state absorption and fluorescence spectra as well as time-resolved fluorescence were measured at pH 5, close to the optimal pH for VDE activity [110]. However, none

of the data in LHCII-Vio nor in LHCII-Zea was affected by the reduction in pH (Figure 5-4). These observations indicate that the presence of neither Zea nor low pH is sufficient to activate quenching in LHCII even in a membrane environment. Based on these results, it is inferred that the site of Zea-dependent quenching observed *in vivo* either is not located within an individual LHCII or requires additional interactions, likely with neighboring proteins, to activate these photophysics.

The pH independence of quenching in LHCII with and without Zea was observed previously for isolated LHCIIs in detergent micelles, at detergent concentrations above the critical micelle concentration (CMC) [287, 288]. In contrast, pH-dependent quenching was observed at detergent concentrations below the CMC, where LHCII aggregates start to form [123]. The pH dependence gradually increased with decreasing detergent concentration, *i.e.*, with increasing extent of LHCII aggregation. It is possible that protein-protein interactions among the large number of antenna complexes *in vivo* lead to similar pH-dependent behaviors of quenching as those observed in LHCII aggregates *in vitro*. Indeed, previous *in vivo* work suggested that the presence of Zea both promotes aggregation of LHCIIs, thereby increasing the magnitude of protein-protein interactions, and also enhances pH-dependent quenching, likely through the induced aggregation as observed *in vitro* [118, 126, 292]. In contrast, membrane-induced quenching appears even for a single trimeric LHCII [289], and therefore does not require protein-protein interactions. This explains the absence of pH dependence observed for both LHCII-Vio and LHCII-Zea in the membrane nanodisc environment, which does not include protein-protein interactions, and implies that the quenching channel activated by the membrane is distinct from the Zea-dependent one observed *in vivo*.

The observed pH independence of quenching in LHCII-Vio and LHCII-Zea is potentially due to the absence of PsbS, which is thought to contribute to NPQ *in vivo* as a sensor for low pH conditions [107]. Although Zea- and pH dependence have not yet been investigated simultaneously, two recent *in vitro* studies on proteoliposomes containing both LHCII and PsbS found Zea-dependent, but pH-independent quenching [129, 293], suggesting that Zea and PsbS may act synergistically for full activation

of NPQ.

5.5 Zeaxanthin Independence of Ultrafast Dissipative Pathways

Ultrabroadband 2DES was employed to map out ultrafast dissipative dynamics of LHCII-Vio and LHCII-Zea in the nanodisc environment. 2D spectra were measured only at neutral pH (pH 7.5) given the pH independence of photophysics as discussed above in Sections 5.3 and 5.4.

5.5.1 Relaxation of Carotenoid Excited States

Figure 5-5A shows the high-energy region of the ultrabroadband 2D spectra, where the bright S_2 states of the Cars are predominantly photoexcited. Because the four Cars bound to LHCII absorb at slightly different energies, it is possible to distinguish the photophysical pathways originating from each Car by probing different regions of the excitation frequency axis [67]. The positive and negative features of this region correspond to the ground-state bleach (GSB)/stimulated emission (SE) of the Car S_2 and excited-state absorption (ESA) of the dark S_1 state. Following photoexcitation into the S_2 state, the Car excited state relaxes via two competing pathways on a sub-200 fs timescale: internal conversion to the S_1 state and energy transfer to lower-lying Chl Q states [49, 67, 75]. The $S_2 \rightarrow S_1$ internal conversion is followed by a dissipative non-radiative relaxation of S_1 to the ground state within tens of picoseconds [49].

Figure 5-5B shows the comparison of the relative intensity of S_1 ESA in LHCII-Vio and LHCII-Zea, obtained by normalizing the integrated 2D intensity of the S_1 ESA region to the initial integrated 2D intensity of S_2 GSB/SE (T = 30 fs). The relative S_1 intensity reports on the efficiency of the $S_2 \rightarrow S_1$ internal conversion. The relative S_1 intensity of LHCII-Vio and LHCII-Zea is within error, with differences less than 10% throughout the entire range of waiting times probed. This indicates that the amplitude and timescale of internal conversion are independent of the xanthophyll

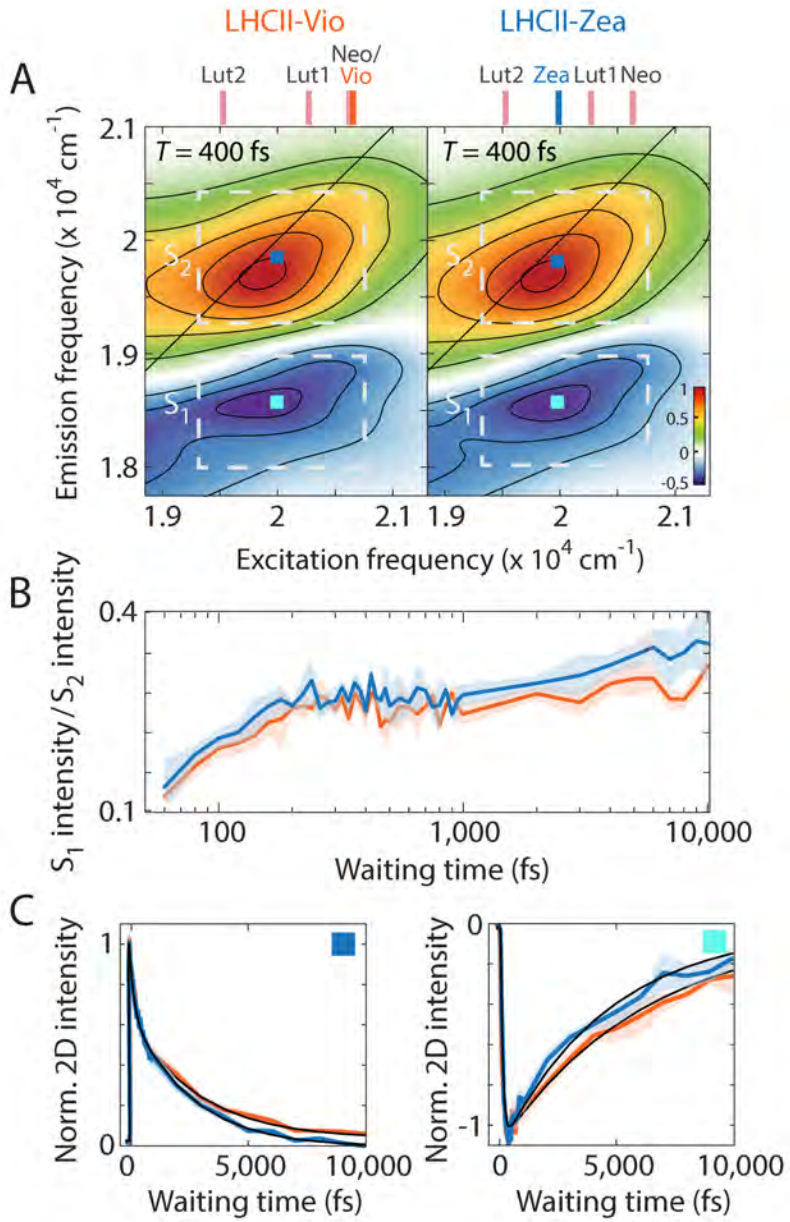

Figure 5-5: **Comparison of the 2D spectra and Car relaxation dynamics in the Car S_2/S_1 region.** (A) Normalized absorptive 2D spectra of LHCII-Vio (left) and LHCII-Zea (right) in the membrane in the Car S_2/S_1 region at $T = 400$ fs. Stick plots indicate the S_2 energy level of each Car. (B) Ratio of S_1 ESA intensity to S_2 GSB/SE intensity in LHCII-Vio (orange) and in LHCII-Zea (blue) plotted as a function of waiting time. The frequency range over which the 2D intensity was integrated is shown in (A) with white dashed boxes. $T = 0 - 50$ fs range is not included due to pulse overlap effects. (C) Normalized fitted waiting time traces of the S_2 GSB/SE (left; $\omega_\tau = 20{,}000$ cm^{-1}, $\omega_t = 19{,}800$ cm^{-1}) and S_1 ESA (right; $\omega_\tau = 20{,}000$ cm^{-1}, $\omega_t = 18{,}650$ cm^{-1}) peaks labeled in (A). Fit curves are shown in black. All traces in (B) and (C) are plotted as the mean (solid lines) ± std. dev. (shaded area) of three independent measurements.

cycle Car, consistent with the identical magnitude of fluorescence quenching observed for both systems. The invariance in dynamics is confirmed by comparing a narrow frequency region around the S_2 energy of Zea, as shown in the waiting time traces in Figure 5-5C. The minor differences in the long, picosecond component likely originate from the different S_1 lifetime between Zea, which is only present in LHCII-Zea, and the other Cars [294]. The similarity in dynamics could be due to either (1) intrinsic similarity in the internal conversion timescales of the Cars, all within 110−163 fs [294] or (2) an inability to resolve the contribution exclusively from Vio or Zea from that of the close-lying Neo and Lut transitions due to their sub-stoichiometric amount within LHCII (see Appendix A, Table A.1).

5.5.2 Relaxation of Chlorophyll Excited States

Figure 5-6A shows the regions of the ultrabroadband 2D spectra that map out the energy transfer pathways of the Q_y states of the Chls. On the diagonal, two positive peaks appear at the energies of Chl *b* Q_y and Chl *a* Q_y.

The Chl *a* Q_y peak is elongated due to the existence of higher-energy (a_H) and lower-energy pools (a_L) of Chl *a*, in agreement with previous 2D results [90, 94, 289]. A positive cross peak initially grows in on a 130−215 fs timescale at the intersection of Chl *b* excitation energy and Chl *a* emission energy due to energy transfer from the Chl *b* to the Chl *a* pools [90, 92, 94, 295]. The temporal evolution of this cross peak is identical for LHCII-Vio and LHCII-Zea in the membrane. Consistently, the Chl *b* diagonal peak shows identical decay profiles between LHCII-Vio and LHCII-Zea, which primarily decays via energy transfer to the Chl *a*. Furthermore, the relaxation dynamics of the Chl *a* diagonal peaks are found to be the same in LHCII-Vio and LHCII-Zea. These observations indicate that the relaxation dynamics of the Chls are unaffected by the binding of Vio or Zea. Similar trends have been observed in a transient absorption study for dark-adapted and *in vitro* de-epoxidized LHCII in detergent micelles, where the ESA of the Chls was probed and no difference in the relaxation dynamics was detected [138].

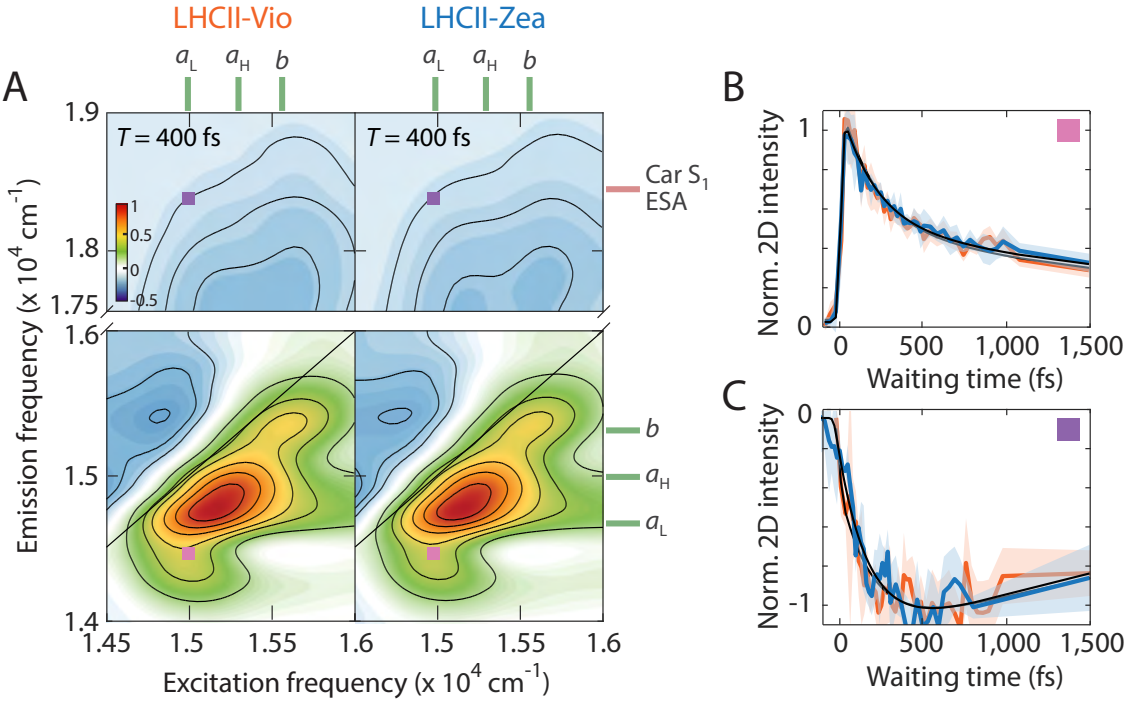

Figure 5-6: **Comparison of the 2D spectra and energy transfer dynamics in the Chl Q_y region.** (A) Normalized absorptive 2D spectra of LHCII-Vio (left) and LHCII-Zea (right) in the membrane in the Chl Q_y region at T = 400 fs. Stick plots label the energy levels of the Chl b and Chl a Q_y states and Car S_1 ESA. (B, C) Normalized waiting time traces of the peaks labeled in (A), shown for the first 1,500 fs. The traces are plotted as the mean (LHCII-Vio in orange, LHCII-Zea in blue lines) ± std. dev. (shaded area) of three independent measurements, and the fit curves are shown as black lines. (ω_τ, ω_t) = (14,925, 14,450) (B), (14,925, 18,400) (C, in cm^{-1}).

5.5.3 Dissipative Energy Transfer from the Terminal Chlorophyll *a* Locus to the Carotenoid S_1 State

The low-energy Chl *a* pool (a_L), the so-called terminal Chl *a* locus (Chls *a*610, *a*611, and *a*612), forms the emissive state of the LHCII complex [263, 268]. This pigment locus is one of the proposed sites of NPQ via a dissipative pathway involving energy or charge transfer between the Chls and the dark S_1 of the Cars followed by non-radiative relaxation of the Car S_1 state [122, 136, 137]. In my previous investigation of LHCII-Vio in the membrane (Chapter 4), correlated decay of the terminal Chl SE and rise of the Car S_1 ESA were revealed upon excitation of the terminal Chls, and assigned to Chl $\rightarrow$ Car energy transfer [289]. Here, the presence and Zea dependence of this dissipative energy transfer pathway were examined by comparing the temporal evolution of the terminal Chl *a* and Car S_1 populations.

Correlated decay and rise components, consistent with those observed for LHCII-Vio in Chapter 4, were also present in LHCII-Zea. As shown in the waiting time traces for the Chl SE and Car S_1 ESA (Figure 5-6B, C), the amplitude and dynamics of this energy transfer pathway are identical between LHCII-Vio and LHCII-Zea with a time constant of 235−260 fs. Lut1 is the Car that most strongly interacts with the terminal Chls, and so likely mediates this energy transfer pathway [122]. In contrast, the xanthophyll cycle Cars exhibit negligible interactions with the terminal Chls primarily due to the large distance between them (center-to-center distances to the terminal Chls: 17.5−29.0 Å from Vio/Zea; 6.3−14.4 Å from Lut1) [17, 262, 278], and thus are unlikely to contribute to this dissipative pathway.

5.6 Models for Zeaxanthin-Dependent Quenching

The mechanism of Zea-dependent NPQ in LHCII is widely debated with four current models. The four models are: (1) direct quenching of the Chl *a* excited states by lowering of the Car excited-state energy level due to the increased conjugation length of Zea relative to Vio, known as the molecular gear shift model [131]; indirect, allosteric

activation of quenching via (2) increasing the proton affinity of the antenna complex or (3) facilitating its conformational change into a quenched form that resembles the conformation of LHCIIs in aggregated state [109, 113, 296]; and (4) absence of a direct or indirect role in quenching without additional factors such as PsbS [121, 125]. All of the data presented here reveal that the presence of Zea alone is not sufficient for the induction of NPQ in LHCII, even in the near-physiological membrane nanodisc environment, consistent with only the last model listed above.

The molecular gear shift model (1) predicts a reversal in the directionality of Chl $Q_y \rightarrow$ Car S_1 energy transfer with the xanthophyll cycle. This model relies on the assumption that the S_1 energy of Vio is energetically higher than the Chl Q_y energy, whereas the S_1 energy of Zea is lower. Thus, when Vio is present, energy is expected to transfer from the Car S_1 to the Chls, whereas when Zea is present, the Chls are expected to donate energy to the Car S_1 state. It is revealed from the 2DES measurements that the Chl $Q_y \rightarrow$ Car S_1 energy transfer dynamics are independent of the xanthophyll cycle Car composition, in contrast with the picture provided by the molecular gear shift model, disproving this proposal. The 2D data exclusively reveal Chl $\rightarrow$ Car energy transfer, and not the reverse pathway, in both LHCII-Vio and LHCII-Zea, strongly indicating that the S_1 states of both Vio and Zea are energetically below the Chl *a* Q_y state. This is in agreement with the negligible difference in the S_1 energies of Vio and Zea reported earlier [297]. Furthermore, the similarity of both the amplitude and timescale of the Chl $Q_y \rightarrow$ Car S_1 energy transfer for LHCII-Vio and LHCII-Zea highlights the absence of any Zea dependence in the dissipative photophysics. Even if the Car S_1 ESA rise shown in Figure 5-6C predominantly arises from Lut1 as speculated above, according to the molecular gear shift model the amplitude and/or the rate of the rise should increase for LHCII-Zea compared to LHCII-Vio, which is not observed.

The proton affinity model (2) predicts a change in the pH dependence of the photophysics. For both LHCII-Vio and LHCII-Zea, no pH dependence was observed in the steady-state absorption, steady-state fluorescence, or time-resolved fluorescence, indicating that the proton affinity of individual LHCIIs is unaffected by Zea in the

nanodisc membrane environment. Moreover, the identical decay kinetics of the Chl fluorescence between the two samples show that, even if the proton affinity of LHCII changes upon Zea binding, there is no resultant change in the quenching at the level of individual LHCIIs, in contrast to the prediction from model (2). However, additional factors, such as the protein-protein interactions discussed earlier or complex lipid mixtures, are present in the native plant thylakoids but absent in the nanodisc platform, and thus may change the proton affinity *in vivo*.

The conformational change model (3) would lead to a difference in the CD spectra between LHCII-Vio and LHCII-Zea, because this measurement is a sensitive reporter on structure. The similarity of the spectra between the two samples indicates that there is no significant conformational change in LHCII in the presence of Zea, even without perturbative effects from detergent, inconsistent with model (3).

The inconsistencies between models (1)−(3) summarized above and the Zea-independent quenching observed here lead to a conclusion that additional factors beyond Zea incorporation and drop in pH, likely external to LHCII, are required for the induction of Zea-dependent NPQ in LHCII. Protein-protein interactions between LHCII and PsbS or between LHCIIs are two such factors. In the case of LHCII and PsbS, the protein-protein interactions are thought to induce conformational changes in the LHCII, which may be Zea-dependent [121, 129, 293]. Indeed, previous work on proteoliposomes containing both LHCII and PsbS revealed an enhancement of quenching in the presence of Zea, although the molecular-level details of the quenching mechanism were not identified [129]. In the case of multiple LHCIIs, previous work showed that the binding of Zea enhances aggregation of LHCIIs, which results in changes in the conformations of LHCII [126, 292]. The Zea dependence of LHCII aggregation was explained by the different hydrophobicity (polarity) of Vio and Zea [298]. In both cases, the protein-protein interactions are likely to take place at the periphery of the LHCII trimers, at the interface between adjacent LHCIIs. Because the binding site of Vio/Zea is located at the periphery of LHCIIs, it is possible that this site mediates the interaction of LHCII with neighboring proteins, which could explain the seemingly contradictory observations of Zea independence of individual LHCIIs

in the membrane and Zea dependence *in vivo*. As discussed earlier and reflected in the CD spectra, the xanthophyll cycle Car is less likely to undergo conformational changes itself by interacting with the external membrane. Therefore, it is speculated that the mechanism of mediation is indirect, such as modulation of the local hydrogen bonding network between adjacent LHCIIs [292].

5.7 Conclusion

In this work, I characterized the Zea dependence of the conformation and photophysics of LHCII in a near-native membrane environment. While the membrane environment induces quenching in individual LHCIIs in both the presence and absence of Zea, the data reveal that the presence of Zea does not enhance this effect, suggesting that Zea-dependent quenching is a separate channel. 2DES data on the dissipative Chl $\rightarrow$ Car energy transfer show that the directionality and timescale of this pathway are independent of the presence of Zea, requiring reevaluations of existing models predicting Zea-dependent dynamics of dissipation. Overall, the results presented here demonstrate Zea-independent photophysics in LHCII at the level of individual antenna complexes, thus highlighting that synergistic interactions with external members of photosystem II are likely required for the full development of NPQ in LHCII.

5.8 Materials and Methods

5.8.1 Sample Preparation

Trimeric LHCII complexes were extracted from spinach leaves, purified and characterized as detailed in Appendix A, Section A.1. The Vio-binding form, LHCII-Vio, was obtained from dark-adapted plants. The Zea-binding form, LHCII-Zea, was prepared by *in vitro* de-epoxidation of Vio in intact dark-adapted thylakoid membranes (Appendix A, Section A.1.2). The presence of Zea was verified by analyzing the pigment composition of the purified LHCII with high-performance liquid chromatog-

raphy (HPLC, Figure A-1B and Table A.1). The detergent-solubilized sample at neutral pH was prepared by thawing the purified LHCII aliquots stored at $-80°$C and adjusting the concentration in a 0.01 M HEPES, 0.02 M NaCl buffer solution (pH 7.5) containing 0.03% *n*-dodecyl α-D-maltopyranoside (α-DM). Low pH detergent sample was prepared by solubilizing buffer exchanging the neutral pH LHCII sample into 0.04 M MES, 0.02 M NaCl buffer (pH 5) containing 0.03% α-DM.

Membrane nanodiscs containing a single trimeric LHCII were prepared with LHCII-Vio and LHCII-Zea as detailed in Appendix A, Section A.2, with MSP1E3D1 as the membrane scaffold protein and soy asolectin lipid. Linear absorption spectra of the purified nanodisc products confirmed that the weakly binding Vio or Zea was retained during nanodisc reaction. All nanodisc assembly reactions were performed at neutral pH (pH 7.5), and low pH samples were prepared by buffer exchanging the nanodiscs assembled at neutral pH into 0.04 M MES, 0.15 M NaCl buffer (pH 5). The final optical density (OD) of all samples used for 2DES was 0.18 and 0.1 (per 0.5 mm) at the Chl *a* Q_y peak (675 nm), for the dataset obtained with spectrum 1 and spectrum 2, respectively.

5.8.2 Steady-State Spectroscopy

Linear absorption and steady-state fluorescence spectra were measured with a Cary 5000 spectrophotometer and a Cary Eclipse fluorimeter (Agilent), respectively, in 1 cm pathlength quartz cuvettes. For fluorescence measurements, the OD of the sample at the excitation wavelength was kept at $0.05 - 0.07$ per cm to ensure absence of any reabsorption effect. Excitation wavelengths of 436, 600, and 640 nm were used, and no excitation wavelength dependence was found in the fluorescence spectra. Relative fluorescence quantum yield of LHCII in nanodiscs compared to LHCII in detergent was calculated by comparing the integrated area of the fluorescence spectrum normalized by the OD at the excitation wavelength (630 nm). CD spectra were measured at 10°C on a Jasco J-1500 spectropolarimeter, in a 1 mm pathlength quartz cuvette. The OD of the sample was 0.2 per mm at 670 nm.

5.8.3 Fluorescence Lifetime Measurement

The fluorescence lifetime of LHCII was measured with TCSPC as described in detail in Chapter 4, Section 4.10.3. Identical excitation and emission filters to those used in Chapter 4 were used (Figure 4-10). A 0.5 mm pathlength flow quartz cuvette was used, and the sample solution was continuously flowed with a peristaltic pump during measurement to prevent sample photodegradation and thermal lensing effect. To prevent reabsorption effect, the OD of all samples at the excitation wavelength range was kept under 0.1 per 0.5 mm. An excitation pulse energy of 10 fJ was employed. Excitation power dependence was checked at three different excitation powers (10 fJ, 30 fJ, and 100 fJ), and no singlet-singlet annihilation was observed.

5.8.4 Ultrabroadband Two-Dimensional Electronic Spectroscopy

A detailed description of the ultrabroadband 2DES setup is provided in Chapter 2 and in [226]. The spectral and temporal profiles of the laser pulses used in 2DES were identical to those described in Chapter 4 (Section 4.10.5, Figure 4-11). A pulse energy of 6.3 nJ was employed with a beam waist of 150 μm at the sample position, corresponding to an excitation density of $2.5 - 2.8 \times 10^{13}$ photons per pulse per cm^2, reported to be in the linear regime for LHCII [94]. τ was sampled in 0.5 fs steps in the range of $\tau = -200 - 200$ fs. T was incremented in steps of 20 fs for $T = -200 - 500$ fs, 40 fs for $T = 540 - 980$ fs, and 1 ps for $T = 1 - 10$ ps. The sample was circulated in a 0.5 mm pathlength quartz flow cell with a peristaltic pump to prevent photodegradation and repetitive excitation of the same spot. The sample reservoir was kept at 4°C throughout the measurement with a home-built water jacket cooling system. The 2DES measurements were performed only on the neutral pH samples (pH 7.5). Each dataset was collected three times, on separate days with freshly prepared samples, to ensure reproducibility of the data. The integrity of the sample was confirmed by comparing the linear absorption spectra and fluorescence decay profiles before and after collection of each dataset.

5.8.5 Analysis of Two-Dimensional Spectra

Each waiting time trace reported here was generated by integrating the 2D signal intensity over finite frequency intervals in both frequencies (100 cm^{-1} in $\omega_\tau \times$ 100 cm^{-1} in ω_t, unless otherwise noted) around the center frequencies reported in each figure. Time constants were extracted by fitting each waiting time trace to an exponential function convolved with a Gaussian pulse with the time resolution (6.2 fs or 6.9 fs) of the experiment.

5.9 Supplementary Information

5.9.1 Characterization of the Nanodiscs

Figure 5-7 show the fast protein liquid chromatography (FPLC), sodium dodecyl sulfate polyacrylamide gel electrophoresis (SDS-PAGE) and transmission electron microscopy (TEM) characterization results of the LHCII nanodiscs produced with both xanthophyll cycle Cars, Vio and Zea. As shown in the figure, all characterization data appear identical regardless of the xanthophyll cycle Car. The presence of Vio or Zea in LHCII after insertion into the membrane nanodiscs was confirmed by comparing the linear absorption spectra of LHCII-Vio and LHCII-Zea nanodiscs, as illustrated in Figure 5-1.

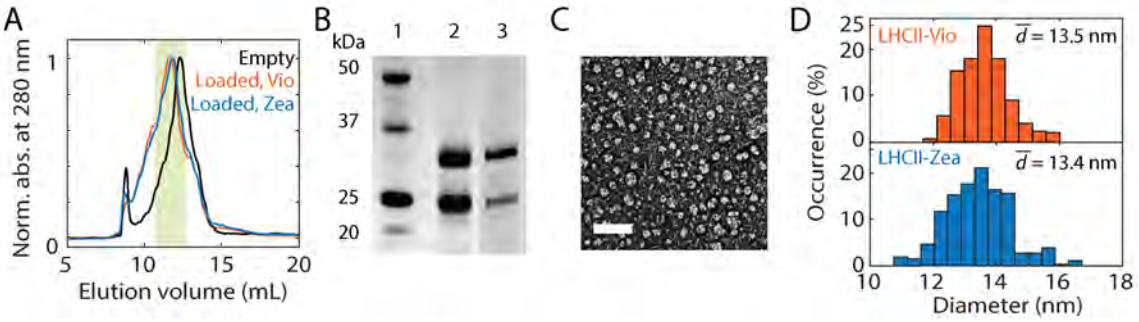

Figure 5-7: **Characterization of LHCII-Vio and LHCII-Zea nanodiscs.** (A) Fast protein liquid chromatogram of empty (black) and loaded (orange: LHCII-Vio, blue: LHCII-Zea) LHCII nanodisc. Shaded area indicates the fraction of loaded discs that was stored for spectroscopic measurements. (B) SDS-PAGE (lane 1: protein standard, lane 2: LHCII-Vio nanodisc, lane 3: LHCII-Zea nanodisc). Both the membrane scaffold protein (MSP1E3D1, 32.6 kDa) and LHCII (25−27 kDa) bands are identified. (C) Representative TEM image of the produced LHCII-Zea nanodiscs. Scale bar is 50 nm. (D) Size distribution analyzed for 300 objects imaged with TEM, showing a mean diameter ($\bar{d}$) of 13.5 nm (LHCII-Vio) and 13.4 nm (LHCII-Zea).

5.9.2 Supplementary Figures and Tables

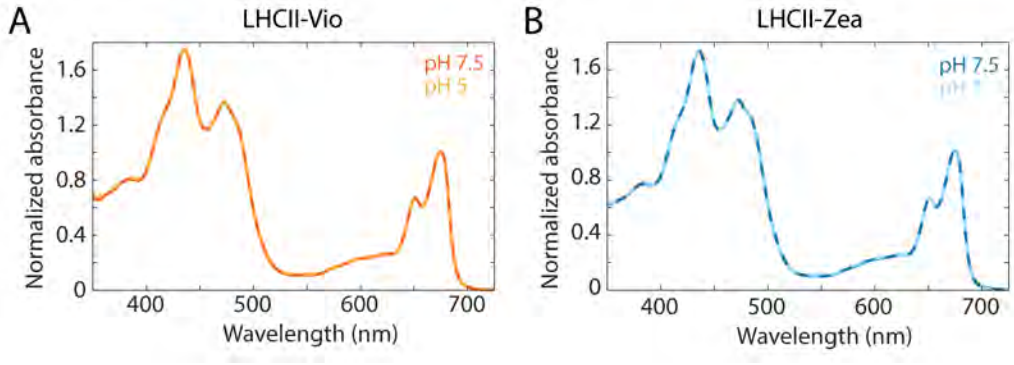

Figure 5-8: **pH comparison of the linear absorption spectra of LHCII-Vio and LHCII-Zea in detergent.** (A) LHCII-Vio and (B) LHCII-Zea. pH 5 data are shown in dashed lines. All spectra are normalized to the 675 nm peak.

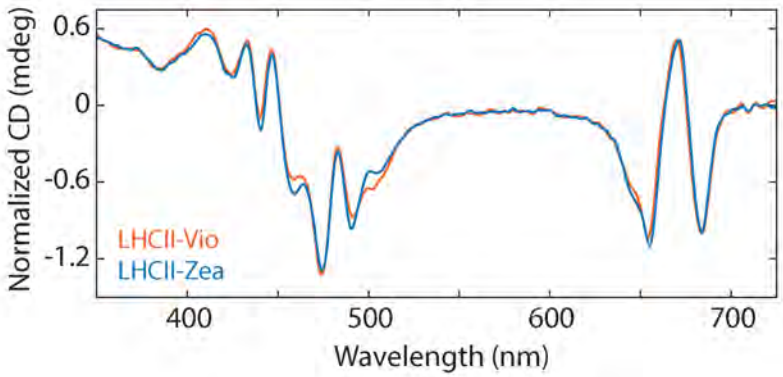

Figure 5-9: **CD spectra of LHCII-Vio and LHCII-Zea in detergent.** Both spectra are normalized to the sample OD at 675 nm. Both spectra were measured at pH 7.5.

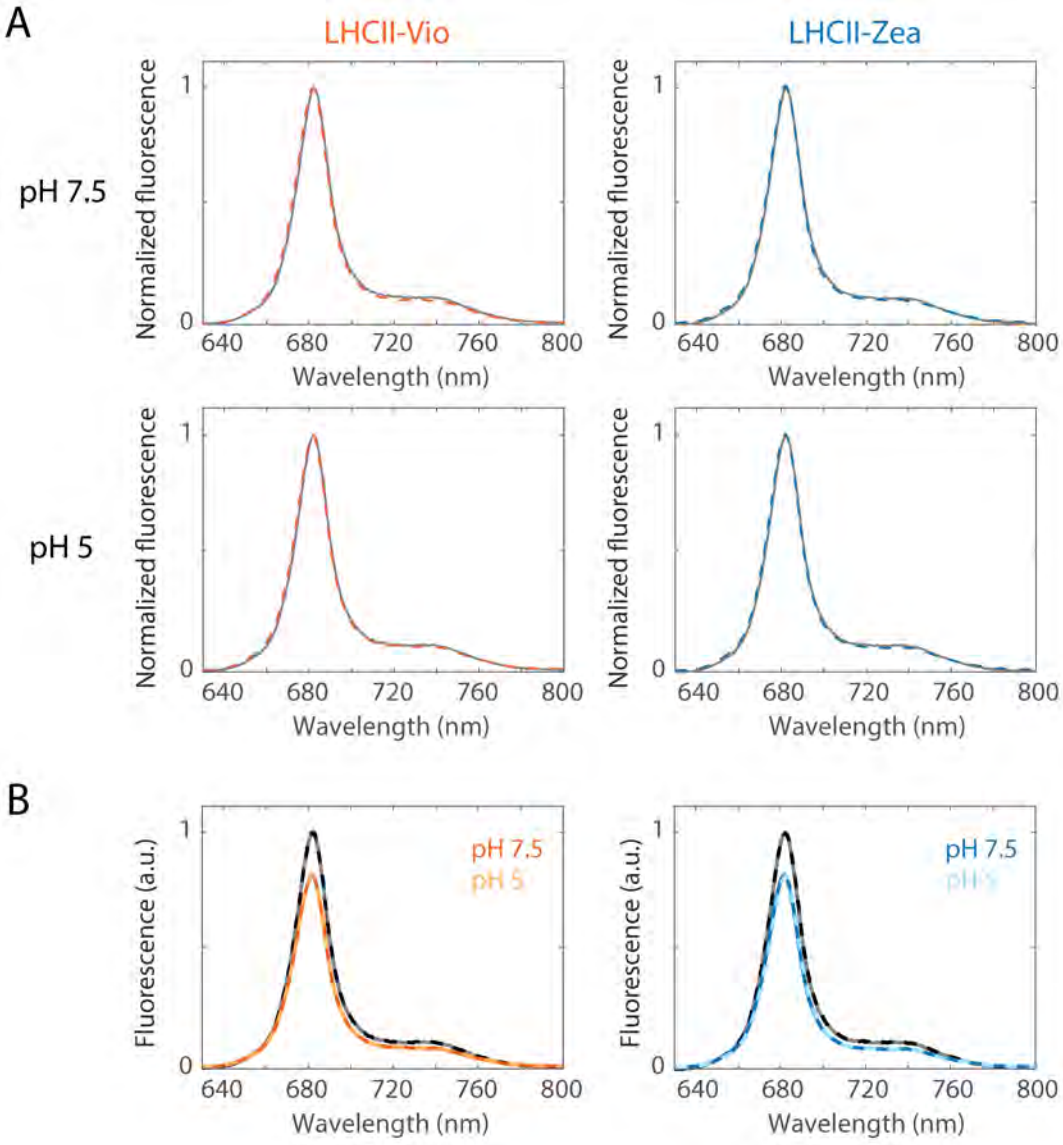

Figure 5-10: **Fluorescence spectra of LHCII-Vio and LHCII-Zea in detergent and in membrane nanodiscs.** (A) Normalized fluorescence spectra of LHCII-Vio (left column) and LHCII-Zea (right column) in both environments at pH 7.5 (top row) and pH 5 (bottom row). Spectra measured in detergent are shown in solid gray lines, and those of nanodiscs are shown in dashed orange (LHCII-Vio) and blue (LHCII-Zea) lines. Each spectrum is normalized to the fluorescence maximum. (B) Fluorescence spectra in (A) normalized to the maximum fluorescence intensity in detergent. Spectra measured in detergent are shown in solid gray (pH 7.5) and dashed black (pH 5) lines. Spectra of LHCII-Vio nanodiscs are shown in orange solid (pH 7.5) and dashed yellow (pH 5) lines, and those of LHCII-Zea nanodiscs are shown in blue solid (pH 7.5) and light blue dashed (pH 5) lines.

Table 5.1: **Fluorescence quantum yields and fit parameters from fluorescence lifetime measurements.**[a]

Environment	pH	Car	Φ_{fl} (%)[b]	A_1 (%)	τ_1 (ns)	A_2 (%)	τ_2 (ns)	$< \tau_{fl} >$[c]
Detergent	7.5	Vio	100	100	3.40 ± 0.05	–	–	3.40 ± 0.05
		Zea	100	100	3.40 ± 0.04	–	–	3.40 ± 0.04
	5	Vio	100	100	3.39 ± 0.04	–	–	3.39 ± 0.04
		Zea	100	100	3.38 ± 0.05	–	–	3.38 ± 0.05
Membrane	7.5	Vio	87 ± 3	10.0 ± 1.0	0.29 ± 0.02	90.0 ± 1.0	3.10 ± 0.06	2.82 ± 0.06
		Zea	87 ± 3	9.7 ± 1.0	0.30 ± 0.02	90.3 ± 0.9	3.09 ± 0.07	2.82 ± 0.07
	5	Vio	87 ± 4	9.8 ± 1.0	0.29 ± 0.03	90.2 ± 1.1	3.12 ± 0.06	2.84 ± 0.07
		Zea	87 ± 4	10.2 ± 0.09	0.30 ± 0.03	89.8 ± 0.8	3.11 ± 0.05	2.83 ± 0.05

[a] Data are reported as mean ± std. dev. from five independent measurements.

[b] Relative fluorescence quantum yield for membrane disc samples calculated by comparing the integrated area of the steady-state fluorescence spectrum in detergent and in the membrane normalized to the OD at the excitation wavelength. The data are reported as mean ± std. dev. from five measurements from five independent measurements.

[c] Amplitude-weighted average fluorescence lifetime ($< \tau_{fl} >= \frac{\sum A_n \tau_n}{\sum A_n}$).

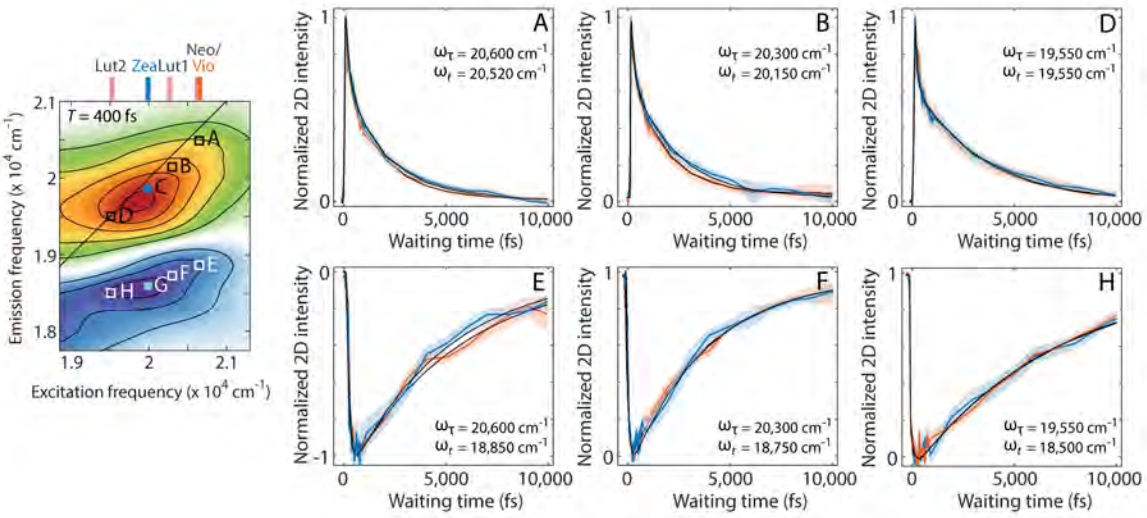

Figure 5-11: **Waiting time traces in the Car S_2/S_1 region of the 2D spectra.** The 2D spectrum on the left (T = 400 fs) illustrates the pigment energy levels (stick plots) and peak positions (open squares) labeled. The traces are plotted as the mean (solid lines; LHCII-Vio in orange, LHCII-Zea in blue) ± std. dev. (shaded area) of three measurements. Black lines are the fit curves. Center frequencies around which the traces were generated are indicated in each panel. The waiting time traces of peaks C and G are shown in Figure 5-5C.

Table 5.2: **Fit parameters from the Car region of the 2D spectra.**[a]

		A_1 (%)	τ_1 (fs)	A_2 (%)	τ_2 (fs)
LHCII-Vio	A (Neo/Vio S_2)	44 ± 6	120 ± 35	56 ± 6	1,860 ± 640
	B (Lut1 S_2)	40 ± 5	130 ± 20	60 ± 5	2,145 ± 520
	C	40 ± 5	180 ± 19	60 ± 5	2,940 ± 480
	D (Lut2 S_2)	47 ± 5	140 ± 20	53 ± 5	3,220 ± 880
	E (Neo/Vio S_1 ESA)	-46 ± 6	136 ± 20	54 ± 6	5,300 ± 1,700
	F (Lut1 S_1 ESA)	-41 ± 5	115 ± 25	59 ± 5	3,800 ± 1,100
	G	-42 ± 4	100 ± 30	58 ± 4	6,280 ± 600
	H (Lut2 S_1 ESA)	-36 ± 8	135 ± 20	64 ± 8	7,070 ± 1,100
LHCII-Zea	A (Neo S_2)	41 ± 6	130 ± 30	59 ± 6	1,910 ± 390
	B (Lut1 S_2)	38 ± 5	140 ± 25	62 ± 5	2,190 ± 510
	C (Zea S_2)	38 ± 4	165 ± 25	62 ± 4	2,580 ± 480
	D (Lut2 S_2)	46 ± 5	120 ± 20	54 ± 5	3,300 ± 650
	E (Neo S_1 ESA)	-45 ± 6	134 ± 20	55 ± 6	4,920 ± 1,920
	F (Lut1 S_1 ESA)	-40 ± 5	105 ± 25	60 ± 5	3,770 ± 780
	G (Zea S_1 ESA)	-46 ± 4	100 ± 30	54 ± 4	4,630 ± 600
	H (Lut2 S_1 ESA)	-38 ± 8	123 ± 25	62 ± 8	7,075 ± 1,100

[a] Each entry reports the 95% confidence interval from fitting to a biexponential function convolved with the pulse width of the 2DES measurement. A and τ report the normalized amplitude in percentage (negative amplitude indicates exponential rise) and the fitted time constant for each component.

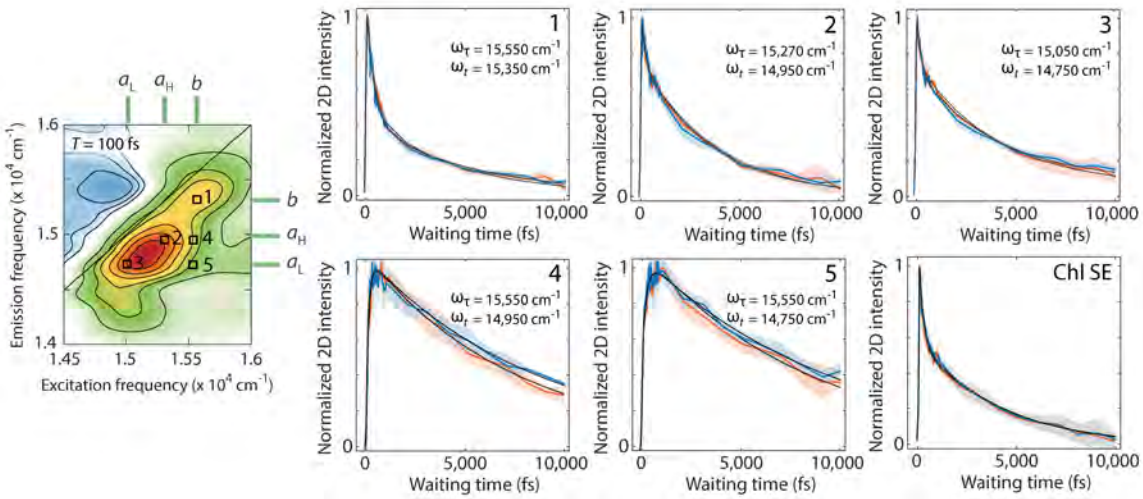

Figure 5-12: **Waiting time traces in the Chl Q_y region of the 2D spectra.** The 2D spectrum on the left (T = 100 fs) illustrates the pigment energy levels (stick plots) and peak positions (open squares) labeled. The traces are plotted as the mean (solid lines; LHCII-Vio in orange, LHCII-Zea in blue) ± std. dev. (shaded area) of three measurements. Black lines are the fit curves. Center frequencies around which the traces were generated are indicated in each panel. The trace for Chl SE is integrated over the area $\omega_\tau = 14,775 - 15,075$ cm^{-1}, $\omega_t = 14,270 - 14,670$ cm^{-1}. The early-time Chl SE traces ($T = 0 - 1,500$ fs) are shown in Figure 5-6B.

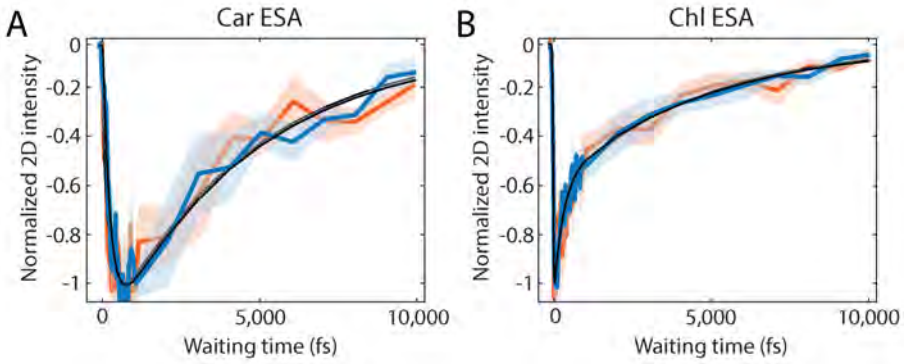

Figure 5-13: **Waiting time traces of Car S_1 ESA and Chl Q_y ESA.** (A) Car ESA (integrated over $\omega_\tau = 14,775 - 15,075$ cm^{-1}, $\omega_t = 18,200 - 18,600$ cm^{-1}) and (B) Chl ESA (integrated over $\omega_\tau = 14,775 - 15,075$ cm^{-1}, $\omega_t = 15,500 - 16,000$ cm^{-1}), plotted as the mean (solid lines; LHCII-Vio in orange, LHCII-Zea in blue) ± std. dev. (shaded area) of three independent measurements.

Table 5.3: **Fit parameters from the Chl Q_y region of the 2D spectra.**[a]

		A_1 (%)	τ_1 (fs)	A_2 (%)	τ_2 (fs)
LHCII-Vio	1 (Chl *b* Q_y)	56 ± 5	378 ± 35	44 ± 5	3,300 ± 460
	2 (Chl a_H Q_y)	32 ± 3	165 ± 20	68 ± 3	3,070 ± 550
	3 (Chl a_L Q_y)	32 ± 3	185 ± 45	68 ± 3	3,500 ± 400
	4 ($b \rightarrow a_H$ transfer)	-44 ± 5	130 ± 20	56 ± 5	7,800 ± 1,100
	5 ($b \rightarrow a_L$ transfer)	-36 ± 4	214 ± 20	64 ± 4	8,820 ± 1,700
	Chl SE [b]	49 ± 5	255 ± 30	51 ± 5	4,300 ± 1,200
	Car S_1 ESA[c]	-42 ± 7	238 ± 20	58 ± 7	4,730 ± 850
	Chl ESA[d]	44 ± 3	290 ± 30	56 ± 3	4,270 ± 1,400
LHCII-Zea	1 (Chl *b* Q_y)	58 ± 4	390 ± 40	42 ± 4	3,500 ± 440
	2 (Chl a_H Q_y)	32 ± 3	168 ± 25	68 ± 3	3,130 ± 420
	3 (Chl a_L Q_y)	37 ± 4	190 ± 30	63 ± 4	3,790 ± 475
	4 ($b \rightarrow a_H$ transfer)	-41 ± 5	126 ± 26	59 ± 5	7,720 ± 1,290
	5 ($b \rightarrow a_L$ transfer)	-34 ± 4	215 ± 20	66 ± 4	8,900 ± 1,020
	Chl SE [b]	48 ± 5	260 ± 25	52 ± 5	4,240 ± 850
	Car S_1 ESA[c]	-43 ± 6	235 ± 40	57 ± 6	4,650 ± 880
	Chl ESA[d]	46 ± 4	283 ± 25	54 ± 4	4,675 ± 1,300

[a] Each entry reports the 95% confidence interval from fitting to a biexponential function convolved with the pulse width of the 2DES measurement. A and τ report the normalized amplitude in percentage (negative amplitude indicates exponential rise) and the fitted time constant for each component.

[b] Integrated over the area $\omega_\tau = 14,775 - 15,075$ cm^{-1}, $\omega_t = 14,270 - 14,670$ cm^{-1}.

[c] Integrated over the area $\omega_\tau = 14,775 - 15,075$ cm^{-1}, $\omega_t = 18,200 - 18,600$ cm^{-1}.

[d] Integrated over the area $\omega_\tau = 14,775 - 15,075$ cm^{-1}, $\omega_t = 15,500 - 16,000$ cm^{-1}.

Chapter 6

Impact of Protein-Protein Interaction on the Dissipative Photophysics of Light-Harvesting Complex II in the Membrane Nanodisc Environment

6.1 Chapter Summary

Non-photochemical quenching (NPQ), the photoprotective process in green plants, is activated by a series of interrelated events: the buildup of a proton gradient (ΔpH) across the thylakoid membrane, accumulation of the xanthophyll cycle carotenoid (Car) zeaxanthin (Zea), and conformational changes of the antenna complexes into a quenched form. One of the proposed origins of the conformational changes is protein-protein interactions between neighboring proteins of the array of antenna complexes embedded in the thylakoid membrane. *In vitro* aggregates of light-harvesting complex II (LHCII), the principal antenna complex in plants, have been widely employed as a mimic of the native antenna arrays and revealed an induction of fluorescence quenching. While the observed quenching of fluorescence shares similar characteristics with that observed *in vivo*, the *in vitro* aggregates are a poor mimic of the native

arrays mainly due to two limitations. First, they have a distinct morphology from that of the native arrays, and so exhibit conformational changes that are likely not relevant to the physiological ones that activate quenching *in vivo*. Second, it is not possible to achieve homogeneous control of the aggregate size, and therefore the extent of protein-protein interaction, preventing systematic analysis of the dependence of quenching on the extent of protein-protein interaction. The work described in this chapter overcomes both limitations; I describe the extension of the membrane nanodisc platform utilized in Chapters 4 and 5 to not only introduce but also systematically control protein-protein interactions between multiple LHCII complexes while maintaining a near-physiological environment. Using nanodiscs co-reconstituting one to four LHCIIs, I investigate how the magnitude and timescales of photoprotective dissipation change as a function of protein-protein interaction with steady-state and time-resolved absorption and fluorescence spectroscopies. Zea- and pH dependence of the photophysics in the presence of protein-protein interactions are also investigated. The data reveal that the extent of fluorescence quenching, *i.e.*, dissipation, increases with increased protein-protein interactions between LHCIIs. Furthermore, it is found that protein-protein interaction switches on pH-dependent dissipative channels, but has no impact on Zea dependence.

6.2 Introduction

The light-harvesting apparatus in the photosystem II (PSII) supercomplex of green plants comprises a densely populated array of pigment-containing membrane proteins termed antenna complexes. The antenna complex array is a dynamic system capable of tuning the balance between the light-harvesting and regulatory functionalities to match physiological need. Under light-limited conditions, the antenna complexes harvest the photoenergy from the sun and efficiently funnel it to the reaction center to power growth [4, 5]. In the presence of excess radiation, the regulatory, or photoprotective, mechanisms are activated, in which harmful excess energy is thermally dissipated to prevent photooxidative damage, known as NPQ [106, 107].

NPQ is activated by a series of changes to the proton affinity, pigment composition, and structural organization of the antenna complex array that are triggered by exposure to high levels of sunlight [106]. The increased activity of the proton pump under high-light conditions results in a reduction of pH on the lumen side of the thylakoid, which forms a proton gradient (ΔpH) across the thylakoid membrane. The reduced pH of the lumen activates the xanthophyll cycle, the conversion of violaxanthin (Vio) into Zea catalyzed by a pH-dependent enzyme, leading to a change in the Car composition of the antenna complexes [109, 110, 286]. In parallel, changes occur to the conformation of individual constituent antenna proteins as well as the overall macro-organization of the antenna array. It is unclear whether these structural changes are dependent on the changes in pH and Car composition or arise independently.

A series of *in vitro* and *in vivo* studies identified several distinct structural alterations that were proposed to be associated with the activation of dissipation. *In vitro* investigations have largely been centered on LHCII accommodated in various environments, ranging from lipid model membranes [143, 148, 289, 290, 299, 300] to solid-state crystals [221] to detergent-free aqueous solutions, which induce self-aggregation of LHCIIs [116–118, 122]. Conformational changes involving perturbations of two peripheral Cars, neoxanthin (Neo) and lutein 1 (Lut1) and the neighboring chlorophylls (Chls) were identified and proposed to be related to the dissipative conformation of LHCII *in vivo*. The peripheral locations of the pigment clusters involved led to the hypothesis that dissipation is activated by the interaction of LHCII with the surrounding local environment, whether that is with the lipid bilayer membrane (lipid-protein interaction) or with adjacent LHCIIs (protein-protein interaction) in the case of LHCII aggregates. *In vivo* characterizations of the macro-organization of PSII under high light have consistently reported that a high light level induces LHCIIs to dissociate from the PSII supercomplex and form arrays amongst themselves, and proposed that this light-induced array formation activates dissipation [115, 301]. The *in vitro* LHCII aggregates mentioned above have been widely employed as a mimic of the native LHCII arrays that form in high light, and exhibited Zea- and pH-dependent

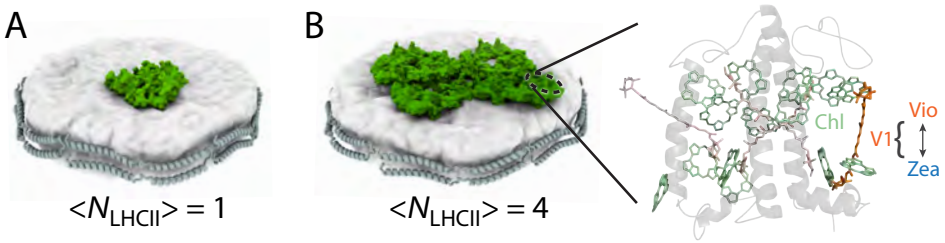

Figure 6-1: **Introduction of protein-protein interaction into the membrane nanodisc platform.** Cartoon illustration of membrane nanodiscs (A) reconstituting a single LHCII trimer ($\langle N_{\mathrm{LHCII}} \rangle = 1$) and (B) co-reconstituting four LHCII complexes ($\langle N_{\mathrm{LHCII}} \rangle = 4$), thus representing near-physiological environments for LHCII without and with protein-protein interaction, respectively. A detailed side view of a monomeric subunit of LHCII is shown on the right, with the V1 binding site for the xanthophyll cycle Car highlighted in orange.

quenching of fluorescence reminiscent of that observed *in vivo* [116–118, 122, 123, 253].

The extensive characterizations of *in vitro* LHCII aggregates and the similarities in their photophysics to those in native LHCII arrays definitively established that there is a correlation between protein-protein interaction and dissipation. However, neither the structural or photophysical mechanism by which protein-protein interaction activates dissipation nor how the extent of dissipation scales with that of protein-protein interaction has been determined, due to two major limitations of the *in vitro* aggregates. First, the morphology of *in vitro* aggregates produced by detergent removal, typically three-dimensional, is distinct from that of the two-dimensional LHCII arrays found *in vivo*, preventing a direct comparison between the conformation and photophysics of the aggregates and the physiological ones appearing in native arrays [143, 149, 302, 303]. Second, the distribution of aggregate size, and in turn, the extent of protein-protein interaction, is neither homogeneous nor systematically controllable, and so it is impossible to elucidate the quantitative correlation between the extent of protein-protein interaction and that of dissipation using *in vitro* aggregates.

In this work, I overcome both limitations by using a controllable and near-native model membrane platform, known as a nanodisc. Nanodiscs are a discoidal lipid bilayer membrane embedding the membrane protein of interest, which is then encircled by a membrane scaffold protein. The size and membrane protein content of nanodiscs can be easily tuned by tuning the stoichiometry of the protein and lipid components

[152, 153]. My previous works demonstrated the applicability of the nanodisc platform to spectroscopic studies of dissipative photophysical pathways for a single, unaggregated LHCII complex [289, 299]. Here, a series of nanodiscs with systematically varied LHCII content, from one to four LHCII complexes, are prepared, and their photophysical properties are compared as a function of the extent of protein-protein interaction (Figure 6-1). Along with the LHCII content, the xanthophyll cycle Car (Vio vs. Zea) and pH (pH 7.5 vs. pH 5), the two established contributors for dissipation, are varied for interrogation of the Zea- and pH dependence of dissipation in the presence of protein-protein interaction. Time-resolved fluorescence measurements reveal that protein-protein interaction enhances quenching of LHCII fluorescence, and that the extent of quenching increases with increased protein-protein interaction. The extent of quenching is dependent on pH but independent of Zea, suggesting that pH-dependent and Zea-dependent quenching, implicated to be strongly correlated from *in vivo* studies, may rather operate with independent mechanisms. Ultrabroadband two-dimensional electronic spectroscopy (2DES) is utilized to uncover the timescale and amplitude of ultrafast dissipative photophysics in these nanodiscs. Preliminary analysis of the 2D spectra reveals that the dissipative Chl-to-Car energy transfer pathway, previously observed in single LHCIIs embedded in the nanodiscs (Chapters 4 and 5), is enhanced in the presence of protein-protein interaction. It is also revealed that this pathway is further enhanced at pH 5, consistent with the pH-dependent quenching observed with time-resolved fluorescence.

6.3 Introduction of Protein-Protein Interaction into the Nanodisc Platform

Membrane nanodiscs co-reconstituting one to four LHCII complexes were prepared by systematically varying the stoichiometry of the assembly reaction (see Appendix A, Section A.2 for details). Both the xanthophyll Car (Vio vs. Zea) and pH (pH 7.5 vs. pH 5) were varied in order to investigate the Zea- and pH dependence of the photo-

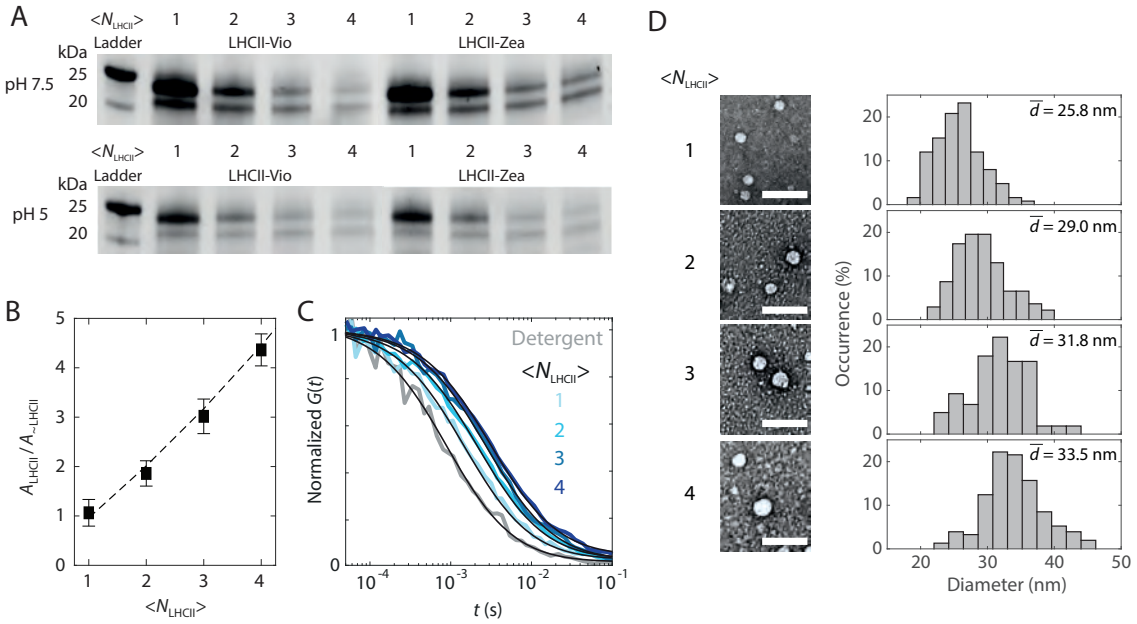

Figure 6-2: **Characterizations of membrane nanodiscs co-reconstituting multiple LHCII proteins.** (A) SDS-PAGE images of nanodiscs with $\langle N_{\mathrm{LHCII}} \rangle = 1{-}4$ prepared with LHCII-Vio and LHCII-Zea at pH 7.5 (top row) and pH 5 (bottom row). (B) Characterization of $\langle N_{\mathrm{LHCII}} \rangle$ with 280 nm absorption. Dashed curve shows the theoretical ratio, and filled squares are obtained from experimental data. Only LHCII-Vio data (pH 7.5) are shown, but LHCII-Zea and pH 5 data exhibited the same trend. Error bars are std. dev. from five different sample preparations. (C) Fluorescence correlogram of nanodiscs with $\langle N_{\mathrm{LHCII}} \rangle = 1{-}4$ (fit curves in black). Only LHCII-Zea data at pH 7.5 are shown, but LHCII-Vio and pH 5 data exhibited the same trend. The correlation curve of LHCII in detergent is also shown for comparison. (D) Representative TEM images for each $\langle N_{\mathrm{LHCII}} \rangle$ (LHCII-Vio, pH 7.5) are shown on the left, and the corresponding size distributions with mean diameters ($\bar{d}$), each constructed from 100 objects, are shown on the right. Scale bars are 100 nm.

physics as a function of the extent of protein-protein interaction. The characterization results shown in Figure 6-2 demonstrate the integrity of the prepared nanodiscs. Both the 20 kDa ApoE422K band and the 25−27 kDa LHCII band were identified in the sodium dodecyl sulfate polyacrylamide gel electrophoresis (SDS-PAGE) of all of the purified nanodisc products, demonstrating the robustness of the nanodisc assembly reaction to varied reaction stoichiometry, xanthophyll Car composition and pH (Figure 6-2A). The gradual increase in the average LHCII content per nanodisc ($\langle N_{\mathrm{LHCII}} \rangle$) was verified with analysis of the absorbance at 280 nm, and was in quantitative agreement with the desired stoichiometry of $\langle N_{\mathrm{LHCII}} \rangle = 1-4$ (Figure 6-2B, see Section 6.9.1 for detailed description of this analysis). Fluorescence correlation spectroscopy (FCS) was employed to ensure the absence of any large-sized LHCII aggregates as well as characterize the hydrodynamic radii of the produced nanodiscs. The correlation curves display a monoexponential diffusion kinetics regardless of $\langle N_{\mathrm{LHCII}} \rangle$, indicating the absence of large aggregates, which, if present, would give rise to additional slow time components (Figure 6-2C). The diffusion becomes gradually slower as $\langle N_{\mathrm{LHCII}} \rangle$ increases, reflecting the gradually increasing hydrodynamic radius of the nanodisc as a function of LHCII content (Table 6.1). The hydrodynamic radii extracted from fitting the correlation curves are in good agreement with the size distributions obtained from transmission electron microscopy (TEM, Figure 6-2D). Taken together, these results demonstrate successful introduction and systematic control of protein-protein interactions between LHCIIs within the nanodisc platform.

6.4 Spectroscopic Markers of Protein-Protein Interaction in Absorption and Circular Dichroism

Linear absorption and circular dichroism (CD) spectroscopies were employed for characterization of the changes in pigment electronic structure and conformations as a function of the extent of protein-protein interaction. The linear absorption spectra of the LHCII nanodiscs containing one and four proteins, with differing xanthophyll

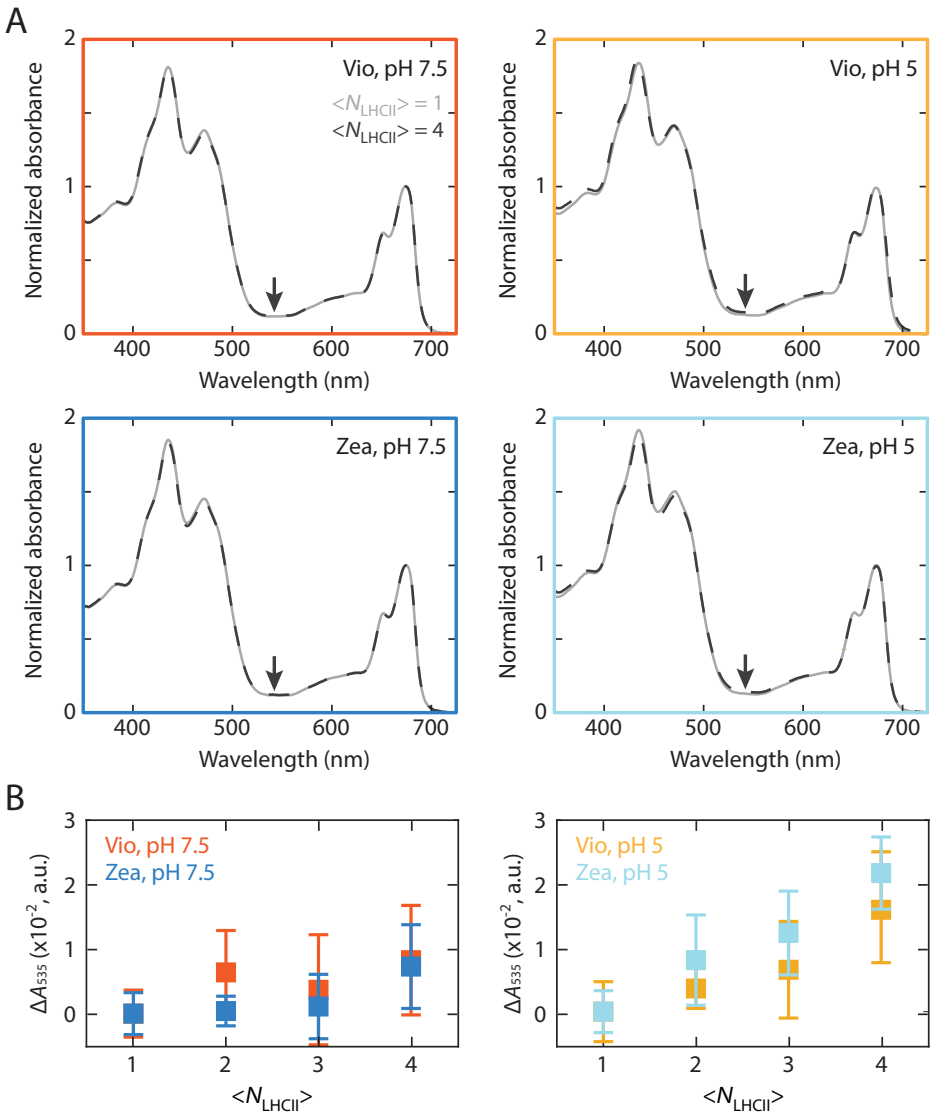

Figure 6-3: **Changes in linear absorption with protein-protein interaction.** (A) Linear absorption spectra of LHCII nanodiscs with $\langle N_{\mathrm{LHCII}} \rangle = 1$ (gray solid line) and 4 (black dashed line). The xanthophyll Car and pH are indicated in each panel. (B) Change in the absorbance at 535 nm (marked with arrows in (A)) plotted as a function of $\langle N_{\mathrm{LHCII}} \rangle$. The data are presented as the mean ± std. dev. of fifteen and eight independent sample preparations for pH 7.5 and pH 5, respectively.

cycle Cars and pH, are shown in Figure 6-3A. The spectral profiles are nearly identical with less than 5% changes in absorbance across the absorption wavelength range, suggesting that the introduction of protein-protein interaction does not significantly affect the energetics of the pigment electronic transitions. Upon closer inspection, a gradual increase in the absorbance at 535 nm (ΔA_{535}) was identified with a linear dependence on the LHCII content, as shown in Figure 6-3B. While the dependence is not obvious at pH 7.5, a much stronger and clearer dependence is observed at pH 5, demonstrating the pH dependence of ΔA_{535}. The increased slope of the dependence with Zea at pH 5 relative to Vio at the same pH indicates that this feature is also Zea-dependent. This characteristic increase in the absorbance at 535 nm has been observed *in vivo* under high-light conditions [113] as well as in *in vitro* aggregates of LHCII [304]. ΔA_{535} was found to be linearly correlated with the level of NPQ, and therefore hypothesized to be related to a quenched state of LHCII [305, 306]. Furthermore, the increase was enhanced in the presence of Zea and at low pH, in accordance with my observations in nanodiscs above. While the origin of ΔA_{535} remains undetermined, a leading hypothesis is that it arises from excitonic interactions between two Zea molecules brought to close contacts upon aggregation of LHCIIs [304]. Theoretical simulations proposed that the excitonic interactions likely result in a strongly coupled Zea dimer with a J-aggregate-like structure, thereby inducing a red-shift of the Zea $S_2(0-0)$ absorption maximum to 535 nm from that of a monomer at 505 nm [307]. A similar increase, but at a slightly blue-shifted wavelength (525 nm), was identified and attributed to an excitonic Vio dimer [304, 308]. The blue-shift in the wavelength arises from the blue-shifted $S_2(0-0)$ energy of Vio compared to Zea due to its shorter conjugation length. Therefore, the presence and gradual increase of ΔA_{535}, a Zea-specific signature, even in the Vio-binding LHCIIs could be due to partially overlapping contributions from ΔA_{525} originating from Vio.

An additional spectroscopic signature that sensitively depends on the LHCII content is found in the CD spectra (Figures 6-4A and 6-8). Similarly to the linear absorption spectra, the overall spectral profiles of the CD spectra are nearly unaffected by the LHCII content, the xanthophyll Car or the pH. The minor changes observed

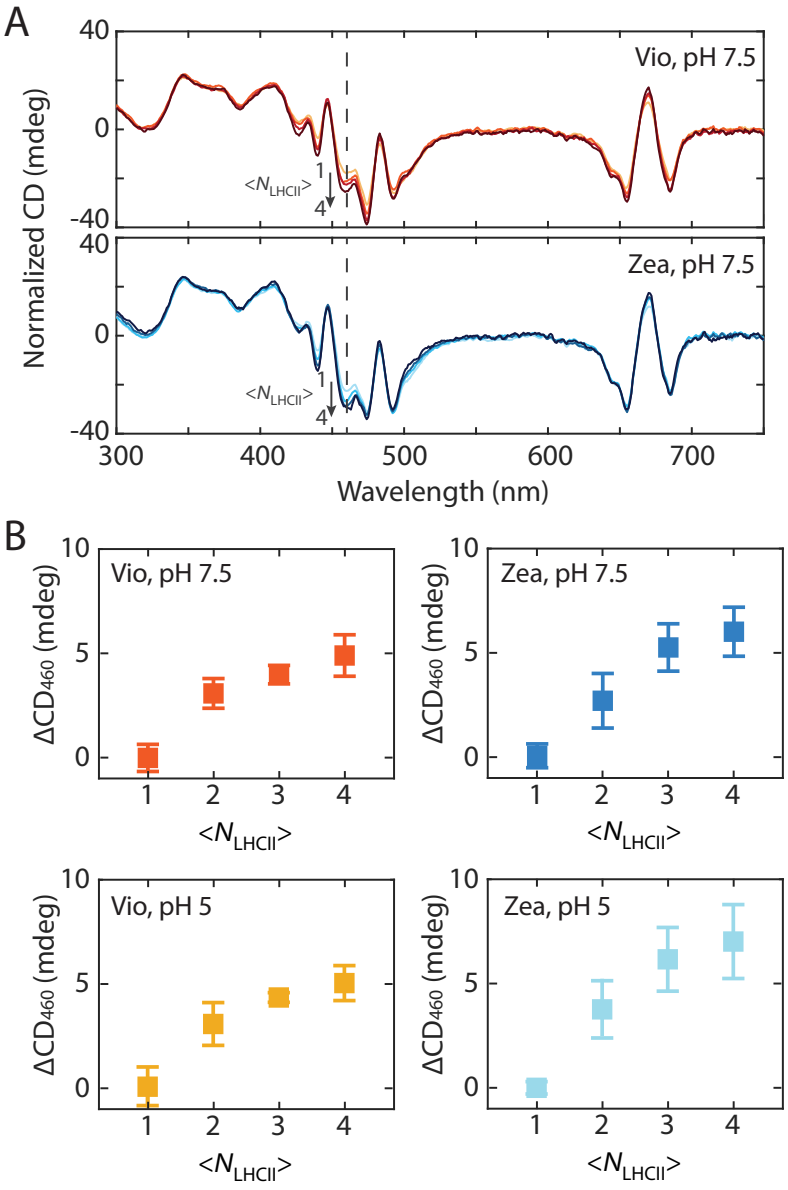

Figure 6-4: **Changes in CD with protein-protein interaction.** (A) CD spectra of LHCII nanodiscs with $\langle N_{\mathrm{LHCII}} \rangle = 1{-}4$ with Vio (top) and Zea (bottom) as the xanthophyll cycle Car, at pH 7.5. The spectra are normalized to the absorbance at 650 nm. The arrows indicate the gradual growth of the 460 nm peak as $\langle N_{\mathrm{LHCII}} \rangle$ is increased from one to four. (B) Change in the CD intensity at 460 nm (marked with dashed line in (A)) plotted as a function of $\langle N_{\mathrm{LHCII}} \rangle$. The xanthophyll cycle Car and pH are indicated in each panel. The data are presented as the mean ± std. dev. of three independent sample preparations.

in the Car S_2 absorption range (425−525 nm), including the slight increase in the CD intensity of the negative 460 nm band in the presence of Zea, likely simply reflect the change in the Car composition, as has been revealed earlier [232, 287, 299]. Two negative peaks, at 440 nm and 460 nm, exhibit a gradual increase in peak intensities as a function of $\langle N_{\mathrm{LHCII}} \rangle$. The change in the CD intensity of the 460 nm peak ($\Delta \mathrm{CD}_{460}$) for both xanthophyll cycle Car and pH conditions plotted as a function of $\langle N_{\mathrm{LHCII}} \rangle$ is shown in Figure 6-4B. $\Delta \mathrm{CD}_{460}$ shows a nonlinear dependence on $\langle N_{\mathrm{LHCII}} \rangle$ in all four cases. The trends observed for Vio-binding LHCII at pH 7.5 and pH 5 are nearly identical, thus revealing no pH dependence. In contrast, comparison of the trends in Zea-binding LHCII reveals a slight pH dependence, where a stronger dependence on $\langle N_{\mathrm{LHCII}} \rangle$ was seen at pH 5. Zea dependence is observed for both pH 7.5 and pH 5, and a more pronounced dependence is seen at pH 5.

The CD bands at 440 and 460 nm appear in the native thylakoid membrane as well as in *in vitro* LHCII aggregates, albeit with much higher intensities than those observed for my nanodiscs [143, 303]. In contrast, the intensities of these bands become negligible in detergent-solubilized, non-aggregated LHCII, with both bands only appearing as weak shoulders. As a result, these two bands have been considered to selectively report on the degree of aggregation of LHCII. In my CD spectra measured in the nanodisc environment, clear peak structures are observed at both wavelengths even in the absence of protein-protein interaction ($\langle N_{\mathrm{LHCII}} \rangle = 1$), reiterating that the conformation of LHCII in the detergent and membrane environments are likely vastly different, as also demonstrated in Chapter 4. The smaller intensities of these bands observed in the nanodiscs than in the native thylakoid membrane and *in vitro* LHCII aggregates are a consequence of the lower extent of protein-protein interactions present in the nanodiscs, which incorporate smaller protein arrays with only up to four LHCIIs, as opposed to the heterogeneous macroaggregates found *in vivo* or formed *in vitro* with detergent removal. While it is established that the CD signal in this wavelength range originates from the Chl Soret and/or Car S_2 states [259], the exact pigment electronic transitions responsible for the appearance of these bands are not identified due to the highly congested energy landscape of LHCII.

Interestingly, the dependence of CD on LHCII content exhibits vastly different qualitative features from the trends observed in the linear absorption spectra. First, ΔCD_{460} nonlinearly depends on $\langle N_{LHCII} \rangle$, in contrast to the linear dependence observed in ΔA_{535}. Second, Zea dependence is observed in ΔCD_{460} for both pH conditions, whereas ΔA_{535} shows Zea dependence only at pH 5. Furthermore, the pH dependence of ΔCD_{460} is only present for Vio-binding LHCII, whereas ΔA_{535} is pH-dependent irrespective of the xanthophyll cycle Car. These differences likely originate from the fact that ΔA_{535} is exclusively sensitive to the photophysics of the xanthophyll cycle Car but not the other Cars or Chls, but that ΔCD_{460} includes contributions from multiple Car S_2 states and potentially also the Chl Soret states, as discussed above.

6.5 pH-Dependent, Zeaxanthin-Independent Fluorescence Quenching in the Presence of Protein-Protein Interaction

To elucidate the impact of protein-protein interaction on the extent of dissipation, time-resolved fluorescence spectra (TRFS) were measured and compared for nanodiscs with $\langle N_{LHCII} \rangle = 1-4$. Regardless of the LHCII content, xanthophyll cycle Car, or pH, all TRFS exhibit identical spectral profiles with one intense band peaking at 682 nm and a weaker red-shifted band at > 710 nm, consistent with the steady-state fluorescence spectra (Figures 6-5 and 6-9). The TRFS uniformly decay across the emission wavelength range without any time-dependent shift in the peak positions or emission-wavelength-dependent dynamics.

The fluorescence decay profiles of the nanodiscs reveal a gradual decrease in the average fluorescence lifetime as a function of $\langle N_{LHCII} \rangle$, for both xanthophyll cycle Cars and at both neutral and low pH conditions (Figure 6-10). A 35% and 32% decrease in average fluorescence lifetime is observed for Vio- and Zea-binding LHCII, respectively, when the decay traces with $\langle N_{LHCII} \rangle = 1$ and 4 were compared at pH 7.5

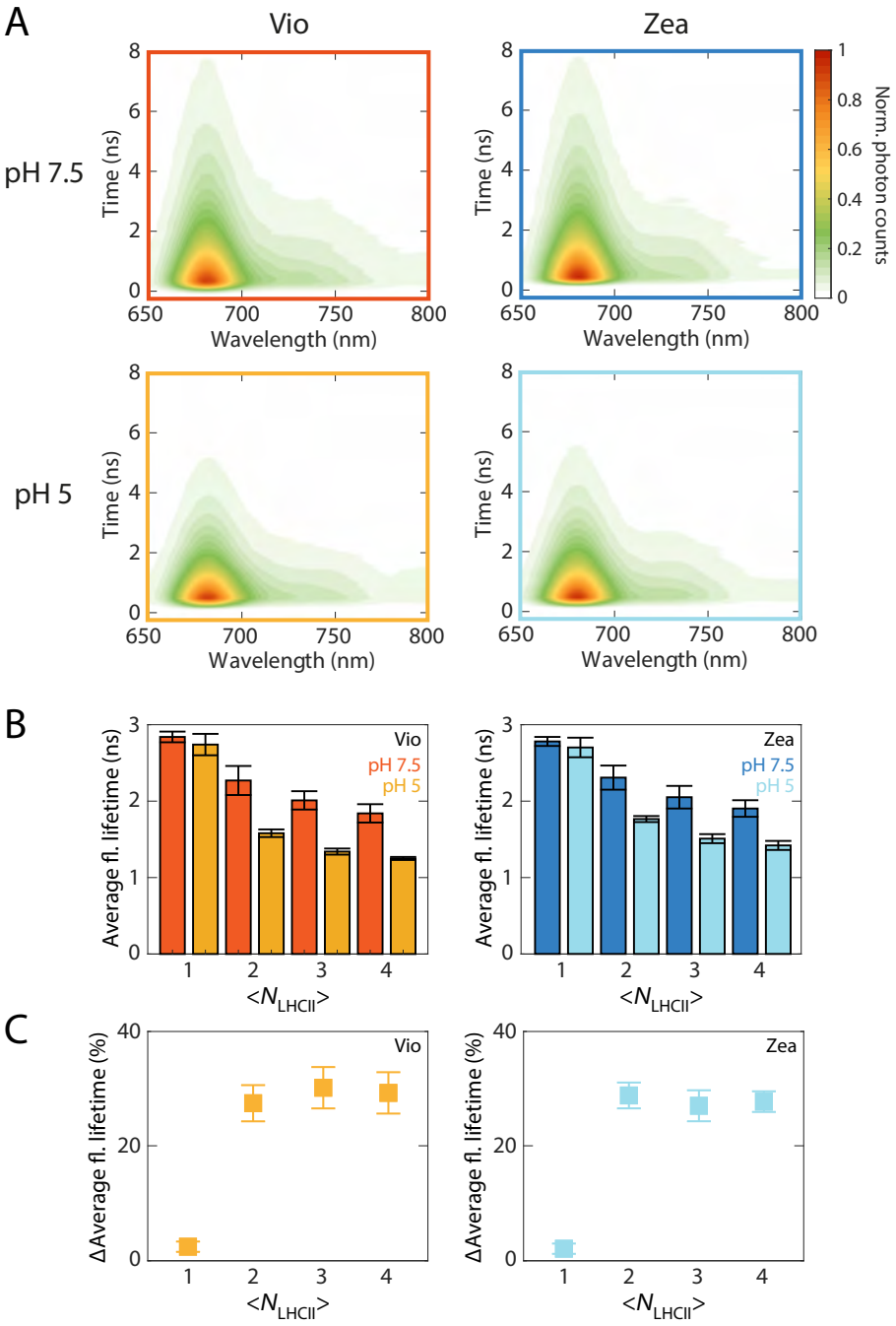

Figure 6-5: **Dependence of fluorescence decay profiles on LHCII content, pH and the xanthophyll cycle Car.** (A) TRFS of $\langle N_{\mathrm{LHCII}} \rangle = 4$ nanodiscs with the xanthophyll Car and pH as labeled in the figure. (B) Bar plots of the fitted average fluorescence lifetimes as a function of $\langle N_{\mathrm{LHCII}} \rangle$ and pH, for Vio-binding (left) and Zea-binding LHCII. (C) Percent decrease in the fluorescence lifetime plotted as a function of $\langle N_{\mathrm{LHCII}} \rangle$ at pH 5. The data in (B) and (C) are presented as the mean $\pm$ std. dev. of eight independent sample preparations.

(Figure 6-5B). At pH 5, the decrease is enhanced to 55% and 52% for Vio- and Zea-binding LHCII, indicating that the fluorescence quenching induced by protein-protein interaction is pH-dependent. In contrast, comparison of the lifetimes with Vio and Zea at each pH reveals no Zea dependence with negligible differences in the fitted time constants. In the absence of protein-protein interaction, the fluorescence dynamics are neither Zea- nor pH dependent, as seen in the identical average fluorescence lifetimes obtained for all four xanthophyll Car/pH combinations of $\langle N_{\mathrm{LHCII}} \rangle = 1$ nanodiscs and also observed earlier in Chapter 5 [299]. While protein-protein interaction activates pH-dependent quenching as mentioned above, it is not capable of further tuning the magnitude of the pH dependence, as evidenced by the uniform percent decrease of $28-33\%$ in the fluorescence lifetime regardless of $\langle N_{\mathrm{LHCII}} \rangle$ (Figure 6-5C).

The results presented above are only partially consistent with the quenching behaviors observed *in vivo* and in *in vitro* LHCII aggregates, which are both pH- and Zea-dependent, the latter of which I do not observe [118, 268, 292]. The observed Zea dependence was explained by hypothesizing a role of Zea as an allosteric promoter of NPQ by inducing a closer packing among LHCIIs within the antenna complex array. Specifically, due to the increased hydrophobicity of Zea compared to Vio, Zea is thought to better stabilize aggregated structures of LHCIIs by modulating the inter-protein hydrogen bonding network between the protein scaffold of adjacent LHCIIs [292, 309]. The inconsistency between the Zea independence observed here and Zea dependence observed *in vivo* may arise from two possible origins. First, the site of Zea-dependent quenching may not be LHCII, but rather the minor complexes, which are present in the native system but absent in the LHCII-only nanodiscs studied here. A second possibility is that Zea-dependent quenching may require the presence of the photosystem II subunit S (PsbS), a non-pigment-binding pH sensor protein thought to be necessary for full activation of NPQ [125–130], which is not present in the nanodiscs. It is unclear at present what gives rise to the inconsistency between the Zea-independent quenching of the nanodiscs and Zea-dependent quenching seen in *in vitro* LHCII aggregates. It should be noted, however, that there are very few examples that report Zea dependence in *in vitro* LHCII aggregates with variations in

sample preparation protocols or Zea content, which may contribute to the observed discrepancies [118, 292].

6.6 Preliminary Analysis of Ultrafast Dissipative Photophysics

The impact of protein-protein interaction on the ultrafast dissipative photophysics was characterized with ultrabroadband 2DES. The 2D spectra were measured only for $\langle N_{\mathrm{LHCII}} \rangle = 4$ nanodiscs, which show the highest extent of protein-protein interaction and therefore are expected to reveal the most pronounced changes in the dynamics. The pH- and Zea dependence was analyzed by varying both the xanthophyll cycle Car and pH conditions.

Figure 6-6A shows a representative ultrabroadband 2D spectrum at $T = 320$ fs, measured for Vio-binding LHCII at pH 7.5. The spectra for the other three conditions revealed qualitatively similar features in the peak positions and spectral profiles. As extensively discussed in Chapters 3−5, this frequency range of the spectrum reveals a pair of intense positive and negative peaks, which correspond to the S_2 ground-state bleach (GSB)/stimulated emission (SE) and S_1 excited-state absorption (ESA) of the Cars. Therefore, this region of the 2D spectra maps out one of the two dissipative photophysical pathways identified earlier, Car $S_2 \rightarrow S_1$ internal conversion [289]. The temporal evolution of the positive S_2 GSB/SE and negative S_1 ESA peaks is shown in Figure 6-6B and C, respectively. The $S_2 \rightarrow S_1$ internal conversion pathway appears in a 2D spectrum as a rapid sub-picosecond decay of the S_2 GSB/SE and an initial growth of S_1 ESA on a matching timescale [49, 228]. The time traces shown in Figure 6-6B, C reveal such correlated decay and rise components with a time constant of 155±25 fs, which is assigned to the timescale of internal conversion. The extracted timescale of internal conversion in the presence of protein-protein interaction is within the range of the 100−180 fs timescale observed in the absence of protein-protein interaction (Chapter 5, Table 5.2). Consistent with the pH-dependent but Zea-independent flu-

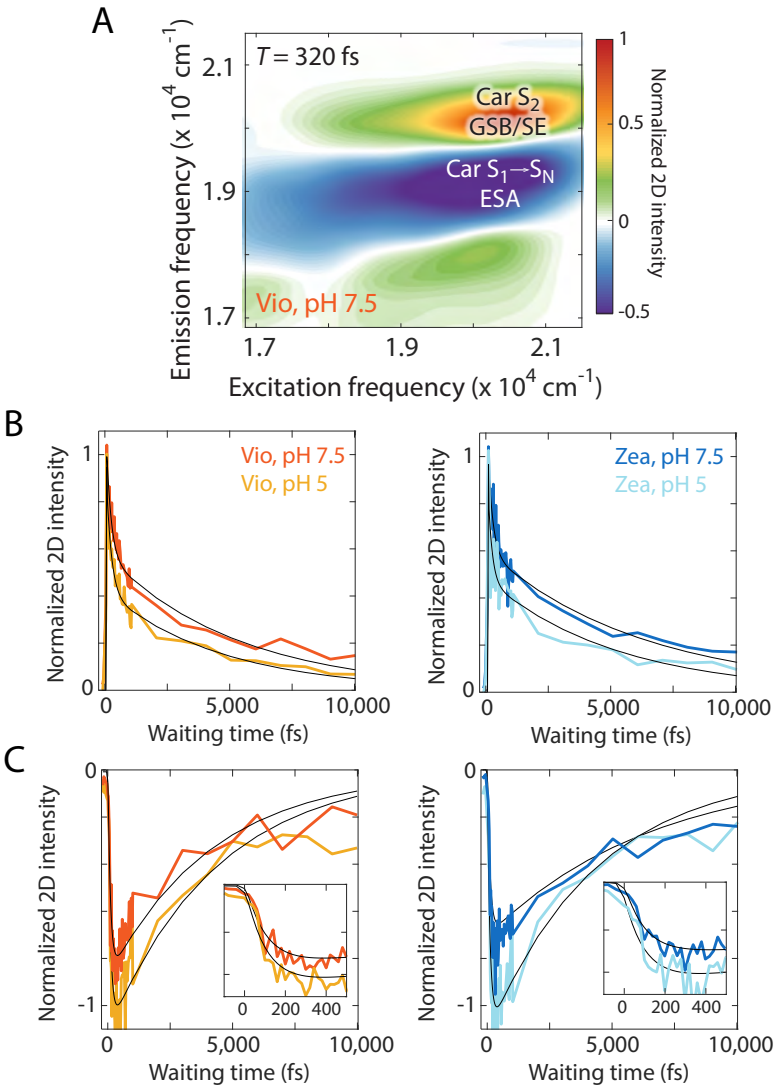

Figure 6-6: **2D spectrum and representative fits of $\langle N_{\mathrm{LHCII}} \rangle = 4$ nanodiscs probing Car internal conversion dynamics.** (A) Representative absorptive 2D spectrum of $\langle N_{\mathrm{LHCII}} \rangle = 4$ nanodiscs, with Vio as the xanthophyll cycle Car at pH 7.5 at $T = 320$ fs. The Car S_2 GSB/SE and S_1 ESA peaks analyzed and mentioned in the text are labeled. (B, C) Fitted time traces of (B) Car S_2 GSB/SE and (C) S_1 ESA. The insets in (C) show the growth of Car S_1 ESA for the initial 500 fs due to internal conversion. The traces in (C) are normalized to the initial S_2 GSB/SE peak intensity immediately after photoexcitation ($T = 30$ fs) so that they visualize the relative intensity of the S_1 population. $(\omega_\tau, \omega_t) = (20{,}300, 20{,}300)$ (B), (20,300, 18,800) (C, in cm^{-1}).

orescence quenching observed in time-resolved fluorescence measurements, the time traces of both S_2 GSB/SE and S_1 ESA exhibit pH dependence and Zea independence. The relative intensity of the S_1 ESA peak, obtained by normalizing the raw peak intensity to the initial S_2 GSB/SE peak intensity immediately after photoexcitation (T = 30 fs), is increased by ~20% at pH 5 compared to at pH 7.5. In agreement with this increase, the S_2 GSB/SE peak decays ~20% faster at pH 5, corroborating the acceleration of this channel in a pH-dependent manner in the presence of protein-protein interaction.

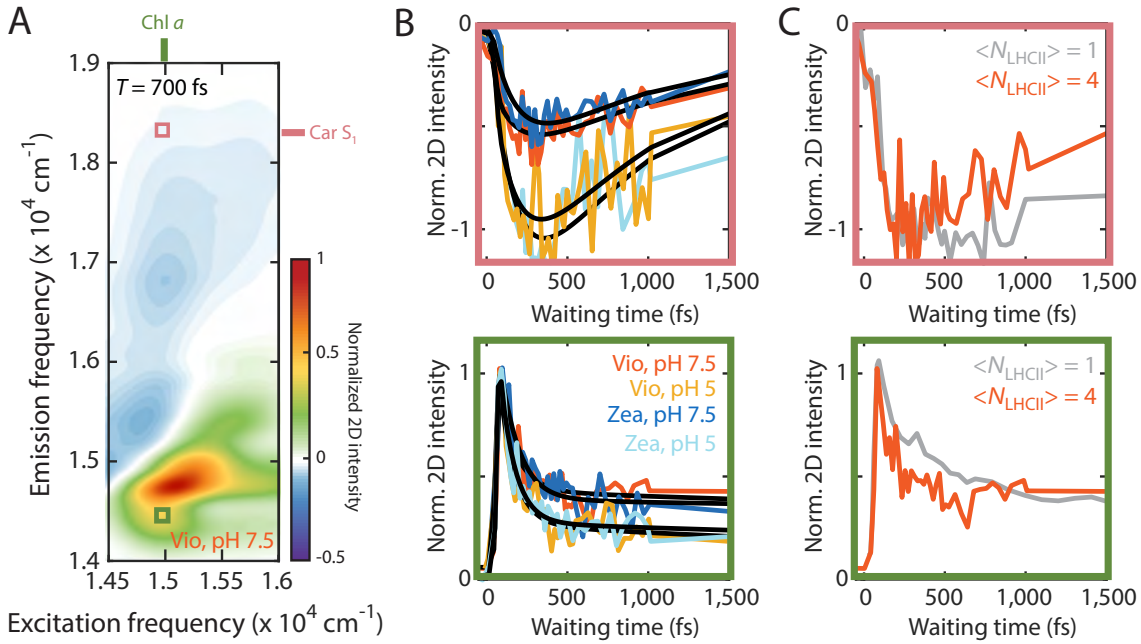

Figure 6-7: **2D spectrum and representative fits of $\langle N_{\mathrm{LHCII}} \rangle = 4$ nanodiscs probing dissipative Chl-to-Car energy transfer.** (A) Representative absorptive 2D spectrum of $\langle N_{\mathrm{LHCII}} \rangle = 4$ nanodiscs, with Vio as the xanthophyll cycle Car at pH 7.5 at $T = 700$ fs. The stick plots label the energy level of the Chl a donor and Car S_1 acceptor of the dissipative energy transfer pathway. (B) Fitted time traces showing the correlated decay of Chl a (bottom, green box in (A)) and growth of Car S_1 (top, pink box in (A)) populations for the initial 1,500 fs. The xanthophyll Car and pH conditions are color-coded in the traces and labeled inside the bottom panel. The top traces are normalized to the initial Chl a GSB/SE peak intensity immediately after photoexcitation (T = 30 fs) so that they visualize the relative intensity of the S_1 population. (ω_τ, ω_t) = (14,950, 18,350) (top), (14,950, 14,450) (bottom, in cm^{-1}). (C) Comparison of the dynamics between $\langle N_{\mathrm{LHCII}} \rangle = 1$ (gray) and $\langle N_{\mathrm{LHCII}} \rangle = 4$ (orange; Vio, pH 7.5 data are plotted) for the Chl a decay (bottom) and Car S_1 rise (top).

The other dissipative photophysical pathway, the dissipative Chl-to-Car energy transfer, appears as correlated decay of the Chl *a* Q_y donor and rise of the Car S_1 acceptor excited-state populations. These spectroscopic signatures appear in the excitation frequency range of the lowest-energy Chl *a* locus and a broad emission frequency range encompassing the energy levels of the Chl *a* GSB/SE as well as the Car S_1 ESA [289]. Figure 6-7A displays a representative 2D spectrum of $\langle N_{\mathrm{LHCII}} \rangle = 4$ nanodiscs at $T = 700$ fs in this frequency region. Only the spectrum for Vio-binding LHCII at pH 7.5 is shown, but the spectra for the other three conditions exhibited qualitatively similar overall spectral profiles. The waiting time traces in Figure 6-7B reveal the characteristic correlated decay of Chl *a* and growth of Car S_1 peaks on a 135 ± 30 fs timescale, indicating that the dissipative Chl-to-Car energy transfer channel is active in the presence of protein-protein interaction. In accordance with the fluorescence data as well as the Car internal conversion dynamics discussed above, this dissipative pathway is pH-dependent yet Zea-independent. At pH 5, the amplitude of the observed 135 ± 30 fs component increases by 20% regardless of the xanthophyll cycle Car. Notably, the 135 ± 30 fs timescale of the dissipative energy transfer extracted for $\langle N_{\mathrm{LHCII}} \rangle = 4$ nanodiscs is significantly faster than the ∼300 fs timescale observed for $\langle N_{\mathrm{LHCII}} \rangle = 1$, *i.e.*, in the absence of protein-protein interaction (Figure 6-7C; see Chapters 4 and 5 for $\langle N_{\mathrm{LHCII}} \rangle = 1$ data) [289, 299]. The LHCII-content-dependent behavior observed for this dissipative pathway is at variance with the trend observed for Car internal conversion, the other dissipative pathway, the timescale of which was found to be independent of $\langle N_{\mathrm{LHCII}} \rangle$.

6.7 Conclusion and Outlook

The series of observations from steady-state and time-resolved spectroscopic characterizations reveal that protein-protein interactions between LHCIIs lead to pH-dependent but Zea-independent dissipative photophysics, which are enhanced with increased protein-protein interaction. The nanodisc platform utilized here presents a novel *in vitro* membrane environment that is both fully controllable in protein content

and near-physiological, enabling quantitative analysis of the correlation between the extent of protein-protein interaction and that of dissipation. Further analysis of the 2D spectra is expected to reveal insights into the possibility of the existence of photophysical mechanisms that appear only in the presence of protein-protein interaction, distinct from the dissipative pathways that already exist in its absence. One such photophysical pathway is the relaxation of excitonically coupled xanthophyll cycle Car dimers, since the analysis of ΔA_{535} revealed the likely formation of these dimers in the presence of protein-protein interaction. A transient absorption study on Zea aggregates reported a shift in the S_1 ESA peak position as well as distinct relaxation kinetics compared to those of monomeric Zea molecules [308]; similar spectral and temporal behaviors may be revealed for the excitonically coupled xanthophyll cycle Car dimers.

Possible future directions include (1) characterization of other types of protein-protein interaction present in the PSII supercomplex that may be relevant to NPQ, *e.g.* the interactions between LHCII and PsbS, and (2) further extension of the nanodisc approach to more closely mimic the *in vivo* antenna network by incorporating other members of the PSII supercomplex. I discuss these two directions in more detail below.

6.7.1 Characterization of Protein-Protein Interaction between Light-Harvesting Complex II and Photosystem II Subunit S

Interactions between LHCIIs investigated in this work are only one of the several different the protein-protein interactions postulated to activate dissipative pathways. Another established yet underexplored interaction is that between LHCII and PsbS, as briefly pointed out in Section 6.5. Although debated, the current model for NPQ induced by LHCII-PsbS interaction assumes that the dimeric PsbS protein found in low light dissociates into a monomer and forms a LHCII-PsbS heterodimer upon exposure to high light [310]. The subsequent protein-protein interaction between LHCII

and PsbS within the heterodimer is thought to activate quenching by causing alterations to the conformation, and in turn, dissipative photophysical pathways of LHCII. Two recent studies using proteoliposomes that co-reconstitute LHCII and PsbS into a lipid membrane revealed PsbS-dependent fluorescence quenching, and proposed an enhancement in the electronic interactions between Chls and the dark S_1 of the Cars [129] or activation of a Chl-Chl charge transfer state [311] as the photophysical mechanisms for PsbS-dependent quenching. Many open questions remain, however, including about the reproducibility of these results [293] as well as the interaction geometry and the resultant conformational changes of the two proteins.

6.7.2 Extension of the Nanodisc Platform towards Mimicking the Native Protein Composition of Plant Thylakoids

Another interesting, longer-term research direction is to further extend the nanodisc platform, the power of which as a systematically controllable and near-native membrane platform for photosynthetic antenna complexes I showcased in Chapters 4−6, towards mimicking the native protein composition of plant thylakoids. The functional antenna array in the native thylakoid membrane that performs photosynthesis includes many different membrane proteins that are missing in the LHCII nanodiscs employed here, such as the minor complexes, core complexes and PsbS. Using the structural and photophysical insights obtained here for dissipation in LHCII-only arrays as a benchmark, the impact of additional parameters, such as the presence of minor complexes and/or core complexes, can be systematically interrogated within the nanodisc platform by constructing larger-sized nanodiscs [258].

6.8 Materials and Methods

6.8.1 Sample Preparation

Trimeric LHCII complexes were extracted from spinach leaves, purified and characterized as detailed in Appendix A, Section A.1. The Vio-binding form was obtained from

dark-adapted plants. The Zea-binding form was prepared by *in vitro* de-epoxidation of Vio in intact dark-adapted thylakoid membranes (Appendix A, Section A.1.2). The presence of Zea was verified by analyzing the pigment composition of the purified LHCII with high-performance liquid chromatography (HPLC, Figure A-1B and Table A.2).

Membrane nanodiscs containing an average LHCII content of one to four trimeric LHCII complexes per disc ($\langle N_{\mathrm{LHCII}} \rangle = 1{-}4$) were prepared with both Vio- and Zea-binding LHCII proteins as detailed in Appendix A, Section A.2, with ApoE422K as the membrane scaffold protein and soy asolectin lipid. Linear absorption spectra of the purified nanodisc products confirmed that the weakly binding Vio or Zea was retained during nanodisc reaction. All nanodisc assembly reactions were initially performed at neutral pH (pH 7.5). Low pH nanodisc samples were prepared by desalting the pH 7.5 products with 0.04 M MES, 0.02 M NaCl buffer (pH 5) on a desalting column (PD-10, GE Healthcare). The final optical density (OD) of all samples used for 2DES was 0.2 and 0.15 (per 0.5 mm) at the Chl *a* Q_y peak (675 nm) for the dataset obtained with spectrum 1 and spectrum 2, respectively.

6.8.2 Steady-State Spectroscopy

Linear absorption and steady-state fluorescence spectra were measured with a Cary 5000 spectrophotometer and a Cary Eclipse fluorimeter (Agilent), respectively, in 1 cm pathlength quartz cuvettes. For fluorescence measurements, the OD of the sample at the excitation wavelength was kept at $0.05 - 0.07$ per cm to ensure absence of any reabsorption effect. Excitation wavelengths of 436, 600, and 640 nm were used, and no excitation wavelength dependence was found in the fluorescence spectra. CD spectra were measured at 10°C on a Jasco J-1500 spectropolarimeter, in a 1 mm pathlength quartz cuvette. The OD of the sample was 0.1 per mm at 670 nm.

6.8.3 Fluorescence Lifetime Measurement

The fluorescence lifetime of LHCII was measured with time-correlated single photon counting (TCSPC) as described in detail in Chapter 4, Section 4.10.3, with identical excitation and emission filters to those used in Chapters 4 and 5 (Figure 4-10). A 1 mm pathlength flow quartz cuvette was used, and the sample solution was continuously flowed with a peristaltic pump during measurement to prevent sample photodegradation and thermal lensing effect. To prevent reabsorption effect, the OD of all samples at the excitation wavelength range was kept under 0.1 per mm. Excitation power dependence was checked at three different excitation powers (6 fJ, 20 fJ, and 60 fJ), and no singlet-singlet annihilation was observed (Figure 6-11).

6.8.4 Measurement of Time-Resolved Fluorescence Spectra

TRFS were measured with the TCSPC apparatus described above coupled with a commercial spectral interferometer (Gemini, NIREOS). Detailed information about the spectral interferometry setup and data analysis can be found elsewhere [312]. Briefly, the fluorescence emitted from the sample was sent into the spectral interferometer, and the glass wedges therein were scanned over a distance of several mm to generate the time-domain interferogram at each photon arrival time determined by the single-photon counting module. The fluorescence spectrum was recovered by Fourier transforming the time-domain data at each photon arrival time, yielding a 2D map of fluorescence as a function of wavelength and photon arrival time. The resolution of the wavelength axis was 0.35 nm. Due to the lower signal-to-noise ratio of this measurement than that of individual trace measurement with TCSPC, an excitation power of 20 fJ was used.

6.8.5 Fluorescence Correlation Spectroscopy

FCS measurements were performed as described in detail in Chapter 4, Section 4.10.4 with identical excitation spectrum and emission path optics (Figure 4-10). The concentration of each nanodisc sample was 10 nM, and the excitation laser fluence on the

sample plane was 888 nJ per cm^2. The correlation curves were fitted and analyzed using the same equations and parameters as described in Chapter 4.

6.8.6 Ultrabroadband Two-Dimensional Electronic Spectroscopy

A detailed description of the ultrabroadband 2DES setup is provided in Chapter 2 and in [226]. The spectral and temporal profiles of the laser pulses used in 2DES were identical to those described in Chapters 4 and 5 (Section 4.10.5, Figure 4-11). A pulse energy of 6.3 nJ was employed with a beam waist of 150 μm at the sample position, corresponding to an excitation density of $2.5 - 2.8 \times 10^{13}$ photons per pulse per cm^2, reported to be in the linear regime for LHCII [94]. τ was sampled in 0.5 fs steps in the range of $\tau = -200 - 200$ fs. T was incremented in steps of 20 fs for $T = -200 - 500$ fs, 40 fs for $T = 540 - 980$ fs, 1 ps for $T = 1 - 10$ ps, and 10 ps for $T = 10 - 100$ ps. The sample was circulated in a 0.5 mm pathlength quartz flow cell with a peristaltic pump to prevent photodegradation and repetitive excitation of the same spot. The sample reservoir was kept at 4°C throughout the measurement with a home-built water jacket cooling system. Each dataset was collected twice, on separate days with freshly prepared samples, to ensure reproducibility of the data. The integrity of the sample was confirmed by comparing the linear absorption spectra and fluorescence decay profiles before and after collection of each dataset.

6.8.7 Analysis of Two-Dimensional Spectra

Each waiting time trace reported here was generated by integrating the 2D signal intensity over finite frequency intervals in both frequencies (100 cm^{-1} in $\omega_\tau \times$ 100 cm^{-1} in ω_t, unless otherwise noted) around the center frequencies reported in each figure. Time constants were extracted by fitting each waiting time trace to an exponential function convolved with a Gaussian pulse with the time resolution (6.2 fs or 6.9 fs) of the experiment.

6.9 Supplementary Information

6.9.1 Supplementary Characterization of Nanodiscs

Detailed description of the analysis of the 280 nm absorbance

The average LHCII content per disc, $\langle N_{\mathrm{LHCII}} \rangle$, of the products, was quantitatively analyzed by inspection of the absorbance of each component of the nanodiscs (LHCII, membrane scaffold protein, and lipids) at 280 nm, where the membrane scaffold protein and lipid have non-zero absorbance and so contribute to the total absorbance along with the absorbance from LHCII. Using the reaction stoichiometry in Table A.3 and the known extinction coefficient for each component, the theoretical contributions from LHCII and from the membrane scaffold protein/lipid to the total absorbance at 280 nm were estimated. The dashed line in Figure 6-2B corresponds to the theoretical curve constructed by calculating the ratio of LHCII absorbance (A_{LHCII}) to membrane scaffold protein/lipid absorbance ($A_{\sim\mathrm{LHCII}}$) at 280 nm. The ratios obtained from experimental measurements of the purified nanodiscs are in agreement with the theoretical ratios, verifying successful production of LHCII nanodiscs with the desired $\langle N_{\mathrm{LHCII}} \rangle$.

Supplementary FCS data

Table 6.1: **Fitted diffusion time constants (τ_{D}), and the diffusion constants (D) and hydrodynamic radii (r) extracted from the fit.**[a]

	$\langle N_{\mathrm{LHCII}} \rangle$	τ_{D} (ms)	D (μm^2/s)	r (nm)
Detergent	–	0.83 ± 0.06	30.2 ± 2.3	7.1 ± 0.5
Nanodisc	1	1.76 ± 0.15	14.3 ± 1.3	15.1 ± 1.3
	2	2.08 ± 0.09	12.1 ± 0.6	17.8 ± 0.8
	3	2.56 ± 0.08	9.8 ± 0.3	21.9 ± 0.7
	4	2.92 ± 0.15	8.6 ± 0.5	25.0 ± 1.3

[a] Each entry reports mean ± std. dev. from five different sample preparations.

6.9.2 Supplementary Figures

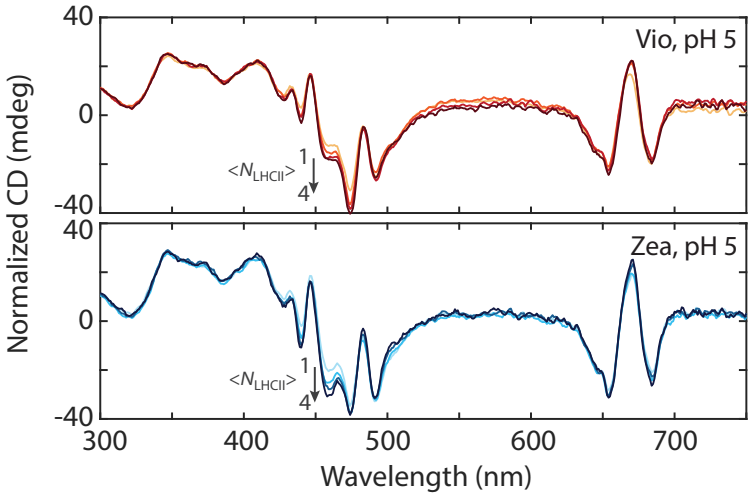

Figure 6-8: **CD spectra at pH 5.** CD spectra of LHCII nanodiscs with $\langle N_{\mathrm{LHCII}} \rangle$ = 1−4 with Vio (top) and Zea (bottom) as the xanthophyll cycle Car, at pH 5. The spectra are normalized to the absorbance at 650 nm. The arrows indicate the gradual growth of the 460 nm peak (dashed line) as $\langle N_{\mathrm{LHCII}} \rangle$ is increased from 1 to 4.

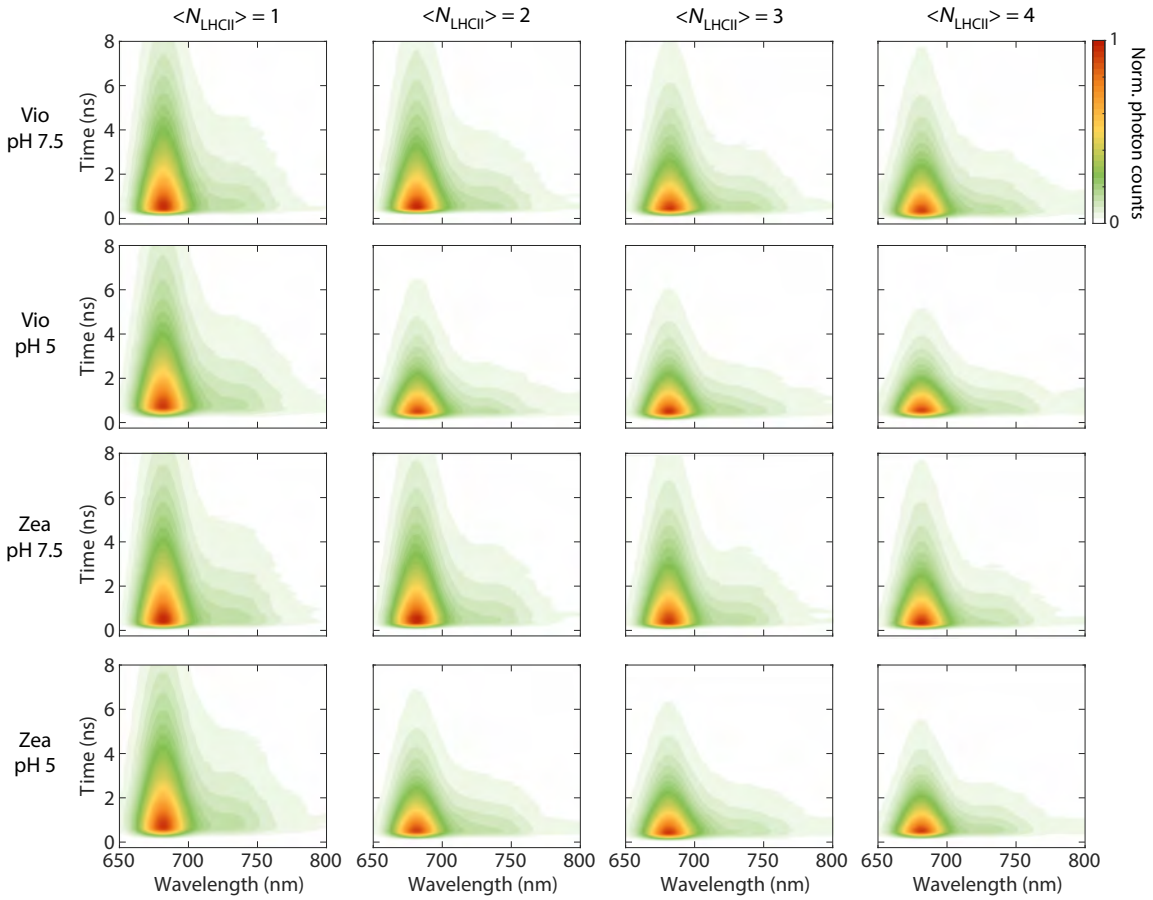

Figure 6-9: **Additional TRFS plots.** Normalized TRFS of LHCII nanodiscs with $\langle N_{\mathrm{LHCII}} \rangle = 1{-}4$ with both xanthophyll cycle Car and pH conditions.

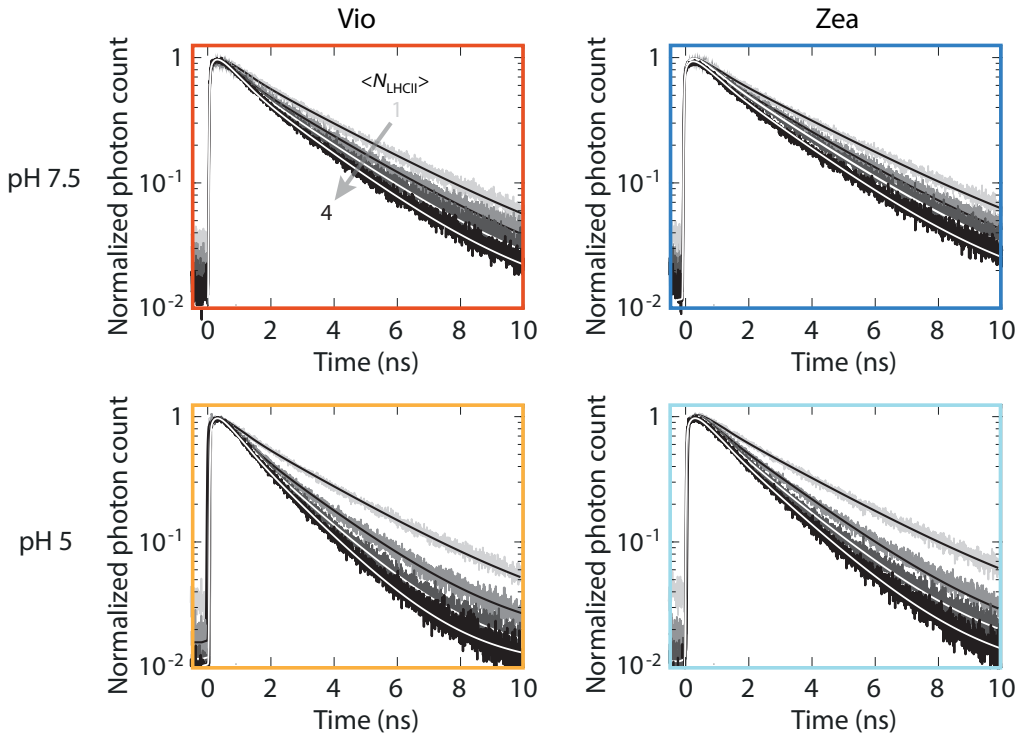

Figure 6-10: **Fitted fluorescence decay traces.** Normalized fluorescence decay profiles of LHCII nanodiscs with $\langle N_{\mathrm{LHCII}} \rangle = 1{-}4$ with the xanthophyll cycle Car and pH as indicated in the figure. The increase in $\langle N_{\mathrm{LHCII}} \rangle$ from one to four is color-coded in the decay traces with the shades of light gray to black.

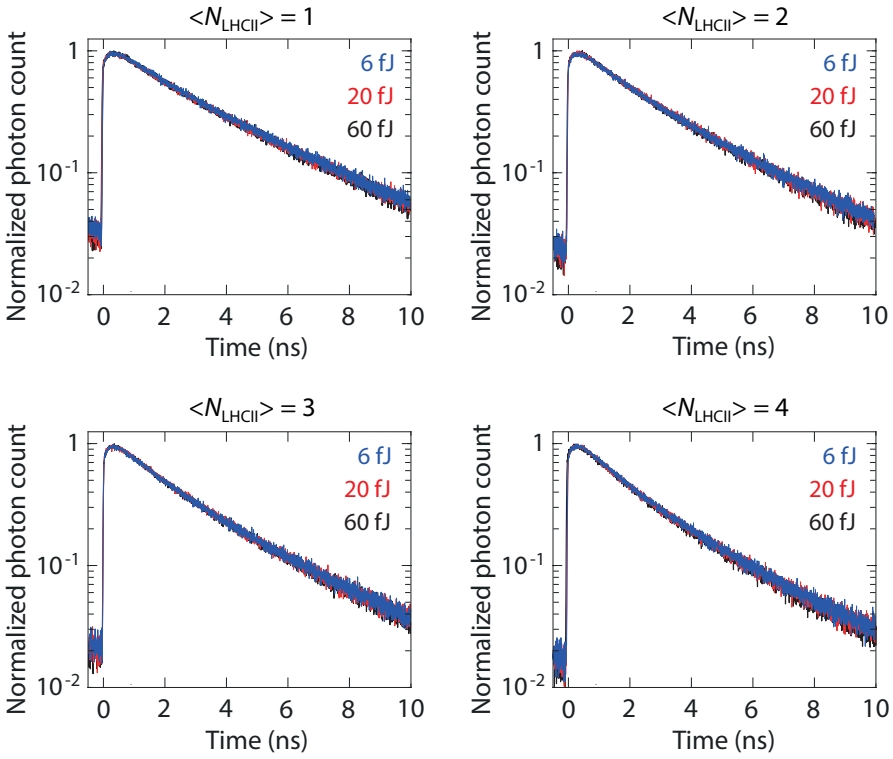

Figure 6-11: **Independence of the fluorescence decay profiles on excitation power.** Normalized fluorescence decay profiles of LHCII nanodiscs with $\langle N_{\mathrm{LHCII}} \rangle = 1-4$ measured with excitation powers of 6 fJ (blue), 20 fJ (red), and 60 fJ (black), confirming the absence of power dependence. The data are shown for LHCII-Zea at pH 7.5 only, but the same trend was observed for LHCII-Vio and at pH 5.

Appendix A

Sample Preparation Protocols

A.1 Extraction and Purification of Light-Harvesting Complex II

A.1.1 Isolation of Thylakoids

Stacked thylakoids were purified from leaves of spinach plants following a previously reported protocol [313] with minor modifications. Tissues were harvested and freshly homogenized in cold extraction buffer (0.5% milk powder, 0.4 M NaCl, 0.02 M Tricine/KOH, pH 7.8, 0.002 M $MgCl_2$ and 0.005 M ϵ-aminocaproic acid, 0.001 M phenylmethylsulfonyl fluoride and 0.001 M benzamidine as protease inhibitors). After filtration, samples were precipitated by centrifugation at 4,000 $\times$ g for 10 min at 4°C and then resuspended in hypotonic buffer (0.015 M NaCl, 0.005 M $MgCl_2$, 0.01 M HEPES/KOH, pH 7.5, and protease inhibitor). After centrifugation for 10 min at 10,000 $\times$ g at 4°C, thylakoids were resuspended in a buffer containing 0.4 M sorbitol, 0.015 M NaCl, 0.005 M $MgCl_2$, and 0.01 M HEPES/KOH, pH 7.5.

A.1.2 *In vitro* De-epoxidation of Violaxanthin

Zeaxanthin (Zea)-containing samples (discussed in Chapters 4−6) were prepared by *in vitro* de-epoxidation of violaxanthin (Vio) in intact thylakoid membranes. Thylakoids

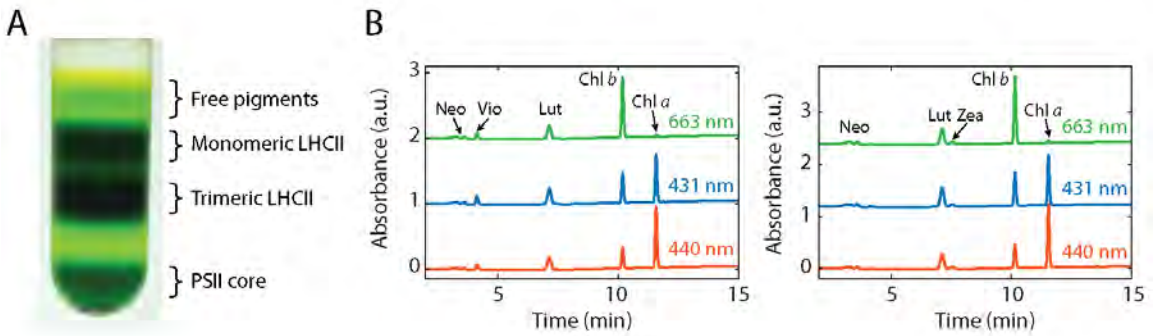

Figure A-1: **Purification and pigment composition analysis of trimeric LHCII.** (A) Representative image from sucrose gradient ultracentrifugation of spinach thylakoid. The band containing LHCII trimers were isolated and used for nanodisc preparation as well as spectroscopic measurements. (B) Representative HPLC chromatograms of dark-adapted (Vio-containing, left) and *in vitro* de-epoxidated (Zea-containing, right) LHCII trimers. The absorbance was simultaneously monitored at 440, 431, and 663 nm, which correspond to predominantly carotenoid (Car), Chl *a*, and Chl *b* absorption, respectively.

were diluted to 50 μg/mL of chlorophyll (Chl) in 0.33 M sorbitol, 0.005 M $MgCl_2$, 0.01 M NaCl, 0.04 M MES/NaOH, pH 5.1, 0.02 M ascorbate, 0.1% (w/v) bovine serum albumin, and protease inhibitors. Thylakoids were stirred for 2 h at room temperature (RT) and then centrifuged at 10,000 $\times$ g for 10 min at 4°C.

A.1.3 Purification of Light-Harvesting Complex II Trimers

Thylakoid membranes at a concentration of 3 mg Chl were washed with 0.005 M EDTA and resuspended at a concentration of 1 mg/mL Chl in 0.01 M HEPES, pH 7.5. The sample was then solubilized at a final concentration of 0.5 mg/mL Chl, by adding 1.6% *n*-dodecyl α-D-maltopyranoside (α-DM) and 0.01 M HEPES, pH 7.5 and vortexing for 1 min. After 10 min of incubation on ice, the sample was centrifuged at 15,000 $\times$ g for 10 min to eliminate unsolubilized material. Trimeric light-harvesting complex II (LHCII) complexes were isolated by sucrose gradient ultracentrifugation with an SW28 rotor (Beckman Coulter), on a 0.1−1 M sucrose gradient containing 0.03% α-DM and 0.01 M HEPES, 0.02 M NaCl, pH 7.5 for 40 h at 103,000 $\times$ g at 4°C (Figure A-1A). The purified LHCII sample was stored at −80°C until further use, and thawed immediately before each laser measurement. Sample integrity was examined

with sodium dodecyl sulfate polyacrylamide gel electrophoresis (SDS-PAGE), linear absorption and steady-state fluorescence spectra.

Table A.1: **Pigment composition of purified LHCII used in Chapters 3−5.**[a]

Pigment	LHCII-Vio	LHCII-Zea
Chl *a*/Chl *b*	1.26 ± 0.02	1.19 ± 0.02
Chl *a* per mol	7.8 ± 0.09	7.6 ± 0.09
Chl *b* per mol	6.2 ± 0.04	6.4 ± 0.04
Neoxanthin (Neo)	0.7 ± 0.05	0.8 ± 0.05
Vio	0.6 ± 0.01	0.08 ± 0.01
Lutein (Lut)	2.0 ± 0.04	2.2 ± 0.04
Zea	0	0.4 ± 0.06
Chl/Car	4.3 ± 0.12	4.1 ± 0.12
Chl total	14	14
Car total	3.3 ± 0.09	3.4 ± 0.10

[a] Each entry represents the mean ± std. dev. from three measurements.

Table A.2: **Pigment composition of purified LHCII used in Chapter 6.**[a]

Pigment	LHCII-Vio	LHCII-Zea
Chl *a*/Chl *b*	1.28 ± 0.03	1.30 ± 0.03
Chl *a* per mol	7.8 ± 0.08	7.9 ± 0.07
Chl *b* per mol	6.1 ± 0.08	6.1 ± 0.04
Neo	0.94 ± 0.09	1.35 ± 0.06
Vio	0.61 ± 0.01	0.11 ± 0.01
Lut	2.06 ± 0.05	2.14 ± 0.05
Zea	0	0.67 ± 0.01
Chl/Car	3.88 ± 0.15	3.28 ± 0.02
Chl total	14	14
Car total	3.6 ± 0.14	4.3 ± 0.10

[a] Each entry represents the mean ± std. dev. from four measurements.

A.1.4 Analysis of Pigment Composition

Pigments were extracted from purified LHCII trimers with 80% acetone and centrifuged two times at 20,000 × g for 15 min at 4°C. The supernatant was analyzed by high-performance liquid chromatography (HPLC) as described in [314]. Representative HPLC chromatograms of the purified LHCII complexes used in the work

described in Chapters 3−5 are shown in Figure A-1B. The analyzed pigment compositions of LHCII used in Chapters 3−5 and Chapter 6 are summarized in Tables A.1 and A.2, respectively.

A.2 Production and Characterization of Light-Harvesting Complex II Membrane Nanodiscs

A.2.1 Assembly of Membrane Nanodiscs Containing a Single Light-Harvesting Complex II

Assembly of nanodiscs embedding a single LHCII was carried out with two different membrane scaffold proteins, MSP1E3D1 and ApoE422K. The former yields smaller disc sizes of ∼13 nm in diameter, while the latter forms larger nanodiscs of ∼25−30 nm diameters [258, 281]. The nanodisc samples were produced immediately before any spectroscopy measurement, and all spectroscopic measurements were completed within 24 hours of sample preparation.

Overexpression and purification of membrane scaffold protein MSP1E3D1

The membrane scaffold protein MSP1E3D1 was overexpressed from the plasmid pMSP1E3D1 containing a 6× histidine tag and kanamycin antibiotic resistance (Addgene), and purified with nickel affinity chromatography according to previously reported protocols [152, 258]. The mass and purity of the final product were verified by reverse-phase liquid chromatography mass spectrometry (LC-MS) and denaturing SDS-PAGE (Figure A-2A). The purified protein was concentrated with a 10 kDa cutoff centrifugal filter to a final concentration of several hundreds of μM (typically $200 - 600$ μM) and aliquoted. Protein concentration was determined using the absorbance of the protein at 280 nm and the known extinction coefficient of MSP1E3D1 at this wavelength [258]. The aliquots were flash frozen in liquid nitrogen and stored at −80°C until further use.

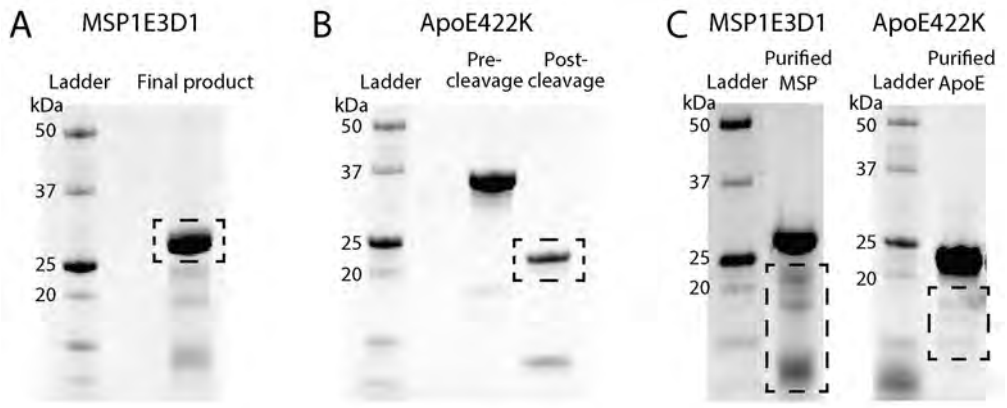

Figure A-2: **SDS-PAGE of purified MSP1E3D1 and ApoE422K membrane scaffold proteins.** (A) MSP1E3D1, and (B) ApoE422K before and after thrombin cleavage reaction. The bands that corresponds to the final, purified product are indicated in each panel with dashed boxes (32.6 kDa for MSP1E3D1, and 22 kDa for ApoE422K). (C) SDS-PAGE of both proteins (left: MSP1E3D1, right: ApoE422K) at saturating concentrations (~ 100 μM loaded in each lane) for evaluation of purity. The impurity bands at lower weights are indicated with dashed boxes.

Overexpression and purification of membrane scaffold protein ApoE422K

ApoE422K, the N-terminal 22 kDa fragment of human apolipoprotein E4, was overexpressed and purified following a previously reported protocol with minor modifications [315]. Briefly, thioredoxin-ApoE422K-full length fusion protein was overexpressed from the plasmid pD451-SR containing containing a 6× histidine tag and kanamycin antibiotic resistance (DNA 2.0), and purified with nickel affinity chromatography similarly to the purification of MSP1E3D1. After nickel affinity purification, thrombin (Sigma Aldrich) was added to the eluate for the cleavage of thioredoxin, and the mixture was incubated overnight at RT. SDS-PAGE was used to monitor the progress of the cleavage reaction (see the protein sequence below and Figure A-2B). Following complete reaction, the product was purified once more with nickel affinity chromatography. The purified protein was concentrated with a 10 kDa cutoff centrifugal filter to a final concentration of several hundreds of μM (typically $100 - 300$ μM) and aliquoted. Protein concentration was determined using the absorbance of the protein at 280 nm and the extinction coefficient of ApoE422K at this wavelength ($30,940$ $\mathrm{M^{-1}cm^{-1}}$). The aliquots were flash frozen in liquid nitrogen and stored at $-80°$C

until further use.

Protein sequence for thioredoxin-ApoE422K-full length fusion protein and thrombin cleavage sites

M S D K I I H L T D D S F D T D V L K A D G A I L V D F W A E W C G
P C K M I A P I L D E I A D E Y Q G K L T V A K L N I D Q N P G T A P
K Y G I R G I P T L L L F K N G E V A A T K V G A L S K G H L K E F L
N A N L A G S G S G H S S **G L V P R** G S G M K E T A A A K F E R Q H
M D S P D L G T D D D D K A L **V P R G** S G H H H H H H H H D Y D I P
T T E N L Y F Q G K V E Q A V E T E P E P E L R Q Q T E W Q S G Q R
W E L A L G R F W D Y L R W V Q T L S E Q V Q E E L L S S Q V T Q E
L R A L M D E T M K E L K A Y K S E L E E Q L T P V A E E T R A R L
S K E L Q A A Q A R L G A D M E D V R G R L V Q Y R G E V Q A M L G
Q S T E E L R V R L A S H L R K L R K R L L R D A D D L Q K R L A V Y Q A G

The thrombin cleavage sites are labeled in bold. The sequence shaded in gray is the cleavage product that was purified through the second nickel affinity column chromatography and saved for nanodisc production.

Integrity of the purified membrane scaffold proteins

As shown in Figure A-2C, the SDS-PAGE images show several low molecular-weight bands below the main band for both membrane scaffold proteins post-purification. These bands originate from impurities known as endotoxin, which are unable to be separated with nickel affinity chromatography, and thus are commonly found impurities in protein purification [316]. While the intensities of these impurity bands vary in each preparation, they are typically $< 20\%$ of that of the main band.

Preparation of lipids

Preparation of lipids was performed similarly to the method reported in earlier work [146, 147]. Soy asolectin, a mixture of phospholipids, was purchased from Sigma

Aldrich and used without further purification. A 25 mg/mL stock solution was prepared by solubilizing asolectin in 0.05 M HEPES, 0.1 M NaCl, 0.04 M sodium cholate (pH 7.5). The molar concentration of the lipid in the stock solution was determined by phosphorus assay [317].

For nanodisc assembly reactions with glycolipid mixtures, monogalactosyldiacylglycerol (MGDG), digalactosyldiacylglycerol (DGDG), sulfoquinovosyldiacylglycerol (SQDG), and phosphatidylglycerol (PG) were purchased from Avanti Polar Lipids, and each solubilized to a 5 mg/mL concentration in 0.05 M HEPES, 0.1 M NaCl, 0.04 M sodium cholate (pH 7.5).

The prepared stock lipid solutions were aliquoted and degassed of oxygen by bubbling in N_2 gas. The aliquots were flash frozen and stored at $-80°C$ until further use.

Assembly of 13 nm diameter LHCII nanodiscs with soy asolectin lipid

Purified MSP1E3D1, soy asolectin, and detergent-solubilized LHCII were mixed at a molar ratio of 1 : 55 : 0.125. 400% excess MSP1E3D1 and lipid were used to minimize contamination of the sample with nanodiscs embedding multiple LHCIIs in order to prevent fluorescence quenching by LHCII self-aggregation. The MSP1E3D1:lipid molar ratio was systematically varied to optimize the yield of the product, and an optimal molar ratio of 1 : 55 : 0.125 was determined. The mixture was incubated at 4°C shaking for 1 h. To remove the detergent, Bio-Beads SM-2 adsorbents (Bio-Rad) were added to the reaction and incubated at 4°C shaking for 1 h. Typically, 50 mg of adsorbents were added per mL of reaction volume. Bio-Beads were removed by centrifugation at 4,000 RPM for 20 min.

The product was purified by the 6× histidine tag of MSP1E3D1 on a nickel affinity column. Following sample equilibration for 2 h at 4°C on a nutating mixer, column flow-through was collected and the column was washed with three column volumes of 0.01 M HEPES, 0.02 M NaCl, 0.02 M imidazole, pH 7.5. The sample was eluted with 0.01 M HEPES, 0.02 M NaCl, 0.4 M imidazole, pH 7.5 in fractions. Fractions containing LHCII-loaded nanodiscs were determined by SDS-PAGE and linear ab-

sorption. Imidazole in the purified nanodiscs was removed by buffer exchange into 0.01 M HEPES, 0.02 M NaCl, 0.5 mM EDTA, pH 7.5. The sample was further buffer exchanged into 0.05 M HEPES, 0.15 M NaCl, pH 7.5.

The loaded nanodiscs were further purified by fast protein liquid chromatography (FPLC) with a BioLogic DuoFlow (Bio-Rad) on a Superdex 200 Increase 10/300 GL (GE Healthcare Life Sciences) at a flow rate of 0.75 mL min^{-1} in 0.05 M HEPES, 0.15 M NaCl, pH 7.5. Fractions of the main peak were collected and analyzed by linear absorption, SDS-PAGE, and transmission electron microscopy (TEM) to identify the peak containing LHCII nanodiscs. TEM samples were prepared by the negative staining method [318] with 2% uranyl acetate on negatively glow-discharged 400-mesh Cu-carbon coated films (Electron Microscopy Sciences). Samples were imaged on a FEI Tecnai (G2 Spirit TWIN) electron microscope operating at 120 kV. Characterization results are shown in Chapter 4, Figure 4-2.

Assembly of 13 nm diameter LHCII nanodiscs with glycolipids

To mimic the lipid composition of the native plant thylakoid membrane (∼50% MGDG, ∼30% DGDG, ∼5−12% SQDG, and ∼5−12% PG) [319], glycolipid mixture containing 50% MGDG, 27% DGDG, 12% SQDG and 11% PG was prepared by mixing the stock aliquots prepared as described in Section A.2.1. Lipid mixture without the non-bilayer-forming lipid MGDG was also prepared (62% DGDG, 17% SQDG, 21% PG). Each lipid mixture was added to the nanodisc reaction at the same molar ratio as for the reaction with asolectin (1 : 55 : 0.125). The nanodiscs were prepared and characterized using the same protocol and methods described above for soy asolectin (Figure A-3).

Assembly of 25 nm diameter LHCII nanodiscs with soy asolectin lipid

Larger-sized LHCII nanodiscs with ApoE422K membrane scaffold protein were prepared similarly to those with MSP1E3D1. 400% excess ApoE422K and lipid were used to minimize contamination of the sample with nanodiscs embedding multiple LHCIIs in order to prevent fluorescence quenching by LHCII self-aggregation. Stoi-

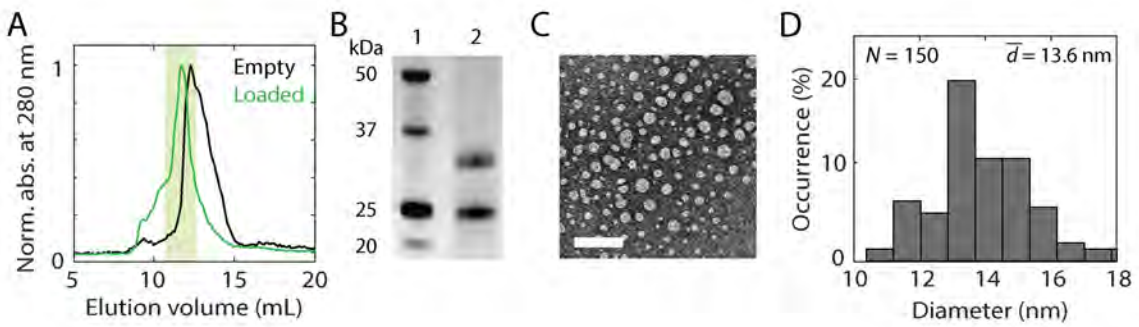

Figure A-3: **Characterization of LHCII nanodiscs with glycolipids.** (A) Fast protein liquid chromatogram of empty (black) and loaded (green) LHCII nanodisc. Shaded area indicates the fraction of loaded discs that was stored for spectroscopic measurements. (B) SDS-PAGE (lane 1: protein standard, lane 2: LHCII nanodisc). Both the membrane scaffold protein (MSP1E3D1, 32.6 kDa) and LHCII (25−27 kDa) bands are identified. (C) Representative TEM image of the produced LHCII nanodiscs. Scale bar is 50 nm. (D) Size distribution analyzed for 150 objects imaged with TEM. Mean diameter ($\bar{d}$) is 13.6 nm.

chiometry of the components was systematically varied to optimize the yield of the product, and an optimal molar ratio of ApoE422K : LHCII: lipid = 1 : 0.042 : 180 was determined.

Incubation, removal of detergent, nickel affinity purification, and buffer exchange were performed exactly as described for the 13 nm diameter nanodiscs. FPLC purification could not be performed because the sample stuck to the size exclusion column, resulting in > 90% loss of the product. The product was characterized with linear absorption, SDS-PAGE, and TEM as described above (Figure 6-2, $\langle N_{\mathrm{LHCII}} \rangle = 1$).

A.2.2 Assembly of Membrane Nanodiscs Containing Multiple Light-Harvesting Complex II Proteins

Purified ApoE422K, soy asolectin lipid, and detergent-solubilized LHCII were mixed at systematically varied molar ratios to produce nanodiscs as shown in Table A.3. Incubation, removal of detergent, nickel affinity purification, and buffer exchange were performed exactly as described for nanodiscs containing a single LHCII complex. Because the LHCIIs do not have histidine tags, self-aggregates of LHCIIs not incorporated into the discs were removed in the flow-through and washes during

Table A.3: **Stoichiometry of the nanodisc reactions (per nanodisc).**

$\langle N_{\mathrm{LHCII}} \rangle$	2	3	4
LHCII	2	3	4
ApoE422K	6	6	6
Asolectin lipid	1,099.8	1,009.7	918.9

nickel affinity purification. FPLC purification could not be performed because the sample stuck to the size exclusion column, resulting in $> 90\%$ loss of the product. The product was characterized with linear absorption, SDS-PAGE, TEM, and fluorescence correlation spectroscopy (FCS). The characterization results and additional descriptions are included in Chapter 6, Section 6.9.1 (Figure 6-2 and Table 6.1).

Bibliography

[1] Lewis, N. S. & Nocera, D. G. Powering the planet: Chemical challenges in solar energy utilization. *Proc. Natl. Acad. Sci. U. S. A* **103**, 15729–15735 (2006).

[2] Blankenship, R. E. *et al.* Comparing photosynthetic and photovoltaic efficiencies and recognizing the potential for improvement. *Science* **332**, 805–809 (2011).

[3] Croce, R. & van Amerongen, H. Natural strategies for photosynthetic light harvesting. *Nat. Chem. Biol.* **10**, 492 (2014).

[4] Blankenship, R. E. *Molecular Mechanisms of Photosynthesis* (John Wiley & Sons, 2014).

[5] Scholes, G. D., Fleming, G. R., Olaya-Castro, A. & van Grondelle, R. Lessons from nature about solar light harvesting. *Nat. Chem.* **3**, 763 (2011).

[6] Martin, A. M. *Bioconversion of Waste Materials to Industrial Products* (Springer Science & Business Media, 2012).

[7] Larkum, A. W. D. Limitations and prospects of natural photosynthesis for bioenergy production. *Curr. Opin. Biotechnol.* **21**, 271–276 (2010).

[8] van Amerongen, H., Valkunas, L. & van Grondelle, R. *Photosynthetic Excitons* (World Scientific, Singapore, 2000).

[9] McConnell, I., Li, G. & Brudvig, G. W. Energy conversion in natural and artificial photosynthesis. *Chem. Biol.* **17**, 434–447 (2010).

[10] Ishizaki, A. & Fleming, G. R. Quantum coherence in photosynthetic light harvesting. *Annu. Rev. Condens. Matter Phys.* **3**, 333–361 (2012).

[11] Chenu, A. & Scholes, G. D. Coherence in energy transfer and photosynthesis. *Annu. Rev. Phys. Chem.* **66**, 69–96 (2015).

[12] Mirkovic, T., Ostroumov, E. E., Anna, J. M., van Grondelle, R. & Scholes, G. D. Light absorption and energy transfer in the antenna complexes of photosynthetic organisms. *Chem. Rev.* **117**, 249–293 (2017).

[13] Mustárdy, L. & Garab, G. Granum revisited. A three-dimensional model−where things fall into place. *Trends Plant Sci.* **8**, 117–122 (2003).

[14] Mullineaux, C. W. Function and evolution of grana. *Trends Plant Sci.* **10**, 521–525 (2005).

[15] Pribil, M., Labs, M. & Leister, D. Structure and dynamics of thylakoids in land plants. *J. Exp. Bot.* **65**, 1955–1972 (2014).

[16] van Bezouwen, L. S. *et al.* Subunit and chlorophyll organization of the plant photosystem II supercomplex. *Nat. Plants* **3**, 17080 (2017).

[17] Liu, Z. *et al.* Crystal structure of spinach major light-harvesting complex at 2.72 Å resolution. *Nature* **428**, 287–292 (2004).

[18] Dekker, J. P. & Boekema, E. J. Supramolecular organization of thylakoid membrane proteins in green plants. *Biochim. Biophys. Acta − Bioenerg.* **1706**, 12–39 (2005).

[19] Caffarri, S., Kouřil, R., Kereïche, S., Boekema, E. J. & Croce, R. Functional architecture of higher plant photosystem II supercomplexes. *EMBO J.* **28**, 3052–3063 (2009).

[20] Jansson, S. A guide to the *Lhc* genes and their relatives in *Arabidopsis*. *Trends Plant Sci.* **4**, 236–240 (1999).

[21] Standfuss, J. & Kühlbrandt, W. The three isoforms of the light-harvesting complex II. Spectroscopic features, trimer formation, and functional roles. *J. Biol. Chem.* **279**, 36884–36891 (2004).

[22] Crepin, A. & Caffarri, S. Functions and evolution of Lhcb isoforms composing LHCII, the major light harvesting complex of photosystem II of green eukaryotic organisms. *Curr. Protein Pept. Sci.* **19**, 699–713 (2018).

[23] Chitnis, P. R. & Thornber, J. P. The major light-harvesting complex of Photosystem II: Aspects of its molecular and cell biology. *Photosynth. Res.* **16**, 41–63 (1988).

[24] Dainese, P. & Bassi, R. Subunit stoichiometry of the chloroplast photosystem II antenna system and aggregation state of the component chlorophyll a/b binding proteins. *J. Biol. Chem.* **266**, 8136–8142 (1991).

[25] van Amerongen, H. & van Grondelle, R. Understanding the energy transfer function of LHCII, the major light-harvesting complex of green plants. *J. Phys. Chem. B* **105**, 604–617 (2001).

[26] Barros, T., Royant, A., Standfuss, J., Dreuw, A. & Kühlbrandt, W. Crystal structure of plant light-harvesting complex shows the active, energy-transmitting state. *EMBO J.* **28**, 298–306 (2009).

[27] Novoderezhkin, V. I., Palacios, M. A., van Amerongen, H. & van Grondelle, R. Excitation dynamics in the LHCII complex of higher plants: Modeling based on the 2.72 Å crystal structure. *J. Phys. Chem. B* **109**, 10493–10504 (2005).

[28] Liguori, N., Periole, X., Marrink, S. J. & Croce, R. From light-harvesting to photoprotection: Structural basis of the dynamic switch of the major antenna complex of plants (LHCII). *Sci. Rep.* **5**, 15661 (2015).

[29] Lambrev, P. H., Akhtar, P. & Tan, H.-S. Insights into the mechanisms and dynamics of energy transfer in plant light-harvesting complexes from two-dimensional electronic spectroscopy. *Biochim. Biophys. Acta − Bioenerg.* **1861**, 148050 (2020).

[30] Bassi, R., Høyer-Hansen, G., Barbato, R., Giacometti, G. M. & Simpson, D. J. Chlorophyll-proteins of the photosystem II antenna system. *J. Biol. Chem.* **262**, 13333–13341 (1987).

[31] Gouterman, M. Spectra of porphyrins. *J. Mol. Spectrosc.* **6**, 138–163 (1961).

[32] Kadish, K. M. *Porphyrin Science: With Applications to Chemistry, Physics, Materials Science, Engineering, Biology and Medicine*, vol. 1 (World Scientific, 2010).

[33] Linnanto, J. & Korppi-Tommola, J. Semiempirical PM5 molecular orbital study on chlorophylls and bacteriochlorophylls: Comparison of semiempirical, *ab initio*, and density functional results. *J. Comput. Chem.* **25**, 123–138 (2004).

[34] Reimers, J. R. *et al.* Assignment of the Q-bands of the chlorophylls: Coherence loss via Q_x−Q_y mixing. *Sci. Rep.* **3**, 2761 (2013).

[35] Hughes, J. L., Conlon, B., Wydrzynski, T. & Krausz, E. The assignment of Q_y (1,0) vibrational structure and Q_x for chlorophyll *a*. *Phys. Procedia* **3**, 1591–1599 (2010).

[36] Bricker, W. P. *et al.* Non-radiative relaxation of photoexcited chlorophylls: Theoretical and experimental study. *Sci. Rep.* **5**, 13625 (2015).

[37] van Zandvoort, M. A. M. J., Wrobel, D., Lettinga, P., van Ginkel, G. & Levine, Y. K. The orientation of the transition dipole moments of chlorophyll *a* and pheophytin *a* in their molecular frame. *Photochem. Photobiol.* **62**, 299–308 (1995).

[38] Connolly, J. S., Janzen, A. F. & Samuel, E. B. Fluorescence lifetimes of chlorophyll *a*: Solvent, concentration and oxygen dependence. *Photochem. Photobiol.* **36**, 559–563 (1982).

[39] Pfarrherr, A., Teuchner, K., Leupold, D. & Hoffmann, P. Chlorophyll *b* in solution: Fluorescence lifetimes, absorption and emission spectra as criteria of purity. *J. Photochem. Photobiol. B, Biol.* **9**, 35–41 (1991).

[40] Moya, I., Silvestri, M., Vallon, O., Cinque, G. & Bassi, R. Time-resolved fluorescence analysis of the photosystem II antenna proteins in detergent micelles and liposomes. *Biochemistry* **40**, 12552–12561 (2001).

[41] Peterman, E. J., Dukker, F. M., van Grondelle, R. & van Amerongen, H. Chlorophyll *a* and carotenoid triplet states in light-harvesting complex II of higher plants. *Biophys. J.* **69**, 2670–2678 (1995).

[42] Shenai, P. M., Fernandez-Alberti, S., Bricker, W. P., Tretiak, S. & Zhao, Y. Internal conversion and vibrational energy redistribution in chlorophyll A. *J. Phys. Chem. B* **120**, 49–58 (2016).

[43] Meneghin, E., Leonardo, C., Volpato, A., Bolzonello, L. & Collini, E. Mechanistic insight into internal conversion process within Q-bands of chlorophyll *a*. *Sci. Rep.* **7**, 11389 (2017).

[44] Fresch, E. & Collini, E. Relaxation dynamics of chlorophyll *b* in the sub-ps ultrafast timescale measured by 2D electronic spectroscopy. *Int. J. Mol. Sci.* **21**, 2836 (2020).

[45] Dong, L.-Q., Niu, K. & Cong, S.-L. Theoretical study of vibrational relaxation and internal conversion dynamics of chlorophyll-a in ethyl acetate solvent in femtosecond laser fields. *Chem. Phys. Lett.* **432**, 286–290 (2006).

[46] Dong, L.-Q., Niu, K. & Cong, S.-L. Theoretical analysis of internal conversion pathways and vibrational relaxation process of chlorophyll-a in ethyl ether solvent. *Chem. Phys. Lett.* **440**, 150–154 (2007).

[47] Hudson, B. & Kohler, B. Linear polyene electronic structure and spectroscopy. *Annu. Rev. Phys. Chem.* **25**, 437–460 (1974).

[48] Tavan, P. & Schulten, K. Electronic excitations in finite and infinite polyenes. *Phys. Rev. B* **36**, 4337 (1987).

[49] Polívka, T. & Sundström, V. Ultrafast dynamics of carotenoid excited states − from solution to natural and artificial systems. *Chem. Rev.* **104**, 2021–2072 (2004).

[50] Llansola-Portoles, M. J., Pascal, A. A. & Robert, B. Electronic and vibrational properties of carotenoids: from *in vitro* to *in vivo*. *J. R. Soc. Interface* **14**, 20170504 (2017).

[51] Gall, A., Pascal, A. A. & Robert, B. Vibrational techniques applied to photosynthesis: Resonance Raman and fluorescence line-narrowing. *Biochim. Biophys. Acta − Bioenerg.* **1847**, 12–18 (2015).

[52] Polívka, T. & Sundström, V. Dark excited states of carotenoids: Consensus and controversy. *Chem. Phys. Lett.* **477**, 1–11 (2009).

[53] de Weerd, F. L., van Stokkum, I. H. M. & van Grondelle, R. Subpicosecond dynamics in the excited state absorption of all-*trans*-β-carotene. *Chem. Phys. Lett.* **354**, 38–43 (2002).

[54] Rondonuwu, F. S., Watanabe, Y., Fujii, R. & Koyama, Y. A first detection of singlet to triplet conversion from the $1^1B_u^-$ to the 1^3A_g state and triplet internal conversion from the 1^3A_g to the 1^3B_u state in carotenoids: Dependence on the conjugation length. *Chem. Phys. Lett.* **376**, 292–301 (2003).

[55] Buckup, T. *et al.* Pump-probe and pump-deplete-probe spectroscopies on carotenoids with $N = 9 - 15$ conjugated bonds. *J. Chem. Phys.* **125**, 194505 (2006).

[56] Niedzwiedzki, D. *et al.* Ultrafast dynamics and excited state spectra of open-chain carotenoids at room and low temperatures. *J. Phys. Chem. B* **111**, 5984–5998 (2007).

[57] Balevičius Jr., V., Abramavicius, D., Polívka, T., Galestian Pour, A. & Hauer, J. A unified picture of S* in carotenoids. *J. Phys. Chem. Lett.* **7**, 3347–3352 (2016).

[58] Ostroumov, E. E., Mulvaney, R. M., Cogdell, R. J. & Scholes, G. D. Broadband 2D electronic spectroscopy reveals a carotenoid dark state in purple bacteria. *Science* **340**, 52–56 (2013).

[59] Beck, W. F., Bishop, M. M., Roscioli, J. D., Ghosh, S. & Frank, H. A. Excited state conformational dynamics in carotenoids: Dark intermediates and excitation energy transfer. *Arch. Biochem. Biophys.* **572**, 175–183 (2015).

[60] Frank, H. A. *et al.* Spectroscopic properties of spheroidene analogs having different extents of π-electron conjugation. *J. Phys. Chem. A* **101**, 149–157 (1997).

[61] Andersson, P. O. & Gillbro, T. Photophysics and dynamics of the lowest excited singlet state in long substituted polyenes with implications to the very long-chain limit. *J. Chem. Phys.* **103**, 2509–2519 (1995).

[62] Papagiannakis, E. *et al.* Excited-state dynamics of carotenoids in light-harvesting complexes. 1. Exploring the relationship between the S_1 and S* states. *J. Phys. Chem. B* **110**, 5727–5736 (2006).

[63] Macpherson, A. N. & Gillbro, T. Solvent dependence of the ultrafast S_2-S_1 internal conversion rate of β-carotene. *J. Phys. Chem. A* **102**, 5049–5058 (1998).

[64] Maiuri, M. *et al.* Solvent-dependent activation of intermediate excited states in the energy relaxation pathways of spheroidene. *Phys. Chem. Chem. Phys.* **14**, 6312–6319 (2012).

[65] Christensen, R. L. *et al.* Energetics and dynamics of the low-lying electronic states of constrained polyenes: Implications for infinite polyenes. *J. Phys. Chem. A* **117**, 1449–1465 (2013).

[66] Yan, H., Zhang, P., Wang, C., Liu, Z. & Chang, W. Two lutein molecules in LHCII have different conformations and functions: Insights into the molecular mechanism of thermal dissipation in plants. *Biochem. Biophys. Res. Commun.* **355**, 457–463 (2007).

[67] Son, M., Pinnola, A., Bassi, R. & Schlau-Cohen, G. S. The electronic structure of lutein 2 is optimized for light harvesting in plants. *Chem* **5**, 575–584 (2019).

[68] Balevičius Jr., V. *et al.* Fine control of chlorophyll-carotenoid interactions defines the functionality of light-harvesting proteins in plants. *Sci. Rep.* **7**, 13956 (2017).

[69] Demmig-Adams, B., Garab, G., Adams III, W. & Govindjee. *Non-photochemical Quenching and Energy Dissipation in Plants, Algae and Cyanobacteria*, vol. 40 (Springer, 2014).

[70] Frank, H. A. *et al.* Spectroscopic and photochemical properties of open-chain carotenoids. *J. Phys. Chem. B* **106**, 2083–2092 (2002).

[71] McCamant, D. W., Kim, J. E. & Mathies, R. A. Vibrational relaxation in β-carotene probed by picosecond Stokes and anti-Stokes resonance Raman spectroscopy. *J. Phys. Chem. A* **106**, 6030–6038 (2002).

[72] Hashimoto, H., Sugisaki, M. & Yoshizawa, M. Ultrafast time-resolved vibrational spectroscopies of carotenoids in photosynthesis. *Biochim. Biophys. Acta − Bioenerg.* **1847**, 69–78 (2015).

[73] Kramer, H. & Mathis, P. Quantum yield and rate of formation of the carotenoid triplet state in photosynthetic structures. *Biochim. Biophys. Acta − Bioenerg.* **593**, 319–329 (1980).

[74] Götze, J. P., Kröner, D., Banerjee, S., Karasulu, B. & Thiel, W. Carotenoids as a shortcut for chlorophyll Soret-to-Q band energy flow. *ChemPhysChem* **15**, 3392–3401 (2014).

[75] Gradinaru, C. C., van Stokkum, I. H. M., Pascal, A. A., van Grondelle, R. & van Amerongen, H. Identifying the pathways of energy transfer between carotenoids and chlorophylls in LHCII and CP29. A multicolor, femtosecond pump-probe study. *J. Phys. Chem. B* **104**, 9330–9342 (2000).

[76] Croce, R., Müller, M. G., Bassi, R. & Holzwarth, A. R. Carotenoid-to-chlorophyll energy transfer in recombinant major light-harvesting complex (LHCII) of higher plants. I. Femtosecond transient absorption measurements. *Biophys. J.* **80**, 901–915 (2001).

[77] Truscott, T. G. The photophysics and photochemistry of the carotenoids. *J. Photochem. Photobiol. B* **6**, 359–371 (1990).

[78] Frank, H. A. & Cogdell, R. J. Carotenoids in photosynthesis. *Photochem. Photobiol.* **63**, 257–264 (1996).

[79] Krieger-Liszkay, A. Singlet oxygen production in photosynthesis. *J. Exp. Bot.* **56**, 337–346 (2005).

[80] Lang, H. P. & Hunter, C. N. The relationship between carotenoid biosynthesis and the assembly of the light-harvesting LH2 complex in *Rhodobacter sphaeroides*. *Biochem. J.* **298**, 197–205 (1994).

[81] Formaggio, E., Cinque, G. & Bassi, R. Functional architecture of the major light-harvesting complex from higher plants. *J. Mol. Biol.* **314**, 1157–1166 (2001).

[82] Lokstein, H., Tian, L., Polle, J. E. W. & DellaPenna, D. Xanthophyll biosynthetic mutants of *Arabidopsis thaliana*: Altered nonphotochemical quenching of chlorophyll fluorescence is due to changes in photosystem II antenna size and stability. *Biochim. Biophys. Acta − Bioenerg.* **1553**, 309–319 (2002).

[83] Dall'Osto, L. *et al.* Lutein is needed for efficient chlorophyll triplet quenching in the major LHCII antenna complex of higher plants and effective photoprotection *in vivo* under strong light. *BMC Plant Biol.* **6**, 32 (2006).

[84] Giuffra, E., Cugini, D., Croce, R. & Bassi, R. Reconstitution and pigment-binding properties of recombinant CP29. *Eur. J. Biochem.* **238**, 112–120 (1996).

[85] Kleima, F. J. *et al.* Energy transfer in LHCII monomers at 77K studied by subpicosecond transient absorption spectroscopy. *Biochemistry* **36**, 15262–15268 (1997).

[86] Connelly, J. P., Müller, M. G., Bassi, R., Croce, R. & Holzwarth, A. R. Femtosecond transient absorption study of carotenoid to chlorophyll energy transfer in the light-harvesting complex II of photosystem II. *Biochemistry* **36**, 281–287 (1997).

[87] Gradinaru, C. C. *et al.* The flow of excitation energy in LHCII monomers: Implications for the structural model of the major plant antenna. *Biophys. J.* **75**, 3064–3077 (1998).

[88] Salverda, J. M. *et al.* Energy transfer in light-harvesting complexes LHCII and CP29 of spinach studied with three pulse echo peak shift and transient grating. *Biophys. J.* **84**, 450–465 (2003).

[89] Agarwal, R. *et al.* Ultrafast energy transfer in LHC-II revealed by three-pulse photon echo peak shift measurements. *J. Phys. Chem. B* **104**, 2908–2918 (2000).

[90] Schlau-Cohen, G. S. *et al.* Pathways of energy flow in LHCII from two-dimensional electronic spectroscopy. *J. Phys. Chem. B* **113**, 15352–15363 (2009).

[91] Calhoun, T. R. *et al.* Quantum coherence enabled determination of the energy landscape in light-harvesting complex II. *J. Phys. Chem. B* **113**, 16291–16295 (2009).

[92] Wells, K. L., Lambrev, P. H., Zhang, Z., Garab, G. & Tan, H.-S. Pathways of energy transfer in LHCII revealed by room-temperature 2D electronic spectroscopy. *Phys. Chem. Chem. Phys.* **16**, 11640–11646 (2014).

[93] Zhang, Z., Lambrev, P. H., Wells, K. L., Garab, G. & Tan, H.-S. Direct observation of multistep energy transfer in LHCII with fifth-order 3D electronic spectroscopy. *Nat. Commun.* **6**, 7914 (2015).

[94] Duan, H.-G. *et al.* Two-dimensional electronic spectroscopy of light-harvesting complex II at ambient temperature: A joint experimental and theoretical study. *J. Phys. Chem. B* **119**, 12017–12027 (2015).

[95] Akhtar, P. *et al.* Temperature dependence of the energy transfer in LHCII studied by two-dimensional electronic spectroscopy. *J. Phys. Chem. B* **123**, 6765–6775 (2019).

[96] Peterman, E. J. G. *et al.* Xanthophylls in light-harvesting complex II of higher plants: Light harvesting and triplet quenching. *Biochemistry* **36**, 12208–12215 (1997).

[97] van Grondelle, R. & Novoderezhkin, V. I. Energy transfer in photosynthesis: Experimental insights and quantitative models. *Phys. Chem. Chem. Phys.* **8**, 793–807 (2006).

[98] Kwa, S. L. S. *et al.* Ultrafast energy transfer in LHC-II trimers from the Chl a/b light-harvesting antenna of photosystem II. *Biochim. Biophys. Acta – Bioenerg.* **1102**, 202–212 (1992).

[99] Connelly, J. P. *et al.* Ultrafast spectroscopy of trimeric light-harvesting complex II from higher plants. *J. Phys. Chem. B* **101**, 1902–1909 (1997).

[100] Du, M., Xie, X., Mets, L. & Fleming, G. R. Direct observation of ultrafast energy-transfer processes in light harvesting complex II. *J. Phys. Chem.* **98**, 4736–4741 (1994).

[101] Akhtar, P. *et al.* Two-dimensional spectroscopy of chlorophyll *a* excited-state equilibration in light-harvesting complex II. *J. Phys. Chem. Lett.* **8**, 257–263 (2017).

[102] Barzda, V. *et al.* Singlet-singlet annihilation kinetics in aggregates and trimers of LHCII. *Biophys. J.* **80**, 2409–2421 (2001).

[103] Morales, A. & Kaiser, E. Photosynthetic acclimation to fluctuating irradiance in plants. *Front. Plant Sci.* **11**, 268 (2020).

[104] Fleming, G. R., Schlau-Cohen, G. S., Amarnath, K. & Zaks, J. Design principles of photosynthetic light-harvesting. *Faraday Discuss.* **155**, 27–41 (2012).

[105] Erickson, E., Wakao, S. & Niyogi, K. K. Light stress and photoprotection in *Chlamydomonas reinhardtii*. *Plant J.* **82**, 449–465 (2015).

[106] Müller, P., Li, X.-P. & Niyogi, K. K. Non-photochemical quenching. A response to excess light energy. *Plant Physiol.* **125**, 1558–1566 (2001).

[107] Ruban, A. V. Nonphotochemical chlorophyll fluorescence quenching: Mechanism and effectiveness in protecting plants from photodamage. *Plant Physiol.* **170**, 1903–1916 (2016).

[108] Niyogi, K. K. Safety valves for photosynthesis. *Curr. Opin. Plant Biol.* **3**, 455–460 (2000).

[109] Jahns, P., Latowski, D. & Strzalka, K. Mechanism and regulation of the violaxanthin cycle: The role of antenna proteins and membrane lipids. *Biochem. Biophys. Acta – Bioenerg.* **1787**, 3–14 (2009).

[110] Rockholm, D. C. & Yamamoto, H. Y. Violaxanthin de-epoxidase (Purification of a 43-kilodalton lumenal protein from lettuce by lipid-affinity precipitation with monogalactosyldiacylglyceride). *Plant Physiol.* **110**, 697–703 (1996).

[111] Bratt, C. E., Arvidsson, P.-O., Carlsson, M. & Åkerlund, H.-E. Regulation of violaxanthin de-epoxidase activity by pH and ascorbate concentration. *Photosynth. Res.* **45**, 169–175 (1995).

[112] Niyogi, K. K., Grossman, A. R. & Björkman, O. *Arabidopsis* mutants define a central role for the xanthophyll cycle in the regulation of photosynthetic energy conversion. *Plant Cell* **10**, 1121–1134 (1998).

[113] Johnson, M. P., Pérez-Bueno, M. L., Zia, A., Horton, P. & Ruban, A. V. The zeaxanthin-independent and zeaxanthin-dependent qE components of nonphotochemical quenching involve common conformational changes within the photosystem II antenna in *Arabidopsis*. *Plant Physiol.* **149**, 1061–1075 (2009).

[114] Johnson, M. P. & Ruban, A. V. Restoration of rapidly reversible photoprotective energy dissipation in the absence of PsbS protein by enhanced ΔpH. *J. Biol. Chem.* **286**, 19973–19981 (2011).

[115] Johnson, M. P. *et al.* Photoprotective energy dissipation involves the reorganization of photosystem II light-harvesting complexes in the grana membranes of spinach chloroplasts. *Plant Cell* **23**, 1468–1479 (2011).

[116] Horton, P. *et al.* Control of the light-harvesting function of chloroplast membranes by aggregation of the LHCII chlorophyll-protein complex. *FEBS Lett.* **292**, 1–4 (1991).

[117] Horton, P., Ruban, A. V. & Walters, R. G. Regulation of light harvesting in green plants. *Annu. Rev. Plant Physiol. Plant Mol. Biol.* **47**, 655–684 (1996).

[118] Ruban, A. V., Phillip, D., Young, A. J. & Horton, P. Carotenoid-dependent oligomerization of the major chlorophyll a/b light harvesting complex of photosystem II of plants. *Biochemistry* **36**, 7855–7859 (1997).

[119] Miloslavina, Y. *et al.* Far-red fluorescence: A direct spectroscopic marker for LHCII oligomer formation in non-photochemical quenching. *FEBS Lett.* **582**, 3625–3631 (2008).

[120] Morosinotto, T., Baronio, R. & Bassi, R. Dynamics of chromophore binding to Lhc proteins *in vivo* and *in vitro* during operation of the xanthophyll cycle. *J. Biol. Chem.* **277**, 36913–36920 (2002).

[121] Dall'Osto, L. *et al.* Two mechanisms for dissipation of excess light in monomeric and trimeric light-harvesting complexes. *Nat. Plants* **3**, 17033 (2017).

[122] Ruban, A. V. *et al.* Identification of a mechanism of photoprotective energy dissipation in higher plants. *Nature* **450**, 575–578 (2007).

[123] Petrou, K., Belgio, E. & Ruban, A. V. pH sensitivity of chlorophyll fluorescence quenching is determined by the detergent/protein ratio and the state of LHCII aggregation. *Biochim. Biophys. Acta − Bioenerg.* **1837**, 1533–1539 (2014).

[124] van Oort, B., van Hoek, A., Ruban, A. V. & van Amerongen, H. Aggregation of light-harvesting complex II leads to formation of efficient excitation energy traps in monomeric and trimeric complexes. *FEBS Lett.* **581**, 3528–3532 (2007).

[125] Li, X.-P. *et al.* A pigment-binding protein essential for regulation of photosynthetic light harvesting. *Nature* **403**, 391 (2000).

[126] Ruban, A. V., Johnson, M. P. & Duffy, C. D. P. The photoprotective molecular switch in the photosystem II antenna. *Biochim. Biophys. Acta − Bioenerg.* **1817**, 167–181 (2012).

[127] Rochaix, J.-D. Regulation and dynamics of the light-harvesting system. *Annu. Rev. Plant Biol.* **65**, 287–309 (2014).

[128] Teardo, E. *et al.* Evidences for interaction of PsbS with photosynthetic complexes in maize thylakoids. *Biochim. Biophys. Acta − Bioenerg.* **1767**, 703–711 (2007).

[129] Wilk, L., Grunwald, M., Liao, P.-N., Walla, P. J. & Kühlbrandt, W. Direct interaction of the major light-harvesting complex II and PsbS in nonphotochemical quenching. *Proc. Natl. Acad. Sci. U. S. A.* **110**, 5452–5456 (2013).

[130] Gerotto, C., Franchin, C., Arrigoni, G. & Morosinotto, T. *In vivo* identification of photosystem II light harvesting complexes interacting with photosystem II subunit S. *Plant Physiol.* **168**, 1747–1761 (2015).

[131] Frank, H. A. *et al.* Photophysics of the carotenoids associated with the xanthophyll cycle in photosynthesis. *Photosynth. Res.* **41**, 389–395 (1994).

[132] Ma, Y.-Z., Holt, N. E., Li, X.-P., Niyogi, K. K. & Fleming, G. R. Evidence for direct carotenoid involvement in the regulation of photosynthetic light harvesting. *Proc. Natl. Acad. Sci. U. S. A* **100**, 4377–4382 (2003).

[133] Liao, P.-N., Holleboom, C.-P., Wilk, L., Kühlbrandt, W. & Walla, P. J. Correlation of Car $S_1 \rightarrow$ Chl with Chl $\rightarrow$ Car S_1 energy transfer supports the excitonic model in quenched light harvesting complex II. *J. Phys. Chem. B* **114**, 15650–15655 (2010).

[134] Bode, S. *et al.* On the regulation of photosynthesis by excitonic interactions between carotenoids and chlorophylls. *Proc. Natl. Acad. Sci. U. S. A* **106**, 12311–12316 (2009).

[135] Holleboom, C.-P. & Walla, P. J. The back and forth of energy transfer between carotenoids and chlorophylls and its role in the regulation of light harvesting. *Photosynth. Res.* **119**, 215–221 (2014).

[136] Holt, N. E. *et al.* Carotenoid cation formation and the regulation of photosynthetic light harvesting. *Science* **307**, 433–436 (2005).

[137] Ahn, T. K. *et al.* Architecture of a charge-transfer state regulating light harvesting in a plant antenna protein. *Science* **320**, 794–797 (2008).

[138] Amarie, S. *et al.* Carotenoid radical cations as a probe for the molecular mechanism of nonphotochemical quenching in oxygenic photosynthesis. *J. Phys. Chem. B* **111**, 3481–3487 (2007).

[139] Avenson, T. J. *et al.* Zeaxanthin radical cation formation in minor light-harvesting complexes of higher plant antenna. *J. Biol. Chem.* **283**, 3550–3558 (2008).

[140] Müller, M. G. *et al.* Singlet energy dissipation in the photosystem II light-harvesting complex does not involve energy transfer to carotenoids. *ChemPhysChem* **11**, 1289 (2010).

[141] Ostroumov, E. E., Götze, J. P., Reus, M., Lambrev, P. H. & Holzwarth, A. R. Characterization of fluorescent chlorophyll charge-transfer states as intermediates in the excited state quenching of light-harvesting complex II. *Photosynth. Res.* **144**, 171–193 (2020).

[142] Chmeliov, J. *et al.* The nature of self-regulation in photosynthetic light-harvesting antenna. *Nat. Plants* **2**, 16045 (2016).

[143] Akhtar, P. *et al.* Pigment interactions in light-harvesting complex II in different molecular environments. *J. Biol. Chem.* **290**, 4877–4886 (2015).

[144] van Oort, B. *et al.* Revisiting the role of xanthophylls in nonphotochemical quenching. *J. Phys. Chem. Lett.* **9**, 346–352 (2018).

[145] Chukhutsina, V. U., Holzwarth, A. R. & Croce, R. Time-resolved fluorescence measurements on leaves: Principles and recent developments. *Photosynth. Res.* **140**, 355–369 (2019).

[146] Pandit, A. *et al.* Assembly of the major light-harvesting complex II in lipid nanodiscs. *Biophys. J.* **101**, 2507–2515 (2011).

[147] Crisafi, E. & Pandit, A. Disentangling protein and lipid interactions that control a molecular switch in photosynthetic light harvesting. *Biochim. Biophys. Acta − Biomembr.* **1859**, 40–47 (2017).

[148] Tutkus, M. *et al.* Fluorescence microscopy of single liposomes with incorporated pigment–proteins. *Langmuir* **34**, 14410–14418 (2018).

[149] Akhtar, P., Görföl, F., Garab, G. & Lambrev, P. H. Dependence of chlorophyll fluorescence quenching on the lipid-to-protein ratio in reconstituted light-harvesting complex II membranes containing lipid labels. *Chem. Phys.* **522**, 242–248 (2019).

[150] Rideau, E., Dimova, R., Schwille, P., Wurm, F. R. & Landfester, K. Liposomes and polymersomes: A comparative review towards cell mimicking. *Chem. Soc. Rev.* **47**, 8572–8610 (2018).

[151] Dorrington, G. *et al.* Light scattering corrections to linear dichroism spectroscopy for liposomes in shear flow using calcein fluorescence and modified Rayleigh-Gans-Debye-Mie scattering. *Biophys. Rev.* **10**, 1385–1399 (2018).

[152] Bayburt, T. H., Grinkova, Y. V. & Sligar, S. G. Self-assembly of discoidal phospholipid bilayer nanoparticles with membrane scaffold proteins. *Nano Lett.* **2**, 853–856 (2002).

[153] Denisov, I. G. & Sligar, S. G. Nanodiscs in membrane biochemistry and biophysics. *Chem. Rev.* **117**, 4669–4713 (2017).

[154] Jonas, D. M. Two-dimensional femtosecond spectroscopy. *Annu. Rev. Phys. Chem.* **54**, 425–463 (2003).

[155] Brixner, T. *et al.* Two-dimensional spectroscopy of electronic couplings in photosynthesis. *Nature* **434**, 625–628 (2005).

[156] Ginsberg, N. S., Cheng, Y.-C. & Fleming, G. R. Two-dimensional electronic spectroscopy of molecular aggregates. *Acc. Chem. Res.* **42**, 1352–1363 (2009).

[157] Fuller, F. D. *et al.* Vibronic coherence in oxygenic photosynthesis. *Nat. Chem.* **6**, 706–711 (2014).

[158] Lim, J. *et al.* Vibronic origin of long-lived coherence in an artificial molecular light harvester. *Nat. Commun.* **6**, 7755 (2015).

[159] Bakulin, A. A. *et al.* Real-time observation of multiexcitonic states in ultrafast singlet fission using coherent 2D electronic spectroscopy. *Nat. Chem.* **8**, 16–23 (2016).

[160] Scholes, G. D. *et al.* Using coherence to enhance function in chemical and biophysical systems. *Nature* **543**, 647–656 (2017).

[161] Cheng, Y.-C. & Fleming, G. R. Dynamics of light harvesting in photosynthesis. *Annu. Rev. Phys. Chem.* **60**, 241–262 (2009).

[162] Schlau-Cohen, G. S., Ishizaki, A. & Fleming, G. R. Two-dimensional electronic spectroscopy and photosynthesis: Fundamentals and applications to photosynthetic light-harvesting. *Chem. Phys.* **386**, 1–22 (2011).

[163] Wang, L., Allodi, M. A. & Engel, G. S. Quantum coherences reveal excited-state dynamics in biophysical systems. *Nat. Rev. Chem.* **3**, 477–490 (2019).

[164] Collini, E. *et al.* Coherently wired light-harvesting in photosynthetic marine algae at ambient temperature. *Nature* **463**, 644–647 (2010).

[165] Davis, J. A. *et al.* Observation of coherent biexcitons in ZnO/ZnMgO multiple quantum wells at room temperature. *Appl. Phys. Lett.* **89**, 182109 (2006).

[166] Stone, K. W. *et al.* Two-quantum 2D FT electronic spectroscopy of biexcitons in GaAs quantum wells. *Science* **324**, 1169–1173 (2009).

[167] Cundiff, S. T., Zhang, T., Bristow, A. D., Karaiskaj, D. & Dai, X. Optical two-dimensional Fourier transform spectroscopy of semiconductor quantum wells. *Acc. Chem. Res.* **42**, 1423–1432 (2009).

[168] Karaiskaj, D. *et al.* Two-quantum many-body coherences in two-dimensional Fourier-transform spectra of exciton resonances in semiconductor quantum wells. *Phys. Rev. Lett.* **104**, 117401 (2010).

[169] Kasprzak, J. & Langbein, W. Coherent response of individual weakly confined exciton–biexciton systems. *J. Opt. Soc. Am. B* **29**, 1766–1771 (2012).

[170] Caram, J. R. *et al.* Persistent inter-excitonic quantum coherence in CdSe quantum dots. *J. Phys. Chem. Lett.* **5**, 196 (2014).

[171] Cassette, E., Pensack, R. D., Mahler, B. & Scholes, G. D. Room-temperature exciton coherence and dephasing in two-dimensional nanostructures. *Nat. Commun.* **6**, 6086 (2015).

[172] Mehlenbacher, R. D. *et al.* Energy transfer pathways in semiconducting carbon nanotubes revealed using two-dimensional white-light spectroscopy. *Nat. Commun.* **6**, 6732 (2015).

[173] Richter, J. M. *et al.* Ultrafast carrier thermalization in lead iodide perovskite probed with two-dimensional electronic spectroscopy. *Nat. Commun.* **8**, 376 (2017).

[174] Jones, A. C., Kearns, N. M., Ho, J.-J., Flach, J. T. & Zanni, M. T. Impact of non-equilibrium molecular packings on singlet fission in microcrystals observed using 2D white-light microscopy. *Nat. Chem.* **12**, 40–47 (2020).

[175] Hybl, J. D., Albrecht, A. W., Faeder, S. M. G. & Jonas, D. M. Two-dimensional electronic spectroscopy. *Chem. Phys. Lett.* **297**, 307–313 (1998).

[176] Hybl, J. D., Albrecht Ferro, A. & Jonas, D. M. Two-dimensional Fourier transform electronic spectroscopy. *J. Chem. Phys.* **115**, 6606–6622 (2001).

[177] Fuller, F. D. & Ogilvie, J. P. Experimental implementations of two-dimensional Fourier transform electronic spectroscopy. *Annu. Rev. Phys. Chem.* **66**, 667–690 (2015).

[178] Cowan, M. L., Ogilvie, J. P. & Miller, R. J. D. Two-dimensional spectroscopy using diffractive optics based phased-locked photon echoes. *Chem. Phys. Lett.* **386**, 184–189 (2004).

[179] Brixner, T., Mančal, T., Stiopkin, I. V. & Fleming, G. R. Phase-stabilized two-dimensional electronic spectroscopy. *J. Chem. Phys.* **121**, 4221–4236 (2004).

[180] Selig, U. *et al.* Inherently phase-stable coherent two-dimensional spectroscopy using only conventional optics. *Opt. Lett.* **33**, 2851–2853 (2008).

[181] Nemeth, A., Sperling, J., Hauer, J., Kauffmann, H. F. & Milota, F. Compact phase-stable design for single-and double-quantum two-dimensional electronic spectroscopy. *Opt. Lett.* **34**, 3301–3303 (2009).

[182] Spokoyny, B., Koh, C. J. & Harel, E. Stable and high-power few cycle supercontinuum for 2D ultrabroadband electronic spectroscopy. *Opt. Lett.* **40**, 1014–1017 (2015).

[183] Bizimana, L. A., Brazard, J., Carbery, W. P., Gellen, T. & Turner, D. B. Resolving molecular vibronic structure using high-sensitivity two-dimensional electronic spectroscopy. *J. Chem. Phys.* **143**, 164203 (2015).

[184] Kearns, N. M., Mehlenbacher, R. D., Jones, A. C. & Zanni, M. T. Broadband 2D electronic spectrometer using white light and pulse shaping: Noise and signal evaluation at 1 and 100 kHz. *Opt. Express* **25**, 7869–7883 (2017).

[185] Kearns, N. M. *et al.* Two-dimensional white-light spectroscopy using supercontinuum from an all-normal dispersion photonic crystal fiber pumped by a 70 MHz Yb fiber oscillator. *J. Phys. Chem. A* **123**, 3046–3055 (2019).

[186] Lomsadze, B., Smith, B. C. & Cundiff, S. T. Tri-comb spectroscopy. *Nat. Photonics* **12**, 676–680 (2018).

[187] Cerullo, G. & De Silvestri, S. Ultrafast optical parametric amplifiers. *Rev. Sci. Instrum.* **74**, 1–18 (2003).

[188] Wilhelm, T., Piel, J. & Riedle, E. Sub-20-fs pulses tunable across the visible from a blue-pumped single-pass noncollinear parametric converter. *Opt. Lett.* **22**, 1494–1496 (1997).

[189] Cerullo, G., Manzoni, C., Lüer, L. & Polli, D. Time-resolved methods in biophysics. 4. Broadband pump-probe spectroscopy system with sub-20 fs temporal resolution for the study of energy transfer processes in photosynthesis. *Photochem. Photobiol. Sci.* **6**, 135–144 (2007).

[190] Dean, J. C. *et al.* Broadband transient absorption and two-dimensional electronic spectroscopy of methylene blue. *J. Phys. Chem. A* **119**, 9098–9108 (2015).

[191] Son, M., Park, K. H., Yoon, M.-C., Kim, P. & Kim, D. Excited-state vibrational coherence in perylene bisimide probed by femtosecond broadband pump-probe spectroscopy. *J. Phys. Chem. A* **119**, 6275–6282 (2015).

[192] Maiuri, M., Ostroumov, E. E., Saer, R. G., Blankenship, R. E. & Scholes, G. D. Coherent wavepackets in the Fenna-Matthews-Olson complex are robust to excitonic-structure perturbations caused by mutagenesis. *Nat. Chem.* **10**, 177 (2018).

[193] Zheng, H. *et al.* Dispersion-free continuum two-dimensional electronic spectrometer. *Appl. Opt.* **53**, 1909–1917 (2014).

[194] Al Haddad, A. *et al.* Set-up for broadband Fourier-transform multidimensional electronic spectroscopy. *Opt. Lett.* **40**, 312–315 (2015).

[195] Ma, X., Dostál, J. & Brixner, T. Broadband 7-fs diffractive-optic-based 2D electronic spectroscopy using hollow-core fiber compression. *Opt. Express* **24**, 20781–20791 (2016).

[196] Seiler, H., Palato, S., Schmidt, B. E. & Kambhampati, P. Simple fiber-based solution for coherent multidimensional spectroscopy in the visible regime. *Opt. Lett.* **42**, 643–646 (2017).

[197] Alfano, R. R. *The Supercontinuum Laser Source* (Springer, 2006).

[198] Bradler, M., Baum, P. & Riedle, E. Femtosecond continuum generation in bulk laser host materials with sub-μJ pump pulses. *Appl. Phys. B* **97**, 561–574 (2009).

[199] Couairon, A. & Mysyrowicz, A. Femtosecond filamentation in transparent media. *Phys. Rep.* **441**, 47–189 (2007).

[200] Hauri, C. P. *et al.* Generation of intense, carrier-envelope phase-locked few-cycle laser pulses through filamentation. *Appl. Phys. B* **79**, 673–677 (2004).

[201] Hagemann, F., Gause, O., Wöste, L. & Siebert, T. Supercontinuum pulse shaping in the few-cycle regime. *Opt. Express* **21**, 5536–5549 (2013).

[202] Polli, D., Lüer, L. & Cerullo, G. High-time-resolution pump-probe system with broadband detection for the study of time-domain vibrational dynamics. *Rev. Sci. Instrum.* **78**, 103108 (2007).

[203] Kanal, F., Keiber, S., Eck, R. & Brixner, T. 100-kHz shot-to-shot broadband data acquisition for high-repetition-rate pump–probe spectroscopy. *Opt. Express* **22**, 16965–16975 (2014).

[204] Brazard, J., Bizimana, L. A. & Turner, D. B. Accurate convergence of transient-absorption spectra using pulsed lasers. *Rev. Sci. Instrum.* **86**, 053106 (2015).

[205] Hamm, P. & Zanni, M. *Concepts and Methods of 2D Infrared Spectroscopy* (Cambridge University Press, New York, 2011).

[206] Cho, M. *Coherent Multidimensional Spectroscopy*, vol. 226 (Springer, 2019).

[207] Cho, M. *Two-Dimensional Optical Spectroscopy* (CRC press, 2009).

[208] Pervak, V., Ahmad, I., Trubetskov, M. K., Tikhonravov, A. V. & Krausz, F. Double-angle multilayer mirrors with smooth dispersion characteristics. *Opt. Express* **17**, 7943–7951 (2009).

[209] Trebino, R. *et al.* Measuring ultrashort laser pulses in the time-frequency domain using frequency-resolved optical gating. *Rev. Sci. Instrum.* **68**, 3277–3295 (1997).

[210] Zhang, Y., Meyer, K., Ott, C. & Pfeifer, T. Passively phase-stable, monolithic, all-reflective two-dimensional electronic spectroscopy based on a four-quadrant mirror. *Opt. Lett.* **38**, 356–358 (2013).

[211] Albrecht, A. W., Hybl, J. D., Gallagher Faeder, S. M. & Jonas, D. M. Experimental distinction between phase shifts and time delays: Implications for femtosecond spectroscopy and coherent control of chemical reactions. *J. Chem. Phys.* **111**, 10934–10956 (1999).

[212] Romero, E. *et al.* Quantum coherence in photosynthesis for efficient solar-energy conversion. *Nat. Phys.* **10**, 676–682 (2014).

[213] Meneghin, E. *et al.* Coherence in carotenoid-to-chlorophyll energy transfer. *Nat. Commun.* **9**, 3160 (2018).

[214] Prokhorenko, V. I., Halpin, A. & Miller, R. J. D. Coherently-controlled two-dimensional photon echo electronic spectroscopy. *Opt. Express* **17**, 9764–9779 (2009).

[215] Bristow, A. D., Karaiskaj, D., Dai, X. & Cundiff, S. T. All-optical retrieval of the global phase for two-dimensional Fourier-transform spectroscopy. *Opt. Express* **16**, 18017–18027 (2008).

[216] Augulis, R. & Zigmantas, D. Two-dimensional electronic spectroscopy with double modulation lock-in detection: Enhancement of sensitivity and noise resistance. *Opt. Express* **19**, 13126–13133 (2011).

[217] Heisler, I. A., Moca, R., Camargo, F. V. & Meech, S. R. Two-dimensional electronic spectroscopy based on conventional optics and fast dual chopper data acquisition. *Rev. Sci. Instrum.* **85**, 063103 (2014).

[218] Fragnito, H. L., Bigot, J.-Y., Becker, P. C. & Shank, C. V. Evolution of the vibronic absorption spectrum in a molecule following impulsive excitation with a 6 fs optical pulse. *Chem. Phys. Lett.* **160**, 101–104 (1989).

[219] Krebs, N., Pugliesi, I., Hauer, J. & Riedle, E. Two-dimensional Fourier transform spectroscopy in the ultraviolet with sub-20 fs pump pulses and 250–720 nm supercontinuum probe. *New J. Phys.* **15**, 085016 (2013).

[220] Anna, J. M., Ostroumov, E. E., Maghlaoui, K., Barber, J. & Scholes, G. D. Two-dimensional electronic spectroscopy reveals ultrafast downhill energy transfer in photosystem I trimers of the cyanobacterium *Thermosynechococcus elongatus*. *J. Phys. Chem. Lett.* **3**, 3677–3684 (2012).

[221] Pascal, A. A. *et al.* Molecular basis of photoprotection and control of photosynthetic light-harvesting. *Nature* **436**, 134 (2005).

[222] Liguori, N. *et al.* Different carotenoid conformations have distinct functions in light-harvesting regulation in plants. *Nat. Commun.* **8**, 1994 (2017).

[223] Hashimoto, H., Uragami, C., Yukihira, N., Gardiner, A. T. & Cogdell, R. J. Understanding/unravelling carotenoid excited singlet states. *J. R. Soc. Interface* **15**, 20180026 (2018).

[224] Mendes-Pinto, M. M. *et al.* Mechanisms underlying carotenoid absorption in oxygenic photosynthetic proteins. *J. Biol. Chem.* **288**, 18758–18765 (2013).

[225] Croce, R. *et al.* Singlet and triplet state transitions of carotenoids in the antenna complexes of higher-plant photosystem I. *Biochemistry* **46**, 3846–3855 (2007).

[226] Son, M., Mosquera-Vázquez, S. & Schlau-Cohen, G. S. Ultrabroadband 2D electronic spectroscopy with high-speed, shot-to-shot detection. *Opt. Express* **25**, 18950–18962 (2017).

[227] Polívka, T. *et al.* Carotenoid S_1 state in a recombinant light-harvesting complex of photosystem II. *Biochemistry* **41**, 439–450 (2002).

[228] Christensson, N. *et al.* Two-dimensional electronic spectroscopy of β-carotene. *J. Phys. Chem. B* **113**, 16409–16419 (2009).

[229] Butkus, V., Zigmantas, D., Valkunas, L. & Abramavicius, D. Vibrational vs. electronic coherences in 2D spectrum of molecular systems. *Chem. Phys. Lett.* **545**, 40–43 (2012).

[230] Frähmcke, J. S. & Walla, P. J. Coulombic couplings between pigments in the major light-harvesting complex LHC II calculated by the transition density cube method. *Chem. Phys. Lett.* **430**, 397–403 (2006).

[231] Cho, M. Coherent two-dimensional optical spectroscopy. *Chem. Rev.* **108**, 1331–1418 (2008).

[232] Caffarri, S., Croce, R., Breton, J. & Bassi, R. The major antenna complex of photosystem II has a xanthophyll binding site not involved in light harvesting. *J. Biol. Chem.* **276**, 35924–35933 (2001).

[233] Dexheimer, S. L. *et al.* Femtosecond impulsive excitation of nonstationary vibrational states in bacteriorhodopsin. *Chem. Phys. Lett.* **188**, 61–66 (1992).

[234] Jonas, D. M., Bradforth, S. E., Passino, S. A. & Fleming, G. R. Femtosecond wavepacket spectroscopy: Influence of temperature, wavelength, and pulse duration. *J. Phys. Chem.* **99**, 2594–2608 (1995).

[235] Vos, M. H., Rappaport, F., Lambry, J.-C., Breton, J. & Martin, J.-L. Visualization of coherent nuclear motion in a membrane protein by femtosecond spectroscopy. *Nature* **363**, 320–325 (1993).

[236] Wang, Q., Schoenlein, R. W., Peteanu, L. A., Mathies, R. A. & Shank, C. V. Vibrationally coherent photochemistry in the femtosecond primary event of vision. *Science* **266**, 422–424 (1994).

[237] McClure, S. D., Turner, D. B., Arpin, P. C., Mirkovic, T. & Scholes, G. D. Coherent oscillations in the PC577 cryptophyte antenna occur in the excited electronic state. *J. Phys. Chem. B* **118**, 1296–1308 (2014).

[238] Dean, J. C. & Scholes, G. D. Coherence spectroscopy in the condensed phase: Insights into molecular structure, environment, and interactions. *Acc. Chem. Res.* **50**, 2746–2755 (2017).

[239] Volpato, A., Bolzonello, L., Meneghin, E. & Collini, E. Global analysis of coherence and population dynamics in 2D electronic spectroscopy. *Opt. Express* **24**, 24773–24785 (2016).

[240] van Stokkum, I. H. M., Larsen, D. S. & van Grondelle, R. Global and target analysis of time-resolved spectra. *Biochim. Biophys. Acta − Bioenerg.* **1657**, 82–104 (2004).

[241] Palacios, M. A. *et al.* Stark spectroscopy of the light-harvesting complex II in different oligomerisation states. *Biochim. Biophys. Acta − Bioenerg.* **1605**, 83–95 (2003).

[242] Rogl, H., Schödel, R., Lokstein, H., Kühlbrandt, W. & Schubert, A. Assignment of spectral substructures to pigment-binding sites in higher plant light-harvesting complex LHC-II. *Biochemistry* **41**, 2281–2287 (2002).

[243] Fragata, M., Nordén, B. & Kurucsev, T. Linear dichroism (250–700 nm) of chlorophyll *a* and pheophytin *a* oriented in a lamellar phase of glycerylmonooctanoate/H_2O. Characterization of electronic transitions. *Photochem. Photobiol.* **47**, 133–143 (1988).

[244] Knox, R. S. & Spring, B. Q. Dipole strengths in the chlorophylls. *Photochem. Photobiol.* **77**, 497–501 (2003).

[245] Hägele, W., Schmid, D., Drissler, F., Nauš, J. & Wolf, H. C. Optical spectra of chlorophyll a and b molecules and complexes in PMMA and MTHF. *Z. Naturforsch. A* **33**, 1197–1205 (1978).

[246] Butkus, V. *et al.* Coherence and population dynamics of chlorophyll excitations in FCP complex: Two-dimensional spectroscopy study. *J. Chem. Phys.* **142**, 212414 (2015).

[247] Moca, R., Meech, S. R. & Heisler, I. A. Two-dimensional electronic spectroscopy of chlorophyll a: Solvent dependent spectral evolution. *J. Phys. Chem. B* **119**, 8623–8630 (2015).

[248] Senlik, S. S., Policht, V. R. & Ogilvie, J. P. Two-color nonlinear spectroscopy for the rapid acquisition of coherent dynamics. *J. Phys. Chem. Lett.* **6**, 2413–2420 (2015).

[249] Policht, V. R., Niedringhaus, A. & Ogilvie, J. P. Characterization of vibrational coherence in monomeric bacteriochlorophyll a by two-dimensional electronic spectroscopy. *J. Phys. Chem. Lett.* **9**, 6631–6637 (2018).

[250] Butkus, V., Zigmantas, D., Abramavicius, D. & Valkunas, L. Distinctive character of electronic and vibrational coherences in disordered molecular aggregates. *Chem. Phys. Lett.* **587**, 93–98 (2013).

[251] Dostál, J., Mančal, T., Vácha, F., Pšenčík, J. & Zigmantas, D. Unraveling the nature of coherent beatings in chlorosomes. *J. Chem. Phys.* **140**, 115103 (2014).

[252] Niyogi, K. K. & Truong, T. B. Evolution of flexible non-photochemical quenching mechanisms that regulate light harvesting in oxygenic photosynthesis. *Curr. Opin. Plant Biol.* **16**, 307–314 (2013).

[253] Horton, P., Wentworth, M. & Ruban, A. Control of the light harvesting function of chloroplast membranes: The LHCII-aggregation model for non-photochemical quenching. *FEBS Lett.* **579**, 4201–4206 (2005).

[254] Gruber, J. M., Malỳ, P., Krüger, T. P. J. & van Grondelle, R. From isolated light-harvesting complexes to the thylakoid membrane: A single-molecule perspective. *Nanophotonics* **7**, 81–92 (2018).

[255] Ogren, J. I. *et al.* Impact of the lipid bilayer on energy transfer kinetics in the photosynthetic protein LH2. *Chem. Sci.* **9**, 3095–3104 (2018).

[256] Park, S. *et al.* Snapshot transient absorption spectroscopy of carotenoid radical cations in high-light-acclimating thylakoid membranes. *J. Phys. Chem. Lett.* **8**, 5548–5554 (2017).

[257] Park, S. *et al.* Chlorophyll-carotenoid excitation energy transfer in high-light-exposed thylakoid membranes investigated by snapshot transient absorption spectroscopy. *J. Am. Chem. Soc.* **140**, 11965–11973 (2018).

[258] Ritchie, T. K. *et al.* Reconstitution of membrane proteins in phospholipid bilayer nanodiscs. *Methods Enzymol.* **464**, 211–231 (2009).

[259] Georgakopoulou, S. *et al.* Understanding the changes in the circular dichroism of light harvesting complex II upon varying its pigment composition and organization. *Biochemistry* **46**, 4745–4754 (2007).

[260] Garab, G. & van Amerongen, H. Linear dichroism and circular dichroism in photosynthesis research. *Photosynth. Res.* **101**, 135–146 (2009).

[261] Wang, K. *et al.* 9-*cis*-Neoxanthin in light harvesting complexes of photosystem II regulates the binding of violaxanthin and xanthophyll cycle. *Plant Physiol.* **174**, 86–96 (2017).

[262] Fox, K. F. *et al.* The carotenoid pathway: What is important for excitation quenching in plant antenna complexes? *Phys. Chem. Chem. Phys.* **19**, 22957–22968 (2017).

[263] Remelli, R., Varotto, C., Sandonà, D., Croce, R. & Bassi, R. Chlorophyll binding to monomeric light-harvesting complex. A mutation analysis of chromophore-binding residues. *J. Biol. Chem.* **274**, 33510–33521 (1999).

[264] Johnson, M. P., Zia, A., Horton, P. & Ruban, A. V. Effect of xanthophyll composition on the chlorophyll excited state lifetime in plant leaves and isolated LHCII. *Chem. Phys.* **373**, 23–32 (2010).

[265] Antognazza, M. R. *et al.* Ultrafast excited state relaxation in long-chain polyenes. *Chem. Phys.* **373**, 115–121 (2010).

[266] Polli, D. *et al.* Carotenoid-bacteriochlorophyll energy transfer in LH2 complexes studied with 10-fs time resolution. *Biophys. J.* **90**, 2486–2497 (2006).

[267] Ishizaki, A., Calhoun, T. R., Schlau-Cohen, G. S. & Fleming, G. R. Quantum coherence and its interplay with protein environments in photosynthetic electronic energy transfer. *Phys. Chem. Chem. Phys.* **12**, 7319–7337 (2010).

[268] Johnson, M. P. & Ruban, A. V. Photoprotective energy dissipation in higher plants involves alteration of the excited state energy of the emitting chlorophyll(s) in LHCII. *J. Biol. Chem.* **284**, 23592–23601 (2009).

[269] Saccon, F. *et al.* Spectroscopic properties of violaxanthin and lutein triplet states in LHCII are independent of carotenoid composition. *J. Phys. Chem. B* **123**, 9312–9320 (2019).

[270] van Oort, B., van Hoek, A., Ruban, A. V. & van Amerongen, H. Equilibrium between quenched and nonquenched conformations of the major plant light-harvesting complex studied with high-pressure time-resolved fluorescence. *J. Phys. Chem. B* **111**, 7631–7637 (2007).

[271] Tian, L., Dinc, E. & Croce, R. LHCII populations in different quenching states are present in the thylakoid membranes in a ratio that depends on the light conditions. *J. Phys. Chem. Lett.* **6**, 2339–2344 (2015).

[272] Mascoli, V. *et al.* Capturing the quenching mechanism of light-harvesting complexes of plants by zooming in on the ensemble. *Chem* **5**, 2900–2912 (2019).

[273] Krüger, T. P. J., Novoderezhkin, V. I., Ilioaia, C. & van Grondelle, R. Fluorescence spectral dynamics of single LHCII trimers. *Biophys. J.* **98**, 3093–3101 (2010).

[274] Schlau-Cohen, G. S. *et al.* Single-molecule identification of quenched and unquenched states of LHCII. *J. Phys. Chem. Lett.* **6**, 860–867 (2015).

[275] Krüger, T. P. J., Wientjes, E., Croce, R. & van Grondelle, R. Conformational switching explains the intrinsic multifunctionality of plant light-harvesting complexes. *Proc. Natl. Acad. Sci. U. S. A* **108**, 13516–13521 (2011).

[276] Kondo, T., Pinnola, A., Chen, D. L., Wei Jia, Bassi, R. & Schlau-Cohen, G. S. Single-molecule spectroscopy of LHCSR1 protein dynamics identifies two distinct states responsible for multi-timescale photosynthetic photoprotection. *Nat. Chem.* **9**, 772 (2017).

[277] Staleva, H. *et al.* Mechanism of photoprotection in the cyanobacterial ancestor of plant antenna proteins. *Nat. Chem. Biol.* **11**, 287 (2015).

[278] Chmeliov, J. *et al.* An 'all pigment' model of excitation quenching in LHCII. *Phys. Chem. Chem. Phys.* **17**, 15857–15867 (2015).

[279] Luchowski, R. *et al.* Instrument response standard in time-resolved fluorescence. *Rev. Sci. Instrum.* **80**, 033109 (2009).

[280] Schwille, P., Haupts, U., Maiti, S. & Webb, W. W. Molecular dynamics in living cells observed by fluorescence correlation spectroscopy with one-and two-photon excitation. *Biophys. J.* **77**, 2251–2265 (1999).

[281] Bello, O. D., Auclair, S. M., Rothman, J. E. & Krishnakumar, S. S. Using ApoE nanolipoprotein particles to analyze SNARE-induced fusion pores. *Langmuir* **32**, 3015–3023 (2016).

[282] Dorne, A.-J., Joyard, J. & Douce, R. Do thylakoids really contain phosphatidylcholine? *Proc. Natl. Acad. Sci. U. S. A* **87**, 71–74 (1990).

[283] Kobayashi, K. Role of membrane glycerolipids in photosynthesis, thylakoid biogenesis and chloroplast development. *J. Plant Res.* **129**, 565–580 (2016).

[284] Seiwert, D., Witt, H., Janshoff, A. & Paulsen, H. The non-bilayer lipid MGDG stabilizes the major light-harvesting complex (LHCII) against unfolding. *Sci. Rep.* **7**, 5158 (2017).

[285] Tietz, S. *et al.* A proteoliposome-based system reveals how lipids control photosynthetic light harvesting. *J. Biol. Chem.* **295**, 1857–1866 (2020).

[286] Havaux, M., Bonfils, J.-P., Lütz, C. & Niyogi, K. K. Photodamage of the photosynthetic apparatus and its dependence on the leaf developmental stage in the *npq*1 Arabidopsis mutant deficient in the xanthophyll cycle enzyme violaxanthin de-epoxidase. *Plant Physiol.* **124**, 273–284 (2000).

[287] Xu, P., Tian, L., Kloz, M. & Croce, R. Molecular insights into zeaxanthin-dependent quenching in higher plants. *Sci. Rep.* **5**, 13679 (2015).

[288] Pinnola, A. *et al.* Functional modulation of LHCSR1 protein from *Physcomitrella patens* by zeaxanthin binding and low pH. *Sci. Rep.* **7**, 11158 (2017).

[289] Son, M., Pinnola, A., Gordon, S. C., Bassi, R. & Schlau-Cohen, G. S. Observation of dissipative chlorophyll-to-carotenoid energy transfer in light-harvesting complex II in membrane nanodiscs. *Nat. Commun.* **11**, 1295 (2020).

[290] Natali, A. *et al.* Light-harvesting complexes (LHCs) cluster spontaneously in membrane environment leading to shortening of their excited state lifetimes. *J. Biol. Chem.* **291**, 16730–16739 (2016).

[291] Croce, R., Weiss, S. & Bassi, R. Carotenoid-binding sites of the major light-harvesting complex II of higher plants. *J. Biol. Chem.* **274**, 29613–29623 (1999).

[292] Gruszecki, W. I., Grudzinski, W., Gospodarek, M., Patyra, M. & Maksymiec, W. Xanthophyll-induced aggregation of LHCII as a switch between light-harvesting and energy dissipation systems. *Biochim. Biophys. Acta − Bioenerg.* **1757**, 1504–1511 (2006).

[293] Crisafi, E., Krishnan, M. & Pandit, A. Time-resolved fluorescence analysis of LHCII in the presence of PsbS at neutral and low pH. *bioRxiv* DOI: 10.1101/456046 (2018).

[294] Niedzwiedzki, D. M., Sullivan, J. O., Polívka, T., Birge, R. R. & Frank, H. A. Femtosecond time-resolved transient absorption spectroscopy of xanthophylls. *J. Phys. Chem. B* **110**, 22872–22885 (2006).

[295] Ramanan, C., Ferretti, M., van Roon, H., Novoderezhkin, V. I. & van Grondelle, R. Evidence for coherent mixing of excited and charge-transfer states in the major plant light-harvesting antenna, LHCII. *Phys. Chem. Chem. Phys.* **19**, 22877–22886 (2017).

[296] Horton, P., Ruban, A. V. & Wentworth, M. Allosteric regulation of the light-harvesting system of photosystem II. *Philos. Trans. R. Soc. Lond. B Biol. Sci.* **355**, 1361–1370 (2000).

[297] Polívka, T., Herek, J. L., Zigmantas, D., Åkerlund, H.-E. & Sundström, V. Direct observation of the (forbidden) S_1 state in carotenoids. *Proc. Natl. Acad. Sci. U. S. A* **96**, 4914–4917 (1999).

[298] Ruban, A. V. & Johnson, M. P. Xanthophylls as modulators of membrane protein function. *Arch. Biochem. Biophys.* **504**, 78–85 (2010).

[299] Son, M., Pinnola, A. & Schlau-Cohen, G. S. Zeaxanthin independence of photophysics in light-harvesting complex II in a membrane environment. *Biochim. Biophys. Acta − Bioenerg.* **1861**, 148115 (2020).

[300] Adams, P. G., Vasilev, C., Hunter, C. N. & Johnson, M. P. Correlated fluorescence quenching and topographic mapping of light-harvesting complex II within surface-assembled aggregates and lipid bilayers. *Biochim. Biophys. Acta − Bioenerg.* **1859**, 1075–1085 (2018).

[301] Betterle, N. *et al.* Light-induced dissociation of an antenna hetero-oligomer is needed for non-photochemical quenching induction. *J. Biol. Chem.* **284**, 15255–15266 (2009).

[302] Barros, T. & Kühlbrandt, W. Crystallisation, structure and function of plant light-harvesting complex II. *Biochim. Biophys. Acta − Bioenerg.* **1787**, 753–772 (2009).

[303] Lambrev, P. H. *et al.* Importance of trimer-trimer interactions for the native state of the plant light-harvesting complex II. *Biochim. Biophys. Acta − Bioenerg.* **1767**, 847–853 (2007).

[304] Ilioaia, C. *et al.* Origin of absorption changes associated with photoprotective energy dissipation in the absence of zeaxanthin. *J. Biol. Chem.* **286**, 91–98 (2011).

[305] Ruban, A. V., Pascal, A. A., Robert, B. & Horton, P. Activation of zeaxanthin is an obligatory event in the regulation of photosynthetic light harvesting. *J. Biol. Chem.* **277**, 7785–7789 (2002).

[306] Li, X.-P. *et al.* Regulation of photosynthetic light harvesting involves intrathylakoid lumen pH sensing by the PsbS protein. *J. Biol. Chem.* **279**, 22866–22874 (2004).

[307] Duffy, C. D. P. *et al.* A theoretical investigation of the photophysical consequences of major plant light-harvesting complex aggregation within the photosynthetic membrane. *J. Phys. Chem. B* **114**, 15244–15253 (2010).

[308] Billsten, H. H., Sundström, V. & Polívka, T. Self-assembled aggregates of the carotenoid zeaxanthin: Time-resolved study of excited states. *J. Phys. Chem. A* **109**, 1521–1529 (2005).

[309] Ware, M. A., Dall'Osto, L. & Ruban, A. V. An *in vivo* quantitative comparison of photoprotection in *Arabidopsis* xanthophyll mutants. *Front. Plant Sci.* **7**, 841 (2016).

[310] Bergantino, E. *et al.* Light-and pH-dependent structural changes in the PsbS subunit of photosystem II. *Proc. Natl. Acad. Sci. U. S. A.* **100**, 15265–15270 (2003).

[311] Pawlak, K. *et al.* On the PsbS-induced quenching in the plant major light-harvesting complex LHCII studied in proteoliposomes. *Photosynth. Res.* **144**, 195–208 (2020).

[312] Perri, A. *et al.* Time-and frequency-resolved fluorescence with a single TCSPC detector via a Fourier-transform approach. *Opt. Express* **26**, 2270–2279 (2018).

[313] Bassi, R. & Simpson, D. Chlorophyll-protein complexes of barley photosystem I. *FEBS J.* **163**, 221–230 (1987).

[314] Gilmore, A. M. & Yamamoto, H. Y. Zeaxanthin formation and energy-dependent fluorescence quenching in pea chloroplasts under artificially mediated linear and cyclic electron transport. *Plant Physiol.* **96**, 635–643 (1991).

[315] Morrow, J. A., Arnold, K. S. & Weisgraber, K. H. Functional characterization of apolipoprotein E isoforms overexpressed in *Escherichia coli*. *Protein Expr. Purif.* **16**, 224–230 (1999).

[316] Moon, S. *et al.* Endotoxin-free purification of recombinant membrane scaffold protein expressed in *Escherichia coli*. *Process Biochem.* **66**, 230–236 (2018).

[317] Boldog, T., Li, M. & Hazelbauer, G. L. Using nanodiscs to create water-soluble transmembrane chemoreceptors inserted in lipid bilayers. *Methods Enzymol.* **423**, 317–335 (2007).

[318] Boekema, E. J. Negative staining of integral membrane proteins. *Micron Microscop. Acta* **22**, 361–369 (1991).

[319] Douce, R. & Joyard, J. Biosynthesis of thylakoid membrane lipids. In Ort, D. R. & Yocum, C. F. (eds.) *Advances in Photosynthesis/Oxygenic Photosynthesis: The Light Reactions* (Kluwer Academic Publishers, 1996).